Spring 1-1-2014

The Particle Based Moving Interface Method for Soft Matter Mechanics and Fluid/membrane Interactions with Applications to Biological Cells

Louis Cyrille Foucard
University of Colorado at Boulder, foucard@colorado.edu

The Particle based Moving Interface Method for soft matter mechanics and fluid/membrane interactions with applications to biological cells

by

Louis C. Foucard

B.A Ecole Special des Travaux Publics, 2010

M.A University of Colorado at Boulder, 2011

A thesis submitted to the

faculty of graduate school of the

University of Colorado in partial fulfilment

of the requirement for the degree of

Doctor of Philosophy

Department of Civil, Environmental

and Architectural Engineering

2014

This thesis entitled:

The Particle based Moving Interface Method for soft matter mechanics and fluid/membrane interactions with applications to biological cells

written by Louis C. Foucard

has been approved by the Department of Civil, Environmental and Architectural Engineering

---

Franck J. Vernerey

John Pellegrino

07/29/2014

The final copy of this thesis has been examined by the signatories, and we find that both the content and the form meet acceptable presentation standards of scholarly work in the above mentioned discipline.

Foucard, Louis Cyrille (Ph.D, Civil, Environmental and Architectural Engineering)
The Particle based Moving Interface Method for soft matter mechanics and fluid/membrane interactions with applications to biological cells.
A thesis directed by Associate Professor Franck J. Vernerey

The mechanics of the interaction between a fluid and a soft interface (such as an elastic membrane or shell) undergoing large deformations appears in many places, such as in biological systems or industrial processes. We present here an Eulerian approach that describes the mechanics of an interface and its interactions with a surrounding fluid via the so-called Navier boundary condition. The interface is modeled as a curvilinear surface with arbitrary mechanical properties across which discontinuities in pressure and tangential fluid velocity can naturally be enforced using a modified version of the extended finite element method. The tracking and evolution of the membrane is then handled with the Grid Based Particle method, and the handling of complex singular boundary conditions around sharp corner is accounted for with the use of an asymptotic/numerical matching method. We show that this method is ideal to describe large membrane deformations, enforce volume constraints, and Navier boundary conditions on the interface with velocity/pressure discontinuities. The method is applied to the study of the filtration of deformable particles through a fibrous network, and an the equivalent permeabilities with respect to the fluid and particles are estimated. The method is then adapted to the study of an elastic material in an Eulerian framework and is shown to be capable of handling arbitrarily large deformations, which is ideal for the study of biological problems.

Dedication

I dedicate my dissertation work to my family and friends. A special feeling of gratitude to my loving parents, Dominique and Veronique Foucard whose words of encouragement and constant support lifted my spirit throughout all these years. My brother and sisters Marie, Charles, Anne-Sophie and Camille have never left my side and are very special.

I also dedicate this dissertation to my friends in France and in the United States who have supported me throughout the process. I will always appreciate for their help in letting off steam when needed. I dedicate this work and give special thanks to Jamie Krey, Nicolas Paulze d'Yvois, Kevin Baud, Laurent and Patrick Larget for being there for me throughout the entire doctorate program.

Acknowledgement

This project would not have been possible without the support of many people. Many thanks to my adviser, Franck J. Vernerey, who read my numerous article revisions, helped make some sense of the confusion and supported me all these years. Our many discussions helped in cultivating my sense of curiosity and sparked many questions which I hope to begin to answer some day. Also thanks to my co-advisor John Pellegrino for the insightful discussions and who made very useful suggestions in redacting this thesis. Finally I would like to thanks to my committee members Richard Regueiro, Ronald Pak and David Bortz who offered guidance and support.

Contents

List of Figures

Introduction

The problem of embedded soft bodies and membranes undergoing large shape changes is relevant to many areas of engineering and biological research but still remains a significant computational challenge. Particular examples of this problem include the mechanics of the cell membrane and vesicles and the extreme deformations they are subjected to during migration [128, 166, 58, 59, 23, 129], blebbing [31, 155, 56, 32], division [16] and budding [109, 174]. The ability of biological tissues to adapt and respond to external mechanical stimuli is also at the heart of a variety of biological phenomena, such as morphogenesis [72], wound healing [107] or cancer dynamics [121, 105, 26]. This behavior arises from the capacity of certain cells (i.e. fibroblasts) to generate a network of contractile *Stress Fibers* (SFs) which attach to the surrounding extracellular matrix (ECM) via *Focal Adhesions* (FAs). This dynamic structure enables cells to sense their mechanical environment and react to any changes in stretch, stress or stiffness by applying contractile forces, which ultimately results in ECM deformation and remodeling [162, 166]. The complex dynamics at the heart of many of these vital cell functions are found to rely heavily on the mechanics that take place inside the cell itself and around the cell's membrane. However, in order to understand such an intricate system and develop predictive models, one needs to be able to simulate the large deformations and constant remodelling of the cell, as well as its interactions with the external environment. The present work therefore aims at developing the theoretical and numerical tools needed to describe: (a) the mechanics of an immersed membrane in part I and (b) the mechanics of immersed soft matter in part II, as these two aspects are fundamental in describing such biological problems. The organization of the thesis is as follows.

In chapter 1 of part I, the reader is first provided with a global overview of the Particle based Moving Interface Method (PMIM) designed to study the immersed membrane problem. The global scope and novelties of the method are described, and a summary of the structure of the PMIM is given. Throughout chapter 1, the reader will be referred to chapter 2 for the theoretical and numerical details of the implementation. The objective of chapter 3 is to adapt the method to more complex boundary conditions by introducing an X-FEM based numerical-asymptotic expansion for simulating a Stokes flow near a sharp corner, which will be needed

when simulating the flow of particle througha fibrous network for example. The fourth and fifth chapters apply the methods introduced in the first three chapters to biologically relevant problems. Chapter 4 studies the permeation of soft particles through filtration membranes and estimates the equivalent permeabilities of different fibrous networks with respect to the vesicles as well as the solvent in which they are immersed. Chapter 5 adapts the immersed thin membrane formulation to the study of the membrane of biological cells and shows that it can successfully describe complex behaviors such as endocytosis or cell blebbing. Finally, chapter 6 walks the reader through the numerical implementation of the method by presenting and commenting extracts from the code itself.

While the six four chapters in part I mainly focus on the mechanics of the cell's and vesicle's membrane, the objective of the two last chapters in part II is to concentrate on the mechanics that take place inside biological cells. Chapter 7 presents a numerical formulation for the mechanics of embedded soft matter in an Eulerian framework. This last formulation reuses many of the numerical tools developed in the first chapter, and constitutes a numerical framework perfectly adapted to the study of the large deformations as well as the anisotropic/viscoelastic constitutive models of live cells. Finally, chapter 8 aims at formulating such a constitutive model by introducing a simple thermodynamical model that describes the formation and orientation of stress fibers in contractile cells. It is shown that the model is able to capture key mechanisms of SF organization in contractile cells on substrate of variable stiffness and subjected to arbitrary stretching conditions.

Part I

The immersed membrane system

Chapter 1

Global overview of the Particle-based Moving Interface Method

The objective of this chapter to give the reader a general view of the proposed numerical framework, which is described in details in chapters 2 and 3. As we go over the structure of the PMIM, the reader will be referred to various sections in the chapters of part I for the details of the implementation.

1.1 Scope and novelties of the method

The PMIM is designed to be able to simulate the mechanics of a membrane undergoing arbitrary large deformations and interacting with an incompressible fluid, within the assumption of a Stokes flow regime. Simulating such problems consists in solving a set of partial differential equations on a domain with a moving boundary. As mentioned in the introduction, various mesh-based methods have been developed to approximate partial differential equations. These methods mostly fall within two categories: the Boundary-Fitted methods and the Immersed-Boundary methods. In the case of the Boundary-Fitted methods, the mesh used to geometrically discretize the system is fitted to the boundary (Fig. 1.1a), which makes the enforcement of constraints or application of forces on the boundary an effortless process. This is commonly used in most finite element methods formulated on curvilinear geometries or unstructured meshes.

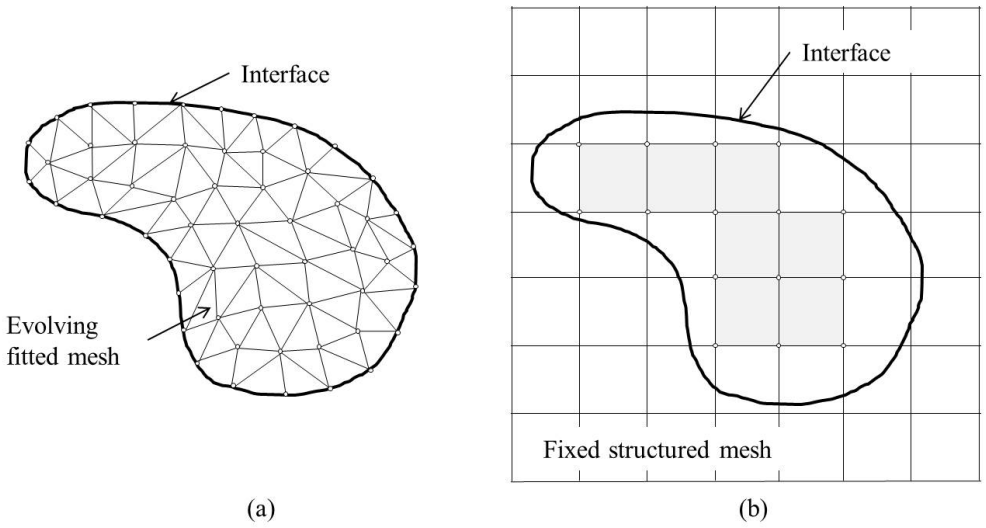

Figure 1.1: *(a) unstructured mesh used in Boundary-Fitted methods and (b) structured mesh used in Immersed-Boundary methods.*

On the other hand, the Immersed-boundary methods correspond to the case where the computational mesh is generated without consideration for the geometry of the boundary (Fig. 1.1b), which considerably simplifies the of generation of the mesh but complicates the enforcement of conditions on the boundary.

Many approximation techniques that belong to the class of Immersed-Boundary methods have been proposed over the last few decades [124, 126, 125]. Indeed, generating a mesh that fits complex geometries still remains a computational challenge and a time consuming task, especially in three dimensions, and the difficulties inherent to the generation of a fitted mesh become particularly clear when dealing with evolving boundaries, as it is the case for the immersed membrane problem. One of the principal advantages of the Immersed-Boundary methods resides in eliminating the issue associated with meshing complicated geometries. The method particularly relies on three features: the fluid flow equations are handled on the structured, fixed Eulerian grid, the membrane deformation are described within a Lagrangian evolving frame and the fluid-structure interactions are handled via a forcing term that is localized on the membrane domain. It is able to simulate the deformation of thin boundaries as well as three-dimensional structures immersed in an incompressible flow [176, 186, 173]. An approach similar to the IB method is

the Distributed Lagrange Multipler/Fictitious Domain (DLM/FD) method [69, 68], which has also been adapted to simulate deformable thin surfaces [158, 7]. Here, the coupling between the fluid and the structure is enforced in the entire domain occupied by the structure. The structure is therefore tied to the underlying fictitious flow and has to deform in an incompressible way, which limits the type of materials that can be simulated.

Another approach developed to study fluid/interface interaction within the creeping flow regime is the Boundary Integral (BI) method, where only the surface of the interface needs to be discretized. The method is very successful at simulating drops in viscous flows [12, 189], and was also extended to elastic interfaces by using the projection of the velocity gradient of the surrounding fluid to find the deformation rate of the interface [131, 180].

Most of these methods have in common a Lagrangian mesh for the structure interacting with the fluid and cannot easily handle the large deformations or viscoelastic behaviors observed in many biological systems. Indeed, when the membrane is described in a Lagrangian framework, extreme deformations often lead to severe distortions of the finite element mesh, an issue that can only be approached by complicated and/or computationally expensive mesh regularization techniques [104, 123].

A solution to this problem was presented by Cottet *et al* in[37] via the introduction of a fully Eulerian description of the system, in which kinematic quantities representing the interface motion (such as position or dilation) are implicitly described by a level-set function which is defined and updated on a fixed underlying Eulerian grid. The approach has the advantage of removing the need for discretizing the two-dimensional surface and effectively eliminates the issue of mesh distortion. Using this formulation, the authors successfully predicted the equilibrium shape of a red blood cell and showed that large membrane deformation could be naturally handled. Similar level-set approaches are typically used to simulate fluid interfaces and bio-film growth [141, 52] and generalized to elasto-plastic materials [156, 117], as well as hyperelastic materials [85, 38, 81, 101]. More recently, the level-set technique was implemented in combination with remeshed smoothed particle hydrodynamics, where the fluid is simulated on adaptive Lagrangian particle and the interface conditions are enforced using the Immersed-Boundary techniques [77].

Two major limitations of existing level-set formulations however are as follows. First, a level-set function is typically unable to carry and transport lagrangian information associated with the interface, such as, for instance, the interface strain or a concentration of interface particles. The technique is therefore restricted to fluid interfaces or limited cases of elastic behaviors [37]. Second, the level-set formulation implicitely assumes that the fluid flow is continuous across the interface ('stick' condition between fluid and interface). This precludes the consideration of 'slip' conditions, that are known to be preponderant in many situations such as flows at the micro or nano scale [108], on hydrophobic surfaces, or even on hydrophilic surfaces under certain conditions [4].

The objective of Part I of the thesis is to introduce the reader to the PMIM, a general theoretical and computational framework that can accurately describe the large deformation of an immersed thin membrane and its interactions with the surrounding fluid in a variety of situations. We specifically propose the following three contributions:

- (a) The model endows the interface with its own independent velocity and curvilinear coordinate system, which is required for the calculation of the surface velocity gradient that dictates the interface deformation, and for the implementation of the Navier boundary condition.

- (b) The method uses a modified version of the X-FEM that naturally handles discontinuities in pressure and tangential velocity arising from the Navier boundary condition and the interface elastic stress. Introducing the tangential enrichment in the velocity field only imposes the discontinuity in the tangential direction and the continuity condition in the normal direction is automatically satisfied, which eliminates the need for an additional Lagrange multiplier field.

- (c) The Extended Finite element method is used in combination with a grid-based particle method [100] to provide an explicit, high definition description of the geometry of the interface and to transport the Lagrangian quantities on the interface. This method of tracking the interface geometry is not subject to mesh distortion and can therefore handle arbitrarily large deformations without needing time consuming mesh reinitialization

algorithms.

Before getting into the details of the implementation in chapter 2 and 3, let us first summarize the basic structure of the PMIM.

1.2 Summary and structure of the PMIM

Concretely, the immersed membrane system consists in an interface Γ immersed in a fluid domain Ω. To remain general, the term interface throughout the thesis will designate an arbitrary surface separating two fluids, and which can be endowed with a wide range of mechanical properties, from the surface tension between two different fluids to more complex elastic behaviors for thin membranes. To fix ideas, let us write down the basic governing equation of the incompressible Stokes flow in the fluid domain:

$$\nabla \cdot \boldsymbol{\sigma} \;=\; \mathbf{0} \quad \text{and} \quad \nabla \cdot \mathbf{v} \;=\; 0 \qquad \forall \mathbf{x} \in \Omega \tag{1.1}$$

where $\boldsymbol{\sigma} = \mu \nabla \mathbf{v} - p\mathbf{I}$ is the viscous stress tensor in the fluid, with μ the fluid viscosity, $\mathbf{v}$ the fluid velocity and p the fluid pressure. The second equation imposes the condition of incompressibility. The above equations are subjected to the following boundary condition at the interface:

$$[\boldsymbol{\sigma} \cdot \bar{\mathbf{n}}] \;=\; \bar{\mathbf{f}} \qquad\qquad \forall \mathbf{x} \in \Gamma \tag{1.2}$$

with the force $\bar{\mathbf{f}}$ is the interface force exerted on the fluid and generated by the deformation of the interface from its equilibrium shape and the brackets $[\boldsymbol{\sigma} \cdot \bar{\mathbf{n}}]$ indicates the jump of viscous stress across the interface Γ in the normal direction $\bar{\mathbf{n}}$. The calculation of the tensor that measures the deformation of the interface in the interface's curvilinear coordinate system is detailed in section 2.1.1, and the different forms taken by the interface force $\bar{\mathbf{f}}$ are given in section 2.1.4. For simplicity, we are assuming here the continuity of the fluid velocity across the interface, i.e. the velocity of the fluid is the same as the the interface velocity. More complex boundary conditions such as the Navier boundary conditions with a non zero slip velocity between the fluid and the interface are detailed in section 2.1.3.

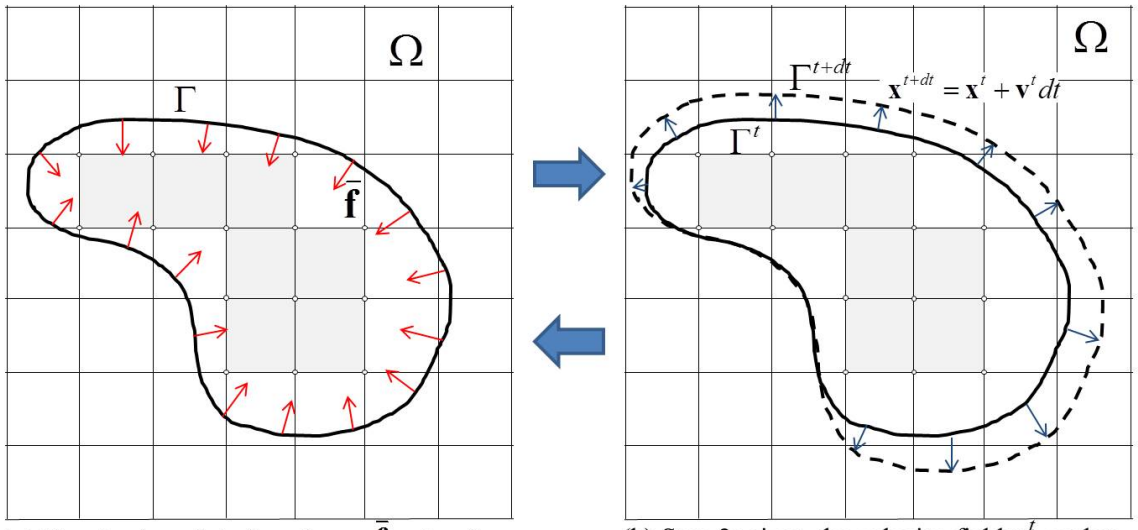

(a) Step 1: given interface force $\bar{\mathbf{f}}$ solve for the velocity $\mathbf{v}^t$ and pressure field with X-FEM

(b) Step 2: given the velocity field $\mathbf{v}^t$, update the position of Γ and calculate $\bar{\mathbf{f}}$

Figure 1.2: *Overview of the PMIM*

To solve equations (1.1) and (1.2), the PMIM marches forward in time by going through two main steps in an explicit, staggered manner as follows:

1. **Step 1** (Fig 1.2a): assuming the position and the deformation of the interface is known, the force $\bar{\mathbf{f}}$ of the interface is calculated and the governing equations mentioned above are solved using the Extended Finite Element Method (X-FEM): first, a structured, fixed finite element mesh is generated as shown in Fig. 1.1b. The fluid velocity and pressure unknowns as well as the pressure jump across the interface are discretized on the finite element mesh as described in section 2.2.1. The spatial discretization of the governing equations used to solve the system for the pressure and velocity degrees of freedom are then found in section 2.2.2.

2. **Step 2** (Fig 1.2b): knowing the velocity field $\mathbf{v}^t$ at time t, the position of the interface is updated using a grid based particle method as detailed in section 2.2.3. Section 2.2.4 describes how the deformation measure of the interface is transported and updated.

At the end of step 2, a complete time step has been simulated, the interface has moved to its new position, and its deformation has been computed. If the convergence criteria that mark the end

of the simulation (given at the end of section 2.2.2) are not satisfied, the algorithm proceeds to the next time step and repeats steps 1 and 2 until convergence is achieved. Commented extracts from the code itself are shown in chapter 6 where the numerical implementation is detailed.

Chapter 2

Particle-based Moving Interface Method for the study of immersed thin membranes

The outline of the chapter is as follows: Section 1 introduces the kinematics and deformation measures used for the fluid and the interface in an Eulerian framework, as well as the governing and constitutive equations. The numerical implementation of the derived equation is then discussed in the context of the X-FEM and the grid based particle method in section 2. The validity and accuracy of the formulation is then assessed in section 3 where we consider, in order, the stability of the Lagrange multiplier fields along the interface, the numerical convergence for an axisymmetrical flow past a spherical capsule with various surface properties and membrane rigidities, the shear flow past a two-dimensional capsule and the effect of slip length. We then study the case of the aspiration of a liquid droplet through a cylindrical channel and the permeation of an elastic capsule through a tight opening. Section 4 finally concludes with a discussion of the results and possible future applications.

2.1 Mathematical formulation for a soft immersed interface

2.1.1 Geometry and deformation measures of a membrane in Eulerian framework

Consider a curvilinear surface Γ in a three-dimensional Euclidean space whose geometry is defined by the position of a point $\mathbf{x}$ through the parameterization $x^i(t) = r^i(\xi^\alpha, t)$, ξ^α, $\alpha = 1, 2$ being fixed surface coordinates and x^i, $i = 1, 2, 3$ being the components of the position vector. In the remainder of the manuscript, greek indices will be considered as running on values $1, 2$, while latin indices will span values $1, 2, 3$, both being summed over their respective range if repeated. With the help of the parameterization $r^i(\xi^\alpha, t)$, one can define the components of two vectors, tangent to the surface Γ, as $a^i_\alpha = \partial r^i / \partial \xi_\alpha$. The two vectors $\mathbf{a}_1$ and $\mathbf{a}_2$ form the basis of the plane tangent to Γ at point $\mathbf{x}$. A third vector $\bar{\mathbf{n}}$, orthogonal to the surface and of unit length is defined as $\bar{\mathbf{n}} = \mathbf{a}_1 \times \mathbf{a}_2 / |\mathbf{a}_1 \times \mathbf{a}_2|$, and represents the orientation of Γ at point $\mathbf{x}$. The induced first fundamental form of the surface Γ, also called metric, is given by the scalar product $a_{\alpha\beta} = \mathbf{a}_\alpha \cdot \mathbf{a}_\beta$, and can be used to define a dual basis to $\mathbf{a}_\alpha$ as $\mathbf{a}^\alpha = a^{\alpha\beta}\mathbf{a}_\beta$, whereby $a^{\alpha\beta} = (a_{\alpha\beta})^{-1}$ and $\mathbf{a}_\alpha \cdot \mathbf{a}^\beta = \delta_{\alpha\beta}$. The second fundamental form is a surface tensor field whose components in the basis of the tangent plane are $b_{\alpha\beta} := -\mathbf{a}_\alpha \cdot \bar{\mathbf{n}}_{,\beta}$. An appropriate measure of surface bending, which we will refer to as the curvature tensor $\bar{\mathbf{C}}$, can then be obtained by calculating the change in the second fundamental form between the reference and the current configurations as follows:

$$\bar{\mathbf{C}} \;=\; (b_{\alpha\beta} - B_{\alpha\beta})\mathbf{a}^\alpha \otimes \mathbf{a}^\beta \;=\; \bar{C}^{ip}_{\alpha\beta}\mathbf{a}^\alpha \otimes \mathbf{a}^\beta \tag{2.1}$$

where $B_{\alpha\beta}$ is the intrinsic interface curvature expressed in the $\mathbf{a}$ basis and $\bar{C}^{ip}_{\alpha\beta} = b_{\alpha\beta} - B_{\alpha\beta}$ the in-plane curvature tensor. Note that the former identically vanishes for a surface that is intrinsically flat. The invariants of the second fundamental form $\mathbf{b}$ yield the mean curvature as:

$$H \;=\; \frac{1}{2}a^{\alpha\beta}b_{\beta\alpha} \;=\; \frac{1}{2}b^\alpha_\alpha. \tag{2.2}$$

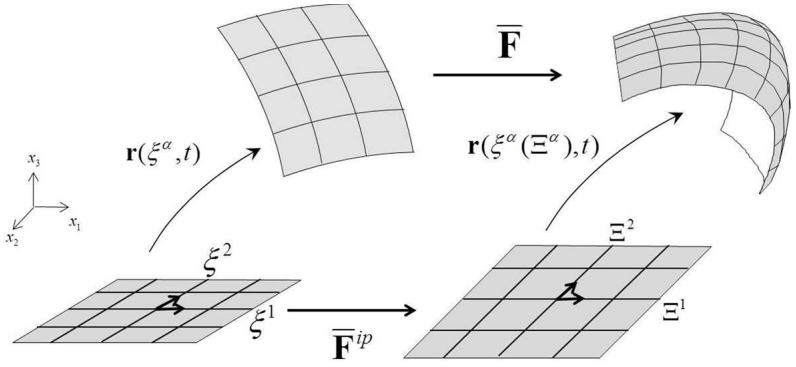

Figure 2.1: *Reference and deformed configuration of the interface. The parametrization* $\mathbf{r}$ *maps the 2D space* ξ^α *to the 3D space* x_i*. The (2*2) deformation tensor* $\bar{\mathbf{F}}^{ip}$ *maps the deformation of a material point* ξ^α *in the 2D reference configuration to the 2D deformed configuration* Ξ^α*. The (3*3) deformation tensor* $\bar{\mathbf{F}}$ *maps the deformation of a material point* $\mathbf{r}(\xi^1,\xi^2)$ *in the 3D reference configuration to the 3D deformed configuration* $\mathbf{r}(\Xi^1(\xi^1,\xi^2),\Xi^2(\xi^1,\xi^2))$

To characterize the in-plane deformation of the interface, let us now introduce the deformation tensor $\bar{\mathbf{F}}$:

$$\bar{\mathbf{F}} \;=\; \bar{F}^{ip}_{\beta\alpha}\mathbf{a}^\beta \otimes \mathbf{a}^\alpha \quad \text{with} \quad \bar{F}^{ip}_{\beta\alpha} \;=\; \frac{\partial \xi^\beta}{\partial \Xi^\alpha} \tag{2.3}$$

where ξ^β and Ξ^α denote in the curvilinear coordinates of an interface material point in the reference and deformed configuration respectively. It can further be seen that the deformation gradient can be represented in two ways: (1) by the full deformation gradient $\bar{\mathbf{F}}$ with dimension (3*3) and (b) by the in-plane deformation gradient $\bar{\mathbf{F}}^{ip}$ with dimension (2*2) (Fig. 2.1). To avoid complication due to rigid body motion, it is more convenient to work with the symmetric part of the deformation gradient, or equivalently, with the Green-Lagrange strain tensor defined as:

$$\bar{\mathbf{E}} \;=\; \frac{1}{2}(\bar{\mathbf{F}}^T\bar{\mathbf{F}} - \mathbf{I}) \;=\; \bar{E}^{ip}_{\alpha\beta}\mathbf{a}^\alpha \otimes \mathbf{a}^\beta \tag{2.4}$$

where the identity tensor $\mathbf{I}$ can be written in terms of the reference configuration basis $\mathbf{I} = a_{\alpha\beta}\mathbf{a}^\alpha \otimes \mathbf{a}^\beta$ and $\bar{\mathbf{E}}^{ip}$ is the in-plane Green-Lagrange strain. Finally, the material time derivative

$\dot{\bar{\mathbf{F}}}$ and $\dot{\bar{\mathbf{E}}}$ are written:

$$\dot{\bar{\mathbf{F}}} \;=\; \bar{\mathbf{L}}\bar{\mathbf{F}} \qquad \text{and} \qquad \dot{\bar{\mathbf{E}}} \;=\; \bar{\mathbf{F}}\bar{\mathbf{D}}\bar{\mathbf{F}}^T, \tag{2.5}$$

where it can be shown that the velocity gradient $\bar{\mathbf{L}}$ has the form [130]:

$$\bar{\mathbf{L}} \;=\; \left(\bar{v}^{\|\alpha}_{|\beta} - b_{\alpha\beta}\bar{v}^{\perp}\right)\mathbf{a}_\alpha \otimes \mathbf{a}^\beta + (v^{\perp}_{,\alpha} + b_{\lambda\alpha}\bar{v}^{\|}_{\lambda})\bar{\mathbf{n}} \otimes \mathbf{a}^\alpha \tag{2.6}$$

Here we used the normal and tangential decomposition of the interface velocity $\bar{\mathbf{v}}$ in the fixed basis $\mathbf{a}_\alpha$, such that $\bar{\mathbf{v}} = \bar{v}^{\|\alpha}\mathbf{a}_\alpha + \bar{v}^{\perp}\bar{\mathbf{n}}$,and the operator $|$ indicates the covariant derivative.

With this, we have a complete description of the interface position, velocity, strain and curvature, as well as their associated rates. The kinematics of the immersed interface are therefore known via the knowledge of the instantaneous velocity field $\bar{\mathbf{v}}(\mathbf{x}, t)$ and the knowledge of the interface geometry at all time. To complete the description, we next discuss the kinematics of the surrounding fluid and its interaction with the interface.

2.1.2 Kinematics of the fluid/interface interactions

Let us now consider that the (closed) interface Γ is immersed in a fluid domain denoted by Ω. Let us further denote as Ω^- the subdomain that is enclosed within the interface and Ω^+ the external subdomain such that $\Omega = \Omega^- \cup \Omega^+$. Before we turn to the governing equations for the interface/fluid system, let us introduce the operators needed to describe the kinematics of the interaction between the interface and the surrounding fluid. For this, we consider an arbitrary Eulerian vector field $\mathbf{f}(\mathbf{x}, t)$ (which may be the velocity) and seek a mathematical representation at a point that is very near the interface, whose normal vector, at this location is $\bar{\mathbf{n}}$. In these conditions, it is convenient to write the vector $\mathbf{f}$ in terms of its normal and tangential projections on Γ as:

$$\mathbf{f} \;=\; \mathbf{f}^{\perp} + \mathbf{f}^{\|} \qquad \text{with} \quad \mathbf{f}^{\perp} \;=\; \mathbf{P}^{\perp}\cdot\mathbf{f} \quad \text{and} \quad \mathbf{f}^{\|} \;=\; \mathbf{P}^{\|}\cdot\mathbf{f} \tag{2.7}$$

where the normal and tangential projection operators are defined by:

$$P_{ij}^{\perp} \;=\; \bar{n}^i \bar{n}^j \quad \text{and} \quad P_{ij}^{\parallel} \;=\; a_1^i a_2^j$$

In addition, to account for the existence of Navier-type boundary conditions at the fluids/interface boundary, one needs to introduce field discontinuities across Γ. Denoting $\mathbf{v}^-$ and $\mathbf{v}^+$ as the fluid velocity field $\mathbf{v}$ in Ω^+ and Ω^- respectively, it is possible to introduce discontinuities in tangential velocity across Γ as [164]:

$$[\mathbf{v}]^{\parallel +} \;=\; \bar{\mathbf{v}}^{\parallel} - \mathbf{v}^{\parallel +}, \qquad [\mathbf{v}]^{\parallel -} \;=\; \mathbf{v}^{\parallel -} - \bar{\mathbf{v}}^{\parallel} \qquad \text{and} \qquad [\mathbf{v}]^{\parallel} = \mathbf{v}^{\parallel +} - \mathbf{v}^{\parallel -} \tag{2.8}$$

Further assuming that no normal separation occurs between the fluids and the interface, we obtain the following normal velocity continuity conditions:

$$\mathbf{v}^{\perp +} = \mathbf{v}^{\perp -} = \bar{\mathbf{v}}^{\perp} \tag{2.9}$$

where we used the decomposition of the velocity vector in normal and tangential components as defined in (2.7). With this formalism, it is important to realize that motion at the interface Γ and the nearby fluids are entirely specified by the combination of three independent variables $\{\bar{\mathbf{v}}, [\mathbf{v}]^{\parallel}, \mathbf{v}^{\parallel -}\}$ or, equivalently $\{\bar{\mathbf{v}}, \mathbf{v}^{\parallel +}, \mathbf{v}^{\parallel -}\}$.

2.1.3 Basic governing equations

Consider a two-dimensional incompressible viscous flow in the domain Ω delimited by a boundary $\partial\Omega$ in which exists a closed vesicle, with surface Γ that is able to move with the surrounding fluid. The problem is characterized by the Reynolds number $\mathcal{R}_e = HV\rho/\mu$ where H is the characteristic length scale, V the characteristic fluid velocity, μ the kinematic viscosity and ρ the fluid densities in and out of the vesicle. We choose here to remain in the Stokes flow assumption with $\mathcal{R}_e \ll 1$, where inertial effect may be neglected. The velocity of a fluid particle is given in terms of its material time derivative $\mathbf{v}(\mathbf{x}, t) = D\mathbf{x}/Dt$, where $\mathbf{x}$ is the current position of the fluid particle at time t. Under these conditions, the governing equations and boundary

conditions for the Stokes flow are written:

$$\nabla \cdot \boldsymbol{\sigma} = \mathbf{0} \qquad \forall \mathbf{x} \in \Omega/\Gamma \tag{2.10}$$

$$\nabla \cdot \mathbf{v} = 0 \qquad \forall \mathbf{x} \in \Omega/\Gamma \tag{2.11}$$

where $\boldsymbol{\sigma}$ is the Cauchy stress tensor in the fluid and the second equation imposes the condition of incompressibility. These equations are combined with the moving interface problem:

$$[\boldsymbol{\sigma} \cdot \bar{\mathbf{n}}] = \bar{\mathbf{f}} \qquad \forall \mathbf{x} \in \Gamma \tag{2.12}$$

$$(\boldsymbol{\sigma} \cdot \bar{\mathbf{n}})^{\parallel \pm} = \frac{\mu}{l^{\pm}} [\mathbf{v}]^{\parallel \pm} \qquad \forall \mathbf{x} \in \Gamma \tag{2.13}$$

$$\frac{d\mathbf{r}(\xi^{\mathbf{1}}, \xi^{\mathbf{2}}, \mathbf{t})}{dt} = \bar{\mathbf{v}}(\xi^1, \xi^2, t) \tag{2.14}$$

with the force $\mathbf{f}$ is the unbalanced interface force due to its deformation. Equation (2.13) is the Navier boundary conditions at the interface, where $l^{\pm} > 0$ is known as the slip length, a physical parameter that depends on the surface roughness. The case $l = 0$ corresponds to the no slip condition while $l = \infty$ is the free sleep condition between the fluid and the interface. Finally, the boundary condition for fluid motion on the external boundary reads:

$$\boldsymbol{\sigma} \cdot \mathbf{n} = p_o \mathbf{n} \qquad \forall \mathbf{x} \in \partial\Omega_p \tag{2.15}$$

$$\mathbf{v}(\mathbf{x}, t) = \mathbf{v}_0 \qquad \forall \mathbf{x} \in \partial\Omega_v. \tag{2.16}$$

where p_0 is an external pressure surrounding the domain Ω, and a Dirichlet type condition can be applied on the velocity on the sub domain $\partial\Omega_v$.

2.1.4 Constitutive equations

To complement the above system of equation, a number of constitutive relation must be introduced. They can be broken down into three components that describe in turns: (a) the behavior of the fluid and (b) the mechanical behavior of the interface. In this work, we consider a simple incompressible Newtownian fluid with viscosity μ that can be different within the enclosed

volume and the external fluid.

$$\boldsymbol{\sigma} = \mu\mathbf{D} - \mathbf{pI} \tag{2.17}$$

where $\mathbf{D}$ is the rate of deformation and p is the hydrostatic pressure enforcing the incompressibility condition. In the case of an elastic thin membrane, a strain energy function $\bar{\Phi} = \bar{\Phi}(\bar{\mathbf{C}}^{ip}, \bar{\mathbf{E}}^{ip})$ can be generally defined in terms of the curvature $\bar{\mathbf{C}}^{ip}$ and strain $\bar{\mathbf{E}}^{ip}$ introduced in the previous section. The in-plane Cauchy stress $\bar{\mathbf{T}}^{ip}$ and bending moment $\bar{\mathbf{M}}^{ip}$ are then found by taking the partial derivatives of $\bar{\Phi}$:

$$\bar{\mathbf{T}}^{ip} = \frac{1}{J}\bar{\mathbf{F}}^{ip}\frac{\partial\bar{\Phi}}{\partial\bar{\mathbf{E}}^{ip}}\bar{\mathbf{F}}^{ipT} \quad \text{and} \quad \bar{\mathbf{M}}^{ip} = \frac{1}{J}\frac{\partial\bar{\Phi}}{\partial\bar{\mathbf{C}}^{ip}} \tag{2.18}$$

where J is the local area dilatation of the surface and Γ_0 is the surface Γ in its reference configuration. The resulting force of the interface is then found to be [6] (the details of the derivation are given in the appendix):

$$\bar{\mathbf{f}} = \underbrace{\left(-\bar{T}^{ip}_{\alpha\beta|\beta}\mathbf{a}^{\alpha} - \bar{T}^{ip}_{\alpha\beta}b_{\alpha\beta}\bar{\mathbf{n}}\right)}_{\text{in-plane stress}} + \underbrace{\left(\bar{M}^{ip}_{\alpha\beta|\alpha\beta}\bar{v}^{\perp} - \bar{M}^{ip}_{\alpha\beta}b^{\lambda}_{\alpha}b_{\lambda\beta}\right)\bar{\mathbf{n}}}_{\text{bending moment}} \tag{2.19}$$

Here, the vector $\bar{\mathbf{f}}$ is the force resulting from stretching and bending the interface. Alternatively, the case of a lipid bilayer can be considered by choosing $\bar{\Phi}$ to be the classical Helfrich-Canham energy per current unit area $\bar{\Phi}(\bar{\mathbf{C}}^{ip}) = \kappa/2(H - H_0)^2$, with κ the elastic moduli and H_0 the spontaneous curvature [76]. Under these conditions, the interface force is written:

$$\bar{\mathbf{f}} = \kappa(\Delta H + \frac{H - H_0}{2}(H^2 - 4K + HC_0))\bar{\mathbf{n}}. \tag{2.20}$$

Finally, the simple case of surface tension at the interface between two liquids can also be modelled by choosing the following well-known equation for the interface force, in the direction opposite to the normal and proportional to the mean curvature:

$$\bar{\mathbf{f}} = -\gamma H\bar{\mathbf{n}}, \tag{2.21}$$

with γ the surface tension.

2.2 Numerical solution: Extended Finite element and grid-based particle method

The solution strategy adopted here aims to attain a state of equilibrium between the interface and the surrounding fluid by solving a sequence of steady state flow and update of the interface in a staggered manner. As we march forward in time, the interface is first considered fixed, and the Extended Finite Element method is used to solve the Eulerian fields $\mathbf{v}^{\pm}, \bar{\mathbf{v}}$ and $p^{\pm}$ for the system subjected to the interface force $\bar{\mathbf{f}}$. The coupling between the interface and the surrounding fluid is handled via the use of Lagrange multipliers, where special care is taken in defining the right Lagrange multiplier space along the interface [113]. This first step is described in section 2.2.1. Next, given the interface velocity field $\bar{\mathbf{v}}$, section 2.2.2 describes how the Grid Based Particle method and a second order Runge-Kutta time integration scheme are used to update the interface position, deformations measures as well as the interface force $\bar{\mathbf{f}}$ for the next time step.

2.2.1 The Extended Finite Element method with directional discontinuities

The examples chosen here to illustrate the method are axisymmetrical or plane-stress and therefore only require a two-dimensional spatial discretization. Every aspect of the method can however be adapted in three dimensions but involve additional computational aspect (such as parallel computing and optimization) which are beyond the scope of this study. Following classical methods for fluid flow at low Reynolds number, the pressure and velocity fields are discretized on a two-dimensional fixed finite element mesh and interpolated with a mixed finite element procedure [91] with (four-node) bilinear shape functions for the pressure and (nine-node) quadratic shape functions for the velocity. Since the framework adopted to describe the system is Eulerian, the finite element discretization is structured and does not conform to the shape of the membrane Γ. The existence of an interface is then accounted for by the zero-level of a level-set function $\phi(\mathbf{x})$ defined as the signed distance function from the interface Γ. An illustration of

this function is given in Fig. 2.2a and 2.2b. This interface then creates discontinuities in the velocity and pressure fields within elements cut by Γ which can be accounted for by adopting the Extended Finite Element Method (X-FEM) in which such elements are enriched with 'jump' degrees of freedom, as described in [114, 20]. For example, the general rule for interpolating the pressure p inside element e is:

$$\tilde{p}^e(\mathbf{x},t) = \sum_{I=1}^{4} N_I^4(\mathbf{x}) p^I(t) + \sum_{I=1}^{4} N_I^4(\mathbf{x}) \left(H(\phi(\mathbf{x})) - H(\phi(\mathbf{x}_I))\right) \hat{p}^I(t) \tag{2.22}$$

where the upper case indices I and J are used for node numbering and the N_I^4 are the four-node element shape functions. The terms p^I denotes the regular pressure at node I while $\hat{p}^I$ represents the pressure jump. Finally, the Heaviside function $H(\phi(\mathbf{x}))$ provides the discontinuity needed to describe the jump in velocity and pressure across the membrane (Fig. 2.2c). In contrast to

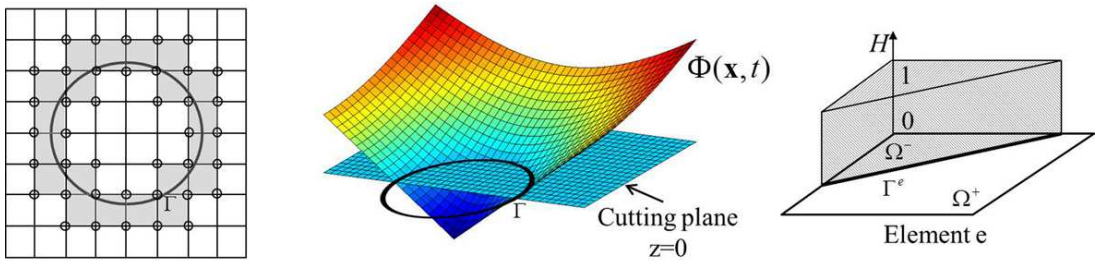

Figure 2.2: *(a) shows the elements split by membrane* Γ *and the enriched nodes (circle). The 3D distance function can be seen in (b) where its intersection with the plan* $z = 0$ *defines* Γ*, and (c) shows the Heaviside function in an element cut by* Γ*.*

the pressure field, the discontinuity that affects the velocity field is directional since only the tangential components of $\mathbf{v}$ are discontinuous across Γ. We here introduce a modification to the shape functions used in X-FEM by making the discontinuity directional as follows:

$$\tilde{v}_i^e(\mathbf{x},t) = \sum_{J=1}^{9} N_J^9(\mathbf{x}) v_i^J(t) + \sum_{J=1}^{9} N_J^9(\mathbf{x}) (H(\phi(\mathbf{x},t)) - H(\phi(\mathbf{x}_J,t))) a_i^J(t) \hat{v}^J(t), \tag{2.23}$$

where the lower case i indicates the component of a vector and N^9 are the nine-node element shape functions. The term a_i^J represents the i^{th} component of the covariant tangent vector to Γ at node J and provides the tangential direction for the velocity jump $\hat{v}^J$ at node J. With this

method of interpolation, the normal velocity continuity condition $v^{\perp+} = v^{\perp-}$ is automatically satisfied across Γ, and the jump in tangential velocity is reduced to a scalar $\hat{v}^J$ multiplied by the tangent vector a_i^J. Note that in the three-dimensional case, the jump discontinuity becomes a two-dimensional vector in the plane tangent to the interface.

Remark: *Although the condition $v^{\perp+} = v^{\perp-}$ ensures the continuity of the velocity field across the interface, a jump in the viscosity of the fluid across the interface can cause kink in the velocity field, i.e. a discontinuity in the velocity gradient in the normal direction across the interface. This can easily be taken into account with the help of an additional enrichment that incorporates a piecewise affine 'hat' function. For the sake of simplicity, we choose to keep the same viscosity on either side of the interface.*

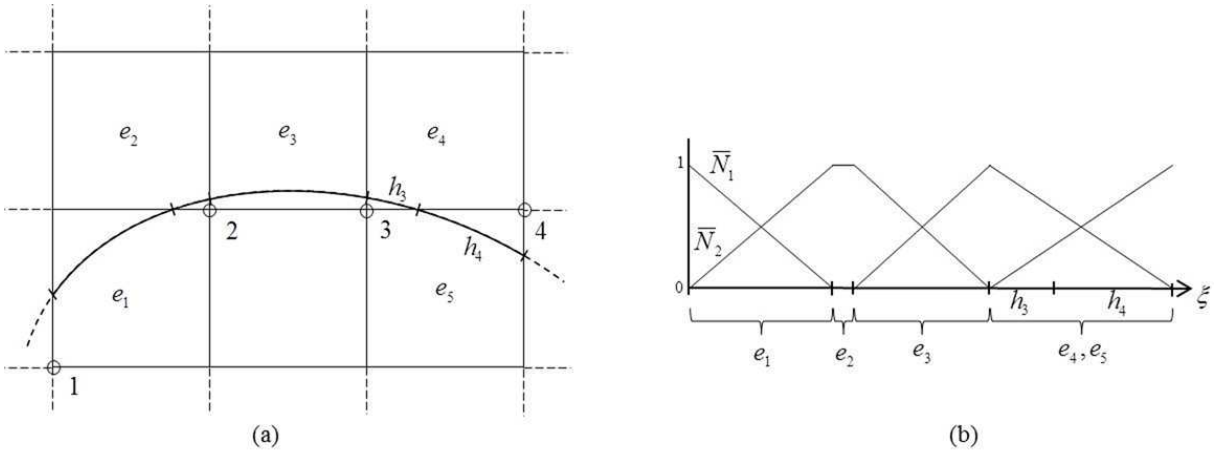

Figure 2.3: *(a) shows how the mesh nodes 1 through 4 are used to discretize the Lagrange multipliers and interface velocity (circled nodes) and (b) shows the value taken by the shape functions $\bar{N}_1$ and $\bar{N}_2$ in each element e_1 to e_5 cut by the interface. Each tick along the absisse One can note that the interpolation of the Lagrange multipliers is constant in e_2 while e_4 and e_5 share the same Lagrange multipliers.*

Finally, to compute the motion of the interface and couple it to the nearby fluids, let us introduce the Lagrange multipliers λ_p, λ^+ and λ^- used in combination with the membrane velocity $\bar{v}^{\parallel}$ to enforce (2.12) and (2.13). Special care needs to be given to the discretization of the Lagrange multipliers along the interface in the context of the X-FEM. Indeed, a 'naive' discretization, i.e. a Lagrange multiplier at each intersection between the interface and the underlying mesh, leads

to a Lagrange multiplier space that does not satisfy the so-called inf-sup (or LBB) condition [54]. This in turn creates oscillations in the Lagrange multiplier field along the interface and affects the convergence rate. To address this issue we here choose to use the method developed by Möes *et al* in [113] to construct the correct Lagrange multiplier space and discretize the fields $\bar{v}^{\parallel}$, λ_p, λ^+ and λ^- on nodes of the underlying Eulerian mesh (Fig. 2.3a), which we will refer to as the M-discretization. Each selected node carry the following four degrees of freedom: $\bar{v}^{\parallel K}$, λ_p^K, λ^{+K} and λ^{-K} . These fields are interpolated along the section Γ^e of Γ that cuts element e as follows:

$$\tilde{\bar{v}}^{\parallel e}(\xi,t) = \sum_{K=1}^{2} \bar{N}_K(\xi)\bar{v}^{\parallel K}(t) \ , \quad \tilde{\lambda}_p^e = \sum_{K=1}^{2} \bar{N}_K(\xi)\lambda_p^K(t) \ , \quad \tilde{\lambda}^{\pm e} = \sum_{K=1}^{2} \bar{N}_K(\xi)\lambda^{\pm K}(t) \tag{2.24}$$

where $\bar{N}_I$ are one-dimensional two-node shape functions and the coordinate ξ runs along Γ^e (Fig 2.3b). More detail about the discretization algorithm that construct the Lagrange multiplier space can be found in [113].

2.2.2 Weak formulation

Introducing the test functions $\mathbf{w_v}$, w_p, $w_{\bar{v}^{\parallel}}$, w_{λ_p}, w_{λ^+} and w_{λ^-}, integrating by parts and using the divergence theorem, the weak form of the governing equations (2.10)-(2.13) in the fluid domain can be written as: given the position $\mathbf{r}$ of the interface Γ at time t, find $\mathbf{v} \in \mathcal{V}$, $p \in \mathcal{P}$, $\bar{v}^{\parallel} \in \mathcal{L}$, $\lambda_p \in \mathcal{L}$, $\lambda^+ \in \mathcal{L}$ and $\lambda^- \in \mathcal{L}$ such that for all $\mathbf{w_v} \in \mathcal{V}$, $w_p \in \mathcal{P}$, $w_{\bar{v}^{\parallel}} \in \mathcal{L}$, $w_{\lambda_p} \in \mathcal{L}$

$w_{\lambda^+} \in \mathcal{L}$ and $w_{\lambda^-} \in \mathcal{L}$:

$$\begin{aligned}
(\nabla \mathbf{w_v}, \mu \nabla \mathbf{v})_\Omega - (\nabla \mathbf{w_v}, p\mathbf{I})_\Omega + \left(\mathbf{w_v}, \frac{\mu}{l^+}\lambda^+ - \frac{\mu}{l^-}\lambda^-\right)_\Gamma + \left(\mathbf{w_v}, \bar{\mathbf{f}}\right)_\Gamma &= 0 \\
(w_p, \nabla \cdot \mathbf{v})_\Omega + (w_p, \lambda_p)_\Gamma &= 0 \\
(w_{\lambda_p}, [p])_\Gamma + (w_{\lambda_p}, \bar{\mathbf{f}}^\perp)_\Gamma &= 0 \\
\left(w_{\bar{v}^\parallel}, \frac{\mu}{l^+}\left(\lambda^+ + [v]^{\parallel +}\right) + \frac{\mu}{l^-}\left(-\lambda^- + [v]^{\parallel -}\right)\right)_\Gamma + \left(w_{\bar{v}^\parallel}, \bar{\mathbf{f}}^\parallel\right)_\Gamma &= 0 \\
\left(w_{\lambda^+}, \left((\boldsymbol{\sigma} \cdot \bar{\mathbf{n}})^{\parallel +} - \frac{\mu}{l^+}[\mathbf{v}]^{\parallel +}\right)\right)_\Gamma &= 0 \\
\left(w_{\lambda^-}, \left((\boldsymbol{\sigma} \cdot \bar{\mathbf{n}})^{\parallel -} - \frac{\mu}{l^-}[\mathbf{v}]^{\parallel -}\right)\right)_\Gamma &= 0
\end{aligned} \tag{2.25}$$

After a long but straightforward calculation using the discretized form of $\mathbf{v}, p, \bar{v}^\parallel, \bar{v}^\perp$ and $\lambda^\pm$ (given in the appendix) , the weak form (2.25) at time t can conveniently be written in the following format:

$$\begin{bmatrix} \mathbf{K}^t & \mathbf{I}_2^t \\ \mathbf{I}_1^t & \bar{\mathbf{K}}^t \end{bmatrix} \cdot \begin{bmatrix} \mathbf{d}(t) \\ \bar{\mathbf{d}}(t) \end{bmatrix} + \begin{bmatrix} \mathbf{F}_f^t \\ \bar{\mathbf{F}}_f^t \end{bmatrix} = 0 \tag{2.26}$$

where $\mathbf{d}$ is a vector composed of the bulk degrees of freedom $\mathbf{d}(t) = [\mathbf{v}(t)\ \mathbf{p}(t)]^\top$ while $\bar{\mathbf{d}}$ corresponds to the interface degrees of freedom $\bar{\mathbf{d}}(t) = \left[\bar{v}^\parallel(t)\ \lambda_p(t)\ \lambda^+(t)\ \lambda^-(t)\right]^\top$. It can be seen that the component $\mathbf{K}^t$ of the tangent matrix corresponds to the fluid domain, the component $\bar{\mathbf{K}}^t$ is associated with the interface while $\mathbf{I}_1^t$ and $\mathbf{I}_2^t$ can be thought of as the fluid/interface interaction matrices. The global force vector $[\mathbf{F}_f^t\ \bar{\mathbf{F}}_f^t]^T$, which include both external forces and the interface force at time t, as well as the tangent matrix components $\mathbf{K}^t$, $\bar{\mathbf{K}}^t$, $\mathbf{I}_1^t$ and $\mathbf{I}_2^t$ are assembled from their element constituents as follows:

$$\mathbf{F}_f^t = \mathcal{A}_{e=1}^{nel}\left(\mathbf{F}_{fe}^t\right) \ , \ \bar{\mathbf{F}}_f^t = \mathcal{A}_{e=1}^{\bar{nel}}\left(\bar{\mathbf{F}}_{fe}^t\right) \ , \ \mathbf{K}^t = \mathcal{A}_e^{nel}\left(\mathbf{K}_e^t\right) \ , \ \bar{\mathbf{K}}^t = \mathcal{A}_e^{\bar{nel}}\left(\bar{\mathbf{K}}_e^t\right),$$
$$\mathbf{I}_1^t = \mathcal{A}_e^{\bar{nel}}\left(\mathbf{I}_{e\,1}^t\right) \quad \text{and} \quad \mathbf{I}_2^t = \mathcal{A}_e^{\bar{nel}}\left(\mathbf{I}_{e\,2}^t\right)$$

where $\mathcal{A}_e$, nel and $\bar{nel}$ respectively denote the conventional FEM assembly operator, the total element number and the number of elements cut by Γ. While precise expressions are provided

in the appendix, the submatrix and subvectors appearing in (2.26) take the form:

$$\mathbf{K}_e^t = \begin{bmatrix} \mathbf{K}_{vv}^e & \mathbf{K}_{vp}^e \\ \mathbf{K}_{pv}^e & 0 \end{bmatrix}, \ \bar{\mathbf{K}}_e^t = \begin{bmatrix} \mathbf{K}_{\bar{v}\|\bar{v}\|}^e & 0 & \mathbf{K}_{\bar{v}\|\lambda^+}^e & \mathbf{K}_{\bar{v}\|\lambda^-}^e \\ 0 & 0 & 0 & 0 \\ \mathbf{K}_{\lambda^+\bar{v}\|}^e & 0 & 0 & 0 \\ \mathbf{K}_{\lambda^-\bar{v}\|}^e & 0 & 0 & 0 \end{bmatrix}, \ \mathbf{I}_{e\,1}^t = \begin{bmatrix} \mathbf{K}_{\bar{v}\|v}^e & 0 \\ 0 & \mathbf{K}_{\lambda_p p}^e \\ \mathbf{K}_{\lambda^+ v}^e & 0 \\ \mathbf{K}_{\lambda^- v}^e & 0 \end{bmatrix} \quad (2.27)$$

$$\mathbf{I}_{e\,2}^t = \begin{bmatrix} 0 & 0 & \mathbf{K}_{v\lambda^+}^e & \mathbf{K}_{v\lambda^-}^e \\ 0 & \mathbf{K}_{p\lambda_p}^e & 0 & 0 \end{bmatrix}, \ \mathbf{F}_{fe}^t = \begin{bmatrix} \mathbf{F}_v^e \\ \mathbf{F}_p^e \end{bmatrix} \text{ and } \bar{\mathbf{F}}_{fe}^t = \begin{bmatrix} \mathbf{F}_{\bar{v}\|}^e \\ \mathbf{F}_{\lambda_p}^e \\ 0 \\ 0 \end{bmatrix} \quad (2.28)$$

Remark: *The computation of these quantities involves the assessment of integrals over elements that can be numerically evaluated using Gaussian quadrature with four integration points in regular elements. However, to carry out the integration over the two sides of* Γ *in split elements, a division into sub-triangles is required as described in [114].*

The finite element equation (2.26) can be solved with a linear solver to yield an expression for the fluid and interface velocities at time t. Given the interface velocity $\bar{\mathbf{v}}(t)$, the position of Γ and its deformation measures $\bar{\mathbf{C}}^t, \bar{\mathbf{E}}^t$ and $\bar{\mathbf{F}}^t$ are then updated using an explicit second order Runge-Kutta time integration scheme to compute $\mathbf{K}_e^{t+dt}$ and $\mathbf{F}_e^{t+dt}$ for the next time step. Convergence is achieved once the two following criteria are met:

1. The pressure and velocity fields of the fluid surrounding the interface are constant with respect to time. This criterion is met when $||\mathbf{v}_{reg}(t+dt) - \mathbf{v}_{reg}(t)|| < TOL_v$ and $||\mathbf{p}_{reg}(t+dt) - \mathbf{p}_{reg}(t)|| < TOL_p$, where $\mathbf{v}_{reg}(t)$ and $\mathbf{p}_{reg}(t)$ are the vectors of all regular fluid pressure and velocity degrees of freedom at each node, and TOL_v and TOL_p the user defined tolerances for the velocity and pressure.

2. The interface tangential velocity field is constant with respect to time. Here, since the number of degrees of freedom associated with the interface changes at each iteration, we rely on the particles tracking the interface (described in the next section) to compare the

interface velocity field between two time steps. The second criterion is therefore written $||\bar{\mathbf{v}}_p^{\parallel}(t+dt) - \bar{\mathbf{v}}_p^{\parallel}(t)|| < TOL_{\bar{v}\parallel}$, with $\bar{\mathbf{v}}_p^{\parallel}(t+dt)$ and $\bar{\mathbf{v}}_p^{\parallel}(t)$ the tangential velocity of the interface interpolated at the same particles at times t and $t+dt$.

Once criteria (1) and (2) are satisfied, the algorithm has converged and the interface is in equilibrium with the surrounding fluid. The next step involves the transport of the interface using a mesh-based particle method, as discussed in the next section.

2.2.3 Tracking the evolution of the interface

Traditionally, the temporal evolution of an interface in an Eulerian framework is handled with the level-set evolution equation [52]. This has the main advantage of turning the evolution of the interface into seeking the solution of a partial differential equation, removing the need for surface parameterization or meshing. A main issue with this class of methods within the context of our study is that a levelset formulation is usually not adapted to contain Lagrangian informations on an interface, which may include strain and concentration fields. They also suffer from the fact that they generally cannot capture in-plane, interface shear deformation since such instances are not associated with a normal interface velocity (the latter being the main component of the level-set evolution equation). To circumvent these limitations, we choose here to use a grid-based particle method similar to what was introduced in [100]. This method indeed possesses the double advantage of tracking the interface explicitly with particles that contain lagrangian information while using the underlying fixed finite element mesh to ensure a fairly uniform repartition of the particles on the interface. Here we summarize the grid based particle method and discuss the update of the interface position and deformations measures.

The particles, whose position vector is denoted by $\mathbf{y}$, are chosen as the normal projection of the underlying mesh nodes, with position vector $\mathbf{p}$, on Γ. Initially, the interface is described implicitly as the zero level-set of a signed distance function $\phi(\mathbf{p}, t=0)$. The initial coordinates of particles $\mathbf{y}$ can then found as follows:

$$\mathbf{y} \quad = \quad \mathbf{p} - \phi(\mathbf{p},0)\nabla\phi(\mathbf{p},0) \tag{2.29}$$

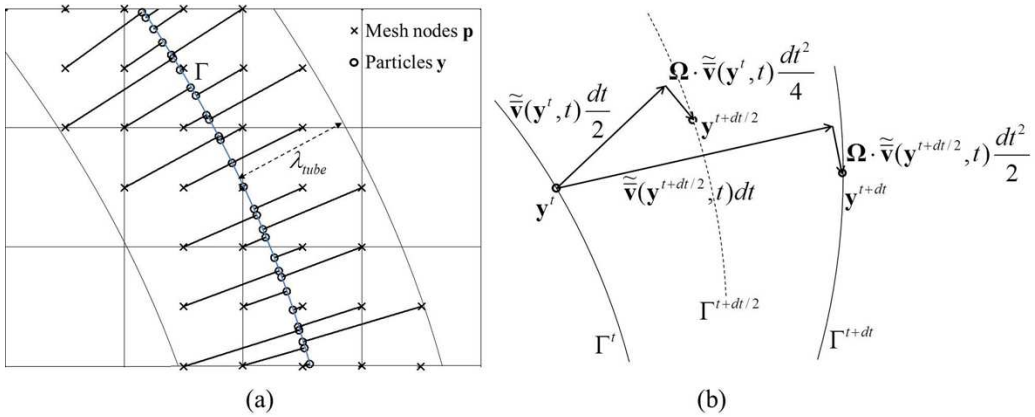

Figure 2.4: *Figure (a) shows the sampling of* Γ *by the particles* $\mathbf{y}$ *represented by a circle while the associated nodes* $\mathbf{p}$ *inside the computational tube* λ_{tube} *are represented by crosses. Figure (b) shows the second order Runge-Kutta time integration of the evolution of the interface:* $\tilde{\tilde{\mathbf{v}}}$ *denotes the velocity of the interface interpolated at the particle's position while* $\mathbf{\Omega}$ *is the angular velocity of the interface's normal* $\bar{\mathbf{n}}$*.*

To limit the number of particles, we define a so-called computational tube such that only nodes $\mathbf{p}$ whose distance to Γ is smaller than a cut-off value λ_{tube} are accounted for (Fig. 2.4a). It is important to note here that there is a one to one correspondence between each particle $\mathbf{y}$ and node $\mathbf{p}$. This ensures a quasi-uniform repartition of particles along the interface throughout its evolution. Between two subsequent time steps, the particles are moved according to the interface velocity $\tilde{\tilde{\mathbf{v}}}(\xi,t)$ and using a second order Runge-Kutta time integration procedure as follows (Fig. 2.4b):

$$\mathbf{y}^{t+dt/2} = \mathbf{y}^t + \tilde{\tilde{\mathbf{v}}}(\mathbf{y}^t,t)\frac{dt}{2} + \mathbf{\Omega}\cdot\tilde{\tilde{\mathbf{v}}}(\mathbf{y}^t,t)\frac{dt^2}{4} \tag{2.30}$$

$$\mathbf{y}^{t+dt} = \mathbf{y}^t + \tilde{\tilde{\mathbf{v}}}(\mathbf{y}^{t+dt/2},t)dt + \mathbf{\Omega}\cdot\tilde{\tilde{\mathbf{v}}}(\mathbf{y}^{t+dt/2},t)\frac{dt^2}{2}, \tag{2.31}$$

where $\mathbf{\Omega}$ is the matricial form of the angular velocity of the interface normal [86]:

$$\frac{d\bar{\mathbf{n}}}{dt} = \boldsymbol{\omega}\times\bar{\mathbf{n}} \quad , \quad \boldsymbol{\omega} = -\left(v^{\perp}_{,\alpha} + b_{\lambda\alpha}v^{\|\lambda}\right)\mathbf{a}^{\alpha} \quad \text{and} \quad \Omega_{ik} = \epsilon_{ijk}\omega_j \tag{2.32}$$

with ϵ_{ijk} the permutation tensor. After the motion of the interface, the particles $\mathbf{y}$ may not be the closest point on Γ to their associated nodes $\mathbf{p}$. Moreover, the motion of the particles may cause their distribution on Γ to become uneven, which can affect the geometrical resolution of

the interface. To overcome this issue, the interface is ressampled after motion by recomputing the particles as the closest points on Γ to the nodes $\mathbf{p}$ inside the updated computational tube (which has moved with the interface). This is done by first locally approximating the interface with polynomials around each particle. The procedure, explained here in the two dimensional case, is as follows: for each node $\mathbf{p}$ inside the computational tube, the closest m particles $\mathbf{y}_0...\mathbf{y}_m$ are collected, carrying with them the tangent $\mathbf{a}_0^t...\mathbf{a}_m^t$ and normal $\bar{\mathbf{n}}_0^t...\bar{\mathbf{n}}_m^t$ to the interface before motion. Denoting $\mathbf{y}_0$ as the particle closest to $\mathbf{p}$, a polynomial of degree $n < m$ is fitted to the particles $\mathbf{y}_0...\mathbf{y}_m$ in the local coordinate system $\{\mathbf{a}_0^t; \bar{\mathbf{n}}_0^t\}$ centered on $\mathbf{y}_0$. The location $\tilde{\mathbf{y}}_i$ of particle i in this local coordinate system is given by:

$$\tilde{\mathbf{y}}_i = \left\{ \begin{array}{c} \xi_i^1 \\ \xi_i^2 \end{array} \right\} = \mathbf{R}^t \cdot (\mathbf{y}_i - \mathbf{y}_0) \quad \text{with} \quad \mathbf{R}^t = \left[\begin{array}{c} (\mathbf{a}_0^t)^T \\ (\bar{\mathbf{n}}_0^t)^T \end{array} \right]. \tag{2.33}$$

Taking the example of a quadratic polynomial ($n = 2$), the interface around particle $\mathbf{y}_0$ is represented in the local referential as the graph function $\xi^2(\xi^1) = c_0 + c_1\xi^1 + c_2(\xi^1)^2$, where the coefficients c_0, c_1 and c_2 are found by minimizing the L^2 difference between the $\xi^2(\xi_i^1)$ and the ξ_i^2. This method of interface approximation can be generalized in three dimension [100], where a quadratic graph function would take the form $\xi^3(\xi^1, \xi^2) = c_{00} + c_{10}\xi^1 + c_{01}\xi^2 + c_{11}\xi^1\xi^2 + c_{20}(\xi^1)^2 + c_{02}(\xi^2)^2$, as shown in Fig. 2.5. The coordinates $\left\{\xi^1, \xi^2, \xi^3(\xi^1, \xi^2)\right\}$ defines a local

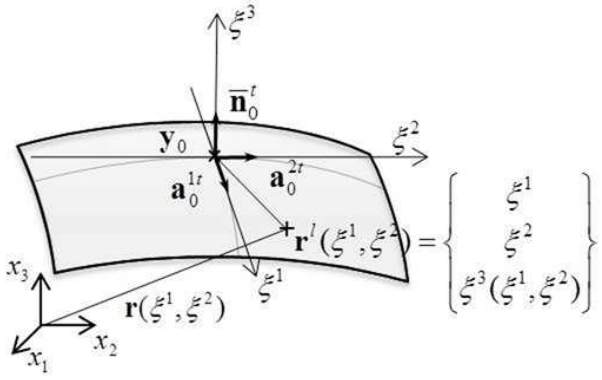

Figure 2.5: *Local polynomial approximation of the surface (and of any Lagrangian field). The polynomial $\xi^3(\xi^1, \xi^2)$ that approximates the interface is constructed via least square fitting using neighbouring particles in the local referential $\{\mathbf{a}_0^{1t}, \mathbf{a}_0^{2t}, \bar{\mathbf{n}}_0^t\}$ centered on particle $\mathbf{y}_0$.*

parameterization $\mathbf{r}^l(\xi^1, \xi^2)$ of Γ in the neighbourhood of $\mathbf{y}_0$ (Fig. 2.4b):

$$\mathbf{r}^l(\xi^1, \xi^2) = \left\{ \begin{array}{c} \xi^1 \\ \xi^2 \\ \xi^3(\xi^1, \xi^2) \end{array} \right\}. \tag{2.34}$$

The relationship between the local parameterization $\mathbf{r}^l(\xi^1, \xi^2)$ and the global parameterization $\mathbf{r}(\xi^1, \xi^2)$ defined in section 2.1.1 is then found via rotation and translation operations in the form:

$$\mathbf{r}(\xi^1, \xi^2, t + dt) = (\mathbf{R}^t)^{-1}\, \mathbf{r}^l(\xi^1, \xi^2) + \mathbf{y}_0. \tag{2.35}$$

The parameterization $\mathbf{r}(\xi^1, \xi^2, t+dt)$ can now be used to ressample the interface, i.e. recalculate the closest point on the interface to the nodes $\mathbf{p}$. This is done by minimizing the distance function $d(\mathbf{r}(\xi^1, \xi^2, t + dt); \mathbf{p}) = 1/2 \left|\mathbf{r}(\xi^1, \xi^2, t + dt) - \mathbf{p}\right|$ with respect to ξ^1 and ξ^2. In three dimensions, this requires the use of an iterative solver, which for small dt is given a good initial guess and converges very quickly. In two dimensions however, the solution can be found explicitly by solving a cubic equation. The quality of approximation of a two-dimensional interface when fitted to a circle using the sequence of second order polynomials detailed above is shown in Table I and in Fig 2.6. It is found that the L^2 error e^2 in the position of the particles decreases with the size of the underlying mesh at with a convergence rate of approximately 4. This is in

mesh size h	0.4	0.2	0.1	0.05
e^2	2.87×10^{-2}	1.73×10^{-3}	1.12×10^{-4}	6.97×10^{-6}

Table 2.1: L^2 error in the position of particles when fitted to a circle.

perfect agreement with results found in [100] and comes from the fact that both the circle and the polynomials are even functions. The approximation error should therefore be of fourth order since there are no contribution from third order terms. Other geometrical quantities such as the

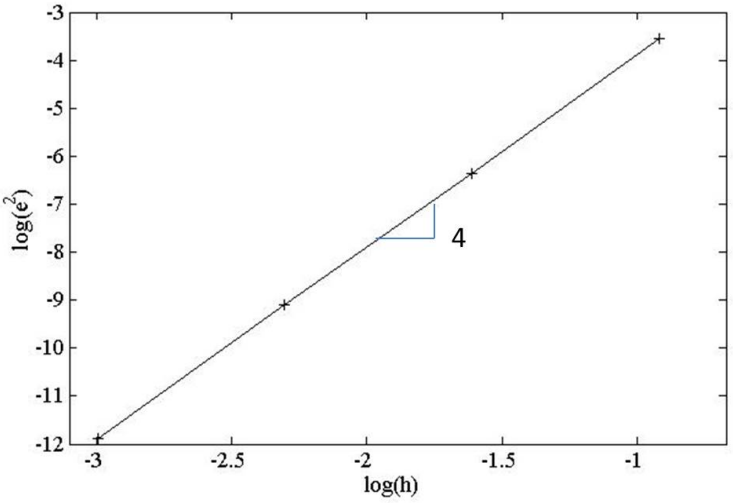

Figure 2.6: *log of the error e^2 as a function of the log of the mesh size h*

updated basis $\left\{\mathbf{a}_1^{t+dt}, \mathbf{a}_2^{t+dt}, \bar{\mathbf{n}}^{t+dt}\right\}$ are then found using the parameterization $\mathbf{r}(\xi^1, \xi^2, t+dt)$:

$$\mathbf{a}_\alpha^{t+dt} = \mathbf{r}(\xi^1, \xi^2, t+dt)_{,\alpha} = \mathbf{R}^t \frac{\partial \mathbf{r}^l(\xi^1, \xi^2)}{\partial \xi^\alpha} \tag{2.36}$$

$$\bar{\mathbf{n}}^{t+dt} = \mathbf{a}_1^{t+dt} \times \mathbf{a}_2^{t+dt} / |\mathbf{a}_1^{t+dt} \times \mathbf{a}_2^{t+dt}|. \tag{2.37}$$

The metric $a_{\alpha\beta}^{t+dt} = \mathbf{a}_\alpha^{t+dt} \cdot \mathbf{a}_\beta^{t+dt}$ or the second fundamental form $b_{\alpha\beta}^{t+dt} = -\mathbf{a}_\alpha^{t+dt} \cdot \bar{\mathbf{n}}_{,\beta}^{t+dt}$ can also be directly obtained from equations (7.42), (7.43), (7.39) and their derivatives.

Finally, the new level-set function $\phi(\mathbf{p}, t+dt)$ is calculated as the signed distance function to Γ at nodes $\mathbf{p}$ as follows [100]:

$$\phi(\mathbf{p}, t+dt) = -\mathbf{sgn}\left(\frac{\mathbf{y}^{t+dt} - \mathbf{p}}{|\mathbf{y}^{t+dt} - \mathbf{p}|} \cdot \bar{\mathbf{n}}_0^t\right) |\mathbf{y}^{t+dt} - \mathbf{p}|, \tag{2.38}$$

where $\mathbf{y}^{t+dt}$ is the particle associated with $\mathbf{p}$ at time $t+dt$ and the sign function $\mathbf{sgn}(((\mathbf{y}^{t+dt} - \mathbf{p})/|\mathbf{y}^{t+dt} - \mathbf{p}|) \cdot \bar{\mathbf{n}}_0^t)$ determines whether node $\mathbf{p}$ is in Ω^+ or Ω^-. The reconstruction of the level-set function using the local polynomial approximation of the interface is computationally inexpensive, and is used the X-FEM part of the algorithm (2.22) and (2.23).

2.2.4 Update of the interface deformation

In addition to the interface geometry, the sampling particles also carry lagrangian fields associated with the interface, such as the deformation gradient. The deformation gradient $\bar{\mathbf{F}}$ is updated at each particle $\mathbf{y}^t$ in their respective basis $\{\mathbf{a}_{0\,1}^t, \mathbf{a}_{0\,2}^t, \bar{\mathbf{n}}_0^t\}$ using the rate equation (2.5) and the velocity gradient $\bar{\mathbf{L}}$ (2.6) as follows (Fig. 2.7a and 2.7b):

$$\bar{\mathbf{L}}^t = \left(\tilde{\bar{v}}^{\parallel}_{\alpha|\beta} - b^t_{\alpha\beta}\tilde{\bar{v}}^{\perp}\right)\mathbf{a}_0^{\alpha\,t} \otimes \mathbf{a}_0^{\beta\,t} + (\tilde{\bar{v}}^{\perp}_{,\alpha} + b^t_{\lambda\alpha}\tilde{\bar{v}}^{\parallel}_{\lambda})\bar{\mathbf{n}}_0^t \otimes \mathbf{a}_0^{\alpha\,t} \tag{2.39}$$

$$(\bar{\mathbf{F}}^t)' = \bar{\mathbf{F}}^t \exp(\bar{\mathbf{L}}^t dt), \tag{2.40}$$

where $\tilde{\bar{v}}$ is the interface velocity interpolated at particle $\mathbf{y}^t$ using equation (2.24). Next, the updated deformation gradient $(\bar{\mathbf{F}}^t)'$ is rotated into the basis $\{\mathbf{a}_1^{t+dt}, \mathbf{a}_2^{t+dt}, \bar{\mathbf{n}}^{t+dt}\}$ to yield $\bar{\mathbf{F}}^{t+dt}$ (Fig. 2.7c and 2.7d.):

$$\bar{\mathbf{F}}^{t+dt} = (\bar{\mathbf{F}}^t)'(\mathbf{R}_t^{t+dt})^T \quad \text{with} \quad \mathbf{R}_t^{t+dt} = (\mathbf{R}^t)^{-1}\mathbf{R}^{t+dt}. \tag{2.41}$$

Similarly to the polynomials that approximates the geometry of the interface in section 4.2, a new set of polynomials is constructed to interpolate the deformation gradient around each particle. The second order polynomial that approximates the deformation gradient $\bar{\mathbf{F}}^{t+dt}$ around a particle $\mathbf{y}^{t+dt}$ is written:

$$\bar{F}^{t+dt}_{\alpha\beta}(\xi_1, \xi_2, t) = c^{\alpha\beta}_{0,0} + c^{\alpha\beta}_{1,0}\xi^1 + c^{\alpha\beta}_{0,1}\xi^2 + c^{\alpha\beta}_{1,1}\xi^1\xi^2 + c^{\alpha\beta}_{2,0}(\xi^1)^2 + c^{\alpha\beta}_{0,2}(\xi^2)^2, \tag{2.42}$$

where the coefficients $c^{\alpha\beta}_{i,j}$ are found with the method of least square fitting, using the values of the deformation gradient at the neighbouring particle. Thanks to the local polynomial reconstructions, the deformation gradient $\bar{\mathbf{F}}^{t+dt}$ can be interpolated anywhere on the interface Γ. The Green-Lagrange deformation tensor and the jacobian of the deformation are then computed as:

$$\bar{\mathbf{E}}^{t+dt} = \frac{1}{2}\left(\bar{\mathbf{F}}^{t+dt}(\bar{\mathbf{F}}^{t+dt})^T - \mathbf{I}\right) \quad \text{and} \quad J^{t+dt} = \det(\bar{\mathbf{F}}^{t+dt})$$

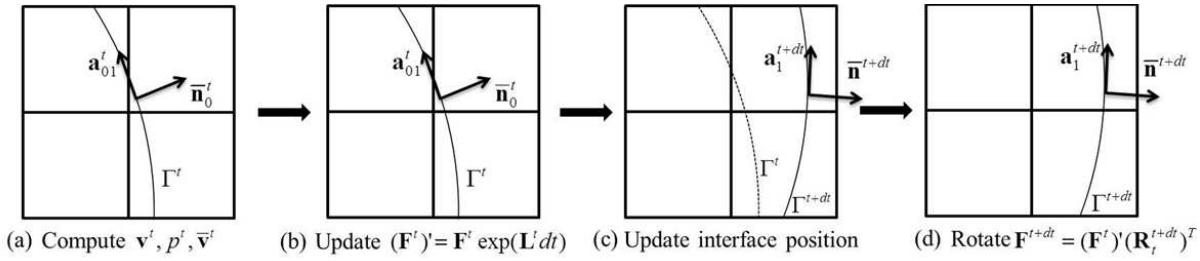

Figure 2.7: *Update and transport of the deformation gradient* $\bar{\mathbf{F}}$*: (a) the fluid and interface velocity field are first computed by solving* (2.26)*. The interface velocity field* $\bar{\mathbf{v}}$ *is then used to update* $\bar{\mathbf{F}}$ *in the basis* $\{\mathbf{a}_{0\,1}^t, \mathbf{a}_{0\,2}^t, \bar{\mathbf{n}}_0^t\}$ *(b). Finally, the interface position is updated (c) and the deformation gradient is rotated in the basis* $\{\mathbf{a}_1^{t+dt}, \mathbf{a}_2^{t+dt}, \bar{\mathbf{n}}^{t+dt}\}$ *to yield* $\bar{\mathbf{F}}^{t+dt}$ *(d).*

Once the different deformation measures of the interface are updated, one can compute the interface force $\bar{\mathbf{f}}$ anywhere on Γ using equation (2.19). Given the new interface force $\bar{\mathbf{f}}$, the algorithm turns back to the X-FEM and computes the velocity and pressure fields for the new time step, as shown in Fig. 2.8.

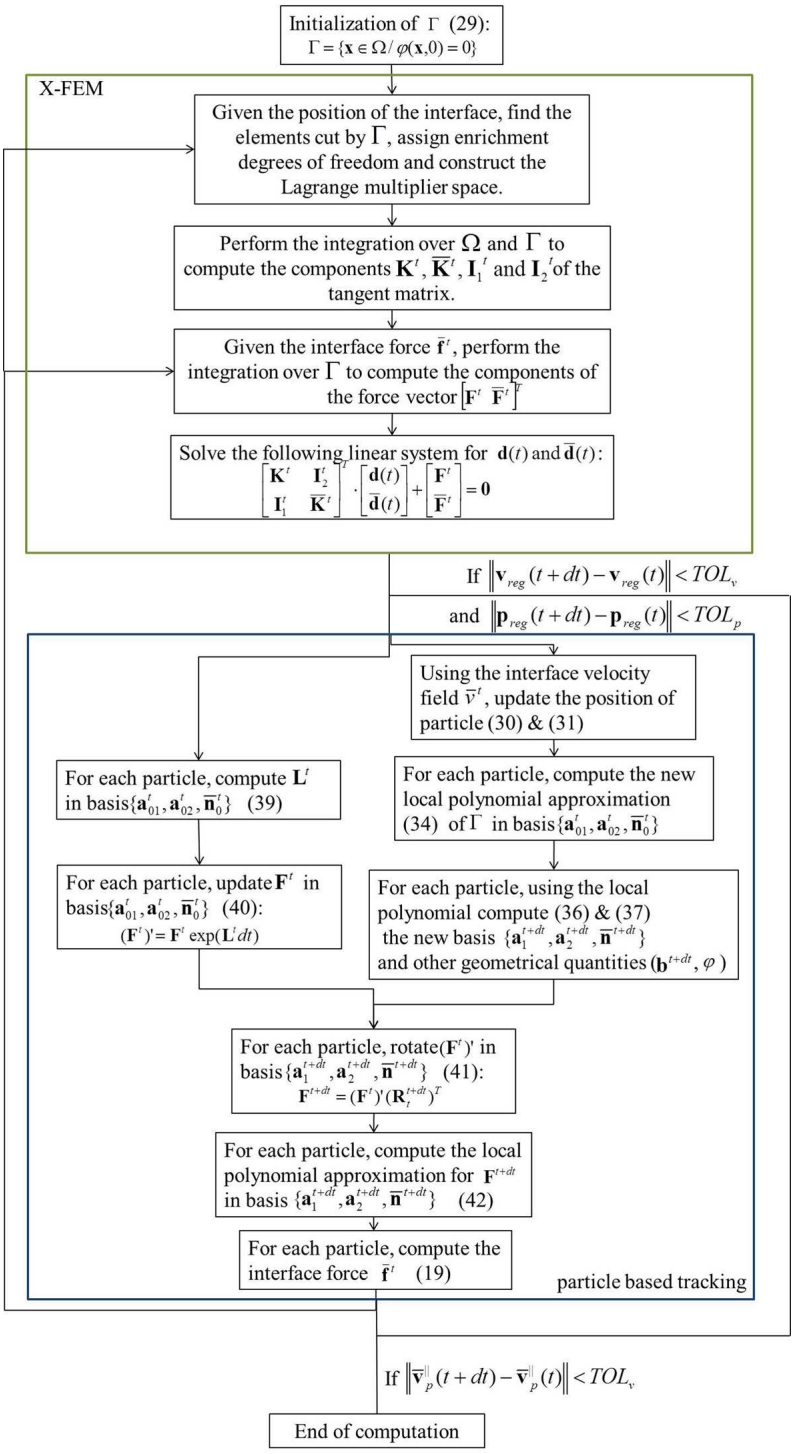

Figure 2.8: *General flowchart: the different velocity and pressure fields are solved using the X-FEM while the tracking and update of the interface geometry and Lagrangian fields is achieved using the grid based particle method.*

2.3 Numerical examples

We now consider several numerical examples with the aim of validating the proposed model and illustrating its ability to simulate some cases of extreme membrane deformations occurring in engineering and biological problems.

2.3.1 Convergence study

Here we first address the ill-conditioning of the tangent matrix usually associated with X-FEM formulation, and verify that the Lagrange multiplier space obtained using the M-discretization leads to stable fields on the interface. We then investigate the convergence of the error made in calculating the flow velocity and pressure around a fixed, rigid spherical capsule. Finally, we allow the capsule to elastically deform in contact with the surrounding fluid and study the CFL condition in time step dt for the temporal evolution of the interface.

X-FEM ill-condition and Lagrange multiplier discretization

A common issue that arises in X-FEM formulations is the typically ill-conditioned tangent matrix in (2.26) [64]. This is caused by the interface cutting through elements in a way that leaves very little support for the enrichment functions (Fig. 2.9a). This can lead to large oscillations in the pressure and velocity fields and affect the rate of convergence.

Several methods have been developed to address that issue, such as using a modified step enrichment function [8], or applying X-FEM specific preconditioners [14, 110]. Here we choose to use the enriched degrees of freedom (EDOF) blocking strategy, which consists in removing the EDOF that have very little support, as described in [136]. This method has the advantage of using the following simple geometrical criterion to determine which enriched degree of freedom should be neutralized. Inside each element cut by the interface, the areas A_e^+ and A_e^- on each side of the interface are computed. The EDOF that are to be neutralized correspond to those whose algebraic sign of the level-set value is opposite to that of the phase occupying the larger area in each cut element, and which only belong to elements where the following condition holds

true [136]:

$$\frac{\min(A_e^+, A_e^-)}{\max(A_e^+, A_e^-)} \quad < \quad C_{\text{block}}, \tag{2.43}$$

where $C_{\text{block}} \ll 1$ is a user-defined constant. The EDOF $\hat{p}^I$ and $\hat{v}^I$ that satisfy these conditions are 'removed' by enforcing the following Dirichlet conditions:

$$\hat{p}^I \;=\; 0 \quad \text{and} \quad \hat{v}^I \;=\; 0 \tag{2.44}$$

To investigate the effect of blocking the poorly supported EDOF on the pressure field across the interface, let us consider the case of an the inflation of an elastic circle of initial radius R_0. The circle is endowed with the following strain energy $\bar{\phi}(\bar{\mathbf{E}}^{ip}) \;=\; \frac{1}{2}\bar{\mathbf{E}}^{ip} : \boldsymbol{\mathcal{C}} : \bar{\mathbf{E}}^{ip}$, where the fourth order tensor $\boldsymbol{\mathcal{C}}$ is the elasticity tensor and can be written in the case of an isotropic linear material as $\boldsymbol{\mathcal{C}} = \bar{\lambda}\mathbf{1} \otimes \mathbf{1} + 2\bar{\mu}\boldsymbol{I}$, with $\bar{\lambda}$ and $\bar{\mu}$ the first and second Lamé coefficients. A point source is placed at the center of the circle until its enclosed area has doubled (Fig. 2.9). Once

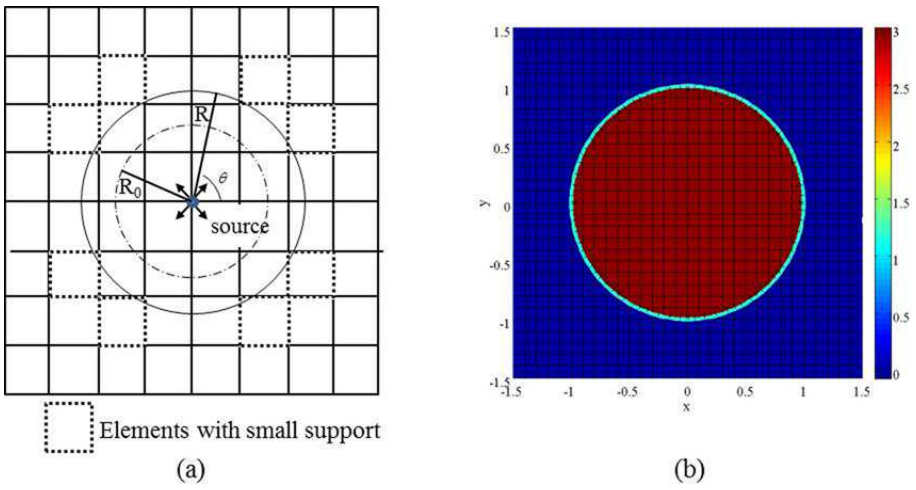

Figure 2.9: *(a) inflation of an elastic circle with a point source at its center and (b) numerical solution at equilibrium.*

the point source is removed, the exact solution to this problem is given by (2.12) as:

$$[p] \quad = \quad f^{\perp} \quad \forall \mathbf{x} \in \Gamma. \tag{2.45}$$

where the interface elastic force $f^{\perp}$ can be calculated using (2.19) as $f^{\perp} = \bar{T}_{11}^{ip}/R$, with R the current radius of the circle and the stress $\bar{T}_{11}^{ip}$ that arises from stretching the circle is written $\bar{T}_{11}^{ip} = (\bar{\lambda} + 2\bar{\mu})\bar{E}_{11}^{ip}\bar{F}_{11}^{ip}$. The deformation measures $\bar{F}_{11}^{ip}$ and $\bar{E}_{11}^{ip}$ can easily be calculated as:

$$\bar{F}_{11}^{ip} = \frac{R}{R_0} \tag{2.46}$$

$$\bar{E}_{11}^{ip} = \frac{1}{2}\left(\left(\frac{R}{R_0}\right)^2 - 1\right) \tag{2.47}$$

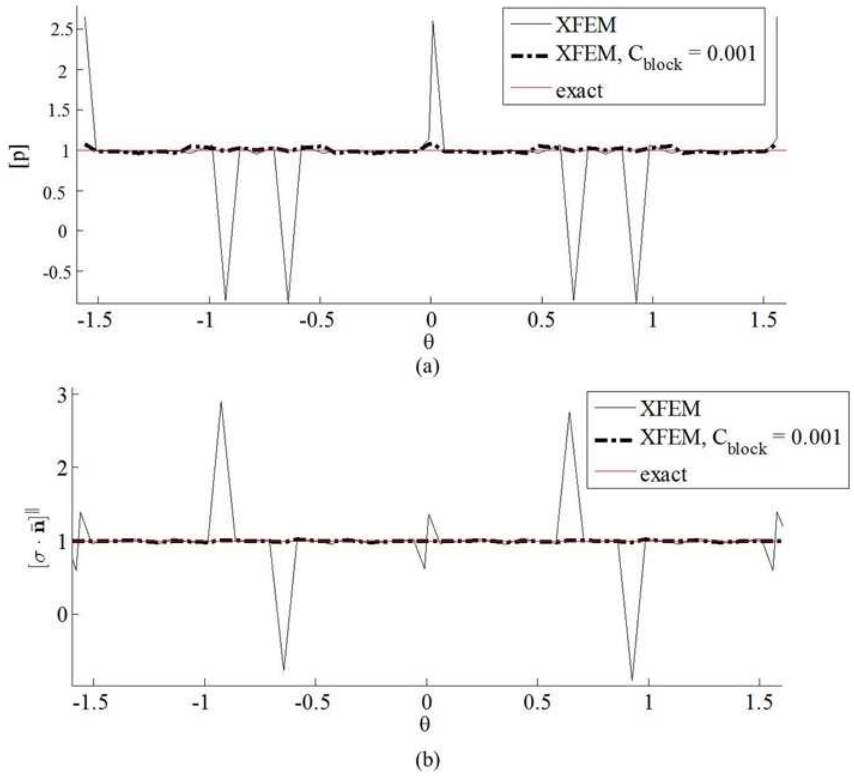

Figure 2.10: *(a) jump of pressure field and (b) jump of tangential viscous stress as a function of angle θ along the interface using both the unmodified X-FEM as well as with the EDOF blocking strategy.*

Fig. 2.10a shows the jump of pressure across the interface as a function of angle θ along the circle (Fig. 2.9a) with mesh size $h = R/10$. One observes that blocking selected EDOF removes the large oscillations of pressure across the interface that otherwise appear when using the unmodified X-FEM. The second column of table II presents the infinite norm of the error $||e_{[p]}||_{\infty}$ made in the pressure jump across the interface, which is observed to drop considerably

when the EDOF blocking strategy is used.

case	$\|\|e_{[p]}\|\|_\infty$	$\|\|e_{[\boldsymbol{\sigma}\cdot\bar{\mathbf{n}}]^\parallel}\|\|_\infty$
X-FEM	1.64	1.95
X-FEM, $C_{block} = 0.001$	6.21×10^{-2}	4.12×10^{-2}

Table 2.2: Maximum pressure and tangential stress jump error using the unmodified X-FEM the EDOF blocking strategy.

Remark: *Since the normal force $f^\perp$ of the interface in* (2.45) *is a function of the interface deformation measure $\bar{\mathbf{E}}^{ip}$, the above example also ensures that the deformation of the interface is properly updated as the circle inflates to its final size.*

Next, in order to investigate the behavior of the jump in tangent viscous stress across the interface, we turn to the case of a circle spinning in an infinite expanse of fluid. A tangential force $f^\parallel$ is applied to the interface and the jump of tangent viscous stress across the interface is computed along the circle (Fig. 2.11). The exact solution for the jump of viscous stress in this problem is given by (2.12):

$$[\boldsymbol{\sigma}\cdot\bar{\mathbf{n}}]^\parallel \quad = \quad f^\parallel \quad \forall \mathbf{x} \in \Gamma. \tag{2.48}$$

The jump of viscous stress is shown in Fig. 2.10b as a function of angle θ around the interface. Similarly to the pressure jump, the oscillations in the tangential viscous stress jump disappear with the neutralization of selected EDOF. The last column of table II shows that the infinite norm of the error $||e_{[\boldsymbol{\sigma}\cdot\bar{\mathbf{n}}]^\parallel}||_\infty$ made in computing the jump of tangential viscous stress across the interface behaves in a similar manner as $||e_{[p]}||_\infty$. Here we chose the slip length on both sides of the interface as $l^+ = l^- = 0$, which correspond to a 'stick' boundary condition between the fluid and the interface.

Finally, let us turn to the Lagrange multiplier fields discretized on the interface Γ. Fig. 2.12a presents the Lagrange multiplier field λ_p that enforces the pressure jump around the interface for the case of the inflating elastic circle while Fig. 2.12b shows the field λ^+ that enforces the

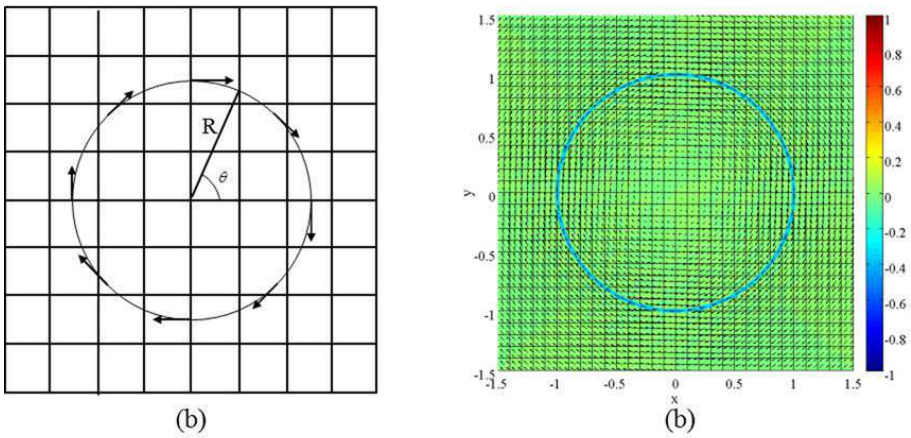

Figure 2.11: *(a) circle spinning in an infinite expanse of fluid under the action of a tangential force and (b) numerical result for the pressure and velocity field.*

'stick' boundary condition for the case of the spinning circle, using both the 'naive' and the M-discretization presented in section 3.1. We observe that using the M-discretization considerably reduces the large oscillations that are otherwise present in the fields λ_p and λ^+ when using the 'naive' discretization.

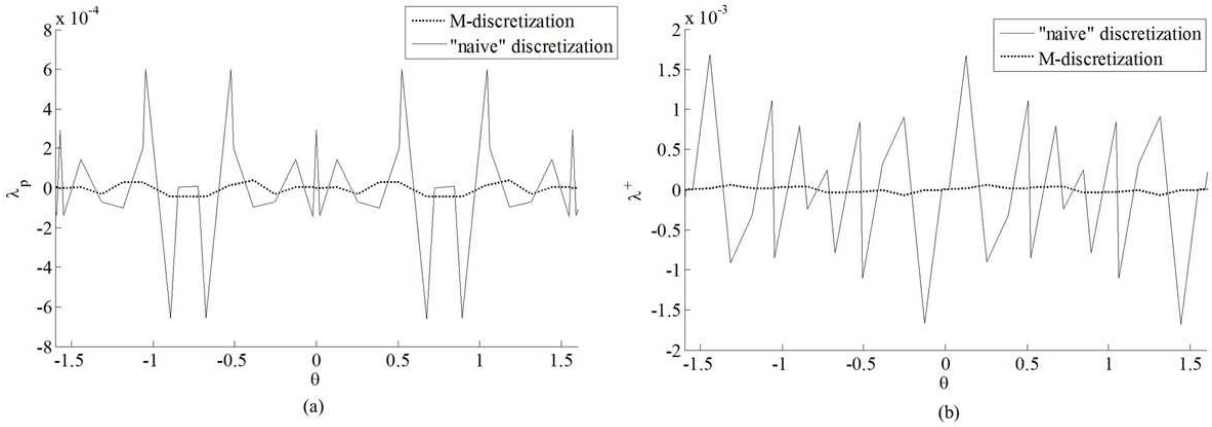

Figure 2.12: *Lagrange multiplier field λ_p (a) and λ^+ (b) along the interface as a function of angle θ, using both the 'naive' and the M-discretization.*

The EDOF blocking strategy used in combination with the proper Lagrange multiplier space are therefore shown to appropriately address both the ill-conditioning of the stiffness matrix K and the oscillations of the Lagrange multiplier fields along the interface.

Rigid spherical shell

Let us consider a uniform incompressible flow past a rigid spherical shell, and investigate the difference between model's prediction and the analytical solution of the flow velocity and pressure around the sphere with 'slip' or 'stick' boundary conditions at its surface. Analytically, the solution of the Stokes flow for an infinite expanse of fluid around a rigid sphere is given, in spherical coordinates (Fig. 2.13a), by [94]:

$$v_r \;=\; \frac{1}{r^2\sin^2(\theta)}\frac{\partial \Psi_{stokes}}{\partial \theta} \;\;,\;\; v_\theta \;=\; \frac{-1}{r\sin\theta}\frac{\partial \Psi_{stokes}}{\partial r} \;\;,\;\; v_\phi \;=\; 0 \tag{2.49}$$

where Ψ_{stokes} is the Stokes stream function that takes the form in the 'stick' and 'slip' cases, respectively [94]:

$$\Psi^{stick}_{stokes}(r,\theta) \;=\; \sin^2(\theta)\frac{U}{4}\left(\frac{R^2}{r} - 3Rr + 2r^2\right) \tag{2.50}$$

$$\Psi^{slip}_{stokes}(r,\theta) \;=\; \sin^2(\theta)\frac{U}{2}\left(-Rr + r^2\right). \tag{2.51}$$

with R is the radius of the sphere and U is the flow velocity away from the sphere $v_{r\to\infty} = U$. In our model, the 'stick' condition corresponds to a Navier boundary condition with $l^+_{slip} = 0$ while the 'slip' boundary condition requires $l_{slip} >> R$. We first investigate the convergence of the error made in calculating the pressure at the surface of the rigid sphere as the mesh size h is decreased. We define the L^2-error in pressure as :

$$e_p^2 \;=\; \frac{1}{\pi p_{max}}\left[\int_0^{\Pi}\left(p_{exact}(r=R,\theta) - p_{num}(r=R,\theta)\right)^2 d\theta\right]^{1/2} \tag{2.52}$$

where p_{exact} can easily be obtained from knowing the Stokes stream functions appearing in (2.50) and (2.51), $p_{max} = \max(p_{exact}(r=R,\theta))$ and p_{num} is the pressure calculated numerically. Fig. 2.13b presents the pressure field around the sphere for the 'stick' case while Fig. 2.13c (log-log scale) shows that the error made in calculating the pressure converges to zero like $O((h/R)^3)$, for both extreme cases $l^+ = 0$ (stick) and $l^+ >> R$ (slip). The Reynolds number chosen in those simulations is $Re = RU\rho/(\mu) = 0.05$, at which inertia forces can be neglected. The solid and

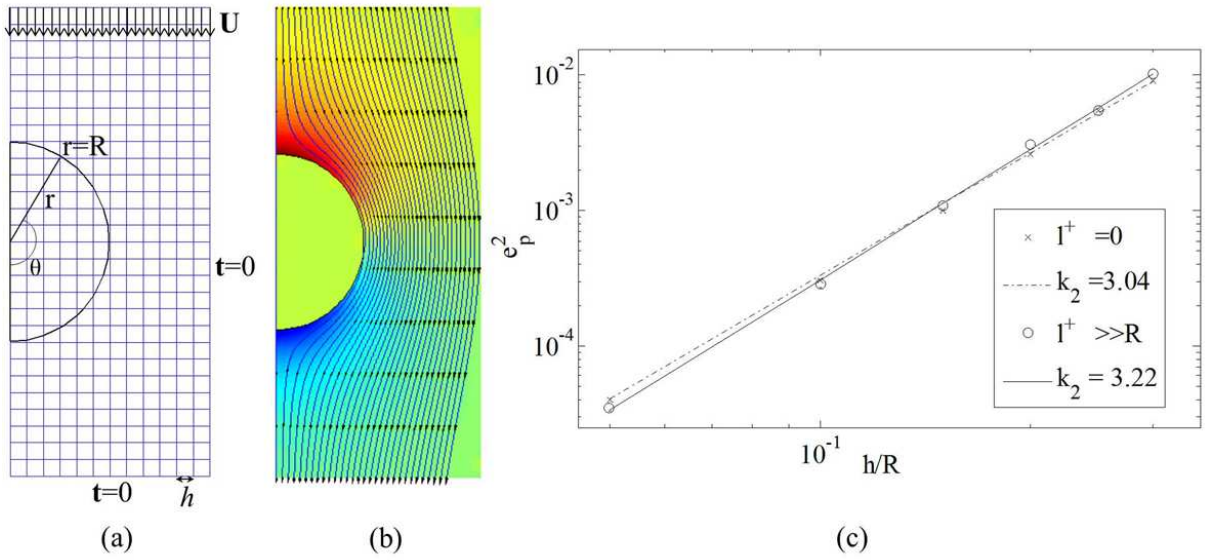

Figure 2.13: *(a) Finite element mesh and boundary conditions, (b) pressure field and velocity stream line for the fluid flowing around the sphere and (c) convergence of the error made on the pressure on the surface of the sphere as the mesh size decreases.*

doted lines show the power law fitting of the error, calculated as:

$$e_{p\,fit} \quad = \quad k_1(h/R)^{k_2} \tag{2.53}$$

where $k_2 \sim 3$ is an approximation of the rate of convergence. This is in excellent agreement with the convergence study done for the grid-based particle method performed in [100].

Figs. 2.14a and 2.14b respectively show the vertical flow velocity $\mathbf{v}_\theta(r, \theta = \pi/2)$ and the surface pressure $p(r = R, \theta)$ for a rigid sphere with different slip length, ranging from $l^+ = 0$ ('stick' condition) to $l^+ >> R$ ('slip' condition). We observe an excellent agreement between the analytical and numerical results for the vertical flow velocity $\mathbf{v}_\theta(r, \theta = \pi/2)$ and surface pressure $p(r = R, \theta)$ in both the 'stick' and 'slip' cases. Intermediate values of l^+ show the capability of the model to continuously transition from a 'stick' to 'slip' boundary condition. As we increase the slip length from $l^+ = 0$, the tangential velocity jump increases (Fig. 2.14a) while the viscous shear stress at the surface of the sphere decreases since $(\boldsymbol{\sigma} \cdot \bar{\mathbf{n}})^{\|+} = (\mu[\mathbf{v}]^+)/l^+$, which in turn lowers the pressure exerted by the fluid on the surface.

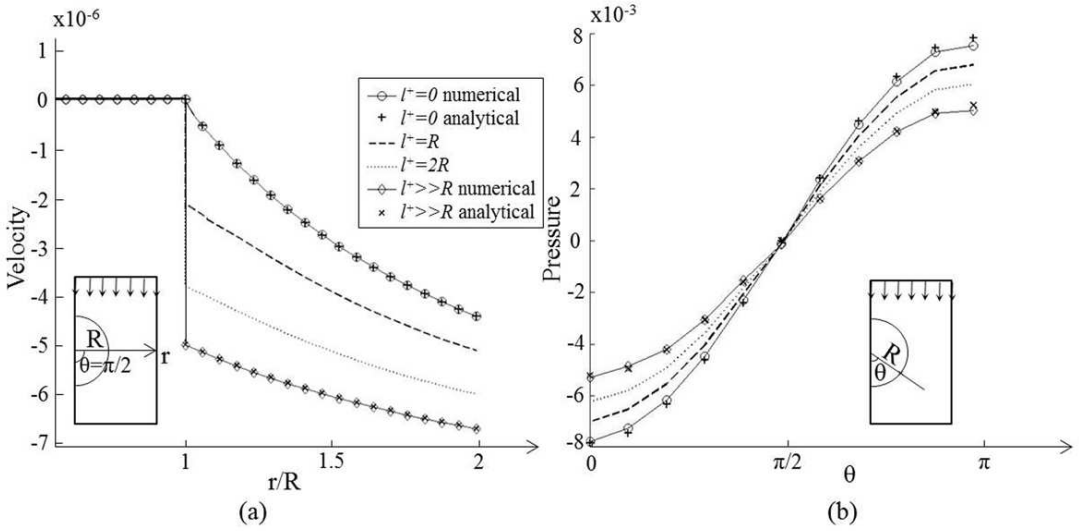

Figure 2.14: *Simulation and analytical results of the velocity (a) and pressure (b) for different slip lengths*

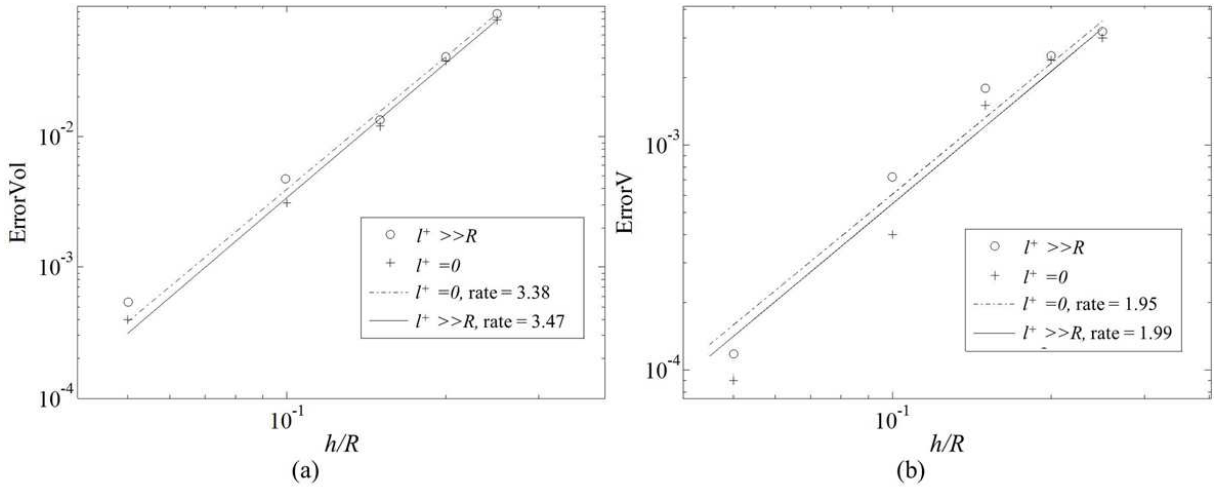

Figure 2.15: *Convergence of the error made in conserving the enclosed volume (a) and residual velocity (b) as the mesh size decreases, for* $\Delta t \sim O(h/R)^4$ *and for different slip lengths*

Remark: *In the enrichment functions that allow the tangential velocity jump for* $l >> R$*, we use the tangent vectors calculated from the second order polynomials that approximate the interface. However, the Gaussian quadrature used to calculate the stiffness matrix in split elements uses a subset of triangles, which leads to a piece-wise linear interface. This inconsistency is believed to lead to the suboptimal convergence rates observed in the coarsest 4 mesh sizes in Fig.2.15b.*

Soft spherical shell

The convergence study shown in Fig. 2.13 is only valid for a fixed, rigid interface. Next, we show convergence with evolution of the interface by allowing the elastic spherical capsule to deform in contact with the surrounding fluid, while its top extremity remains fixed. We first endow the capsule with elastic mechanical properties. To this end, we write the capsule's strain energy function $\bar{\phi}(\bar{\mathbf{E}}^{ip}, \bar{\mathbf{C}}^{ip})$ as the sum of a quadratic potential function of $\bar{\mathbf{E}}^{ip}$ and the Helfrich surface energy function of the mean curvature H [75]:

$$\bar{\phi}(\bar{\mathbf{E}}^{ip}, \bar{\mathbf{C}}^{ip}) \;=\; \frac{1}{2}\bar{\mathbf{E}}^{ip} : \boldsymbol{\mathcal{C}} : \bar{\mathbf{E}}^{ip} + \frac{\kappa}{2}(H - H_0)^2, \tag{2.54}$$

where the spontaneous curvature was taken to be $H_0 = 0$. Next, to characterize the capsule's elasticity relative to the fluid velocity, we introduce a dimensionless parameter $G = (\mu U)/E$, where $E = \bar{\mu}(3\bar{\lambda} + 2\bar{\mu})/(\bar{\lambda} + \bar{\mu})$ is the in-plane elastic modulus of the capsule. The membrane Poisson's ratio was taken to be $\nu = \bar{\lambda}/(2(\bar{\lambda} + \bar{\mu})) = 0.25$. A second parameter $E_b = \kappa/(R^2 E)$ relates the bending elasticity κ to E.

We show in Fig. 2.15 the convergence of the residual velocity of the membrane as well as the error made in conserving the enclosed volume when the capsule reaches equilibrium, for values of G and E_b that produces large deformations of the capsule's membrane, e.g. $G = 0.1$ and $E_b = 0.01$. Fig. 2.15a shows that for both cases $l^+ = 0$ and $l^+ >> R$, the velocity residual converges like $O(h/R)^2$. This is consistent with the convergence rate found [100] and the fact that we used a second-order Runge-Kutta algorithm in time discretization. Furthermore, the error made in conserving the enclosed volume converges like $O(h/R)^3$. However, due to the presence of fourth order terms in the membrane bending force, the explicit time evolutive simulations are subjected to a strict Courant-Friedrichs-Lewy (CFL) condition on the time step of the fourth order in mesh size $\Delta t \sim O(h/R)^4$ [99].

The shapes adopted at equilibrium by the capsule with $l^+ = 0$ and for different values of G are shown in Fig. 2.16a. As expected, one can see that the capsule deformation increases with the ratio of the fluid velocity to capsule elasticity. Fig. 2.16b illustrates the effect of the

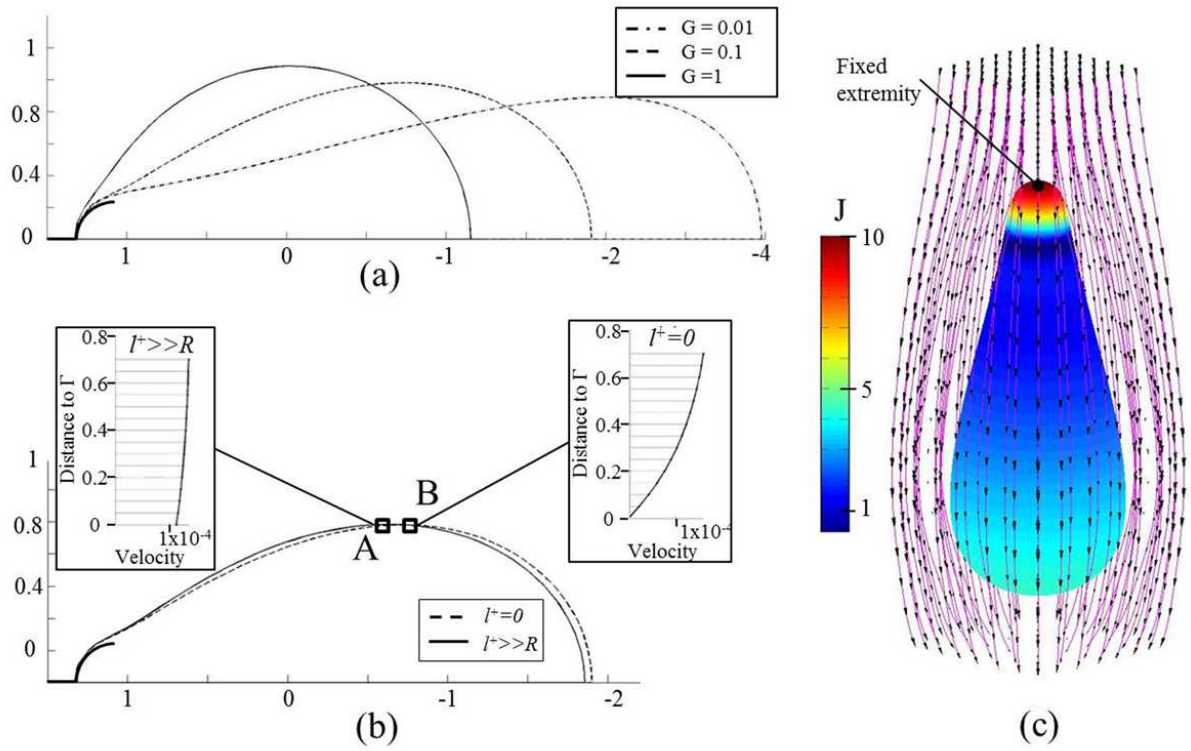

Figure 2.16: *figure (a) shows the capsule deformations for different values of G while figure (c) shows the effect of the slip length on the capsule deformation and velocity profile. Figure (c) shows the fluid streamlines around the capsule and the surface jacobian J. The time step used was* $\Delta t = (h/R) \times 1e^{-4}$ *and the tolerances* $TOL_v = TOL_p = TOL_{\bar{v}\|} = 1e^{-5}$

slip length l^+ on the capsule deformation for $G = 0.1$. As the slip length increases, the pressure exerted on the capsule decreases, which in turn reduces the deformation. Furthermore, Fig. 2.16b shows the fluid velocity profiles along a direction normal to the capsule at the points A and B respectively for $l^+ >> R$ and $l^+ = 0$. The discontinuity in tangential velocity between the fluid and the membrane is clearly apparent in the case $l^+ >> R$, while setting $l^+ = 0$ ensures a continuous tangential velocity that decreases to zero at the surface of the capsule. As the capsule deforms under the action of the fluid flow, the jacobian J of the deformation represented as a color gradient on the surface in Fig. 2.16c is shown to take very large values around the fixed extremity. The particle ressampling ensures that the spatial discretization and the geometrical resolution of the membrane remains uniform throughout the simulation.

2.3.2 Capsule in shear flow

Our second example now investigates the equilibrium shapes of an initially circular capsule in shear flow, with the objectives of replicating the results from [149] for validation and showing the effect of slip length on the deformation and 'tank-threading' motion. The capsule is endowed with the same elastic properties as (2.54) and its initial circular shape corresponds to an in-plane stress free configuration. However, since the spontaneous curvature H_0 is chosen to be zero (which corresponds to a flat surface), the capsule has a non-zero bending energy at time $t = 0$. The capsule is subjected to a shear flow on the top and bottom boundaries of the

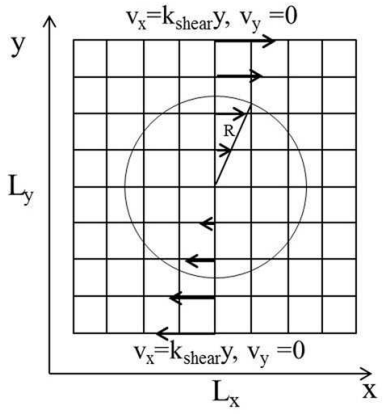

Figure 2.17: *Figure (a) shows the computational domain and the boundary conditions for the elastic capsule in shear flow.*

computational domain of size L_x by L_y, as shown in Fig. 2.17. The shear flow is characterized by a shear rate k_{shear} with $\mathbf{v} = (k_{shear}y, 0)$. The magnitude of the shear flow relative to the capsule's elasticity is captured by the dimensionless parameter G such that $G = (\mu k_{shear}R)/E$. The ratio between the bending elasticity κ and the in-plane elasticity E constitutes a second dimensionless parameter written as $E_b = \kappa/(R^2E)$. The Reynolds number in these simulations is calculated as $Re = (4R^2k_{shear}\rho)/(\mu)$ and is set to 0.05, where inertia effects can be neglected. The size of the computational domain is $L_x = 4R$ by $L_y = 4R$ and is discretized using square elements of size $h = 0.1R$, as this was shown to be sufficient to make the simulation independent of the mesh size.

Fig. 2.18a and 2.18b show the streamlines, velocity magnitude and pressure field for the

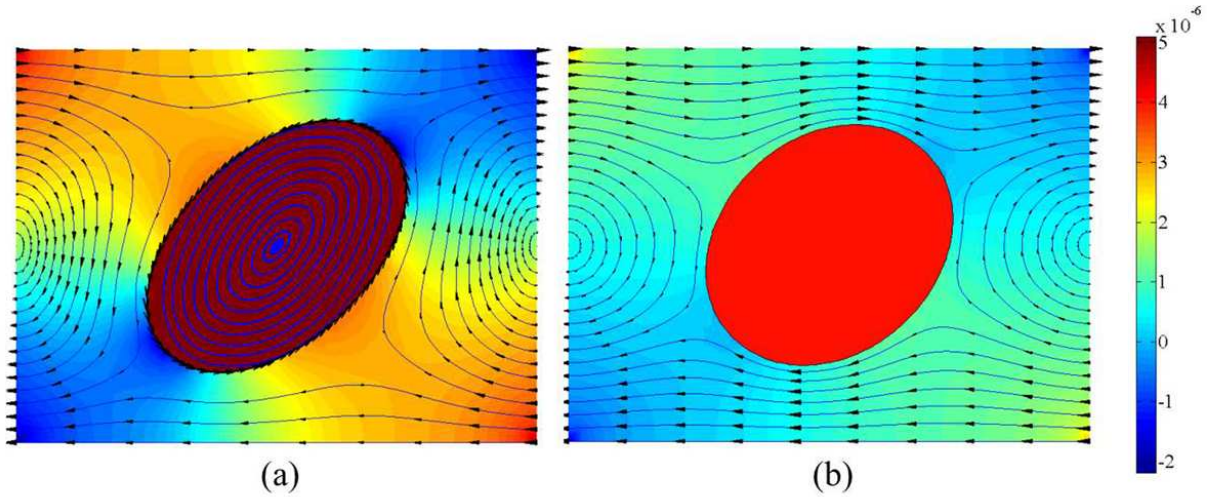

Figure 2.18: *Figures (a) and (b) show the pressure fields, streamlines and velocity magnitude for the steady states of a capsule in shear flow, with respectively stick and slip surfaces. The time step used was* $\Delta t = (h/R) \times 1e^{-4}$ *and the tolerances* $TOL_v = TOL_p = TOL_{\bar{v}\|} = 1e^{-5}$

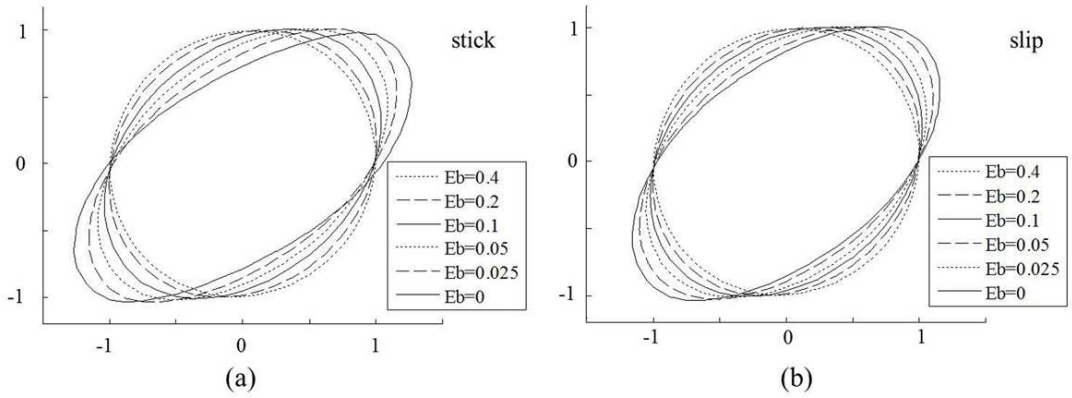

Figure 2.19: *Figure shows the capsule deformation with different bending rigidities in the cases (a)* $l^+ = 0$ *(stick) and (b)* $l^+ >> R$ *(slip).*

'stick' $l^+ = 0$ and 'slip' $l^+ >> R$ capsules at steady state. As expected, the effect of the capsule's surface property is quite apparent: for the same values of G and E_b, the 'stick' capsule clearly displays a tank threading motion, as observed in [149]. However, the tank threading motion is totally absent for a 'slip' capsule. The magnitude of the pressure field and the capsule deformation are also much higher in the 'stick' than in the 'slip' case since a greater slip length increases the viscous shear stress around the capsule.

The equilibrium shapes of the capsule with different values of E_b are shown in Fig. 2.19, in

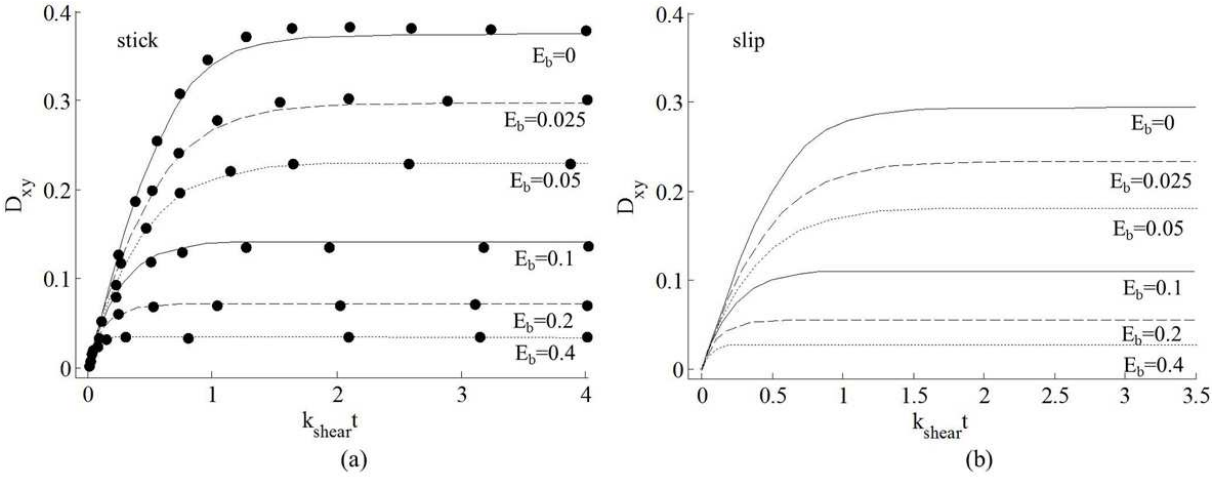

Figure 2.20: *Figures (a) and (b) show the Taylor deformation parameter D_{xy} as a function of the non-dimensional time $k_{shear}t$ for different bending rigidities in the stick and slip cases respectively. The black dots in (a) represent data point from [149].*

the 'slip' and 'stick' case. One can see that the effect of the bending elasticity has a direct impact on the equilibrium shapes of the capsules: a higher bending rigidity reduces the curvature at both ends of the capsule and for a high enough value of E_b, the capsule undergoes almost no deformation. Here again, the effect of surface properties can be observed as the deformations of a 'slip' capsule are smaller compared to the 'stick' case, for equal bending elasticity. More quantitatively, the temporal evolution of the Taylor deformation parameter is presented in Fig. 2.20. The Taylor deformation parameter is defined by $D_{xy} = (a - b)/(a + b)$, where a and b are the length and width of the capsule. The black dots in Fig.2.20a represent data points from [149] for the 'stick' case. Although the Taylor deformation parameter appears somewhat lower for $E_b = 0$ and $E_b = 0.025$, the temporal evolution of the capsule in the 'stick' case are in very good agreement with the results from [149]. The 'slip' boundary condition is shown to decrease the maximum value of the Taylor deformation parameter compared to the 'stick' case for the same bending rigidities E_b in Fig. 2.20b.

2.3.3 Pipette aspiration

Let us now turn to the aspiration of an immersed liquid droplet into a spherical channel (which corresponds to the tip of a pipette for example), where the fluid/interface and membrane/inter-

face interactions as well as the large deformations play an essential role. We choose to investigate the well studied case of an incompressible liquid droplet with surface tension γ and radius R_c being aspired into a pipette of radius R_p by a constant pressure gradient $\Delta p = P_{ex} - P_{in}$, where P_{ex} and P_{in} are respectively the pressure outside and inside the pipette (Fig. 2.21a). There exists a critical surface tension γ_{crit} such that for $\gamma < \gamma_{crit}$ the droplet is entirely aspired

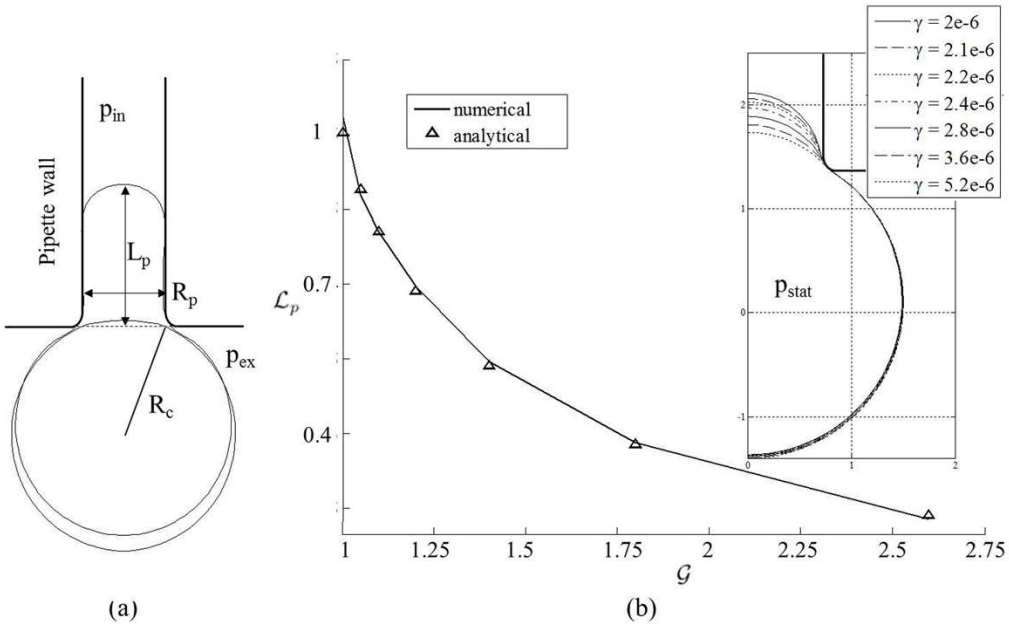

Figure 2.21: *Figure (a) shows the pipette aspiration geometry and figure (b) shows the analytical and numerical results for the penetration length $\mathcal{L}_p$ as a function of capillarity $\mathcal{G}$. The time step used was $\Delta t = (h/R) \times 1e^{-2}$ and the tolerances $TOL_v = TOL_p = TOL_{\vec{v}\|} = 1e^{-5}$*

into the pipette whereas for $\gamma > \gamma_{crit}$, the droplet is partially uptaken and reaches mechanical equilibrium at the entry of the pipette [51]. This allows us to characterize the droplet/pipette system with two dimensionless numbers: a version of the capillarity number $\mathcal{G} = \gamma/\gamma_{crit}$ and the dimensionless radius $\mathcal{R}_p = R_p/R_c$.

For values of $\mathcal{G} > 1$, the equilibrium shape of the partially aspired droplet can found analytically as follows. Considering that at equilibrium the velocity field vanishes and the pressure in the droplet is constant, the Laplace law combined with some geometrical considerations yields the following system of equations that describe the pressure and shape of the droplet at equi-

librium [51]:

$$\frac{p_{eq} - p_{in}}{2\gamma} = \frac{2L_{p\,eq}}{R_p^2 + L_{p\,eq}^2} \tag{2.55}$$

$$\frac{p_{eq} - p_{ex}}{2\gamma} = \beta(8R_c^3 - 3R_p^2 L_{p\,eq} - L_{p\,eq}^3)^{-1/3} \tag{2.56}$$

where p_{eq} and $L_{p\,eq}$ are respectively the pressure and the distance travelled by the droplet inside the pipette when it reaches equilibrium, and we used the fact that the interface force caused by the droplet surface tension is given by (2.21) as:

$$\bar{\mathbf{f}} = \gamma H \bar{\mathbf{n}}.$$

Fig. 2.21b shows the analytical and numerical results for the dimensionless travel distance $\mathcal{L}_p = L_p/R_p$ for stable values of surface tension $\mathcal{G} > 1$. The contact between the droplet interface and the pipette wall is handled by the penalty method and by taking advantage of the level-set function that is locally reconstructed at each iteration. Knowing the level-set function instantaneously yields the closest distance from any point on the pipette wall to the droplet interface, which considerably simplifies the contact problem. The computational domain was discretized using elements of size $h = R/10$ with R the radius of the droplet in its initial spherical shape. The CFL condition on the time step is less strict here since the interface force here only depends on the mean curvature which is a second order term (as opposed to fourth order terms for an elastic interface). The time step was therefore chosen as $\Delta t = (h/R)^2$. The numerical and analytical solutions for the travel distance $\mathcal{L}_p$ show a very good agreement and predict the same critical surface tension below which the droplet cannot find a stable equilibrium and is entirely aspired.

2.3.4 Droplet subjected to surface tension and gravity

To further assess the formulation's validity, we considered the more complicated problem of a fluid droplet subjected gravitational fluid and laying on a flat rigid substrate. Although the strain energy $\bar{\phi}$ and the membrane force $\bar{\mathbf{f}}$ take the same form as in the precedent example,

this example is particularly interesting to demonstrate the applications of Dirichlet boundary conditions on the membrane by imposing a zero vertical velocity at the section of the membrane in contact with the substrate. This problem also serves as a benchmark as the analytical solution for the height h of a droplet characterized by different surface tensions γ is known. Following [42], the analytical solution has the form:

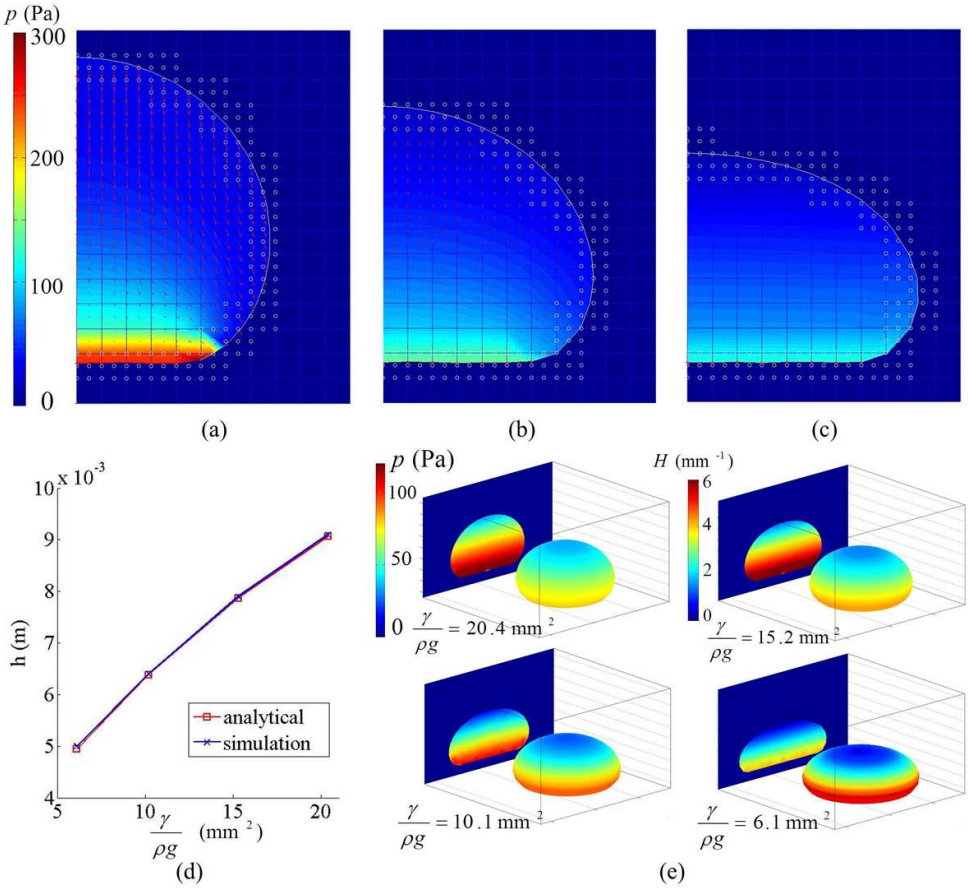

Figure 2.22: *Finite element mesh on which the governing equations are solved and nodes with enriched degrees of freedom (white circles). Images (a), (b) and (c) show the droplet progressively finding its equilibrium position where the pressure gradient is vertical and the velocity (red arrows) null. In figure (d) the Droplet's height is plotted as a function of surface tension over density times the gravity and figure (b) is a 3D representation of the droplet's equilibrium shapes for different surface tension. The internal pressure field is projected onto the plan $z = 0$ and the membrane curvature is plotted on the surface as a color gradient. The viscosity chosen here is $\mu = 1.10^{-3} Pa.s$ (water) and the surface tension corresponding to water is $\gamma/\rho g = 6.1mm^2$*

$$h = \sqrt{\frac{2\gamma(1-\cos\theta)}{\rho g}} \tag{2.57}$$

where the contact angle θ chosen was chosen to 180°, corresponding to a non-wettable surface. Regarding the numerical formulation, Fig.2.22a-c. shows the eulerian domain, the associated finite element discretization and the pressure field in the droplet as it reaches its equilibrium position. We also note that the enriched nodes of split elements, represented with white circle, are subjected to Dirichlet boundary conditions as the membrane comes in contact with the substrate. Numerical and analytical prediction of the droplet height h are then shown for four different values of surface tension in Fig. 2.22d. We observe a very good agreement between these results, with a maximum error of 0.2%. The three-dimensional shape of the droplet is then depicted in Fig.2.22c. at equilibrium for different surface tension. It can clearly be seen that both surface curvature (plotted on the droplet surface as a color gradient) and the internal pressure (projected on a vertical plan) a strongly influenced by surface tension.

2.3.5 Elastic capsule through a tight opening

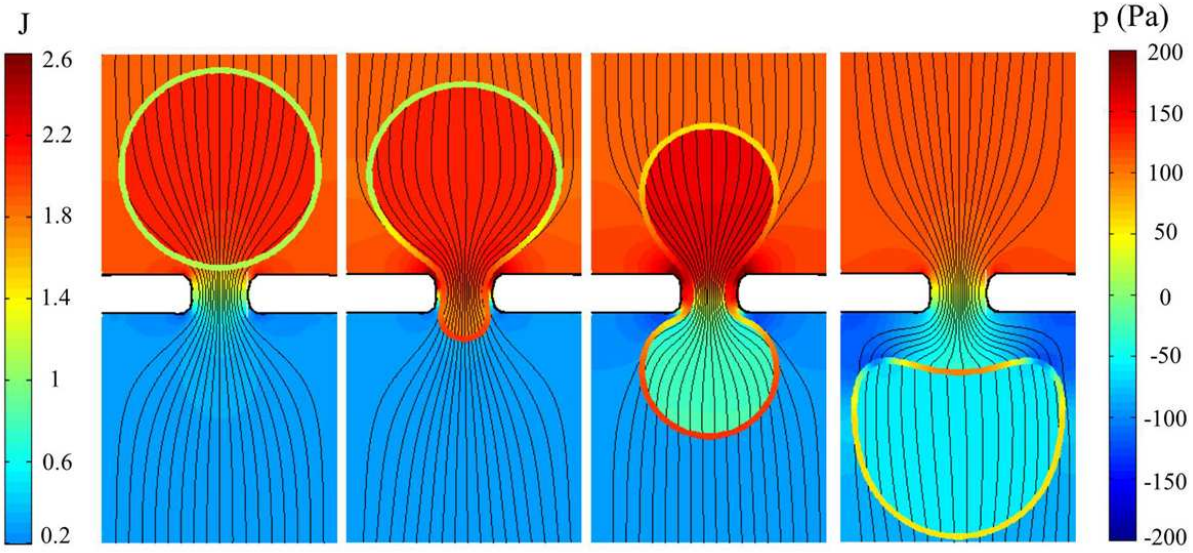

Figure 2.23: *The surface Jacobian J of the vesicle is shown as a color gradient along the interface, along with the surrounding fluid pressure field and streamlines. The time step used was $\Delta t = (h/R) \times 1e^{-4}$ and the tolerances $TOL_v = TOL_p = TOL_{\bar{v}\|} = 1e^{-5}$*

This example shows an elastic vesicle forced through a small opening by a pressure gradient Δp, and illustrates the very large deformations the vesicle can go through using the presented

method, both in terms of the stretching and bending of the interface. The surface Jacobian (or dilation) of the vesicle is shown as a color gradient along the interface in Fig.2.23, along with the surrounding fluid pressure field and streamlines. A slip boundary condition was applied on the walls of the opening and a double pressure and velocity enrichment was implemented in the elements cut by both the walls and the interface. The computational domain was discretized using elements of size $h = R/10$ with R the radius of the vesicle in its initial circular shape, and the time step was chosen as $\Delta t = (h/R)^{-4}$. One can observe the wide range of values taken by the surface Jacobian (> 2.5 and as low as 0.2) as the vesicle goes through the opening. Simulating such deformations with a Lagrangian description of the interface would require the use of complicated remeshing algorithms at several points during the simulation to prevent large mesh distortion. The advantages of using a Eulerian point of view in combination with the grid based particle tracking of the interface become clear here as it ensures a homogeneous spatial discretization of the interface throughout the simulation.

2.4 Conclusion

In this chapter, we presented a full Eulerian formulation for the analysis of the large deformations of an immersed interface arising in a large number of soft matter mechanics problems. The model is versatile enough to accommodate various material behaviors from a hyperelastic membrane to a fluid interface. The introduction of a tangential velocity degree of freedom for the interface in combination with discontinuities in velocity and pressure fields enables us to simulate a wide variety of boundary conditions between the interface and the surrounding fluid while automatically satisfying the normal velocity continuity condition. These contributions were made numerically possible by coupling two very efficient methods: the extended finite element and the grid-based particle methods, which used in an Eulerian framework completely circumvents the problem of mesh distortion usually associated with Lagrangian finite elements. The combination of these methods has two key advantages: (a) the X-FEM makes it possible to account for field discontinuities within the finite element framework and (b) the grid based particle method removes the need for time consuming reinitialization that are usually associ-

ated with the use of of level-set in X-FEM. Furthermore, as opposed to the traditional level-set method, the grid based particle method is very well suited to the computation of higher order derivative on a curved surface and can accurately track the Lagrangian fields associated with an elastic interface. We showed, via a number of examples, that the approach gives very satisfactory results for a wide variety of problems involving the effect slip lengths, membrane elasticity, and characterized by very large shape changes. In this context, future research can describe various mechanisms that may include the phoretic transport of highly deformable cells [3], the diffusion of membrane associated molecules on curved manifolds and its coupling with mechanical deformation [150, 62], or the effect of slip length on vesicles tumbling under the effect of shear flow [149].

Appendix: Derivation of the interface force $\bar{\mathbf{f}}$

The interface force $\bar{\mathbf{f}}$ can be found by writing the interface elastic power as the dot product of the interface velocity $\bar{\mathbf{v}}$ and $\bar{\mathbf{f}}$. First recalling the expressions of $\bar{\mathbf{D}}$ and $\dot{\bar{\mathbf{C}}}$ as functions of $\bar{\mathbf{v}}$, respectively equations:

$$\begin{aligned} \bar{\mathbf{D}} &= \left(\frac{1}{2}\left(\bar{v}^{\parallel}_{\alpha|\beta}+\bar{v}^{\parallel}_{\beta|\alpha}\right)-b_{\alpha\beta}\bar{v}^{\perp}\right)\mathbf{a}^{\alpha}\otimes\mathbf{a}^{\beta} \\ \text{and}\quad \dot{\bar{\mathbf{C}}} &= \dot{b}_{\alpha\beta} = \left(\bar{v}^{\perp}_{|\alpha\beta}-\bar{v}^{\perp}b^{\lambda}_{\alpha}b_{\lambda\beta}\right)\mathbf{a}^{\alpha}\otimes\mathbf{a}^{\beta}, \end{aligned}$$

one can write the interface elastic power as follows:

$$\begin{aligned} \dot{\bar{\mathcal{E}}}[\bar{\mathbf{v}}] &= \int_{\Gamma}\left(\bar{\mathbf{T}}:\bar{\mathbf{D}}+\bar{\mathbf{M}}:\dot{\bar{\mathbf{C}}}\right)\,ds \\ &= \int_{\Gamma}\left(\bar{\mathbf{T}}:\left(\frac{1}{2}\left(\bar{v}^{\parallel}_{\alpha|\beta}+\bar{v}^{\parallel}_{\beta|\alpha}\right)-b_{\alpha\beta}\bar{v}^{\perp}\right)\mathbf{a}^{\alpha}\otimes\mathbf{a}^{\beta}+\bar{\mathbf{M}}:\left(\bar{v}^{\perp}_{|\alpha\beta}-\bar{v}^{\perp}b^{\lambda}_{\alpha}b_{\lambda\beta}\right)\mathbf{a}^{\alpha}\otimes\mathbf{a}^{\beta}\right)ds \\ &= \int_{\Gamma}\left(\bar{T}^{ip}_{\alpha\beta}\frac{1}{2}\left(\bar{v}^{\parallel}_{\alpha|\beta}+\bar{v}^{\parallel}_{\beta|\alpha}\right)-\bar{T}^{ip}_{\alpha\beta}b_{\alpha\beta}\bar{v}^{\perp}+\bar{M}^{ip}_{\alpha\beta}\bar{v}^{\perp}_{|\alpha\beta}-\bar{M}^{ip}_{\alpha\beta}b^{\lambda}_{\alpha}b_{\lambda\beta}\bar{v}^{\perp}\right)ds, \end{aligned}$$

where $\bar{T}^{ip}_{\alpha\beta}$ and $\bar{M}^{ip}_{\alpha\beta}$ are the in-plane components of the stress and moment tensor, such that $\bar{\mathbf{T}}=T^{ip}_{\alpha\beta}\mathbf{a}^{\alpha}\otimes\mathbf{a}^{\beta}$ and $\bar{\mathbf{M}}=M^{ip}_{\alpha\beta}\mathbf{a}^{\alpha}\otimes\mathbf{a}^{\beta}$. Next, using the divergence theorem once on the first

integrand $\bar{T}^{ip}_{\alpha\beta}\frac{1}{2}\left(\bar{v}^{\parallel}_{\alpha|\beta}+\bar{v}^{\parallel}_{\beta|\alpha}\right)$ and twice on the third integrand $\bar{M}^{ip}_{\alpha\beta}\bar{v}^{\perp}_{|\alpha\beta}$ yields:

$$\dot{\bar{\mathcal{E}}}[\bar{\mathbf{v}}] = \int_\Gamma \left(-\bar{T}^{ip}_{\alpha\beta|\beta}\bar{v}^{\parallel}_{\alpha} - \bar{T}^{ip}_{\alpha\beta}b_{\alpha\beta}\bar{v}^{\perp} + \bar{M}^{ip}_{\alpha\beta|\alpha\beta}\bar{v}^{\perp} - \bar{M}^{ip}_{\alpha\beta}b^{\lambda}_{\alpha}b_{\lambda\beta}\bar{v}^{\perp}\right) ds,$$

where the boundary terms on $\delta\Gamma$ do not appear since the interface Γ is considered closed in this work. Finally, recalling that $\bar{\mathbf{v}} = \bar{v}^{\parallel\alpha}\mathbf{a}_\alpha + \bar{v}^{\perp}\bar{\mathbf{n}}$ we can write:

$$\begin{aligned}
\dot{\bar{\mathcal{E}}}[\bar{\mathbf{v}}] &= \int_\Gamma \left(-\bar{T}^{ip}_{\alpha\beta|\beta}\mathbf{a}^{\alpha} - \bar{T}^{ip}_{\alpha\beta}b_{\alpha\beta}\bar{\mathbf{n}} + \left(\bar{M}^{ip}_{\alpha\beta|\alpha\beta} - \bar{M}^{ip}_{\alpha\beta}b^{\lambda}_{\alpha}b_{\lambda\beta}\right)\bar{\mathbf{n}}\right)\cdot\bar{\mathbf{v}}ds \\
&= \int_\Gamma \bar{\mathbf{f}}\cdot\bar{\mathbf{v}}ds \\
\text{with}\quad \bar{\mathbf{f}} &= \underbrace{\left(-\bar{T}^{ip}_{\alpha\beta|\beta}\mathbf{a}^{\alpha} - \bar{T}^{ip}_{\alpha\beta}b_{\alpha\beta}\bar{\mathbf{n}}\right)}_{\text{in-plane stress}} + \underbrace{\left(\bar{M}^{ip}_{\alpha\beta|\alpha\beta}\bar{v}^{\perp} - \bar{M}^{ip}_{\alpha\beta}b^{\lambda}_{\alpha}b_{\lambda\beta}\right)\bar{\mathbf{n}}}_{\text{bending moment}}
\end{aligned}$$

Appendix: components of the tangent matrix

To obtain the dicretized weak form of the governing equations, let us turn to the weak form (2.25) and decompose the integration over $\Omega\cup\Gamma$ into the sum of the integration over the element domain Ω_e:

$$\begin{aligned}
\sum_{e=1}^{nel}\Bigg[\int_{\Omega^e}(\mu\nabla\mathbf{w}_v:\nabla\mathbf{v} - p\nabla\mathbf{w}_v:\mathbf{I})\,dV^e + \int_{\Gamma^e}\mathbf{w}_v\cdot\left(\frac{\mu}{l^+}\lambda^+ - \frac{\mu}{l^-}\lambda^- + +\bar{\mathbf{f}}\right)ds^e \\
+\int_{\Omega^e} w_p\nabla\cdot\mathbf{v}dV^e + \int_{\Gamma^e} w_p\lambda_p ds^e + \int_{\Gamma^e}\lambda_p([p]+\bar{\mathbf{f}^{\perp}})ds^e \\
+\int_{\Gamma^e} w^{\parallel}_{\bar{v}}\left(\frac{\mu}{l^+}(\lambda^+ + [v]^{\parallel+}) + \frac{\mu}{l^-}(\lambda^+ + [v]^{\parallel-}) + \bar{\mathbf{f}}^{\parallel}\right)ds^e \\
+\int_{\Gamma^e} w_{\lambda^+}\left((\mu\nabla\mathbf{v}\cdot\bar{\mathbf{n}})^{\parallel+} - \frac{\mu}{l^+}[v]^{\parallel+}\right)ds^e \\
+\int_{\Gamma^e} w_{\lambda^-}\left((\mu\nabla\mathbf{v}\cdot\bar{\mathbf{n}})^{\parallel-} - \frac{\mu}{l^-}[v]^{\parallel-}\right)ds^e\Bigg] = 0 \quad (2.58)
\end{aligned}$$

Next, we replace the different fields $\mathbf{v}, p, \bar{v}^{\parallel}, \lambda_p, \lambda^+$ and λ^- with their discretized form (2.22), (2.23) and (2.24). In order to minimize the length of the discretized governing equations, we first rewrite the interpolation equations as the product of a shape function matrix and the element

nodal values vector as follows. Equation (2.23) can be rewritten as

$$\begin{aligned}
\tilde{\mathbf{v}}^e(\mathbf{x},t) &= \mathbf{N}^9(\mathbf{x})\cdot\mathbf{v}^e(t) \\
\text{with}\quad \mathbf{N}^9(\mathbf{x}) &= \left[\begin{array}{cccccc} N_1^9 & 0 & & N_9^9 & 0 \\ 0 & N_1^9 & \cdots & 0 & N_9^9 \end{array}\right. \\
&\qquad \left.\begin{array}{cccc} (H-H_1)N_1^9a_1^1 & 0 & (H-H_9)N_9^9a_1^9 & 0 \\ 0 & (H-H_1)N_1^9a_2^1 & 0 & (H-H_9)N_9^9a_2^9 \end{array}\right] \\
\text{and}\quad \mathbf{v}^e(t) &= \left\{v_1^1\, v_2^1\, v_1^2\, v_2^2 \ldots v_1^9\, v_2^9, \hat{v}^1 \ldots \hat{v}^9\right\}^T,
\end{aligned}$$

while (2.22) takes the form:

$$\begin{aligned}
\tilde{p}^e(\mathbf{x},t) &= \mathbf{N}^4(\mathbf{x})\cdot\mathbf{p}^e(t) \\
\text{with}\quad \mathbf{N}^4(\mathbf{x}) &= \left[N_1^4 \ldots N_4^4 \;\; (H-H_1)N_1^4 \ldots (H-H_4)N_4^4\right] \\
\text{and}\quad \mathbf{p}^e(t) &= \left\{p^1 \ldots p^4 \;\; \hat{p}^1 \ldots \hat{p}^4\right\}^T,
\end{aligned}$$

and (2.24) reads:

$$\tilde{\bar{v}}^{\parallel e}(\mathbf{x},t) = \bar{\mathbf{N}}(\mathbf{x})\cdot\bar{\mathbf{v}}^{\parallel e}(t) \quad , \quad \tilde{\lambda}_p^e(\mathbf{x},t) = \bar{\mathbf{N}}(\mathbf{x})\cdot\boldsymbol{\lambda}_p^e(t) \quad \text{and} \quad \tilde{\lambda}^{\pm e}(\mathbf{x},t) = \bar{\mathbf{N}}(\mathbf{x})\cdot\boldsymbol{\lambda}^{\pm e}(t)$$

with $\bar{\mathbf{N}} = \left[\bar{N}_1\; \bar{N}_2\right]$

and $\bar{\mathbf{v}}^{\parallel e}(t) = \left\{\bar{v}^{\parallel 1}\; \bar{v}^{\parallel 2}\right\}^T \quad , \quad \boldsymbol{\lambda}_p^e(t) = \left\{\lambda_p^1\; \lambda_p^2\right\}^T \quad , \quad \boldsymbol{\lambda}^{\pm e}(t) = \left\{\lambda^{\pm 1}\; \lambda^{\pm 2}\right\}^T$

We further write the rate of deformation of the fluid $\mathbf{D}^e$ (in Voigt notation) and the velocity divergence $\nabla.\mathbf{v}^e$ in element e in the two-dimensional plane strain case as:

$$\{\mathbf{D}^e\} = \left[\begin{array}{c} D_{11}^e \\ D_{22}^e \\ 2D_{12}^e \end{array}\right] = \mathbf{B}\cdot\mathbf{v}^e \;\text{ and }\; \nabla\cdot\mathbf{v}^e = \check{\mathbf{B}}\cdot\mathbf{v}^e$$

where the $\mathbf{B}$ and $\check{\mathbf{B}}$ matrices relates the nodal velocities to the deformation rate and velocity divergence:

$$\mathbf{B} = [\mathbf{B}_1 \ \mathbf{B}_2 \ ... \ \mathbf{B}_{n_9+m_9}] \text{ with } \mathbf{B}_I = \begin{bmatrix} \frac{\partial N_I^9(\mathbf{x})}{\partial x_1} & 0 \\ 0 & \frac{\partial N_I^9(\mathbf{x})}{\partial x_2} \\ \frac{\partial N_I^9(\mathbf{x})}{\partial x_2} & \frac{\partial N_I^9(\mathbf{x})}{\partial x_1} \end{bmatrix}$$

and

$$\check{\mathbf{B}} = \left[\check{\mathbf{B}}_1 \ \check{\mathbf{B}}_2 \ ... \ \check{\mathbf{B}}_{n_9+m_9}\right] \text{ with } \check{\mathbf{B}}_I = \begin{bmatrix} \frac{\partial N_I^9(\mathbf{x})}{\partial x_1} & \frac{\partial N_I^9(\mathbf{x})}{\partial x_2} \end{bmatrix}$$

with these definition, one can rewrite the weak form in its discretized form as follows:

$$\begin{aligned} \sum_{e=1}^{nel}\{\mathbf{w}_v^e\}^T \Bigg[\int_{\Omega_e} \mathbf{B}^T \cdot \left(\mu \mathbf{B}\cdot\mathbf{v}^e - \mathbf{N}^4\cdot\mathbf{p}^e\right) dV^e + \int_{\Gamma_e} (\mathbf{N}^9)^T \cdot \mathbf{a}_1 \left(\frac{\mu}{l^+}\bar{\mathbf{N}}\cdot\boldsymbol{\lambda}^{e+} - \frac{\mu}{l^-}\bar{\mathbf{N}}\cdot\boldsymbol{\lambda}^{e-}\right) ds^e \\ + \int_{\Gamma_e} (\mathbf{N}^9)^T \cdot \bar{\mathbf{f}} ds^e \Bigg] \\ + \sum_{e=1}^{nel}\{w_p^e\}^T \left[\int_{\Omega_e} (\mathbf{N}^4)^T \cdot \check{\mathbf{B}} \cdot \mathbf{v}^e dV^e + \int_{\Gamma_e} (\mathbf{N}^4_{[]})^T \cdot \bar{\mathbf{N}} \cdot \boldsymbol{\lambda}_p^e ds^e \right] \\ + \sum_{e=1}^{nel}\{w_{\bar{v}\parallel}^e\}^T \Bigg[\int_{\Gamma_e} \bar{\mathbf{N}}^T \cdot \left(\frac{\mu}{l^+}\bar{\mathbf{N}}\cdot\left(\boldsymbol{\lambda}^{e+} + \bar{\mathbf{v}}^{\parallel e}\right) - \frac{\mu}{l^+}\mathbf{N}_+^9\cdot\mathbf{a}_1\cdot\mathbf{v}^e\right) ds^e \\ \int_{\Gamma_e} \bar{\mathbf{N}}^T \cdot \left(\frac{\mu}{l^-}\bar{\mathbf{N}}\cdot\left(-\boldsymbol{\lambda}^{e-} - \bar{\mathbf{v}}^{\parallel e}\right) + \frac{\mu}{l^-}\mathbf{N}_-^9\cdot\mathbf{a}_1\cdot\mathbf{v}^e\right) ds^e + \int_{\Gamma_e} \bar{\mathbf{N}}^T\cdot\bar{\mathbf{f}}^{\parallel} ds^e \Bigg] \\ + \sum_{e=1}^{nel}\{w_{\lambda_p}^e\}^T \left[\int_{\Gamma_e} \bar{\mathbf{N}}^T \cdot \mathbf{N}^4_{[]} \cdot \mathbf{p}^e ds^e + \int_{\Gamma_e} \bar{\mathbf{N}}^T \cdot \bar{\mathbf{f}}^{\perp} ds^e \right] \\ + \sum_{e=1}^{nel}\{w_{\lambda^+}^e\}^T \left[\int_{\Gamma_e} \bar{\mathbf{N}}^T \cdot \left(\mu \mathbf{a}_1^T\cdot\mathbf{P}^{\perp}\cdot\mathbf{B}_+\cdot\mathbf{v}^e - \frac{\mu}{l^+}\left(\bar{\mathbf{N}}\cdot\bar{\mathbf{v}}^{\parallel e} - \mathbf{N}_+^9\cdot\mathbf{a}_1\cdot\mathbf{v}^e\right)\right) ds^e \right] \\ + \sum_{e=1}^{nel}\{w_{\lambda^-}^e\}^T \left[\int_{\Gamma_e} \bar{\mathbf{N}}^T \cdot \left(\mu \mathbf{a}_1^T\cdot\mathbf{P}^{\perp}\cdot\mathbf{B}_-\cdot\mathbf{v}^e + \frac{\mu}{l^-}\left(\bar{\mathbf{N}}\cdot\bar{\mathbf{v}}^{\parallel e} - \mathbf{N}_-^9\cdot\mathbf{a}_1\cdot\mathbf{v}^e\right)\right) ds^e \right] = 0 \end{aligned} \tag{2.59}$$

where the subscript $+$ and $-$ on the $\mathbf{B}$ and $\mathbf{N}^9$ indicates whether the fluid velocity (and its derivative) is interpolated on the $+$ or $-$ side of Γ while $\mathbf{N}^4_{[]} = \left[0..0 \ N_1^4...N_4^4\right]$ is used to interpolate the pressure jump across the interface. The above equation can then conveniently

be written in the following format:

$$\begin{bmatrix} \mathbf{K}^t & \mathbf{I}_2^t \\ \mathbf{I}_1^t & \bar{\mathbf{K}}^t \end{bmatrix} \cdot \begin{bmatrix} \mathbf{d}(t) \\ \bar{\mathbf{d}}(t) \end{bmatrix} + \begin{bmatrix} \mathbf{F}^t \\ \bar{\mathbf{F}}^t \end{bmatrix} = 0$$

Where the matrices The various component of the element matrix $\mathbf{K}^e$ in are calculated as:

$$\begin{aligned}
\mathbf{K}^e_{vv} &= \int_{\Omega^e} \mu \mathbf{B}^T \cdot \mathbf{B}\, dV^e \\
\mathbf{K}^e_{vp} &= \int_{\Omega^e} -\mathbf{B}^T \cdot \mathbf{N}^4\, dV^e \\
\mathbf{K}^e_{v\lambda^+} &= \int_{\Gamma^e} \frac{\mu}{l^+} (\mathbf{N}^9_-)^T \cdot \mathbf{a}_1 \cdot \bar{\mathbf{N}}\, ds^e \\
\mathbf{K}^e_{v\lambda^-} &= \int_{\Gamma^e} -\frac{\mu}{l^-} (\mathbf{N}^9_-)^T \cdot \mathbf{a}_1 \cdot \bar{\mathbf{N}}\, ds^e \\
\mathbf{K}^e_{pv} &= \int_{\Omega^e} (\mathbf{N}^4)^T \cdot \check{\mathbf{B}} dV^e \\
\mathbf{K}^e_{p\lambda_p} &= \int_{\Gamma^e} (\mathbf{N}^4_{[]})^T \cdot \bar{\mathbf{N}} ds^e \\
\mathbf{K}_{\bar{v}\|v} &= \int_{\Gamma^e} \bar{\mathbf{N}}^T \cdot \mathbf{a}_1 \cdot \left(\frac{\mu}{l^-} \cdot \mathbf{N}^9_- - \frac{\mu}{l^+} \cdot \mathbf{N}^9_+ \right) ds^e \\
\mathbf{K}^e_{\bar{v}\|\bar{v}\|} &= \int_{\Gamma^e} \bar{\mathbf{N}}^T \cdot \left(\frac{\mu}{l^+} - \frac{\mu}{l^-} \right) \cdot \bar{\mathbf{N}} ds^e \\
\mathbf{K}^e_{\bar{v}\|\lambda^+} &= \int_{\Gamma^e} \frac{\mu}{l^+} \bar{\mathbf{N}}^T \cdot \bar{\mathbf{N}} ds^e \\
\mathbf{K}^e_{\bar{v}\|\lambda^-} &= \int_{\Gamma^e} -\frac{\mu}{l^-} \bar{\mathbf{N}}^T \cdot \bar{\mathbf{N}} ds^e \\
\mathbf{K}^e_{\lambda_p p} &= \int_{\Gamma^e} \bar{\mathbf{N}}^T \cdot \mathbf{N}^4_{[]} ds^e \\
\mathbf{K}^e_{\lambda^+ v} &= \int_{\Gamma^e} \bar{\mathbf{N}}^T \cdot \left(\mu \mathbf{a}_1^T \cdot \mathbf{P}^\perp \cdot \mathbf{B}_+ + \mathbf{N}^9_+ \cdot \mathbf{a}_1 \right) ds^e \\
\mathbf{K}^e_{\lambda^+ \bar{v}\|} &= \int_{\Gamma^e} -\frac{\mu}{l^+} \bar{\mathbf{N}}^T \cdot \bar{\mathbf{N}} ds^e \\
\mathbf{K}^e_{\lambda^- v} &= \int_{\Gamma^e} \bar{\mathbf{N}}^T \cdot \left(\mu \mathbf{a}_1^T \cdot \mathbf{P}^\perp \cdot \mathbf{B}_- - \mathbf{N}^9_- \cdot \mathbf{a}_1 \right) ds^e \\
\mathbf{K}^e_{\lambda^- \bar{v}\|} &= \int_{\Gamma^e} \frac{\mu}{l^-} \bar{\mathbf{N}}^T \cdot \bar{\mathbf{N}} ds^e
\end{aligned}$$

while the external forces associated with element e are written:

$$\begin{aligned}
\mathbf{F}_{v}^{e} &= \int_{\Omega^e} -(\mathbf{N}^9)^T \cdot \bar{\mathbf{f}} \; dV^e \\
\mathbf{F}_{\bar{v}^{\parallel}}^{e} &= \int_{\Gamma^e} \bar{\mathbf{N}}^T \cdot \bar{\mathbf{f}}^{\parallel} \; ds^e \\
\mathbf{F}_{\lambda_p}^{e} &= \int_{\Gamma^e} \bar{\mathbf{N}}^T \cdot \bar{\mathbf{f}}^{\perp} \; ds^e
\end{aligned}$$

where $\bar{\mathbf{f}}$ is computed using the updated strain and curvature.

Chapter 3

An X-FEM based numerical-asymptotic expansion for simulating a Stokes flow near a sharp corner

A large number of the flows considered in Fluid-structure interaction problems include their interactions with structures with sharp corners or tips. Examples of these problems include the flow inside a channel with sudden changes of radius [1, 11, 139, 60, 116], the flow through cracks and interfaces [165] or the filtration of particles through a porous membrane [178, 84, 80]. The presence of local curvature singularities where the fluid interacts with the structure results in the appearance of pressure or velocity singularities, as described by Moffat in [115]. These singularities at the small scale are often associated with flow separation or stagnation regions at the larger scale that are of great importance in many engineering applications, and to describe them accurately still remains a significant computational challenge.

Traditionally in this type of fluid/interaction problem, the geometry of sharp corner and the singular fields around them are resolved through the use of local refinement of the spatial dis-

cretization [1, 11, 139, 60, 116]. However, these types of algorithms are computationally costly and can never truly resolve the local field discontinuities. Indeed, the standard finite element method uses a linear or quadratic continuous space that ultimately fails to describe the hyperbolic pressure field that appears at the corner tips [115].

To address that issue, Hawa and Rusak [74] developed an asymptotic/numerical matching method to simulate a viscous flow through a suddenly expanding channel. In this work, the inner analytical solution around the corner is matched with the outer numerical solution computed with the finite difference method. They successfully simulated the singularities near the corner for various Reynolds number and channel expansion ratios. However, their numerical method still requires some level of mesh refinement around the corner and the spatial discretization of the corner is mesh dependent, which limits the method to the study of right angle corners.

Another numerical/asymptotic matching method is the extended finite element method, which was originally developed by Moës *et al* in the framework of the Extended Finite Element method (X-FEM) to compute the discontinuous displacement and singular stress field around cracks inside an elastic body [114]. The idea was to locally enrich the traditional $\mathcal{C}^0$ finite element space around the crack tips with the asymptotic solution for the displacement and stress fields. This enriched space allowed the finite element method to describe the singular fields around the crack tip without the need for refinement or remeshing [114, 73, 134, 28]. The method has also successfully been applied to the simulation of the Stokes flow around rigid particles, where the asymptotic solution for the pressure and velocity field around a cylinder are used to enrich the finite elements cut by the particle [169].

Recognizing the similarities between the pressure field of the flow around a corner and the stress field around a crack tip, we here follow the same approach as taken by Moës *et al* in [114] and present a collocation method in the framework of the X-FEM to simulate the Stokes flow around structures with sharp corners. We enrich the finite element space around corner tips with the first order symmetric and anti-symmetric modes of the asymptotic solution for a Stokes

flow near a sharp corner, following Moffatt's solution [115]. These special enrichment functions provide the finite element method with the flexibility needed to accurately describe the singular pressure and velocity field around sharp corners. The no-slip boundary condition on the walls of the corner is enforced via the use of Lagrange multipliers. The proposed approach has the following three contributions:

- The local field singularities near sharp corners are resolved without the need for computationally expensive mesh refinement.

- The enrichment functions are calculated for any convex sharp corners .

- The technique presented holds for any simultaneous combinations of sharp corners, and can handle the simulation of a Stokes flow with complex boundary condition without any refinement and on a fixed structured mesh.

We show that the formulation is well adapted for investigating problems where physics at the small scale have a large impact on the overall large scale behavior. The outline of the chapter is as follows: Section 2 presents the governing equations and the asymptotic solution for the Stokes flow near a sharp corner. Section 3 follows with the extended finite element discretization scheme and the derivation of the weak form. The special enrichment functions used in the numerical discrezation are derived from the asymptotic solution in section 4. We then verify in section 5 the accuracy of the method by calculating the error made when computing the flow velocity around corners of different angle, with and without special enrichment. The present method is also compared with the X-FEM without corner enrichment but with different levels mesh refinement for the problem of a Stokes flow through a suddenly expanding channel. Finally, the method is applied to the estimation of the permeability of a network of fibers, where it is shown that neglecting the pressure and velocity singularities around the fiber tips leads to a significant underestimation of the overall network permeability.

3.1 Governing equations

3.1.1 Basic equations

Consider a two-dimensional incompressible viscous flow in a domain Ω, in which exists one or multiple no-slip rigid boundaries Γ taking the shape of thin plates or sharp corners (Fig.4.1). The problem is characterized by the Reynolds number $\mathcal{R}_e = HU\rho/\mu$ where H is the characteristic length scale, U the characteristic fluid velocity, μ the kinematic viscosity and ρ the fluid density. We choose here to remain in the Stokes flow assumption with $\mathcal{R}_e \ll 1$, where inertial effect may be neglected. The velocity of a fluid particle is given in terms of its material time derivative $\mathbf{v}(\mathbf{x}) = D\mathbf{x}/Dt$, where $\mathbf{x} = \{x \;\; y\}$ is the current position of the fluid particle at time t. In these conditions, the governing equations with the associated boundary conditions for the Stokes flow at the steady state are written:

$$\left.\begin{array}{rcl} \mu\nabla^2\mathbf{v} - \nabla p &=& \rho\mathbf{f} \;\; \forall\mathbf{x}\in\Omega \\ \nabla\cdot\mathbf{v} &=& 0 \;\; \forall\mathbf{x}\in\Omega \\ \text{with} \;\; \mathbf{v}(\mathbf{x}) &=& 0 \;\; \forall\mathbf{x}\in\Gamma. \end{array}\right\} \tag{3.1}$$

where p is the fluid pressure and $\mathbf{f}$ a body force. These equations govern the fluid flow in the domain Ω and can generally be easily solved using the finite element method, as long as the geometry of the boundary Γ does not include any curvature singularities, such as a sharp corner. However, when such a sharp corner occur in the geometry of Γ, equations (3.1) admit a singular solution near the tip of the corner, which cannot be resolved with the classical finite element method. First, let us turn to the asymptotic solutions for the fluid velocity and pressure near the corner tip, as they will be needed when deriving the corresponding enrichment functions.

3.1.2 Asymptotic solution for the flow near a sharp corner

For simplicity, we adopt a polar coordinate system (r, θ) centred on the corner, where $r = \sqrt{x'^2 + y'^2}$, $\theta = \arctan(y'/x')$ and the axis x' and y' are aligned with the corner's bisector (see Fig.3.1). The corner is defined by the angle α made with its bisector, where $\alpha = \pi/2$ and $\alpha = \pi$ respectively correspond to a flat wall and a semi infinite plate.

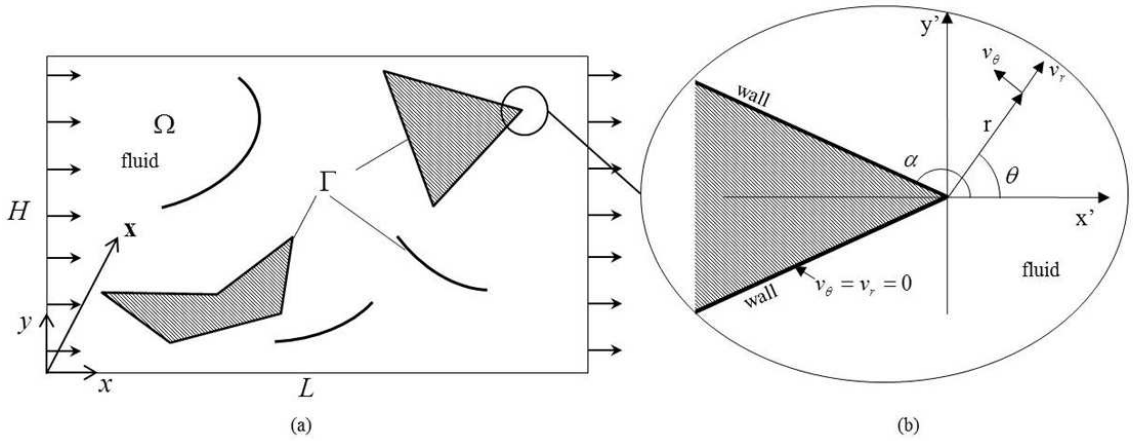

Figure 3.1: *(a) fluid domain* Ω *and fixed structure* Γ *with no-slip/no-penetration boundary condidtion. (b) local polar coordinate system centred at the corner.*

The asymptotic solution of the viscous flow near a sharp corner follows the paper of Moffat [115]. The streamline function $\psi(r,\theta)$ solution to the Stokes equation $\nabla\psi = 0$ in the region $0 < r \ll H$ can be written in the following separated form:

$$\psi(r,\theta) \;=\; r^{\gamma} f_{\gamma}(\theta) \tag{3.2}$$

where γ is an unknown complex exponent that determines the structure of the flow, and is to be found as part of the solution, as described in section 3.1.3. According to [115], the function $f_\gamma(\theta)$ takes the general form:

$$f_{\gamma}(\theta) \;=\; A\cos(\gamma\theta) + B\sin(\gamma\theta) + C\cos((\gamma-2)\theta) + D\sin((\gamma-2)\theta) \tag{3.3}$$

where A, B, C and D are arbitrary complex constants. In the cases where $\gamma = 0, 1$ or 2, the above equation degenerates into other forms that are not relevant to the problem studied here, and we will henceforth only consider values of γ such that $\gamma \neq 0, 1, 2$. The axial and radial velocities of the flow are deduced from the stream function $\psi(r,\theta)$ as follows:

$$v_r \;=\; \frac{1}{r}\frac{\partial\psi}{\partial\theta} \quad \text{and} \quad v_\theta \;=\; -\frac{\partial\psi}{\partial r}, \tag{3.4}$$

and are subjected to the following no-splip/no-penetration boundary conditions at the wall:

$$v_r(r, \theta = \alpha) \;=\; 0, \quad v_\theta(r, \theta = \alpha) \;=\; 0 \tag{3.5}$$

$$v_r(r, \theta = -\alpha) \;=\; 0, \quad v_\theta(r, \theta = -\alpha) \;=\; 0. \tag{3.6}$$

In general, any Stokes flow near a corner can be calculated as the linear superposition of an anti-symmetrical (mode I) and symmetrical (mode II) solution with respect to the corner's bisector x' (see Fig.3.2). We now briefly present these two cases.

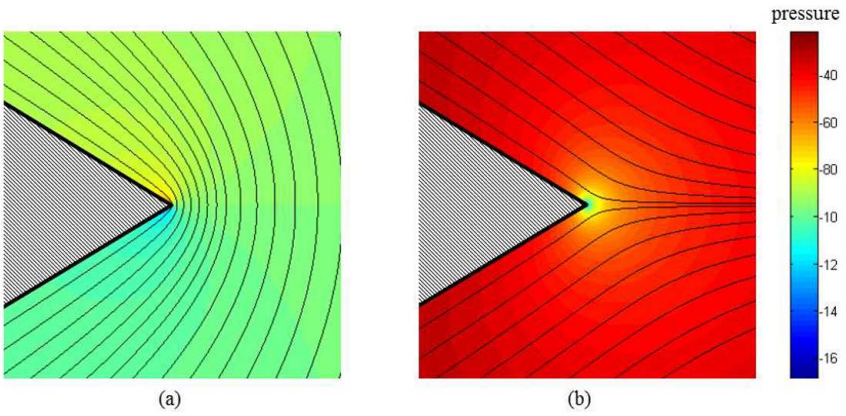

Figure 3.2: *Asymptotic solution: pressure and stream lines for a viscous flow near a sharp corner* $\alpha = 0.8\pi$ *for (a) mode I and (b) mode II. The pressure field is singular at* $r = 0$.

3.1.3 Mode I: anti-symmetrical case

In the anti-symmetrical case, which we will refer to as mode I, the flow is even so the constants B and D in (3.3) vanish, and $f_\gamma(\theta)$ reads:

$$f_\gamma(\theta) \quad = \quad A\cos(\gamma\theta) + C\cos((\gamma - 2)\theta). \tag{3.7}$$

Enforcing the boundary condition at the wall requires that $f_\gamma(\pm\alpha) = \partial f_\gamma(\pm\alpha)/\partial\theta = 0$, and yields a system of two equations for A and C:

$$\begin{cases} A\cos(\gamma\theta) + C\cos((\gamma - 2)\theta) & = & 0 \\ A\gamma\sin(\gamma\theta) + C(\gamma - 2)\sin((\gamma - 2)\theta) & = & 0 \end{cases}, \tag{3.8}$$

which admits non trivial solutions only if γ satisfies the following simple algebraic equation [115]:

$$\sin\left((\gamma-1)2\alpha\right) \quad = \quad (1-\gamma)\sin\left(2\alpha\right). \tag{3.9}$$

Combining (3.2), (3.7) and (3.8), one finds that the stream function in the anti-symmetrical case is written:

$$\psi(r,\theta) \quad = \quad r^{\gamma}\left(\cos\left(\gamma\theta\right)\cos\left((\gamma-2)\alpha\right)-\cos\left(\gamma\alpha\right)\cos\left((\gamma-2)\theta\right)\right). \tag{3.10}$$

The resulting stream lines and pressure field for $\alpha = 0.8\pi$ in mode I are shown in Fig.3.2a, where the pressure is calculated by solving the momentum equation

$$\nabla p \quad = \quad \mu\nabla^2\mathbf{v} \tag{3.11}$$

where $\mathbf{v} = v_r\mathbf{e}_r + v_\theta\mathbf{e}_\theta$ is computed using equations (3.2) and (3.4).

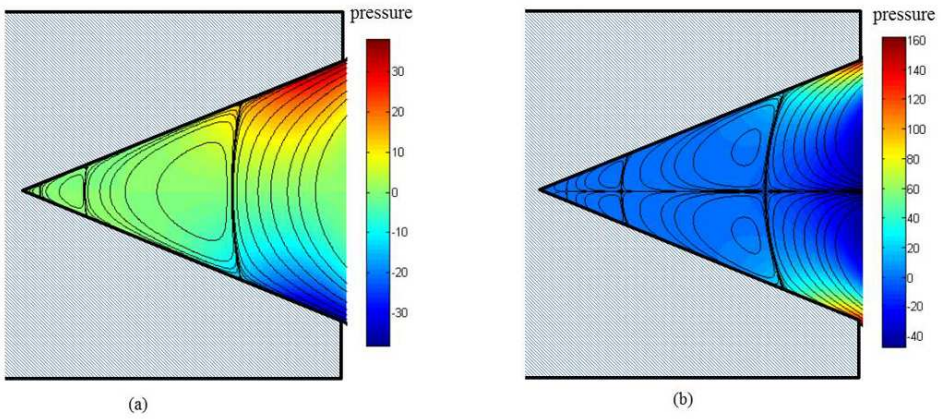

Figure 3.3: *Asymptotic solution: pressure and stream lines forming eddies for a viscous flow near a sharp corner $\alpha = 0.3\pi$ for (a) mode I and (b) mode II. The pressure and velocity fields vanish at $r = 0$ and show no singularity.*

When the angle α made by the two walls of the corner is less than a critical angle $\alpha < 0.405\pi$ (or $\alpha < 73°$), equation (3.9) admits complex solutions [115]. To calculate the stream function $\psi(r,\theta)$ in this case, we first decompose the exponent into its real and complex components

$\gamma = \gamma_R + i\gamma_I$ and rewrite (3.9) as the following system of equations [132]:

$$\begin{cases} \sin\left(2\alpha(\gamma_R - 1)\right)\cosh\left(2\alpha\gamma_I\right) &= (1-\gamma_R)\sin(2\alpha) \\ \cosh\left(2\alpha(\gamma_R - 1)\right)\sinh\left(2\alpha\gamma_I\right) &= (-\gamma_I)\sin(2\alpha) \end{cases} \tag{3.12}$$

which can be solved for γ_R and γ_I using a Newton-Raphson non-linear solver, given a good initial guess. Finally, using (4.10), (3.7) and (3.8), one can write the stream function $\psi(r,\theta)$ in the case $\alpha < 0.405\pi$ as [132, 115]:

$$\begin{aligned} \psi(r,\theta) &= r^{\gamma_R}\left[\text{Real}\left\{Q\right\}\cos\left(\gamma_I \ln r\right) - \text{Imag}\left\{Q\right\}\sin\left(\gamma_I \ln r\right)\right] \\ \text{with} \quad Q &= \left(\cos\left(\gamma\theta\right)\cos\left((\gamma-2)\alpha\right) - \cos\left(\gamma\alpha\right)\cos\left((\gamma-2)\theta\right)\right) \end{aligned} \tag{3.13}$$

The resulting stream lines and pressure field are shown in Fig.3.3.a, where one notes the appearance of an infinite number of self repeating eddies as r decreases to zero.

3.1.4 Mode II: symmetrical case

The derivation of the solution for the symmetrical flow, or mode II is extremely similar to mode I, and we will therefore omit some details. In this case, $f_\gamma(\theta)$ should be an odd function, and we therefore set A and C to be zero in (3.3):

$$f_\gamma(\theta) = B\sin\left(\gamma\theta\right) + D\sin\left((\gamma-2)\theta\right). \tag{3.14}$$

Enforcing the no-slip and no-penetration boundary conditions yields to following alebraic equation for γ:

$$\sin\left((\gamma-1)2\alpha\right) = (\gamma-1)\sin\left(2\alpha\right). \tag{3.15}$$

Combining (3.2), (3.14) and the boundary conditions one finds the stream function for mode 2 to read:

$$\psi(r,\theta) = r^\gamma\left(\sin\left(\gamma\theta\right)\sin\left((\gamma-2)\alpha\right) - \sin\left(\gamma\alpha\right)\sin\left((\gamma-2)\theta\right)\right). \tag{3.16}$$

Similarly to mode 1, for $\alpha < 0.405\pi$, equation (3.15) admits complex solutions. Taking the same approach as for mode 1, a decomposition of the exponent γ into its real and imaginary components leads to the following form of the stream function:

$$\begin{aligned} \psi(r,\theta) &= r^{\gamma_R}\left[\text{Real}\left\{Q\right\}\cos\left(\gamma_I \ln r\right) - \text{Imag}\left\{Q\right\}\sin\left(\gamma_I \ln r\right)\right] \\ \text{with} \quad Q &= \left(\sin\left(\gamma\theta\right)\sin\left((\gamma-2)\alpha\right) - \sin\left(\gamma\alpha\right)\sin\left((\gamma-2)\theta\right)\right). \end{aligned} \tag{3.17}$$

The resulting stream lines and pressure field are shown in Fig.3.3.b where similarly to mode I, one notes the apparition of an infinite number of self repeating eddies as r decreases to zero. Let us now turn to the numerical formulation and use the asymptotic solution presented above to derive the corresponding enrichment functions.

3.2 Extended finite element formulation

The idea of the Extended Finite Element Method is to enrich a finite element space with additional functions. Our numerical technique takes the same approach: the Stokes flow is solved using the traditional $\mathcal{C}_0$ conforming finite elements (in our cases 4 nodes bilinear elements for the pressure and 9 nodes quadratic elements for the velocity) space, and we enrich this space with additional degrees of freedom that allow the pressure jump across an interface (the velocity stays continuous) and singular pressure/velocity fields around the corner tip. The velocity and pressure fields in this enriched space are interpolated as follows:

$$p(\mathbf{x}) = \sum_i N_i(\mathbf{x})p_i + \sum_j N_j(\mathbf{x})(H(\mathbf{x}) - H_j)\check{p}_j + \sum_k \sum_l N_k(G^l\left(r(\mathbf{x}),\theta(\mathbf{x})\right) - G_k)\tilde{p}_k \tag{3.18}$$

$$\mathbf{v}(\mathbf{x}) = \sum_i \hat{N}_i(\mathbf{x})\mathbf{v}_i + \sum_k \sum_l \hat{N}_k(F^l\left(r(\mathbf{x}),\theta(\mathbf{x})\right) - F_k)\tilde{\mathbf{v}}_k \tag{3.19}$$

where N and $\hat{N}$ are the regular 4 nodes and 9 nodes shape functions, H is the Heaviside function that provides the needed discontinuity, and $\mathbf{F} = \{\mathbf{F}_I, \mathbf{F}_{II}\}$ and $\mathbf{G} = \{\mathbf{G}_I, \mathbf{G}_{II}\}$ are the special asymptotic corner tip functions for modes I and II. They are derived in section 3.3 from the asymptotic solution presented in section 3.1.2 . The term $\check{p}_j$ corresponds to the enriched degrees

of freedom associated with the jump in pressure across an interface while the terms $\tilde{p}_k$ and $\tilde{\mathbf{v}}_k$ are the enrichment degrees of freedom associated with the near corner tip pressure and velocity fields.

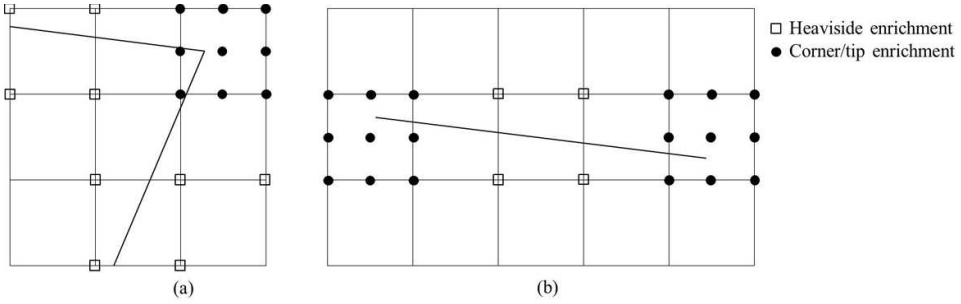

Figure 3.4: *Node selection for the slip and tip enrichment of a (a) corner and (b) plate. The black dots denote tip enrichment for the velocity and pressure (only the four corner nodes in the case of the pressure) while the squares indicate split enrichment for the pressure.*

Fig.3.4a and b illustrate the enrichment strategy used to model the flow around sharp corners and tips. The full circles denote the node enriched with corner/tip functions and belong to the element that contains the corner/tip. The empty squares represent the nodes enriched with a Heaviside function and belong the elements fully cuts by the corner walls.

In addition to the velocity and pressure degrees of freedom and their respective enrichment, let us introduce the Lagrange multipliers $\boldsymbol{\lambda^I}$. These are used to enforce the no-slip/no-penetration boundary condition (3.1) on the corner walls and tip and are discretized at the intersection between the corner walls and the underlying mesh, as shown in Fig.3.5. They are

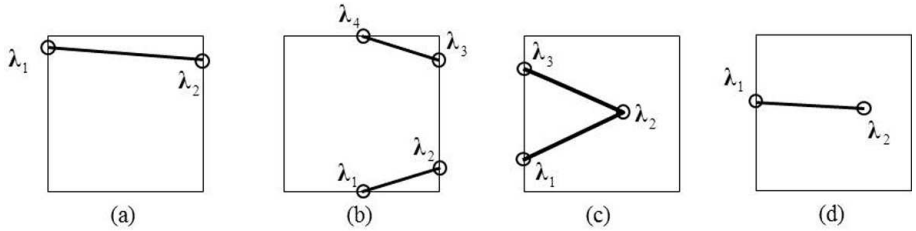

Figure 3.5: *Discretization of the Lagrange multipliers in (a) simple cut element, (b) double cut element, (c) corner tip element and (d) tip element.)*

interpolated along the interface Γ using one-dimensional shape functions $\lambda_i(\mathbf{x}) = \sum_{I=1}^{2} \bar{N}^I(\mathbf{x})\lambda_i^I$ where I denotes the numbering of the nodes for each segment of the corner walls, and i runs over the dimensions 1 and 2 (in 2D).

3.2.1 Weak formulation

Introducing the test functions $\mathbf{w_v}$ and w_p, integrating by parts and using the divergence theorem, the weak form of the governing equations (3.1) in the fluid domain can be written as:

$$\begin{aligned} (\nabla \mathbf{w_v}, \mu \nabla \mathbf{v})_\Omega - (\nabla \mathbf{w_v}, p\mathbf{I})_\Omega + (\mathbf{w_v}, \rho \mathbf{f})_\Omega &= 0 \\ (w_p, \nabla \cdot \mathbf{v})_\Omega &= 0 \end{aligned} \tag{3.20}$$

where the notation $(\cdot, \cdot)_\Omega$ indicates the L^2 inner product with respect to the domain Ω. We also need to enforce the no-slip/no-penetration boundary conditions given in (3.1) on the corner walls. This is done by using the Lagrange multipliers $\boldsymbol{\lambda}$. The corresponding variational form is then given by: find $\mathbf{v} \in \mathcal{V}$, $p \in \mathcal{P}$ and $\boldsymbol{\lambda} \in \mathcal{L}$ such that for all $\mathbf{w_v} \in \mathcal{V}$, $w_p \in \mathcal{P}$ and $\mathbf{w_\lambda} \in \mathcal{L}$

$$\begin{aligned} (\nabla \mathbf{w_v}, \mu \nabla \mathbf{v})_\Omega - (\nabla \mathbf{w_v}, p\mathbf{I})_\Omega + (\mathbf{w_v}, \rho \mathbf{f})_\Omega + (\mathbf{w_v}, \boldsymbol{\lambda})_\Gamma &= 0 \\ (w_p, \nabla \cdot \mathbf{v})_\Omega &= 0 \\ (\mathbf{w_\lambda}, \mathbf{v})_\Gamma &= 0 \end{aligned} \tag{3.21}$$

where $\mathbf{w}_\lambda$ are the test functions associated with the Lagrange multipliers and $\mathcal{V}$, $\mathcal{P}$ and $\mathcal{L}$ are admissible spaces for the velocity, pressure and Lagrange multipliers.

3.2.2 Discretized form

The discretized form of the equilibrium can be written from the weak form (3.21) by using the XFEM approximation as follows:

$$\mathbf{Kd} = \mathbf{f} \tag{3.22}$$

where $\mathbf{K}$ is the consistent tangent matrix, $\mathbf{d} = \{\mathbf{v} \;\; p \;\; \boldsymbol{\lambda}\}$ the global vector of unknowns and $\mathbf{f}$ the force vector. The element contribution to $\mathbf{K}$ and $\mathbf{f}$ are as follows:

$$\mathbf{k}^e = \begin{bmatrix} \mathbf{k}^e_{\mathbf{vv}} & \mathbf{k}^e_{\mathbf{v}p} & \mathbf{k}^e_{\mathbf{v}\boldsymbol{\lambda}} \\ \mathbf{k}^e_{p\mathbf{v}} & 0 & 0 \\ \mathbf{k}^e_{\boldsymbol{\lambda}\mathbf{v}} & 0 & 0 \end{bmatrix} \tag{3.23}$$

$$\mathbf{f}^e = \begin{Bmatrix} \mathbf{f}^e_{\mathbf{v}} & 0 & 0 \end{Bmatrix}^T \tag{3.24}$$

with

$$\mathbf{k}_{\mathbf{vv}} = \int_{\Omega^e} \mu \mathbf{B}^T \cdot \mathbf{B} \; d\Omega \tag{3.25a}$$

$$\mathbf{k}^e_{\mathbf{v}p} = \int_{\Omega^e} -\mathbf{B}^T \cdot \hat{\mathbf{N}} \; d\Omega \tag{3.25b}$$

$$\mathbf{k}^e_{\mathbf{v}\lambda} = \int_{\Gamma^e} \mathbf{N}^T \cdot \bar{\mathbf{N}} d\Gamma \tag{3.25c}$$

$$\mathbf{k}^e_{p\mathbf{v}} = \int_{\Omega^e} \hat{\mathbf{N}}^T \cdot \mathbf{B} \; d\Omega \tag{3.25d}$$

$$\mathbf{k}^e_{\lambda\mathbf{v}} = \int_{\Gamma^e} \bar{\mathbf{N}}^T \cdot \mathbf{N} d\Gamma \tag{3.25e}$$

and

$$\mathbf{f}^e_{\mathbf{v}} = \int_{\Omega^e} \mathbf{N}^T \cdot \rho \mathbf{f} \; d\Omega. \tag{3.26}$$

The shape function matrices $\mathbf{N}$, $\hat{\mathbf{N}}$, $\bar{\mathbf{N}}$ and $\mathbf{B}$ take the following form:

$$\mathbf{N} = \left[\mathbf{N}^1, ..., \mathbf{N}^9, \tilde{\mathbf{N}}^1, ..., \tilde{\mathbf{N}}^9\right] \tag{3.27a}$$

$$\hat{\mathbf{N}} = \left[\hat{N}^1, ..., \hat{N}^4, \check{\hat{N}}^1, ..., \check{\hat{N}}^4, \tilde{\hat{N}}^1, ..., \tilde{\hat{N}}^4\right] \tag{3.27b}$$

$$\bar{\mathbf{N}} = \left[\bar{N}^1 \;\; \bar{N}^2\right] \tag{3.27c}$$

$$\mathbf{B} = \left[\mathbf{B}^1, ..., \mathbf{B}^9, \tilde{\mathbf{B}}^1, ..., \tilde{\mathbf{B}}^9\right] \tag{3.27d}$$

with

$$\mathbf{N}^i = \begin{bmatrix} N^i & 0 \\ 0 & N^i \end{bmatrix} \quad , \quad \tilde{\mathbf{N}}^i = \left[(F - F^1) \begin{bmatrix} N^i & 0 \\ 0 & N^i \end{bmatrix}, ..., (F - F^8) \begin{bmatrix} N^i & 0 \\ 0 & N^i \end{bmatrix} \right] \tag{3.28a}$$

$$\check{N}^i = (H - H^i)\hat{N}^i \quad , \quad \tilde{\hat{N}}^i = \left[(G - G^1)\hat{N}^i, ..., (G - G^4)\hat{N}^i \right] \tag{3.28b}$$

$$\mathbf{B}^i = \begin{bmatrix} N^i_{,1} & 0 \\ 0 & N^i_{,2} \\ N^i_{,2} & 0 \\ 0 & N^i_{,1} \end{bmatrix} \tag{3.28c}$$

$$\tilde{\mathbf{B}}^i = \left[\begin{bmatrix} (F - F^1)N^i)_{,1} & 0 \\ 0 & (F - F^1)N^i)_{,2} \\ (F - F^1)N^i)_{,2} & 0 \\ 0 & (F - F^1)N^i)_{,1} \end{bmatrix}, ..., \begin{bmatrix} (F - F^8)N^i)_{,1} & 0 \\ 0 & (F - F^8)N^i)_{,2} \\ (F - F^8)N^i)_{,2} & 0 \\ 0 & (F - F^8)N^i)_{,1} \end{bmatrix} \right]. \tag{3.28d}$$

where F^i and G^i are the asymptotic functions used to enriched the standard finite element space around the corner tips. They are derived in the next section.

Remark: *The computation of these quantities involves the assessment of integrals over elements that can be numerically evaluated using Gaussian quadrature with four integration points in regular elements. However, for the elements cut by the corners, the integration is performed by splitting the element into sub-triangles using a Delaunay triangulation on the four corner points, the point at the corner tip, and the two intersection points between the corner walls and the element edges. A fourth order Gauss integration is then carried out in each triangle, as described in [114].*

3.3 Enrichment functions

Here we aim at identifying the asymptotic corner tip functions **F** and **G** that can span all the solutions for the velocity and pressure fields of a flow near a sharp corner. Similar to the asymptotic solutions presented in section 3.1.2, we proceed by considering mode I and mode II separately.

3.3.1 Mode I: asymptotic enrichment for the anti-symmetrical case

Recalling equation (3.10) for the stream function in mode I, one can use (3.4) to compute the axial and radial velocities as follows:

$$v_r(r,\theta) = \frac{1}{r}\frac{\partial \psi}{\partial \theta} = r^{\gamma-1}((\gamma-2)\cos(\gamma\alpha)\sin(\theta(\gamma-2)) - \gamma\cos(\alpha(\gamma-2))\sin(\theta\gamma)) \quad (3.29)$$

$$v_\theta(r,\theta) = -\frac{\partial \psi}{\partial r} = \gamma\left(-r^{\gamma-1}\right)(\cos(\alpha(\gamma-2))\cos(\theta\gamma) - \cos(\gamma\alpha)\cos(\theta(\gamma-2))). \quad (3.30)$$

Next, we write the flow velocity in the local Cartesian coordinate system $\{x', y'\}$:

$$\begin{aligned} v_{x'} = v_r\cos\theta - v_\theta\sin\theta &= \gamma\sin(\theta)r^{\gamma-1}(\cos(\alpha(\gamma-2))\cos(\theta\gamma) - \cos(\gamma\alpha)\cos(\theta(\gamma-2))) \\ &+ \cos(\theta)r^{\gamma-1}((\gamma-2)\cos(\gamma\alpha)\sin(\theta(\gamma-2)) - \gamma\cos(\alpha(\gamma-2))\sin(\theta\gamma)) \quad (3.31) \\ v_{y'} = v_r\sin\theta + v_\theta\cos\theta &= \sin(\theta)r^{\gamma-1}((\gamma-2)\cos(\gamma\alpha)\sin(\theta(\gamma-2)) - \gamma\cos(\alpha(\gamma-2))\sin(\theta\gamma)) \\ &- \gamma\cos(\theta)r^{\gamma-1}(\cos(\alpha(\gamma-2))\cos(\theta\gamma) - \cos(\gamma\alpha)\cos(\theta(\gamma-2))) \quad (3.32) \end{aligned}$$

Finally, we write the functions F_I as the basis of functions that can span all the solutions $v_{x'}$ and $v_{y'}$ in mode I. After some calculation, and making use of trigonometry identities, the basis of function $\mathbf{F}_I$ for mode I is found to be:

$$\begin{aligned} \mathbf{F}_I = \big\{ & r^{\gamma-1}\sin((\gamma-2)\theta)\sin\theta, r^{\gamma-1}\cos((\gamma-2)\theta)\cos\theta, \\ & r^{\gamma-1}\sin((\gamma-2)\theta)\cos\theta, r^{\gamma-1}\cos((\gamma-2)\theta)\sin\theta\big\} \end{aligned} \quad (3.33)$$

where γ is found using a non-linear solver on (3.9), given α and a good initial guess. The basis functions $\mathbf{G_I}$ for the pressure are derived in a similar manner. Given the stream function (3.10)

and the momentum equation (3.11), the pressure field around the corner tip for mode I is found to be:

$$\begin{aligned} p(r,\theta) &= -\frac{1}{(\gamma-2)\mathrm{Re}} r^{\gamma-2}\left(\gamma^2((\gamma-2)\cos(\gamma\alpha)\sin(\theta(\gamma-2)) - \gamma\sin(\gamma\theta)\cos(\alpha(\gamma-2))\right. \\ &+ \left.\gamma^3\sin(\gamma\theta)\cos(\alpha(\gamma-2)) + (\gamma-2)^3(-\cos(\gamma\alpha))\sin(\theta(\gamma-2))\right) + p_\infty \end{aligned} \tag{3.34}$$

where p_∞ is the pressure away from the corner tip when $r \to \infty$. An important feature of equation (3.34) is the fact that for $\alpha < \pi/2$, the pressure shows no singular behavior at $r = 0$. Indeed, for $\alpha < 0.405\pi$, equation (3.9) yields $\gamma > 2$, and the term $r^{\gamma-2}$ in (3.34) becomes zero at $r = 0$. In that case, the corner always become a stagnation point where the pressure and velocity are identically zero. In this work, we choose to focus on the cases where the pressure shows a singular behavior and therefore only use enrichment functions for $\alpha > 0.405\pi$. The basis functions for the pressure in mode I are therefore written:

$$\mathbf{G}_I = \left\{r^{\gamma-2}\sin(\gamma\theta), r^{\gamma-2}\sin((\gamma-2)\theta)\right\} \tag{3.35}$$

Remark: *Alternatively to solving* (3.9) *a priori, the parameter* γ *in the enrichment functions above can also be found via an adaptive method for parametric X-FEM [170]. This method considers the residual error based on the strong form to drive the algorithm and determine the parameter of the enrichment function.* .

3.3.2 Mode II: asymptotic enrichment for the symmetrical case

Finding the corner tip asymptotic function for mode II is very similar to mode I. The basis of functions $\mathbf{F}_{II}$ that can span all the solutions $v_{x'}$ and $v_{y'}$ in mode II is found to be same as for mode I, only the value of the exponent γ changes:

$$\begin{aligned} \mathbf{F}_{II} = \big\{&r^{\gamma-1}\sin((\gamma-2)\theta)\sin\theta, r^{\gamma-1}\cos((\gamma-2)\theta)\cos\theta, \\ &r^{\gamma-1}\sin((\gamma-2)\theta)\cos\theta, r^{\gamma-1}\cos((\gamma-2)\theta)\sin\theta\big\} \end{aligned} \tag{3.36}$$

Next, the pressure field around the corner tip for mode II is found to be:

$$\begin{aligned} p(r,\theta) &= -\frac{1}{(\gamma-2)\mathrm{Re}} r^{\gamma-2}\left(\gamma^2((\gamma-2)\sin(\gamma\alpha)\cos(\theta(\gamma-2)) - \gamma\cos(\gamma\theta)\sin(\alpha(\gamma-2))\right. \\ &+ \left.\gamma^3\cos(\gamma\theta)\sin(\alpha(\gamma-2)) + (\gamma-2)^3(-\sin(\gamma\alpha))\cos(\theta(\gamma-2))\right) + p_\infty \end{aligned} \tag{3.37}$$

The basis functions for the pressure in mode II is therefore written:

$$\mathbf{G}_{II} = \left\{r^{\gamma-2}\cos(\gamma\theta), r^{\gamma-2}\cos((\gamma-2)\theta)\right\} \tag{3.38}$$

Table 1 shows a summary of the asymptotic functions used as enrichment for both pressure and velocity fields for both modes, which constitutes the main result of the present work.

Mode I	$\mathbf{G}_I$	$\left\{r^{\gamma-2}\sin(\gamma\theta), r^{\gamma-2}\sin((\gamma-2)\theta)\right\}$
	$\mathbf{F}_I$	$\left\{r^{\gamma-1}\sin((\gamma-2)\theta)\sin\theta, r^{\gamma-1}\cos((\gamma-2)\theta)\cos\theta,\right.$ $\left. r^{\gamma-1}\sin((\gamma-2)\theta)\cos\theta, r^{\gamma-1}\cos((\gamma-2)\theta)\sin\theta\right\}$
Mode II	$\mathbf{G}_{II}$	$\left\{r^{\gamma-2}\cos(\gamma\theta), r^{\gamma-2}\cos((\gamma-2)\theta)\right\}$
	$\mathbf{F}_{II}$	$\left\{r^{\gamma-1}\sin((\gamma-2)\theta)\sin\theta, r^{\gamma-1}\cos((\gamma-2)\theta)\cos\theta,\right.$ $\left. r^{\gamma-1}\sin((\gamma-2)\theta)\cos\theta, r^{\gamma-1}\cos((\gamma-2)\theta)\sin\theta\right\}$

Table 3.1: *Corner tip asymptotic functions*

3.4 Results

In this section, the numerical scheme presented above is used to solve for fluid flows with different boundary conditions and the results are compared with both the analytical solution and the X-FEM without special enrichment. It is then applied to estimate the permeability of a two-dimensional fibrous network.

3.4.1 Flow around a corner

Here we investigate the accuracy of the numerical technique by comparing it with the analytical solution developed by Moffat [115]. The velocity given by the analytical solution is imposed at the boundary of the computational domain while a no-slip/no-penetration condition is enforced along the wall of the corner (Fig. 3.7). The Reynolds number is given by [115]:

$$\mathcal{R}_e = \frac{U r^{\text{Real}[\gamma]}}{\nu} \tag{3.39}$$

with ν the kinematic viscosity and U the fluid velocity away from the corner. The inertial

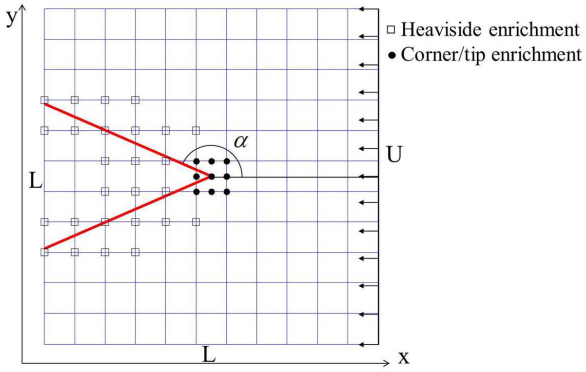

Figure 3.6: *Flow around a corner of angle α.The velocity given by the analytical solution is imposed at the boundary of the computational domain while a no-slip/no-penetration condition is enforced along the wall of the corner (shown in red).*

effect can therefore be neglected sufficiently close to the corner since for the cases investigated here, Real$[\gamma] > 0$. The parameters U and ν are chosen such that $\mathcal{R}_e \ll 1$ everywhere in the computational domain. The error made in computing the velocity of the flow near a corner is calculated as follows:

$$E_v = \int_0^{L/2} \int_{-\pi}^{\pi} \frac{||\mathbf{v}_{num}(r,\theta) - \mathbf{v}_{asymp}(r,\theta)||}{||\mathbf{v}_{asymp}(r,\theta)||} dr d\theta, \tag{3.40}$$

where $\mathbf{v}_{num}$ denotes the velocity calculated using the numerical method, $\mathbf{v}_{asymp}$ the asymptotic solution and L the length of the computational domain.

Fig.3.6 shows the error for different corner angle α, with or without special enrichment. We

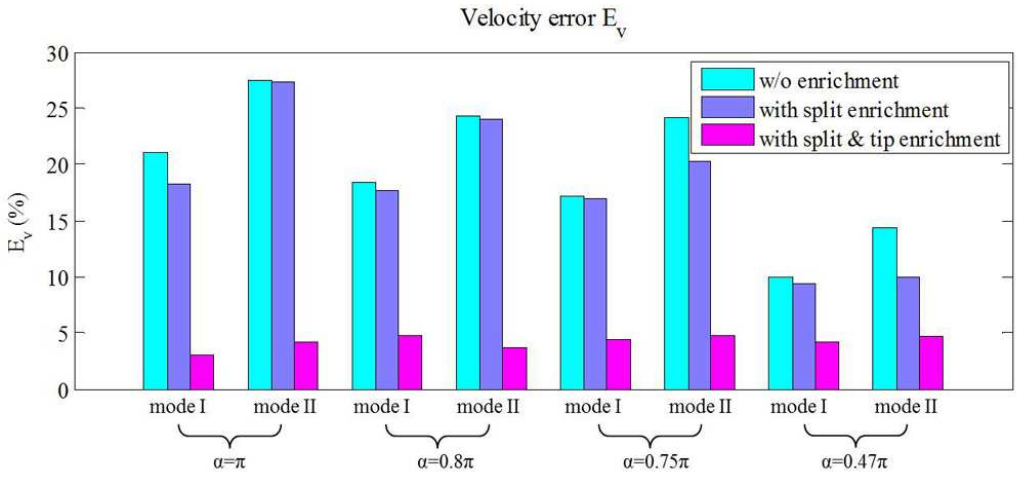

Figure 3.7: *Error E_v made in computing the flow velocity around the corner tip in mode I and II, for different corner angle α. The error can be divided by up to a factor of 8 by using corner tip enrichment.*

observe that without enrichment, the error varies between 10% up to 27%, and decreases as the corner angle increases. However, the incorporation of the corner tip enrichment developed above reduces the error for all corner angles, by up to a factor of 8 and always stays under 5%. Fig.3.8 shows the streamlines for the flow around the different corners. One notes that without corner tip enrichment, the streamlines intersect the corner wall, which denotes a poor enforcement of the no-penetration boundary condition. The effect of incorporating the corner tip enrichment can also be clearly seen on the pressure field inside elements containing the corner tip, in Fig.3.9: with enrichment (Fig.3.9e-h), the pressure field is singular around the corner tip and matches the behavior shown in the asymptotic solution (Fig.3.2) , whereas without corner enrichment (Fig.3.9a-d), the pressure field only varies linearly inside the element and does not show any pressure concentration around the corner tip.

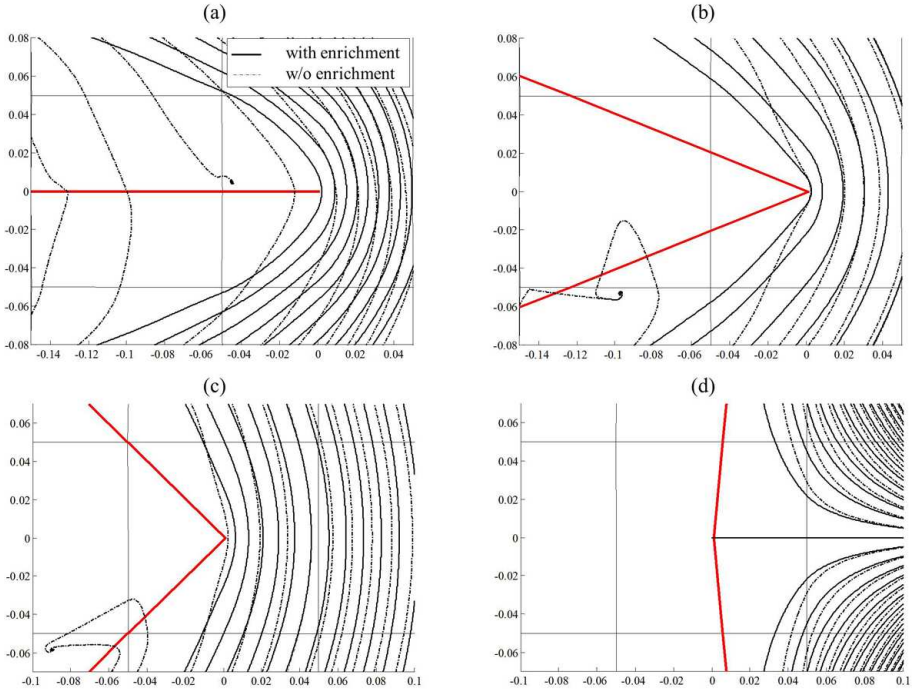

Figure 3.8: *Streamlines with and without enrichment for (a)* $\alpha = \pi$*, (b)* $\alpha = 0.87\pi$*,(c)* $\alpha = 0.75\pi$ *and (c)* $\alpha = 0.47\pi$*.*

3.4.2 Channel with a sudden expansion

In this section the proposed numerical method is applied to a simulation of a viscous flow through a symmetric two dimensional long channel of height h which suddenly expands into a long channel of height H. The flow through the channel is described in a Cartesian coordinate $\{x, y\}$ system where x runs along the length of the channel and y along the height of the channel . The sudden expansion forms a sharp right angle located at $x = 0$, and the centerline of the channel corresponds to $y = 0$ (Fig.3.10). A steady Poiseuille flow is imposed at the channel inlet section located at $x = x_0$:

$$v_x = \frac{U_{ave}}{3h^2/16}((h/2)^2 - y^2) \tag{3.41}$$

$$v_y = 0 \tag{3.42}$$

where U_{ave} is the average flow velocity at the channel entry. The outlet section $x = x_1$ is located far enough from the corner to have a steady Poiseuille flow profile. The Reynolds number is

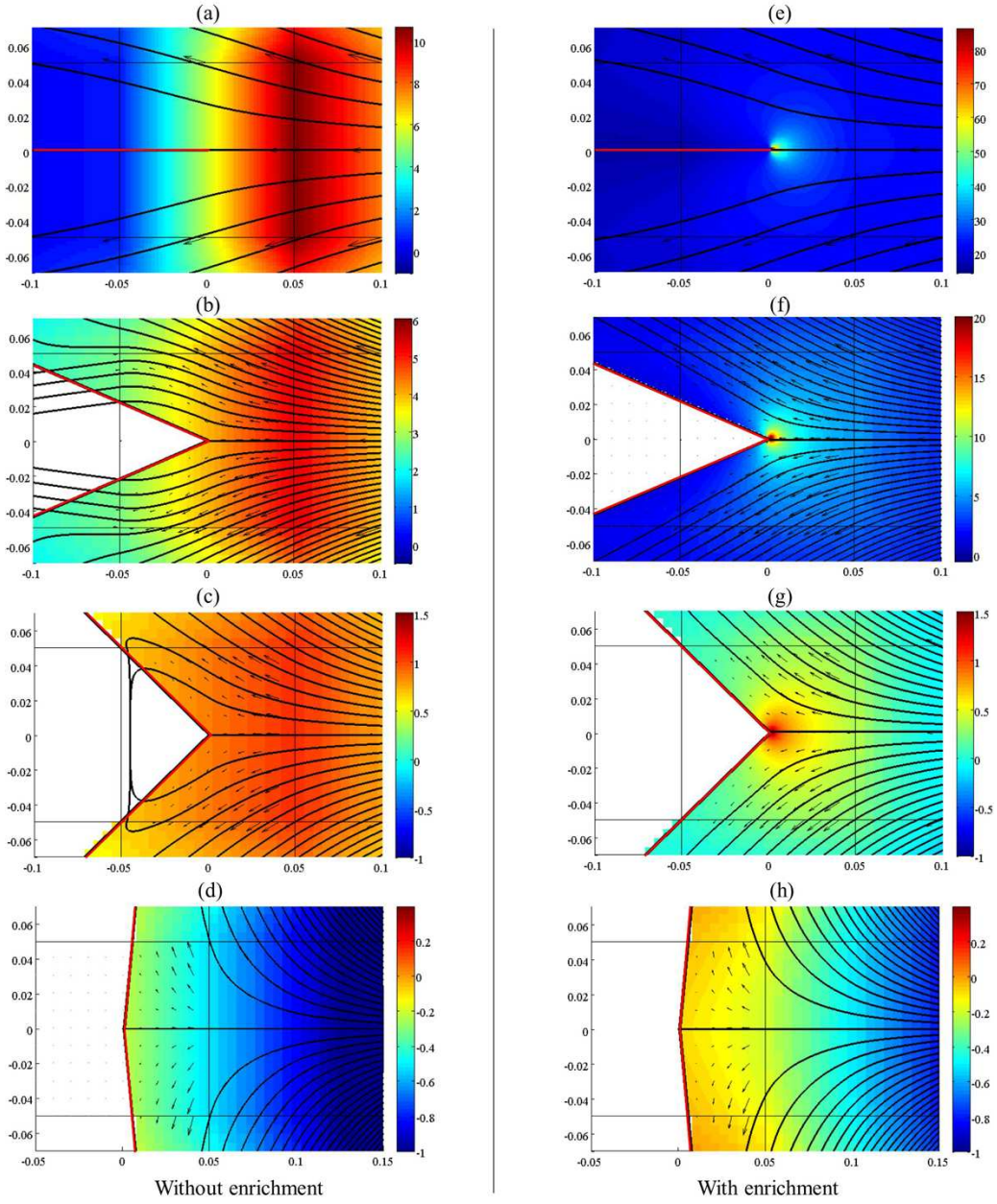

Figure 3.9: *Streamlines and pressure fields for* $\alpha = \pi$, $\alpha = 0.87\pi$, $\alpha = 0.75\pi$ *and* $\alpha = 0.47\pi$. *Left column (a)-(d), without enrichment and right column (e)-(h) with enrichment.*

given by $\mathcal{R}_e = U_{ave}h/\nu$ and $\mathcal{R}_e$ is chosen such that $\mathcal{R}_e \ll 1$ in order to stay within the Stokes flow assumptions.

The results for the flow in an expanding channel were obtained from the X-FEM without corner tip enrichment but with several levels of mesh refinement, and compared to the results

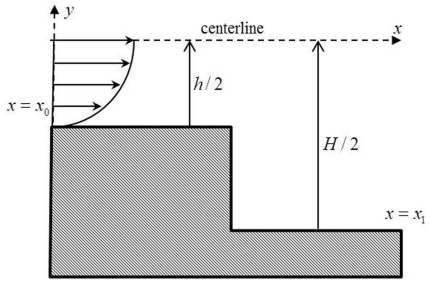

Figure 3.10: *Two-dimensional channel with sudden symmetrical expansion. The expansion is characterized by the ratio h/H)*

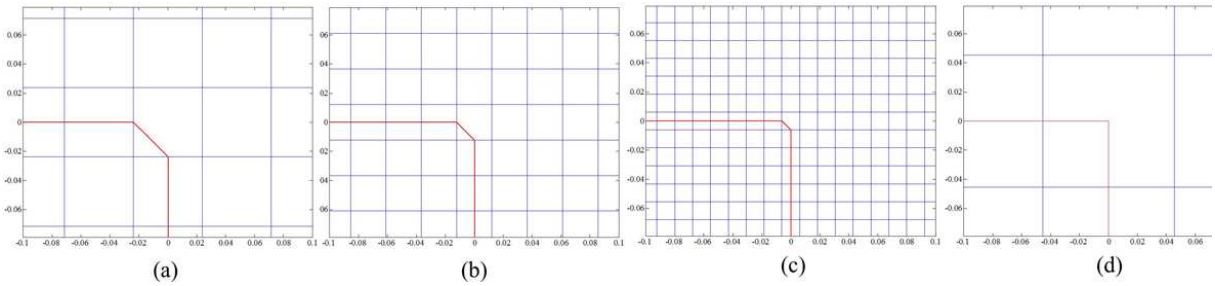

Figure 3.11: *Corner discretization for the two-dimensional channel with sudden symmetrical expansion. (a) 2 level refinement, (b) 3 level refinement, (c) 4 level refinement. (d) shows the 1 level refinement discretization of the corner when using the enrichment functions.*

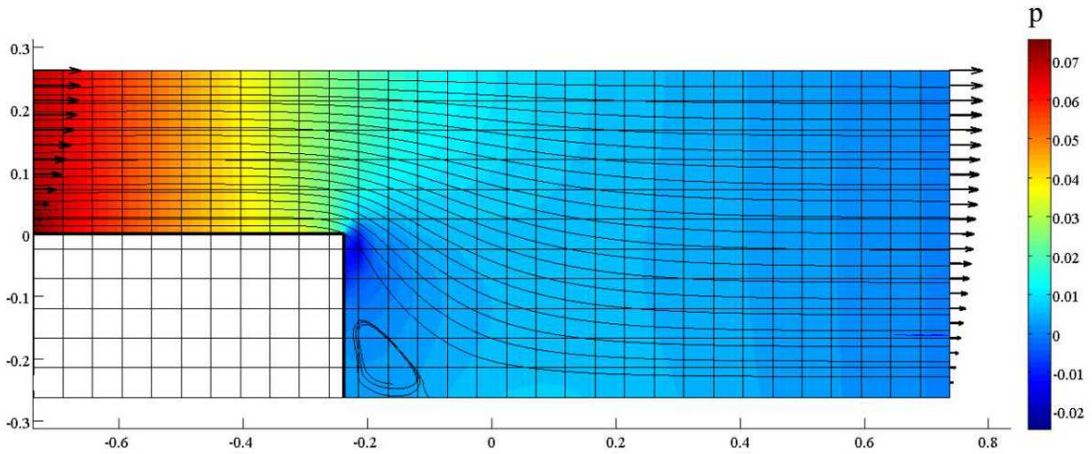

Figure 3.12: *Pressure field and velocity streamlines for the two-dimensional channel with sudden symmetrical expansion. The expansion is characterized by the ratio $h/H = 0.5$.*

from the X-FEM with corner tip enrichment. The different mesh sizes and the corresponding corner discretization are shown in Fig.3.11. One can see that as mesh size decreases for the X-FEM without tip enrichment, the resolution of the corner geometry improves but can never

be fully resolved as being infinitely sharp (Fig.3.11.a-c), whereas the use of tip enrichment allows a perfect geometrical discretization while using a larger mesh size (Fig.3.11.d).

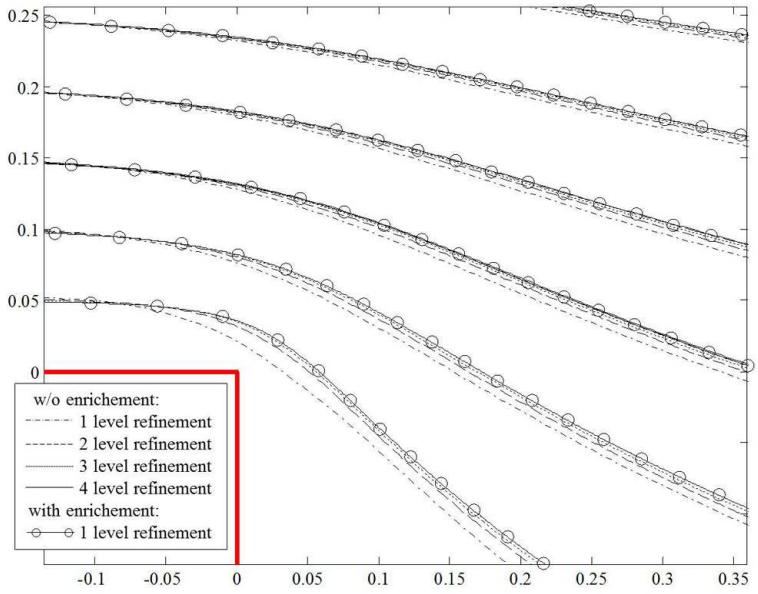

Figure 3.13: *Velocity streamlines for the two-dimensional channel with sudden symmetrical expansion, using the X-FEM without tip enrichment with 4 different level of mesh refinement. The streamlines are shown to converge towards those from using the present numerical technique.*

The streamline patterns for the flow in an expanding channel for $\mathcal{R}_e \ll 1$ and $h/H = 0.5$ with and without tip enrichment and for different mesh sizes are compared in Fig.3.13. It is found that at least four levels of mesh refinement were necessary without tip enrichment, whereas the same results could be obtained without mesh refinement using the tip enrichment numerical scheme. It is also important to note that the results of the X-FEM without tip enrichment converge toward those from the present numerical method as the mesh size decreases.

3.4.3 Permeability of a fibrous network

In this example, we simulate a viscous flow through a fibrous network and estimate the equivalent permeability. A possible application for this type of problem is filtration membranes, which are present in many important processes in bio-medical engineering [9, 47], food or renewable

fuel industry [34]. The system modelled here represents a cross sectional area of a filtration membrane, where the fibers constitute the membrane itself. For a low enough Reynolds number and pressure gradient (or, equivalently, for an elastic modulus of the fibers high enough), the fibers can be considered as rigid and fixed in place . A cross section of a fibrous network of size $L \times H$ is considered, with an influx $q = 1ms^{-1}$ prescribed at $y = H/2$ while a no-penetration boundary conditions are enforced at $x = -L/2$ and $x = L/2$ (Fig.3.14). Since the flow considered here is two-dimensional, the fibers are actually plates that extend infinitely in the out of plane direction. Different densities of fibers with random shapes and sharp tips are generated inside

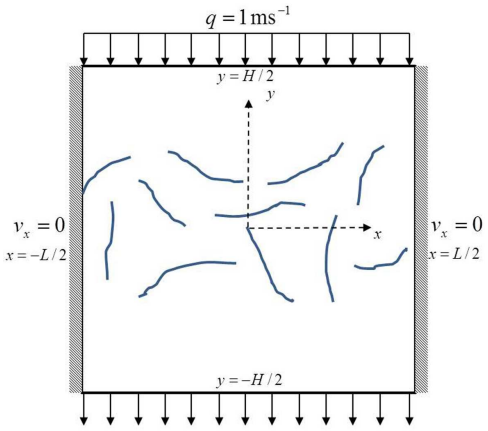

Figure 3.14: *Flow though a fibrous network. No-penetration boundary conditions are enforced at $x = L$ and $x = -L$ while an influx of $q = 1ms^{-1}$ is prescribed at $y = H/2$.)*

the computational domain. Recalling Darcy's law for a flow through a permeable medium, one can estimate the equivalent permeability of the network as follows [40]:

$$k_{eq} = -\frac{2H\mu q}{P_{av}(y = -H/2) - P_{av}(y = H/2)} \tag{3.43}$$

where $P_{av}(y = -H/2)$ and $P_{av}(y = H/2)$ are the average pressure calculated at $y = H/2$ and $y = -H/2$, and μ the fluid's viscosity. Fig.3.15 shows the pressure field and streamline patterns for the flow through networks with different fiber densities. It is important to note that the fibers are generated independently from the underlying finite element mesh and can take any size, shape and orientation, therefore making the generation of a network a straightforward process.

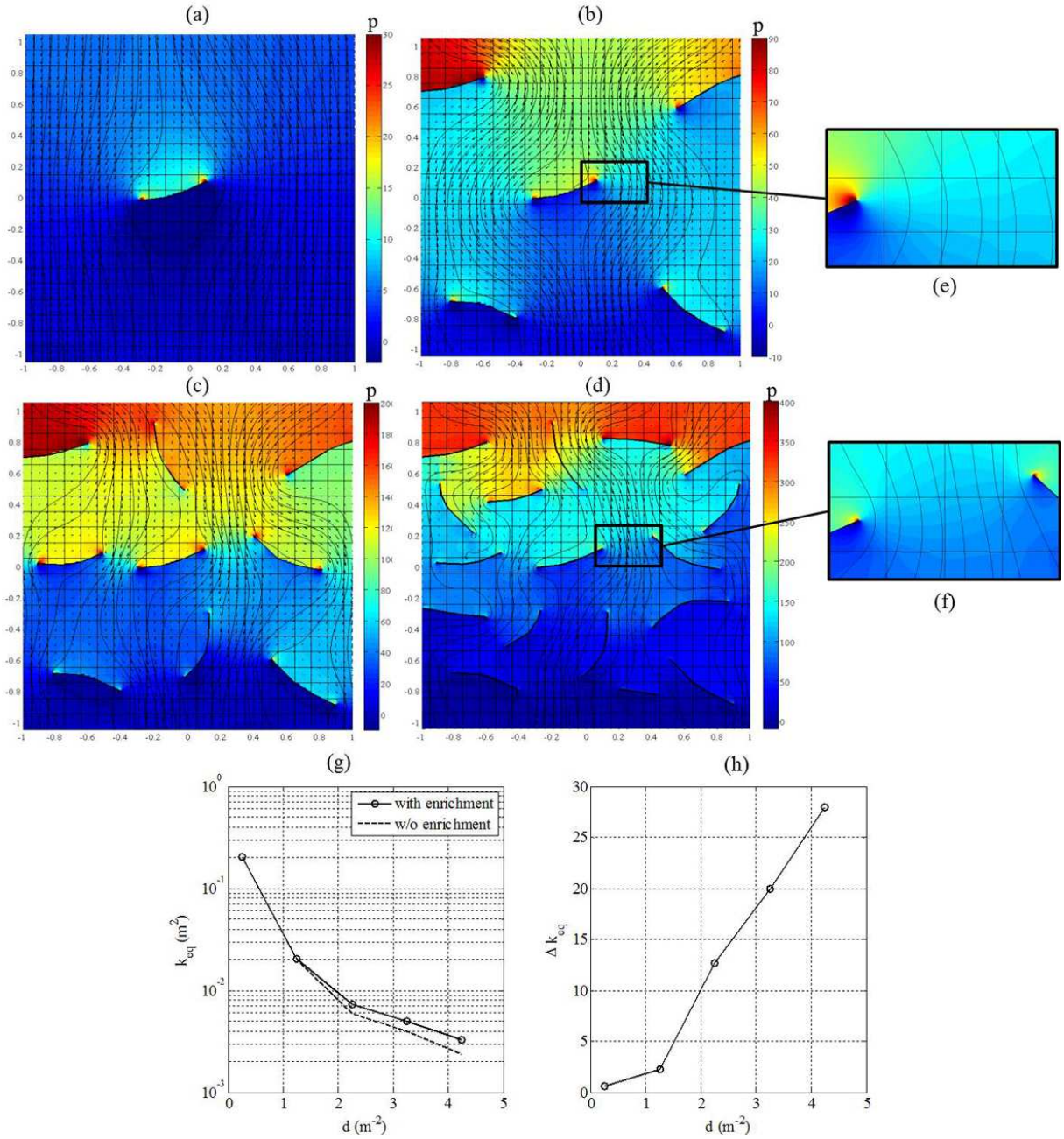

Figure 3.15: *Pressure field and streamline patterns for a viscous flow through a network with fiber density (a) $d = 0.1$, (b) $d = 0.5$, (c) $d = 0.9$ and (d) $d = 1.7$. Figures (e) and (f) are a close up on the pressure singularities around fiber tips. Figure (g) shows the equivalent permeability k_{eq} as a function of fiber density with enrichment (continuous line with circles) and without enrichment (dashed line). The relative difference $\Delta k_{eq} = (k_{eq} - k_{eq\ w/o})/k_{eq}$ is shown in (h).*

Assuming an average fiber length l_0, with the length of each fiber in the region $[0.8l_0 \;\; 1.2l_0]$, the

network is characterized by the following two parameter:

$$d = \frac{n}{HL}, \tag{3.44}$$

$$S_\theta = \left\langle \frac{3\cos^2(\theta) - 1}{2} \right\rangle, \tag{3.45}$$

where d is the fiber density computed as the number of fibers n in the area considered $H \times L$, and S_θ is the order parameter [145] of the fibers with respect to their preferred alignment direction θ. The brackets $\langle \cdot \rangle$ denotes the spacial averaging operation. For an isotropic distribution, $S_\theta = 0$ while for perfectly aligned fibers, $S_\theta = 1$. Assuming that the fibers do not intersect or touch, the case $d = 0$ corresponds to a perfectly permeable material while $d = \infty$ denotes a perfectly impermeable material. The equivalent network permeability k_{eq} is plotted as a function of fiber density d for $S_\theta = 0$ in Fig.3.15g, using the finite element method with (continuous lines) and without tip enrichment (dashed line). As expected, one can observe that as the equivalent network permeability decreases as the fiber density increases. However, it is important to note that without enrichment, the equivalent network permeability is consistently underestimated. Indeed, the relative difference between the two permeabilities $\Delta k_{\text{eq}} = (k_{\text{eq}} - k_{\text{eq w/o}})/k_{\text{eq}}$ (where $k_{\text{eq w/o}}$ is the permeability calculated without enrichment) increases with the fiber density, reaching 27% for $d = 4.2m^{-2}$ (Fig.3.15h), and is likely to keep diverging as the density of fibers increases. This discrepancy illustrates the multiscale nature of this problem. While the present method can compute the pressure gradient at the larger scale H, it also accurately describes the small scale pressure singularities which have a large impact on the overall permeability. This multiscale description of a viscous flow through a network of fibers is achieved while keeping the discretization of the fibers completely mesh-independent, which ensures a great robustness and efficiency of the method.

Finally, network anisotropy is considered and the effect of a preferred fiber orientation on the equivalent network permeability is studied. Fig.3.16.a-c shows the pressure field and streamline patterns for the flow through an anisotropic network ($S_\theta = 1$) with different orientation $\theta = 0, \pi/4$ and $\pi/2$. The equivalent network permeability is found to decrease with the orientation angle θ (Fig.3.16) until it finds a minimum at $\theta = \pi/2$ when the preferred orientation of the

fibers is perpendicular to the flow direction.

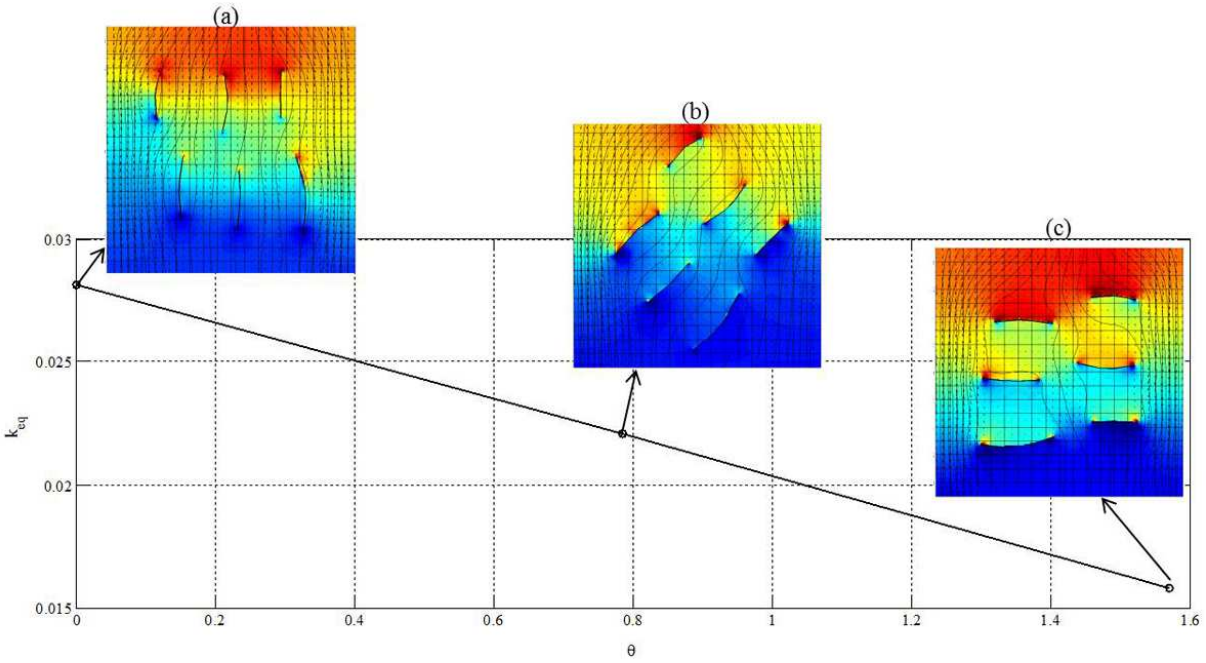

Figure 3.16: *Equivalent permeability as a function of fiber orientation, with* $S_\theta = 1$. *Pressure field and streamline patterns are shown for (a)* $\theta = 0$, *(b)* $\theta = \pi/4$ *and (c)* $\theta = \pi/2$

3.5 Conclusion

A new computational technique based the Extended Finite Element method for describing the Stokes flow around structures with any number of sharp corners/tips in combination with Lagrange multipliers to enforce the no-slip boundary condition was developed. The enrichment functions for the pressure and velocity fields are derived for any convex corner. The results compared with the analytical solution for the flow around corners of various angle show a good accuracy of the method and a large improvement over the standard finite element method. It is also found that results from the X-FEM without tip enrichment for the flow through a suddenly expanding channel converge towards those of the present numerical scheme as the level of mesh refinement increases. These results demonstrate that enriching the finite element space with the asymptotic solution near the corner lead to converged and accurate results for the problem of a viscous flow around sharp corners without the need for complicated and time consuming mesh refinement algorithms.

The equivalent permeability k_{eq} of networks with various fiber densities and anisotropy is estimated using the X-FEM with and without the proposed tip enrichment strategy. It is found that the local microscale pressure and velocity singularities around the fiber tips have a large impact on the macroscale behavior of the network; neglecting them can lead to an underestimation of the permeability of as low as 30% for the finite element mesh size considered. The present numerical method is therefore well adapted for situations where the flow at different scales play an important role, and the mesh independent discretization of corners and walls make it ideal to compute the viscous flow around multiple obstacles with sharp corners. The extension of the method in 3 dimensions is being considered. Moffat's solution and the present enrichment functions can easily be used in 3 dimensions with minimum modification for the case of the flow around the edges of a plate. Possible complications might occur in defining the correct Lagrange multiplier space to enforce the zero velocity condition on the surface of the plate in 3 dimensions. Another difficulty resides in resolving the flow around the corners of the plate in 3 dimensions, although there exist asymptotic solutions for the flow past a quarter plate [82] which can be used to develop the corresponding enrichment functions.

Chapter 4

Applications of the Immersed Membrane formulation to the study of the interaction between soft colloid particles and immersed fibrous network

Filtration membranes are ubiquitous to most biological systems and are at the heart of important applications in bio-medical engineering [9, 47], food industry and both fossil and renewable fuels processes [34]. In the majority of these applications, membranes are used to either (a) separate undesired particles from a solution or (b) produce (and fractionate) stable emulsions with specific size controls (such as liposomes) used in medical diagnosis and therapy [27]. In addition, a novel area of biological medicine is drug delivery using liposomes [70, 2]. A liposome is a micron-sized vesicle (bubble) whose interfacial surface is stabilized by lipids. The interior of the liposome can be filled with drugs to be delivered for treatment of various diseases. Filtration of fluids containing liposomes are required at various steps within their manufacture and delivery to patients, in order to provide sterility. These filtration steps can require both allowing liposomes

to freely pass through the porous filter, while retaining possible biological contaminants, as well as, retaining and concentrating the liposomes. Despite the very soft nature of these colloidal particles, current membrane designs have consistently relied on the assumptions that they are rigid particles [57, 146, 79]. In fact, it has only been in recent years that hindrance factors for transport of non-spheroidal (rod) shaped rigid particles in ideal pores has been theoretically addressed [10, 43]. This has strongly hindered the performance of current membrane systems. The incorporation of deformation is, however, expected to critically affect the above mechanisms since particles can easily change their shape to accommodate a variety of pore shapes and sizes. It can also increase the adhesion between a particle and a surface (by effectively increasing the contact surface area) and thus hinder particle entry and permeation.

From a computational modeling viewpoint, studies of the mechanics of soft vesicles and their interactions with an immersed porous network has been hindered by a number of theoretical challenges, which include the coupled fluid-structure interactions, intense particle deformations and perhaps separation, as well as the effect of surface forces that are very significant at micron (and lower) length scales. Furthermore, when fibers are present, the geometry of sharp tips create singular flow fields which have been resolved through the use of refinement methods [1, 116]. Such approaches are not only costly but can never truly resolve the steep gradient and hyperbolic pressure field that appears at the fiber tips [115].

To address these issues, the objectives of the work are two-folds. First, we integrate a recently developed Particle-based Moving Interface Method (PMIM) [61] to describe the mechanics of immersed and porous interfaces [164, 165] with a numerical technique to describe creeping flow through a fibrous network [63]. In this framework, the motion of an immersed soft vesicle is coupled with an Eulerian fluid description via a particle-enriched interface that can evolve as dictated by mechanical force equilibrium. Using an updated Lagrangian description of the vesicle, the motion of the deformable vesicle is completely independent from the spatial numerical discretization and it enables a very precise description of the curvature and motion of the vesicle over time. The method also use a enriched finite element approach to match the analytical asymptotic fields near the tip of fibers to smoothen far-field velocity and pressure fields. This ensures that a high fidelity solution is obtained without using refinement techniques. Note

that the model is presented in two dimensions and fibers can actually be better described as plates that extend to infinity in the third dimension. The second contribution of the chapter is the introduction of a homogenization approach, inspired by research efforts in solid mechanics [163], to bridge the microscale mechanics of flow and vesicle transport to the estimation of the macroscale permeability of the network. For this, we introduce a so-called elementary volume element in which one can computationally average the flux of fluid/vesicles subjected to macroscopic pressure gradients. This operation eventually permits the determination of macroscopic network permeabilities as illustrated in subsequent examples. To showcase the potential of the method, we then predict the role of a microscopic parameter, the surface tension at the vesicle-solvent interface, on the overall permeation of particles through the network. This study highlights the role of surface tension, pressure differential and porosity configuration on the entry and perhaps immobilization of the vesicle within a porous media. It should be noted that in our current model, the colloidal vesicle is actually a deformable fluid "cylinder" that extent in the third dimension. The closest physical embodiment of this type of vesicles might be coalescing media for oil in water separations.

The chapter is organized as follows. In the next section, we provide a mathematical description to describe the deformation of a soft fluid-like colloid interacting with an immersed fibrous network. In section 3, we then discuss the numerical formulation based on a mixed-finite element and particle method. Section 4 then concentrates on the derivation of a homogenization technique that bridges the micro-mechanisms of vesicle permeation to macroscopic permeabilities. We finally conclude the chapter with a discussion of the method, results and potential for improvement.

4.1 Multiscale mathematical formulation for a soft droplet in an immersed fibrous network

4.1.1 Basic governing equations

Consider a two-dimensional incompressible viscous flow in a domain Ω delimited by a boundary $\partial\Omega$ in which exists one or multiple no-slip rigid boundaries Γ_F taking the shape of thin fibers (or

plates) (Fig.4.1). We also consider a number of closed vesicles, with boundaries Γ_I and that are able to move with the surrounding fluid. The problem is characterized by the Reynolds number $\mathcal{R}_e = HV\rho/\mu$ where H is the characteristic length scale, V the characteristic fluid velocity, μ the kinematic viscosity and ρ the fluid densities in and out of the vesicles. We choose here to remain in the Stokes flow assumption with $\mathcal{R}_e \ll 1$, where inertial effect may be neglected. The velocity of a fluid particle is given in terms of its material time derivative $\mathbf{v}(\mathbf{x},t) = D\mathbf{x}/Dt$, where $\mathbf{x} = \{x \;\; y\}$ is the current position of the fluid particle at time t. Under these conditions, the governing equations and boundary conditions for the Stokes flow are written:

$$\nabla \cdot \boldsymbol{\sigma} = \mathbf{0} \qquad \forall \mathbf{x} \in \Omega/\Gamma \tag{4.1}$$

$$\nabla \cdot \mathbf{v} = 0 \qquad \forall \mathbf{x} \in \Omega/\Gamma \tag{4.2}$$

where $\boldsymbol{\sigma}$ is the Cauchy stress tensor in the fluid and the second equation imposes the condition of incompressibility. These equations are combined with the moving interface problem:

$$[\boldsymbol{\sigma} \cdot \mathbf{n}] = \mathbf{f}_I + \mathbf{f}_{F/I} \qquad \forall \mathbf{x} \in \Gamma_I \tag{4.3}$$

$$D\mathbf{X}_I(t)/Dt = \mathbf{v}(\mathbf{x}(\mathbf{X}_I,t),t) \qquad \forall \mathbf{x} \in \Gamma_I \tag{4.4}$$

Here $\mathbf{X}_I$ denotes a point on the vesicle boundary, the vector $\mathbf{n}$ represent the normal direction to the moving interface, the force $\mathbf{f}_I$ is the unbalanced interface force due to its deformation and $\mathbf{f}_{F/I}$ is the interaction force between fibers and the moving interface. Finally, the boundary conditions for fluid motion on the external boundary and on fibers read:

$$\boldsymbol{\sigma} \cdot \mathbf{n} = p_o \mathbf{n} \qquad \forall \mathbf{x} \in \partial\Omega \tag{4.5}$$

$$\mathbf{v}(\mathbf{x},t) = \mathbf{0} \qquad \forall \mathbf{x} \in \Gamma_F. \tag{4.6}$$

where p_0 is an external pressure surrounding the domain Ω, and a zero-velocity condition is applied on the fiber domain. The latter assumption arises from the model that (a) the fiber are rigid and (b) a no-slip condition is assumed between the fluid and the fibers.

4.1.2 Constitutive equations

To complement the above system of equation, a number of constitutive relation must be introduced. They can be broken down into three components that describe in turns: (a) the behavior of the fluid, (b) the mechanical behavior of the interface and (c) the interactions forces between interface and fibers. In this work, we consider a simple incompressible Newtownian fluid with viscosity μ that can be different within the colloids and the external fluid.

$$\boldsymbol{\sigma} = \mu\mathbf{D} - \mathbf{pI} \tag{4.7}$$

where $\mathbf{D}$ is the rate of deformation and p is the hydrostatic pressure enforcing the incompressibility condition. For the sake of simplicity, we consider here a bi-fluid interface without elastic stiffness and characterized by the liquid-liquid surface tension γ between the vesicle and the continuum fluid. More complex cases can later be considered as discussed in the first chapter. In these conditions, the force $\mathbf{f}_I$ of the interface can be written:

$$f_I \quad = \quad -\gamma\mathcal{H} \tag{4.8}$$

with $\mathcal{H}$ the mean curvature of the surface. Finally, the fiber-interface interaction forces is considered to be of repulsive nature at short distance. For this initial modeling effort, we have used an interaction energy function of the same form as the electrostatic potential function. That is, the force is inversely proportional to the distance between hypothetical point charges on the surface of the flake (fiber):

$$f_{F/I} \propto 1/\phi_F(\mathbf{X}_I) \tag{4.9}$$

where ϕ_F is the distance function with respect to the fiber. Future work can incorporate more complex formulations including van derWaals interactions.

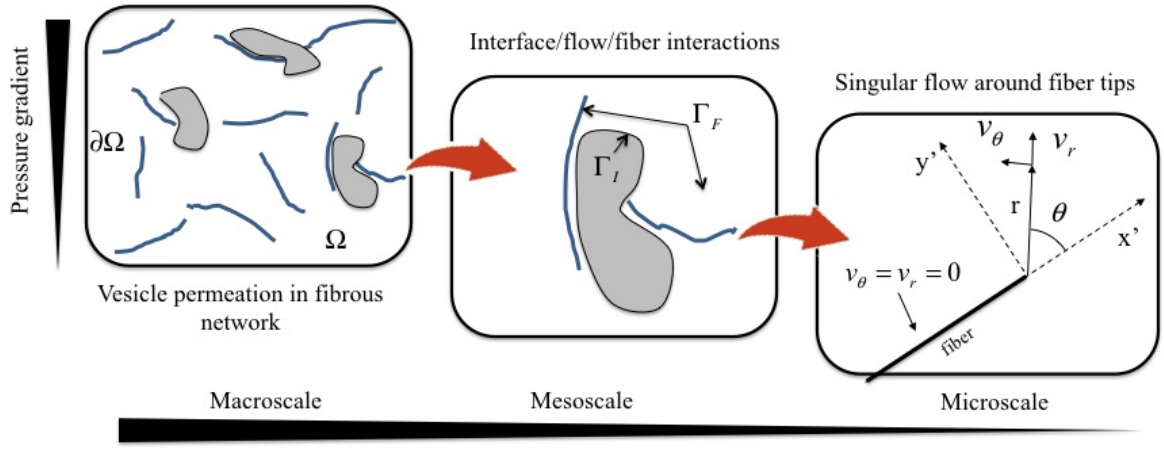

Figure 4.1: *fluid domain* Ω*, interface* Γ_I *and fixed structure* Γ_F *with no-slip/no-penetration boundary condition. The local polar coordinate system is centred at the fiber tip and oriented in the direction of the fiber.*

4.1.3 A two-scale asymptotic solution to describe the fluid flow around thin fibers

When the diameter of fibers constituting the network is very small compared to characteristic size of a particle, the above mathematical problem admits a solution that displays variation across three disparate length-scales (Fig. 4.1): macroscopic fields variations are on the order of the domain size, mesoscopic variations are on the order of the particle size and finally, microscopic fields vary on the order of the fiber diameter size. This creates a significant issue to later derive an accurate numerical solution at a reasonable computational cost. Inspired by asymptotic methods [74, 114], we here propose to address the problem as follows; First, we derive a solution for the fluid flow around the tip of a fiber and subjected to the far-fields boundary conditions. Then, we enrich our macroscopic solution with this solution in the regions of interests, which result in introducing a limited number of "microscopic" degrees of freedom. Finally, we compute a solution that ensures that both microscopic and mesoscopic are consistent within the entire computational domain.

To simplify our analysis, let us first assume that the width of our fibers is infinitesimally small compared to other dimensions of the problem. In this case, the flow field near the tip of fibers admits a singular solution that was derived by Moffat in [115]. Adopting a polar coordinate system (r, θ) centred on the fiber tip, where $r = \sqrt{x'^2 + y'^2}$, $\theta = \arctan(y'/x')$ and the axis

x' and y' are aligned with the fiber (Fig. 4.1). The streamline function $\psi(r,\theta)$ solution to the Stokes equation $\nabla\psi = 0$ in the region $0 < r \ll H$ can be written in the following separated form:

$$\psi(r,\theta) \;=\; r^{\alpha} f_{\alpha}(\theta) \tag{4.10}$$

where α is an unknown complex exponent that determines the structure of the flow, and is to be found as part of the solution. Following [115], the function $f_{\alpha}(\theta)$ is written:

$$f_{\alpha}(\theta) \;=\; A\cos(\alpha\theta) + B\sin(\alpha\theta) + C\cos((\alpha-2)\theta) + D\sin((\alpha-2)\theta) \tag{4.11}$$

where A, B, C and D are arbitrary complex constants. In the cases where $\alpha = 0, 1$ or 2, the above equation degenerates into other forms that are not relevant to the problem studied here, and we will henceforth only consider values of α such that $\alpha \neq 0, 1, 2$. The axial and radial velocities of the flow are deduced from the stream function $\psi(r,\theta)$ as follows:

$$v_r \;=\; \frac{1}{r}\frac{\partial\psi}{\partial\theta} \quad \text{and} \quad v_{\theta} \;=\; -\frac{\partial\psi}{\partial r}, \tag{4.12}$$

and are subjected to the following no-slip/no-penetration boundary conditions at the wall:

$$v_r(r,\theta=\alpha) \;=\; 0, \quad v_{\theta}(r,\theta=\alpha) \;=\; 0 \tag{4.13}$$

Enforcing these boundary conditions on (4.12) and (4.11) yields the constant A, B, C and D [[115]]:

$$A \;=\; \cos(\alpha-2)\alpha,\; B \;=\; \sin(\alpha-2)\alpha,\; C \;=\; -\sin\alpha\alpha \text{ and } D \;=\; -\cos\alpha\alpha \tag{4.14}$$

as well as the exponent α, found to be $\alpha = 3/2$ in the particular case of infinitesimally thin fibers [115]. The pressure can then be calculated by solving the momentum equation

$$\nabla p \;=\; \mu\nabla^2\mathbf{v} \tag{4.15}$$

where $\mathbf{v} = v_r \mathbf{e}_r + v_\theta \mathbf{e}_\theta$ is computed using equations (4.10) and (4.12).

4.2 Numerical approach: the Particle Enriched Moving Interface Method

The idea of the Extended Finite Element Method is to enrich a finite element space with additional functions. Our numerical technique takes the same approach: the Stokes flow is solved using the traditional $\mathcal{C}_0$ conforming finite elements (in our cases 4 node bilinear elements for the pressure and 9 node quadratic elements for the velocity) space, and we enrich this space with additional degrees of freedom that allow the pressure jump across the interface (the velocity stays continuous) and singular pressure and velocity fields around the corner tip. To enrich the standard finite element space, we make use of the linearity of the Stokes flow and simply sum the enrichments for the pressure jump and the asymptotic solution around the corner tip. The velocity and pressure fields in this enriched space are therefore interpolated as follows:

$$\begin{aligned} p(\mathbf{x}) &= \sum_i N_i(\mathbf{x}) p_i + \sum_j N_j(\mathbf{x})(H(\phi_F(\mathbf{x})) - H_j)\check{p}_j + \sum_k \sum_l N_k(G^l\left(r(\mathbf{x}), \theta(\mathbf{x})\right) - G_k)\hat{p}_k \\ &+ \sum_j N_j(\mathbf{x})(H(\phi_I(\mathbf{x})) - H_j)\check{p}_j \qquad (4.16) \\ \mathbf{v}(\mathbf{x}) &= \sum_i \hat{N}_i(\mathbf{x})\mathbf{v}_i + \sum_k \sum_l \hat{N}_k(F^l\left(r(\mathbf{x}), \theta(\mathbf{x})\right) - F_k)\tilde{\mathbf{v}}_k \qquad (4.17) \end{aligned}$$

where N and $\hat{N}$ are the regular 4 nodes and 9 nodes shape functions, H is the Heaviside function that provides the needed discontinuity, and $\mathbf{F}$ and $\mathbf{G}$ are the special asymptotic corner tip functions. The terms ϕ_I and ϕ_F denote level-set functions, i.e. the signed distance functions with respect to the interface and the fibers. Table 1 shows a summary of asymptotic functions used as enrichment for both pressure and velocity fields calculated in chapter 3: The terms $\check{p}_j$

Table 4.1: Corner tip asymptotic functions

$\mathbf{G}$	$\left\{r^{\alpha-2}\sin(\alpha\theta), r^{\alpha-2}\sin((\alpha_1-2)\theta), r^{\alpha-2}\cos(\alpha\theta), r^{\alpha-2}\cos((\alpha-2)\theta)\right\}$
$\mathbf{F}$	$\left\{r^{\alpha-1}\sin((\alpha-2)\theta)\sin\theta, r^{\alpha-1}\cos((\alpha-2)\theta)\cos\theta\ ,\right.$ $\left. r^{\alpha-1}\sin((\alpha-2)\theta)\cos\theta, r^{\alpha-1}\cos((\alpha-2)\theta)\sin\theta\right\}$

and $\hat{p}_j$ correspond to the enriched degrees of freedom associated with the jump in pressure across the fibers and the droplet interface respectively, while the terms $\tilde{p}_k$ and $\tilde{\mathbf{v}}_k$ are the enrichment degrees of freedom associated with the near corner tip pressure and velocity fields. In addition to

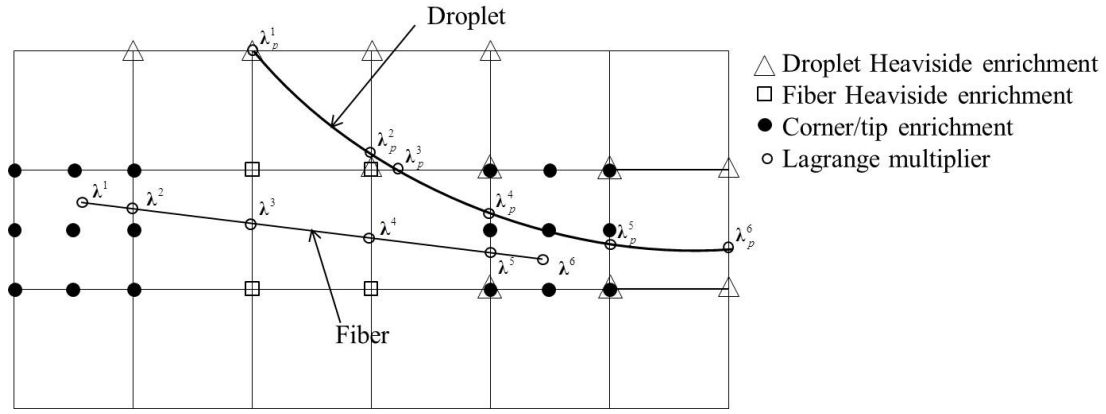

Figure 4.2: *Black dots denote tip enrichment for the velocity and pressure (only the four corner nodes in the case of the pressure) while squares and triangles indicate split enrichment for the pressure for the fibers and the interface respectively.*

the velocity and pressure degrees of freedom and their respective enrichment, let us introduce the Lagrange multipliers $\boldsymbol{\lambda^I}$ and λ_p^I. These are used to enforce the no-slip/no-penetration boundary condition (4.6) on the corner walls and tip and the pressure jump condition at the interface. They are discretized at the intersection between the corner walls and the underlying mesh for $\boldsymbol{\lambda^I}$, and at the intersection between the interface and the underlying mesh for λ_p^I, as shown in Fig.4.2. They are interpolated along the interface Γ using one-dimensional shape functions $\lambda_i(\mathbf{x},t) = \sum_{I=1}^{2} \bar{N}^I(\mathbf{x})\lambda_i^I(t)$ where I denotes the numbering of the nodes for each segment of the corner walls, and i runs over the dimensions 1 and 2 (in 2D).

4.2.1 Weak formulation

Introducing the test functions $\mathbf{w_v}$, w_p, $\mathbf{w_\lambda}$ and w_{λ_p}, integrating by parts and using the divergence theorem, the weak form of the governing equations (4.1)-(4.5) in the fluid domain can be written as: given the position $\mathbf{X}_I$ at time t, find $\mathbf{v} \in \mathcal{V}$, $p \in \mathcal{P}$, $\boldsymbol{\lambda} \in \mathcal{L}$ and $\lambda_p \in \mathcal{L}_p$ such that for all

$\mathbf{w_v} \in \mathcal{V}$, $w_p \in \mathcal{P}$, $\mathbf{w_\lambda} \in \mathcal{L}$ and $w_{\lambda_p} \in \mathcal{L}_p$

$$\begin{aligned}
(\nabla \mathbf{w_v}, \mu \nabla \mathbf{v})_\Omega - (\nabla \mathbf{w_v}, p\mathbf{I})_\Omega + (\mathbf{w_v}, \rho \mathbf{f})_\Omega + (\mathbf{w_v}, \boldsymbol{\lambda})_\Gamma + \big(\mathbf{w_v}, \mathbf{f}_I + \mathbf{f}_{R/I})\big)_\Gamma &= 0 \\
(w_p, \nabla \cdot \mathbf{v})_\Omega + (w_p, \lambda_p)_\Gamma &= 0 \\
(w_{\lambda_p}, [p])_\Gamma + (w_{\lambda_p}, (\mathbf{f}_I + \mathbf{f}_{R/I}) \cdot \mathbf{n})_\Gamma &= 0 \\
(\mathbf{w_\lambda}, \mathbf{v})_\Gamma &= 0 \qquad (4.18)
\end{aligned}$$

where the notation $(\cdot, \cdot)_\Omega$ indicates the L^2 inner product with respect to the domain Ω. The Lagrange multipliers $\boldsymbol{\lambda}$ and λ_p enforce the no-slip/no-penetration boundary conditions (4.6) and the pressure jump conditions on the implicitly defined corner walls. The test functions $\mathbf{w}_\lambda$ and w_{λ_p} are associated with the Lagrange multipliers and $\mathcal{V}$, $\mathcal{P}$, $\mathcal{L}$ and $\mathcal{L}_p$ are admissible spaces for the velocity, pressure and Lagrange multipliers.

4.2.2 Discretized form

The weak form (4.18) is then discretized in space by using the XFEM approximation, and after simplifications yields the following linear system:

$$\mathbf{K}^t \mathbf{d}^t = \mathbf{f}^t \qquad (4.19)$$

where $\mathbf{K}^t$ is the consistent tangent matrix, $\mathbf{d}^t = \{\mathbf{v} \;\; p \;\; \lambda_p \;\; \boldsymbol{\lambda}\}$ the global vector of unknowns and $\mathbf{f}^t$ the global force vector at time t. The element contribution to $\mathbf{K}^t$ and $\mathbf{f}^t$ are as follows:

$$\mathbf{k}^e = \begin{bmatrix} \mathbf{k}^e_{\mathbf{vv}} & \mathbf{k}^e_{\mathbf{v}p} & 0 & \mathbf{k}^e_{\mathbf{v}\boldsymbol{\lambda}} \\ \mathbf{k}^e_{p\mathbf{v}} & 0 & \mathbf{k}^e_{p\lambda_p} & 0 \\ 0 & \mathbf{k}^e_{\lambda_p p} & 0 & 0 \\ \mathbf{k}^e_{\boldsymbol{\lambda}\mathbf{v}} & 0 & 0 & 0 \end{bmatrix}, \quad \mathbf{f}^e = \begin{Bmatrix} \mathbf{f}^e_{\mathbf{v}} & 0 & \mathbf{f}^e_{\lambda_p} & 0 \end{Bmatrix}^T. \qquad (4.20)$$

The form of the components in the $\mathbf{k^e}$ matrix and and the $\mathbf{f}^e$ are given in appendix A. The finite element equation (4.19) can be solved with a linear solver to yield an expression for the fluid (and interface) velocity $\mathbf{v}$ at time t. Given the interface velocity $\mathbf{v}$, the position $\mathbf{X}_I$ of

the vesicle interface Γ_I is then updated to compute $\mathbf{K}^{t+dt}$ and $\mathbf{f}^{t+dt}$ for the next time step, with dt the time step increment. Once the vesicle has left the computational domain, or once $||\mathbf{d}^{t+dt} - \mathbf{d}^t|| < TOL$, the algorithm has converged and the interface is in equilibrium with the surrounding fluid. The next step involves the transport of the interface using a mesh-based particle method, as discussed next.

4.2.3 Grid based particle method for interface evolution

To track the deformation of the interface Γ_I, we choose here to use a grid-based particle method similar to what was introduced in [99]. This method indeed possesses the double advantage of tracking the interface explicitly with particles while using the underlying fixed finite element mesh to ensure a fairly uniform repartition of the particles on the interface. Here we summarize the grid based particle method and discuss the update of the interface position and deformations measures. The particles, whose position vector is denoted by $\mathbf{y}$, are chosen as the normal projection of the underlying mesh nodes, with position vector $\mathbf{p}$, on Γ (Fig. 4.3a.). Initially, the interface is described implicitly as the zero level-set of a signed distance function $\phi_I(\mathbf{p}, t = 0)$. The initial coordinates of particles $\mathbf{y}$ can then found as follows:

$$\mathbf{y} \quad = \quad \mathbf{p} - \phi_I(\mathbf{p}, 0)\nabla\phi_I(\mathbf{p}, 0) \tag{4.21}$$

To limit the number of particles, we define a so-called computational tube such that only nodes $\mathbf{p}$ whose distance to Γ_I is smaller than a cut-off value λ_{tube} are accounted for. It is important to note here that there is a one to one correspondence between each particle $\mathbf{y}$ and node $\mathbf{p}$. This ensure a quasi-uniform repartition of particles along the interface throughout its evolution. Between two subsequent time steps, the particles are moved according to the normal component of the interface velocity $\mathbf{v}^{\perp}(\xi, t)$ as follows:

$$\mathbf{y}^{t+dt} \quad = \quad \mathbf{y}^t + \mathbf{v}^{\perp}(\mathbf{y}^t, t)dt + \mathbf{\Omega} \cdot \mathbf{v}^{\perp}(\mathbf{y}^t, t)\frac{dt^2}{2} \tag{4.22}$$

where $\mathbf{\Omega}$ is the matricial form of the angular velocity of the interface normal [86]:

$$\boldsymbol{\omega} \;=\; -\left(v^{\perp}_{,\xi_1}\right)[0\;0\;1]^T \quad \text{and} \quad \Omega_{ik} \;=\; \epsilon_{ijk}\omega_j \tag{4.23}$$

with ϵ_{ijk} the permutation tensor and ξ_1 the local coordinate running along the interface (Fig. 4.3b.). After the motion of the interface, the particles $\mathbf{y}$ may not be the closest point on Γ_I to their associated nodes $\mathbf{p}$. Moreover, the motion of the particles may cause their distribution on

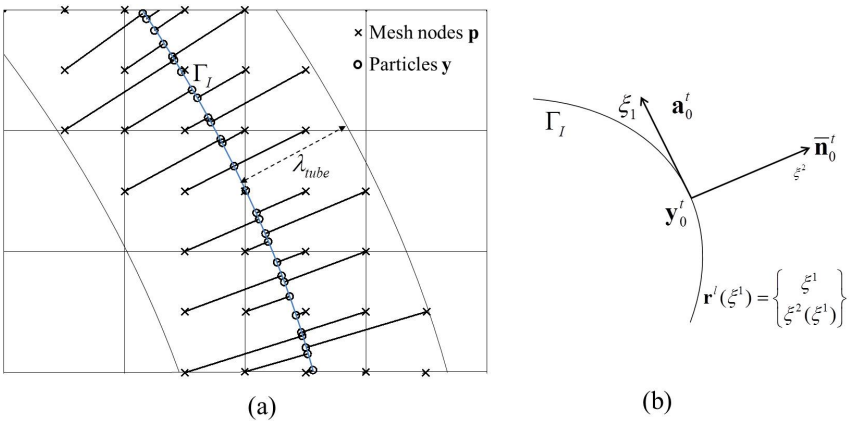

Figure 4.3: *(a) particles and associated nodes in the computational tube. (b) Local polynomial approximation of the surface (and of any Lagrangian field). The polynomial $\xi^3(\xi^1,\xi^2)$ that approximates the interface is constructed via least square fitting using neighbouring particles in the local referential $\{\mathbf{a}_0, \bar{\mathbf{n}}_0\}$ centered on particle $\mathbf{y}_0$.*

Γ_I to become uneven, which can affect the geometrical resolution of the interface. To overcome this issue, the interface is ressampled after motion by recomputing the particles as the closest points on Γ_I to the nodes $\mathbf{p}$ inside the updated computational tube (which has moved with the interface) (Fig.4.3a.). This is done by first approximating the interface with polynomials locally around each particle. The procedure, explained here in the two dimensional case, is as follows: for each node $\mathbf{p}$ inside the computational tube, the closest m particles $\mathbf{y}_0...\mathbf{y}_m$ are collected, carrying with them the tangent $\mathbf{a}_0^t...\mathbf{a}_m^t$ and normal $\bar{\mathbf{n}}_0^t...\bar{\mathbf{n}}_m^t$ to the interface before motion. Denoting $\mathbf{y}_0$ as the particle closest to $\mathbf{p}$, a polynomial of degree $n < m$ is fitted to the particles $\mathbf{y}_0...\mathbf{y}_m$ in the local coordinate system $\{\mathbf{s}_0^t; \bar{\mathbf{n}}_0^t\}$ centered on $\mathbf{y}_0$ (Fig.4.3b). The location

$\tilde{\mathbf{y}}_i$ of particle i in this local coordinate system is given by:

$$\tilde{\mathbf{y}}_i \;=\; \left\{ \begin{array}{c} \xi_i^1 \\ \xi_i^2 \end{array} \right\} \;=\; \mathbf{R}^t \cdot (\mathbf{y}_i - \mathbf{y}_0) \quad \text{with} \quad \mathbf{R}^t \;=\; \left[\begin{array}{c} (\mathbf{a}_0^t)^T \\ (\bar{\mathbf{n}}_0^t)^T \end{array} \right]. \tag{4.24}$$

Taking the example of a quadratic polynomial ($n = 2$), the interface around particle $\mathbf{y}_0$ is represented in the local referential as the graph function $\xi^2(\xi^1) = c_0 + c_1\xi^1 + c_2(\xi^1)^2$, where the coefficients c_0, c_1 and c_2 are found by minimizing the L^2 difference between the $\xi^2(\xi_i^1)$ and the ξ_i^2. The coordinates $\left\{\xi^1, \xi^2(\xi^1)\right\}$ defines a local parameterization $\mathbf{r}^l(\xi^1)$ of Γ in the neighbourhood of $\mathbf{y}_0$:

$$\mathbf{r}^l(\xi^1) \;=\; \left\{ \begin{array}{c} \xi^1 \\ \xi^2(\xi^1) \end{array} \right\}. \tag{4.25}$$

The relationship between the local parameterization $\mathbf{r}^l(\xi^1)$ and the global parameterization $\mathbf{X}_I(\xi^1)$ defined in section 2.1 is then found via rotation and translation operations in the form:

$$\mathbf{X}_I(\xi^1, t + dt) = (\mathbf{R}^t)^{-1}\, \mathbf{r}^l(\xi^1) + \mathbf{y}_0. \tag{4.26}$$

The parameterization $\mathbf{X}_I(\xi^1, t + dt)$ can now be used to ressample the interface, i.e. recalculate the closest point on the interface to the nodes $\mathbf{p}$. This is done by minimizing the distance function $d(\mathbf{r}(\xi^1, t + dt); \mathbf{p}) = 1/2\left|\mathbf{r}(\xi^1, t + dt) - \mathbf{p}\right|$ with respect to ξ^1. In two dimensions, the solution can be found explicitly by solving a cubic equation. Other geometrical quantities can also be found using the parameterization $\mathbf{X}_I(\xi^1, t+dt)$, such as the updated basis $\left\{\mathbf{a}^{t+dt}, \bar{\mathbf{n}}^{t+dt}\right\}$:

$$\mathbf{a}^{t+dt} \;=\; \mathbf{r}(\xi^1, t + dt)_{,1} \;=\; \mathbf{R}^t\, \frac{\partial \mathbf{r}^l(\xi^1, t + dt)}{\partial \xi_1} \tag{4.27}$$

$$\bar{\mathbf{n}}^{t+dt} \;=\; \mathbf{a}^{t+dt} \times \mathbf{z}/|\mathbf{a}^{t+dt} \times \mathbf{z}|. \tag{4.28}$$

and the mean curvature can be found as follows [[100]]:

$$\mathcal{H} \;=\; \frac{\xi_2''}{(1 + \xi_2')^{3/2}} \tag{4.29}$$

where $'$ denotes the derivative with respect to ξ_1. Finally, a new level-set function $\phi_I(\mathbf{p}, t+dt)$ can be calculated as the signed distance function to Γ_I at nodes $\mathbf{p}$ as follows:

$$\phi_I(\mathbf{p}, t+dt) = -\mathbf{sgn}(\frac{\mathbf{y}^{t+dt}-\mathbf{p}}{|\mathbf{y}^{t+dt}-\mathbf{p}|}\cdot\bar{\mathbf{n}}_0^t)|\mathbf{y}^{t+dt}-\mathbf{p}|, \tag{4.30}$$

where $\mathbf{y}^{t+dt}$ is the particle associated with $\mathbf{p}$ at time $t+dt$ and the sign function $\mathbf{sgn}(((\mathbf{y}^{t+dt}-\mathbf{p})/|\mathbf{y}^{t+dt}-\mathbf{p}|)\cdot\bar{\mathbf{n}}_0^t)$ determines whether node $\mathbf{p}$ is in Ω^+ or Ω^-. The reconstruction of the level-set function using the local polynomial approximation of the interface is computationally inexpensive, and is used in the X-FEM part of the algorithm.

4.2.4 Validation for the pressure/velocity field in the tip vicinity

Here we investigate the accuracy of the numerical technique by comparing it with the analytical solution developed by Moffat [115] for the velocity and the pressure field around the fiber tip, with and without a circular droplet in the vicinity. The velocity given by the analytical solution is imposed at the boundary of the computational domain. The Reynolds number is given by:

$$\mathcal{R}_e = \frac{V r^{\mathrm{Real}[\lambda]}}{\nu} \tag{4.31}$$

with μ the kinematic viscosity and V the fluid velocity away from the corner. The parameters V and μ are chosen such that $\mathcal{R}_e \ll 1$ everywhere in the computational domain. The error made in computing the velocity of the flow near a corner is calculated as follows:

$$E_v = \int_{\mathbf{x}_0}^{\mathbf{x}_1} \frac{||\mathbf{v}_{num}(\mathbf{x}) - \mathbf{v}_{asymp}(\mathbf{x})||}{||\mathbf{v}_{asymp}(\mathbf{x})||} d\mathbf{x}, \tag{4.32}$$

$$E_p = \int_{\mathbf{x}_0}^{\mathbf{x}_1} \frac{||p_{num}(\mathbf{x}) - p_{asymp}(\mathbf{x})||}{||p_{asymp}(\mathbf{x})||} d\mathbf{x} \tag{4.33}$$

where $\mathbf{v}_{num}$ denotes the velocity calculated using the numerical method, $\mathbf{v}_{asymp}$ the asymptotic solution and $\mathbf{x}_0, \mathbf{x}_1$ two points in the vicinity of the fiber tip (Fig.4.4a.).

The circular vesicle in the neighbourhood of the fiber tip is shown in Fig.4.4a., as well as a close up of the singular pressure field around the fiber tip and the pressure jump across the

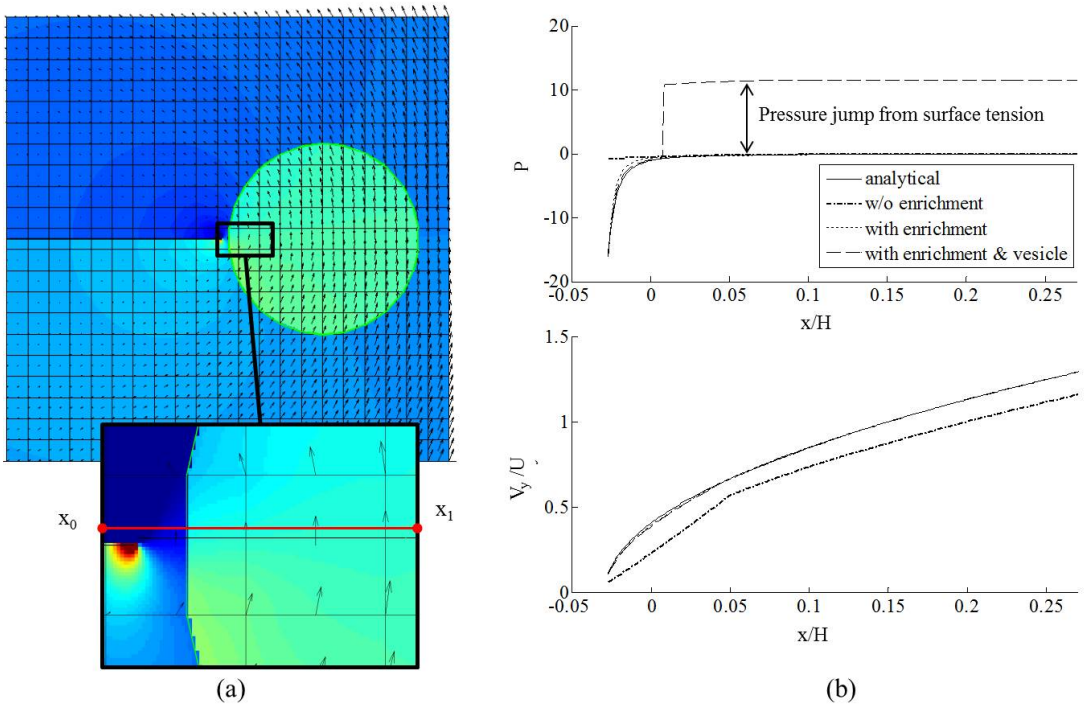

Figure 4.4: *Error E_v made in computing the flow velocity around the corner tip in mode I and II, for different corner angle α. The error can be lessened by more then a factor of 10 using corner tip enrichment.*

Table 4.2: Error made in computing the pressure and velocity fields E_p and E_v, without enrichment, with enrichment and with a vesicle in the vicinity of the fiber tip.

	w/o enrichment	with enrichment	with enrichment & vesicle
E_v	18.2%	0.7%	0.7%
E_p	22.1%	3.1%	3.1%

vesicle interface. Fig.4.4b. shows the velocity and the pressure field in the neighbourhood of the fiber tip, along the line from point $\mathbf{x}_0$ to $\mathbf{x}_1$. We observe in table 2 that without enrichment, the errors E_v and E_p are fairly high, at 18.2% and 22.1% respectively. However, the incorporation of the tip enrichment developed above reduces the errors down to 0.7% and 3.1% respectively. The presence of a circular vesicle in the vicinity of the fiber tip does not significantly affect the accuracy of the scheme, and we can note the appearance of a pressure jump across the vesicle interface from its surface tension, as expected. The source of the remaining error stems from the weak enforcement of the no-slip/no-penetration condition on the corner wall. Future studies will investigate reducing the error by using quadratic instead of linear shape function for the

interpolation of Lagrange multipliers. Overall, the numerical technique presented here is shown to significantly increase the accuracy of the simulation of a flow near a sharp corner using the extended finite element method, at a much lesser computational cost than classical methods since no mesh refinement is needed.

4.3 Numerical approach to predict the permeation of a soft colloids though a fibrous network

In this section, we present a generalized homogenization scheme to determine how different phases of a fluid (such as solvent or various vesicles present in the solvent) can permeate through a fibrous filtration membrane. For this, we first present a general homogenization scheme based on the Hill-Mendel conditions that then served as a basis to express macroscopic permeabilities in terms of flux and pressure on the boundary of a volume element. We then apply these concepts to the specific problem of soft vesicles travelling through a small fibrous network and pay particular attention to the role of surface tension at the vesicle-solvent interface.

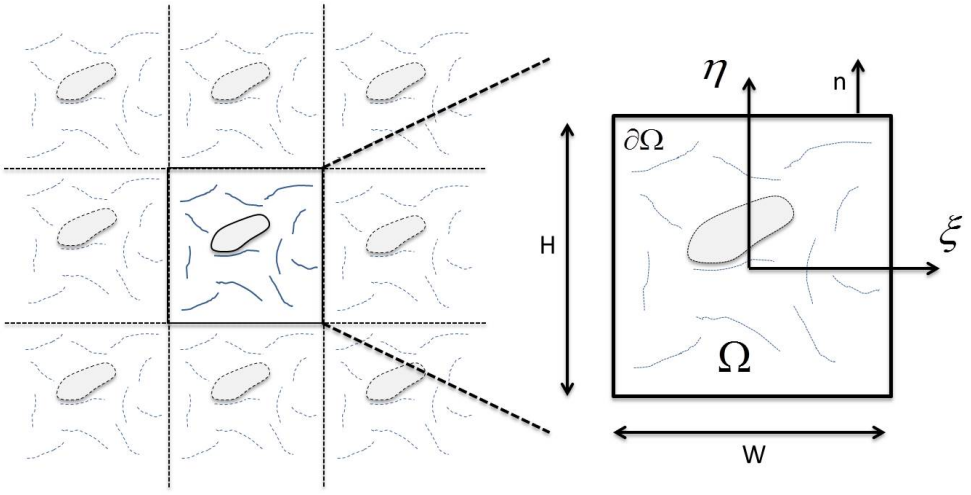

Figure 4.5: *Periodic assumption of a fibrous network with a population of permeating particles. A unit periodic cell is identified and analysized to extract the macroscopic properties of the network.*

4.3.1 General homogenization scheme to compute macroscopic permeabilities

From a macroscopic viewpoint, the phenomenon of fluid flow through porous media has traditionally been described by Darcy's law relating volumic flux to pressure gradient throughout a porous network. The relationship between the flux $\mathbf{Q}_\alpha$ of fluid α and the macroscopic pressure gradient $\bar{\nabla}\bar{p}$ is established via the definition of so-called macroscopic permeability tensor $\boldsymbol{\kappa}_\alpha$ in the form

$$\mathbf{Q}_\alpha = -\frac{\boldsymbol{\kappa}_\alpha}{\mu_\alpha}\bar{\nabla}\bar{p} \tag{4.34}$$

where μ_α is the fluid viscosity. We note that for isotropic porous network such as those studied in this chapter, the permeability can be expressed in terms of a single scalar quantity κ_α such that $\boldsymbol{\kappa}_\alpha = \kappa_\alpha \mathbf{I}$ with $\mathbf{I}$ representing the second order identity tensor.

It is clear here that the quantity κ_α represents the ease by which a fluid permeated through the network. Theoretically, it may therefore be determined through a thorough study of the micromechanisms of vesicle flow and deformation and a consistent averaging operation to bridge micro to macroscale. We propose here to use classical homogenization theory where we assume that at the mesoscale, a membrane is made of a periodic array of unit cells comprised of a pseudo-random fiber distribution. For the sake of simplicity, we also assume that a number of vesicles can be found within each of these cells and that they all have the same position relative the their corresponding unit cells (Fig. 4.5). For each elementary volume (of dimension, $W \times H$), it is possible to introduce a local coordinate system (ξ, η) whose origin is at the center of the volume. With this, it is possible to express the microscopic pressure field p in such a domain as a first order expansion as follows:

$$p(\boldsymbol{\xi}, t) = \left(\bar{\nabla}\bar{p}\right)(t) \cdot \boldsymbol{\xi} + \Delta\tilde{p}(t) \tag{4.35}$$

where $\bar{\nabla}\bar{p}$ is the macroscopic pressure gradient and $\Delta\tilde{p}(t)$ is a fluctuation field arising from the presence of random fibers and vesicles in the domain. Using the fact that the macroscopic

pressure gradient is an average of the microscopic pressure gradient over the unit cell, one can show that:

$$\bar{\nabla}\bar{p} = \frac{1}{\Delta t}\int_{\Delta t}\left[\frac{1}{V_0}\int_{\Omega}(\nabla p)dV\right]dt = \frac{1}{\Delta t}\int_{\Delta t}\left[\frac{1}{V_0}\int_{\Gamma} p\mathbf{n}dS\right]dt \tag{4.36}$$

with $\mathbf{n}$ the unit vector normal to the boundary Γ and V_0 the volume of the domain. Note that we used the divergence theorem to obtain the last equality. The above relation is particularly useful as it enables to characterise the macroscopic pressure gradient in terms of the microscopic pressure field on the boundary of the unit cell. We also obtain that

$$\frac{1}{\Delta t}\int_{\Delta t}\left[\frac{1}{V_0}\int_{\Omega}\tilde{p}dV\right]dt = 0 \tag{4.37}$$

In other words, the macroscopic average of the microscopic fluctuation fields identically vanish. To further establish a relationship between fluxes and pressure gradients, we invoke the Hill-Mendel condition on energy dissipation. More precisely, we postulate that the macroscopic energy dissipation per unit volume and time is equal to the average of the microscopic dissipation over the elementary volume and during a characteristic time period Δt. Note that this elementary time increment is related to the time needed for a vesicle α to go through the elementary volume. We write:

$$\left(\mathbf{Q}_\alpha \cdot \bar{\nabla}\bar{p}\right) V\Delta t = \int_{\Delta t}\left[\int_{\Gamma}(\mathbf{q}_\alpha \cdot p\mathbf{n})dS\right]dt \tag{4.38}$$

On the left hand side, we expressed the energy dissipation of a Darcy-type flow over a volume $V_0 = W \times H \times 1$ and a period Δt. On the right hand side, we expressed this same energy in terms of the product of surface forces $p\mathbf{n}$ where p is the pressure and $\mathbf{n}$ the normal to the boundary, and the velocity $\mathbf{v}$ of fluid particle moving across the boundary. Substituting the expression (4.35) for p into (4.38) and identifying the terms, one can show that:

$$\mathbf{Q}_\alpha = \frac{1}{\Delta t}\int_{\Delta t}\left[\frac{1}{V_0}\int_{\Gamma}(\mathbf{q}_\alpha \cdot \mathbf{n})\boldsymbol{\xi}dS\right]dt \tag{4.39}$$

This establishes a relation between the macroscopic volumic flux $\bar{\mathbf{Q}}_\alpha$ and the microscopic flux $\mathbf{q}_\alpha$ across the boundary of the elementary volume. The macroscopic permeability can then be numerically determined by relating the macroscopic flux (4.39) to pressure gradient (4.43) via equation (4.34).

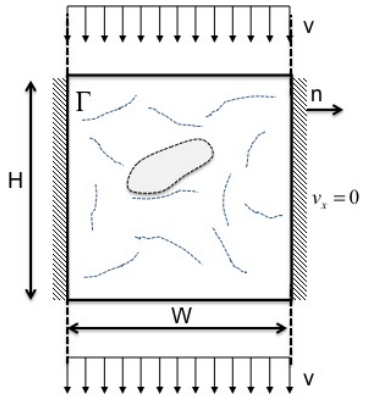

Figure 4.6: *Schematic of the geometry, dimensions and boundary conditions for assessing the permeation of a soft colloid particle through a fibrous network.*

4.3.2 Application to the numerical evaluation of the permeation of soft colloidal particles

Let us now apply the above findings to the computation of a network permeability to two fluids: (a) the solvent and (b) the immersed vesicles. To simplify the analysis, we consider a two-dimensional vertical porous flow (Fig. 4.6) for which boundary conditions are given in terms of the macroscopic solvent flow $q_s = V$ and a no-flux boundary condition on the left and right boundaries of the domain. The relevant quantities to compute are therefore (a) the overall vertical solvent flux Q_y^s, (b) the overall vertical vesicle flux Q_v^s and the vertical macroscopic pressure gradient $\bar{\nabla}_y \bar{p}$. For each simulation, the elementary time Δt is computed as the time required for a vesicle to travel the entire (vertical) length of the domain.

Flux. For this particular problem, the homogenization relation (4.39) becomes, for the solvent:

$$Q_y^s = \frac{1}{WH\Delta t} \int_{\Delta t} \left[\int_{\xi=-W/2}^{W/2} (-HV d\xi) \right] dt = -V \tag{4.40}$$

where the final equality was obtained by realizing that the volumic flux of the fluid across the boundary is constant in time. The volumic flux of vesicle can similary be computed by:

$$Q_y^v = \frac{1}{WH\Delta t}\int_{\Delta t}\left[\int_{\xi=-W/2}^{W/2}(-Hv_v d\xi)\right]dt = -f^v\frac{H}{\Delta t} \tag{4.41}$$

where we used the fact that for incompressible fluids, the cumulative volumic flux entering the domain during a time interval Δt is equal to the volume Ω^v in the vesicle. In other words, we have:

$$\Omega^v = \int_{\Delta t}\left[\int_{\xi=-W/2}^{W/2}(v_v d\xi)\right]dt \tag{4.42}$$

This relation, together with the expression of the volume fraction of a vesicle $f^v = \Omega^v/(WH)$ yields the second equality in (4.41). This result indicates that the volumic flux of vesicles is proportional to their volume fraction and inversely proportional to the time Δt needed to travel a vertical distance H in the network.

Pressure gradient. As mentioned above, we are here interested in computing the vertical macroscopic velocity gradient $\bar{\nabla}_y\bar{p}$. Using (4.43) for the geometry shown in Fig. 4.6, it is straightforward to show that:

$$\bar{\nabla}_y\bar{p} = \frac{1}{HW\Delta t}\int_{\Delta t}\int_{\Gamma}\left(p(\xi,\frac{H}{2}) - p(\xi,-\frac{H}{2})\right)d\xi dt \tag{4.43}$$

Numerically, the above spatial integrals over the top and bottom boundaries of the domain can be evaluated using a surface gausian quadrature rule while the time integral can be evaluated using the trapezoidal rule.

Macroscopic permeabilities With the knowledge of (4.40), (4.41) and (4.43), it is now possible to compute the macroscopic permeabilities of the network. Indeed, writing (4.34) in the vertical direction, it is straightforward to show that:

$$\kappa_s = \frac{\mu V}{\bar{\nabla}_y\bar{p}} \qquad \text{and} \qquad \kappa_v = \frac{\mu H f^v}{\Delta t\,\bar{\nabla}_y\bar{p}} \tag{4.44}$$

In summary, our numerical approach can be divided into four steps: (a) Build a fibrous network, apply given boundary conditions and simulate the permeation of a vesicle through the elementary volume, (b) Determine the elementary time Δt, (c) Using numerical integration of the boundary of the elementary volume, compute fluxes and pressure gradients as given by (4.40), (4.41) and (4.43) and (d) Compute the macroscopic permeabilities using (4.44).

4.3.3 Numerical investigation of the role of surface tension soft vesicles permeation

The objective of this last section is to illustrate how the proposed numerical and homogenization scheme can give precious insights regarding the effect of vesicle deformability on its permeation through a fibrous network. For this, we consider the problem shown in Fig. 4.6 and studied four quasi-random fibrous networks distinguished by similar fiber densities and distributions. For each network, we then investigate the permeation of vesicles that are characterized by a range of deformability, measured in terms of a nondimensional capillary number $C_a = \mu V/\gamma$. Small capillary numbers correspond to vesicles with high surface tension and low deformability; in contrast, a high capillary number reduces the solvent-vesicle surface tension and allows vesicles to undergo very large deformation and flow though narrow pores. Other parameters needed to describe the permeation of the vesicle include the non-dimensional time and permeabilities, written as:

$$t^* = \frac{tH}{V}, \quad \kappa_s^* = \frac{\kappa_s}{\bar{\kappa}} \text{ and } \kappa_v^* = \frac{\kappa_v}{\bar{\kappa}} \tag{4.45}$$

where $\bar{\kappa}$ is the average fluid permeability for networks 1-4 without vesicle. The simulations were run on finite element mesh of size 26×31 (806 elements), sufficiently small to resolve the high curvature of the vesicle interface at large capillary numbers. Due to the presence of second order terms (e.g. the mean curvature) in the force generated by the vesicle-solvent surface tension, the explicit time evolutive simulations are subjected to a strict Courant-Friedrichs-Lewy (CFL) condition on the time step of the second order in mesh size $dt \approx O(\Delta h)^2$, with Δh the size of a single element. In this context, Fig. 4.7 shows the history of the non-dimensional speed of

the vesicle v_v/V as it travels through network 1 for capillary numbers $C_a = 0.04$ (Fig.4.7a) and $C_a = 0.2$ (Fig.4.7b). We observe that for a capillary number low enough ($C_a = 0.04$), the vesicle is too rigid to squeeze through the network (Fig. 4.7a). As a result, it remains trapped between two fibers while the surrounding fluid is diverted away from the obstructed pore. For higher capillary numbers ($C_a = 0.2$), the vesicle is slowed downed at the pore but is deformable enough to fully permeate through the same network (Fig 4.7b). These two example clearly indicate that deformation, in addition to size, dictate wether a vesicle can go through a porous medium. We further see that low deformability may result in the accumulation of trapped vesicles within the network and thus decrease the overall effective permability. This phenomenon is known as fouling [REF].

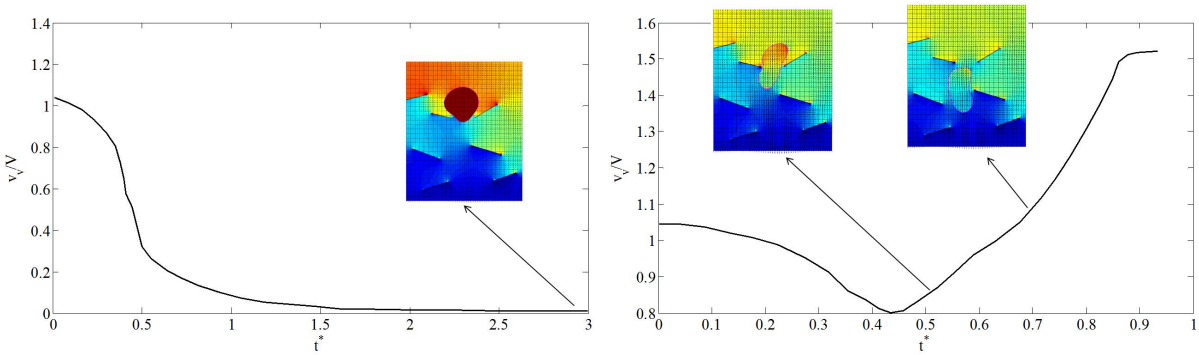

Figure 4.7: *Vesicle speed as a function of non-dimensionalized time t^* for network 1, $C_a = 0.04$ (a) and $C_a = 0.2$ (b).*

Let us now turn to the macroscopic effects of these observations. For this, we compute for each network and capillary numbers the macroscopic permeabilities given in (4.44). For clarity, we particularly focus on understanding how the non-dimensional vesicle and solvent permeabilities κ_v^* and κ_s^* change as functions of the capillary number C_a in Fig. 4.8 and Fig. 4.9 respectively. For all networks, we observe, as expected, that the vesicle permeability decreases with the capillary number, since less deformable vesicles have more difficulties squeezing through the tight pores. We also note that the vesicle permeability decreases to zero in the cases where the capillary number is low enough to cause the vesicle to be permanently trapped into the pores (fouling). On the other hand, the vesicle permeability is shown to approach that of the

fluid without vesicle as the capillary number increases. Similarly, the solvent permeability κ_f^* is shown to decrease with the capillary number in Fig. 4.9. This is explained by the fact that more rigid vesicles hinder the fluid flow through the network, and that pores can be permanently obstructed by the most rigid vesicles. More importantly, even when pores are not obstructed, Fig. 4.9 shows that the presence of the vesicles can lessen the fluid permeability by as much as 20% for the network studied here.

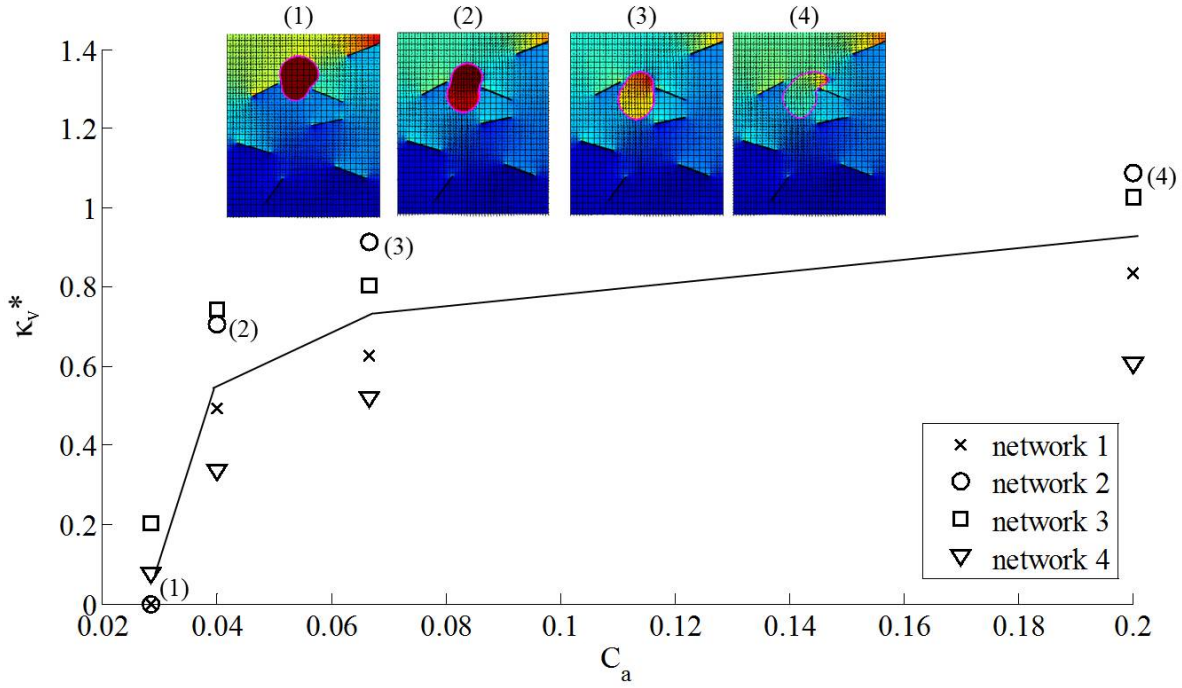

Figure 4.8: *Vesicle permeability as a function of the capillary number* $C_a = \frac{\mu U}{\gamma}$

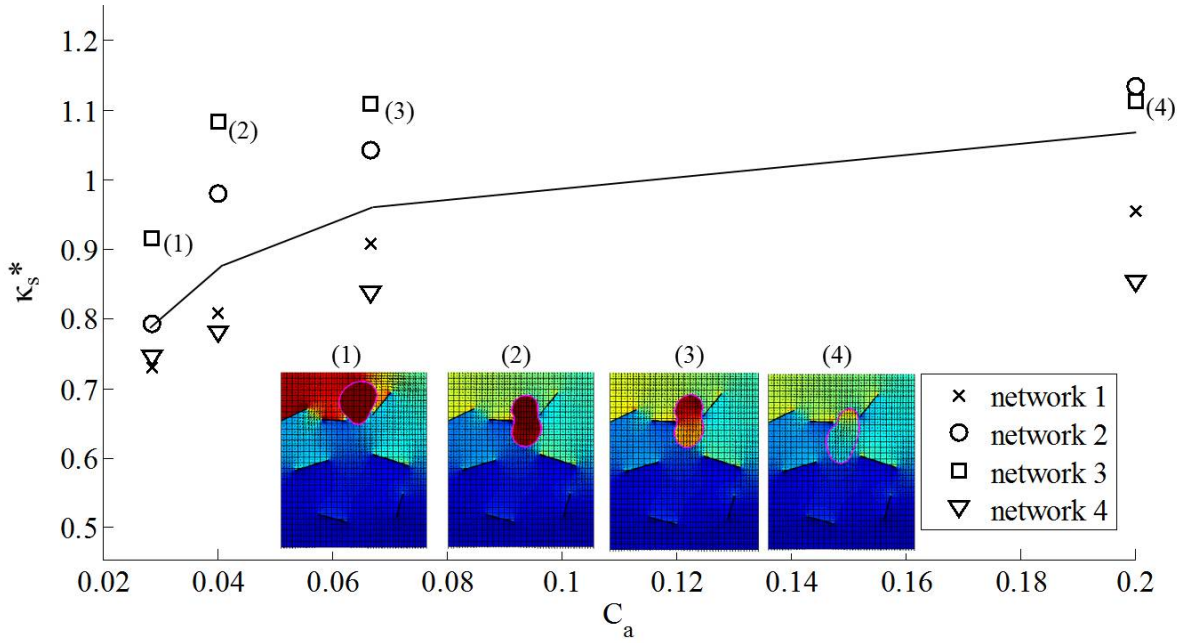

Figure 4.9: *Fluid permeability as a function of the capillary number* $C_a = \frac{\mu U}{\gamma}$

4.4 Summary and future work

We have described a new numerical modeling approach that can be used to quantitatively examine the interplay between a rigid media's structure, the surface energy of deformable, immiscible, suspended particles (vesicles), and an externally imposed continuum flow, on the particles' conductance through that media. The novelty of the approach is two-fold: (a) the inclusion of locally-explicit continuum solutions for the pressure and velocity fields that eliminate the need for the computational cost of mesh refinement and (b) the derivation of a numerical homogenization scheme that permits to calculate the macroscopic permeabilities of a fibrous network for complex fluids. We have illustrated the usefulness of the approach by performing a study on an idealized two-dimensional problem containing deformable, "cylindrical-shaped" vesicles being transported in a simple fluid through a media containing rigid flakes (which project as "fibers" in our 2-d problem). The major macroscopic figures-of-merit were the permeability coefficients of the continuous fluid and the vesicles. For the range of parameters studied, our results have illustrated that vesicles are always retarded relative to the continuum flow, and that the relative selectivity for the continuum versus the vesicle is inversely proportional to

the Capillary number (based on the vesicle's surface energy relative to the continuum fluid). Overall, these results show the capability of the proposed approach to both accurately describe the micro-scale physics of a vesicle permeation, and their effects at the macroscale in terms of effective permeability estimations. A number of improvements is however necessary to increase the fidelity of the models. First, a thorough study of the physical interaction between fibers and vesicles must be carried out. For instance, the consideration of a repulsive force between the two entities in the proposed study ultimately facilitated the flow of vesicles away from fibers. In an alternate case, where fiber-vesicle adhesion occurs, one may predict very different behaviors [41]. Our two-dimensional (2D) assumptions may also drastically affect the overall behavior of the system for several reasons. First, in 3D, one might expect a lower flow resistance from the fibers, but an increase in fiber-fiber connections, which might act as traps for vesicles. On the other hand, 3D vesicles possess more deformation potential to escape from these obstacles. From a modeling viewpoint, the proposed computational scheme is applicable in 3D although it is not straightforward. Asympotic flows around fibers and the deformation of 3D vesicles are indeed significantly more complex than in a 2D setting, involving numerous theoretical and numerical challenges. Such research endeavors are however necessary as a fundamental undertanding of the interactions between soft vesicles and porous media can help design new membranes for medical and energy applications [70, 2], but also help understand fundamental problems in biology such as the interactions between cells and their surrounding fibrous matrix [62, 159, 166].

Appendix A

Using the spatial discretization scheme from section 3, the components of the matrix $\mathbf{k}^e$ and vector $\mathbf{f}^e$ take the following form:

$$\mathbf{k_{vv}} = \int_{\Omega^e} \mu \mathbf{B}^T \cdot \mathbf{B}\ d\Omega \tag{4.46a}$$

$$\mathbf{k}^e_{\mathbf{v}p} = \int_{\Omega^e} -\mathbf{B}^T \cdot \hat{\mathbf{N}}\ d\Omega \tag{4.46b}$$

$$\mathbf{k}^e_{\mathbf{v}\lambda} = \int_{\Gamma^e} \mathbf{N}^T \cdot \bar{\mathbf{N}} d\Gamma \tag{4.46c}$$

$$\mathbf{k}^e_{p\mathbf{v}} = \int_{\Omega^e} \hat{\mathbf{N}}^T \cdot \mathbf{B}\ d\Omega \tag{4.46d}$$

$$\mathbf{k}^e_{\lambda\mathbf{v}} = \int_{\Gamma^e} \bar{\mathbf{N}}^T \cdot \mathbf{N} d\Gamma \tag{4.46e}$$

$$\mathbf{k}^e_{\lambda_p p} = \int_{\Gamma^e} \bar{\mathbf{N}}^T \cdot \hat{\mathbf{N}} d\Gamma \tag{4.46f}$$

$$\mathbf{k}^e_{p\lambda_p} = \int_{\Gamma^e} \hat{\mathbf{N}}^T \cdot \bar{\mathbf{N}} d\Gamma \tag{4.46g}$$

and

$$\mathbf{f}^e_{\mathbf{v}} = \int_{\Omega^e} \mathbf{N}^T \cdot \rho \mathbf{f}\ d\Omega + \int_{\Gamma^e} \mathbf{N}^T \cdot (\mathbf{f}_I + \mathbf{f}_{R/I})\ d\Gamma. \tag{4.47}$$

$$\mathbf{f}^e_{\lambda_p} = \int_{\Gamma^e} \bar{\mathbf{N}}^T \mathbf{n} \cdot (\mathbf{f}_I + \mathbf{f}_{R/I})\ d\Gamma. \tag{4.48}$$

The shape function matrices $\mathbf{N}$, $\hat{\mathbf{N}}$, $\hat{\mathbf{N}}$ and $\mathbf{B}$ take the following form:

$$\mathbf{N} = \left[\mathbf{N}^1, ..., \mathbf{N}^9, \tilde{\mathbf{N}}^1, ..., \tilde{\mathbf{N}}^9\right] \tag{4.49a}$$

$$\hat{\mathbf{N}} = \left[\hat{N}^1, ..., \hat{N}^4, \check{\hat{N}}^1, ..., \check{\hat{N}}^4, \tilde{\hat{N}}^1, ..., \tilde{\hat{N}}^4\right] \tag{4.49b}$$

$$\bar{\mathbf{N}} = \left[\bar{N}^1\ \bar{N}^2\right] \tag{4.49c}$$

$$\mathbf{B} = \left[\mathbf{B}^1, ..., \mathbf{B}^9, \tilde{\mathbf{B}}^1, ..., \tilde{\mathbf{B}}^9\right] \tag{4.49d}$$

with

$$\mathbf{N}^i = \begin{bmatrix} N^i & 0 \\ 0 & N^i \end{bmatrix} \quad , \quad \tilde{\mathbf{N}}^i = \left[(F - F^1) \begin{bmatrix} N^i & 0 \\ 0 & N^i \end{bmatrix}, ..., (F - F^8) \begin{bmatrix} N^i & 0 \\ 0 & N^i \end{bmatrix} \right] \tag{4.50a}$$

$$\check{N}^i = (H - H^i)\hat{N}^i \quad , \quad \tilde{\check{N}}^i = \left[(G - G^1)\hat{N}^i, ..., (G - G^4)\hat{N}^i \right] \tag{4.50b}$$

$$\mathbf{B}^i = \begin{bmatrix} N^i_{,1} & 0 \\ 0 & N^i_{,2} \\ N^i_{,2} & 0 \\ 0 & N^i_{,1} \end{bmatrix} \tag{4.50c}$$

$$\tilde{\mathbf{B}}^i = \left[\begin{bmatrix} (F - F^1)N^i)_{,1} & 0 \\ 0 & (F - F^1)N^i)_{,2} \\ (F - F^1)N^i)_{,2} & 0 \\ 0 & (F - F^1)N^i)_{,1} \end{bmatrix}, ..., \begin{bmatrix} (F - F^8)N^i)_{,1} & 0 \\ 0 & (F - F^8)N^i)_{,2} \\ (F - F^8)N^i)_{,2} & 0 \\ 0 & (F - F^8)N^i)_{,1} \end{bmatrix} \right]. \tag{4.50d}$$

where F^i and G^i are the asymptotic functions used to enriched the standard finite element space around the corner tips introduced earlier.

Chapter 5

Applications of the Immersed Membrane formulation to the study of the membrane-cortex complex

In this chapter we use the formulation presented in chapter two to describe the rich mechanics and interactions between the cell membrane and cortex and between the membrane and the external environment. The formulation takes into account the mechanics of both the lipid bilayer membrane and the cortex as well as their interactions. We show that these considerations are of critical importance in situations that lead to debonding between the two the membrane and the cortex, as it is the case in the cell blebbing problem for example. The formulation is then coupled with the Extended Finite Element Method (X-FEM), a numerical method that naturally allows for pressure and velocity discontinuities across the membrane, and the grid bases particle method that allows us to accurately track the membrane geometry and large deformations as it evolves in a Eulerian frame.

The outline of this chapter is as follows: first we provide a biological and mechanical description of the MCC, and introduce the main constitutive equations. In section 5.1, the mathematical formulation used to describe the membrane mechanics, membrane-cortex interactions, and the membrane-fluid interactions in a Eulerian framework is presented, followed with the derivation

of the governing equations from energetic considerations. Section 5.2 discusses the numerical implementation in the framework of the X-FEM and the grid based particle method. In section 5.3, the problems of the cell blebbing and the cell endocytosis are investigated to demonstrate the model's abilities to describe the rich mechanics of the MCC. Section 5.4 finally concludes with a discussion of the results and recommendations for future improvements.

5.1 The physics of the membrane-cortex complex and its interactions

In many biological problems such as endocytosis, blebbing or the red blood cell biconcavity, the evolution of the shape the cell is driven by the mechanics of the cell membrane and its interaction and adhesion with surrounding fluids or objects. In order to understand the debonding that occurs during cell blebbing between the membrane and the cortex, or the intake by the cell membrane of nanoparticles during endocytosis, one must therefore first investigate the mechanics of each component as well as the forces responsible for their interactions.

5.1.1 The mechanics of the membrane-cortex complex

In most cells the membrane consists of the juxtaposition of two layers: the lipid bilayer and the cortex, often refereed as the membrane-cortex complex. The lipid bilayer itself is made of a double layer of phospholipids, whose hydrophylic heads point outside of the membrane and hydrophobic tails point in to the core of the membrane. Attached to the lipid bilayer via membrane-cortex attachment proteins is the cortex, composed of a mesh of actin/myosin/spectrin filaments that provides the cell with resistance to deformations and possesses contractile abilities [32] (Fig.5.1.). The membrane-cortex complex is generally viewed as an elastic membrane with values of stretching and bending stiffnesses that vary with the type of cell considered. For example, a leukocyte (or white blood cell) has reserves of membrane area stored in microfolds that reduce its stretching stiffness whereas the membrane of a erythrocyte (or red blood cell) has no such reserves and is assumed in most studies to be essentially inextensible (maximum area change $\leq 4\%$ [133]). Some biological processes, such as cell blebbing can lead to debonding

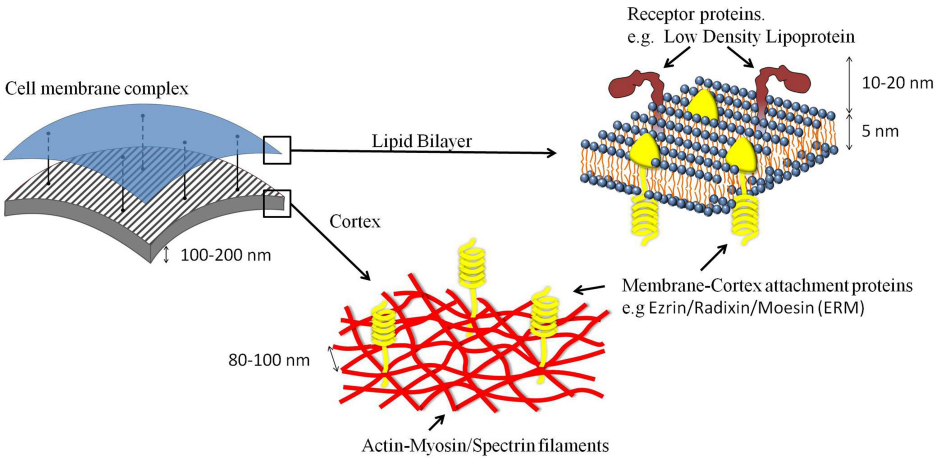

Figure 5.1: *Global scheme of the cell membrane with the detailed parts of the cortex and the lipid bilayer*

between the cortex and the lipid bilayer by rupturing the membrane-cortex attachment proteins. In this context, the cortex and the lipid bilayer become two separate membranes with different parameters of elasticity. The mechanical characteristics of the membrane also vary with the scale of the problem considered: in the case of endocytosis, only the lipid bilayer mechanics are relevant in the uptake of nanoparticles by the cell membrane since the spacing between the cortical filament (200 nm) is much larger than the size of the particles ($10 - 20\,\text{nm}$). Here, we propose to model the MCC, the cortex and the lipid bilayer as elastic membranes with different elasticies. In this view, let us consider a generic elastic membrane (that can be the MCC, the cortex or the lipid bilayer) whose geometry is characterized by a thickness negligible compared to its other dimensions. The analysis of this membrane can then be viewed as a multiscale problem. At the microscale, the membrane is described as a thin layer of thickness h with a elastic energy density W, function of the membrane strain $\mathbf{E}$ that varies along the membrane thickness. At the mesoscale, the membrane is considered as a zero-thickness surface in which the strain $\mathbf{E} = \mathbf{E}\left(\bar{\mathbf{E}}^{ip}, \bar{\mathbf{C}}^{ip}\right)$ and the elastic energy density $\bar{\Phi} = \bar{\Phi}\left(\bar{\mathbf{E}}^{ip}, \bar{\mathbf{C}}^{ip}\right)$ can be approximated as functions of the membrane in-plane strain $\bar{\mathbf{E}}^{ip}$ and second fundamental form $\bar{\mathbf{C}}^{ip}$. An averaging operation is then introduced in order to reconcile the microscopic and mesoscopic descriptions of the membrane, such that the elastic energy and densities at the two scales are related as follows

[164]:

$$\bar{\Phi} = \frac{1}{h}\int_{-h/2}^{h/2} \bar{\Phi} dr_3 \quad \text{and} \quad \tilde{\rho} = \frac{1}{h}\int_{-h/2}^{h/2} \rho dr_3 \tag{5.1}$$

Although the formulation allows for more complex strain energy functions, we here concentrate on a linear elastic material with a quadratic elastic energy density function:

$$\bar{\Phi}(\bar{\mathbf{E}}^{ip}, \bar{\mathbf{C}}^{ip}) = \bar{\Phi}^0 + \underbrace{\mathbf{T}^0 : \bar{\mathbf{E}}^{ip} + \frac{1}{2}\bar{\mathbf{E}}^{ip} : \boldsymbol{\mathcal{C}} : \bar{\mathbf{E}}^{ip}}_{\text{strain energy}} + \underbrace{\mathbf{M}^0 : \bar{\mathbf{C}}^{ip} + \frac{1}{2}\mathbf{C}^{ip} : \boldsymbol{\mathcal{D}} : \bar{\mathbf{C}}^{ip}}_{\text{bending energy}} + \underbrace{\bar{\mathbf{E}}^{ip} : \boldsymbol{\mathcal{F}} : \bar{\mathbf{C}}^{ip}}_{\text{mixed}} \tag{5.2}$$

where W_0 is the initial energy (per mass) stored in the membrane when undeformed, $\mathbf{T}^0$ and $\mathbf{M}^0$ are the pre-stress and pre-moment and the fourth order tensor $\boldsymbol{\mathcal{C}}$ is the elasticity tensor. In addition, the tensors $\boldsymbol{\mathcal{D}}$ and $\boldsymbol{\mathcal{F}}$ (also fourth order) characterize the resistance to bending and the interaction between the two modes of deformation $\bar{\mathbf{E}}^{ip}$ and $\bar{\mathbf{C}}^{ip}$. For the sake of clarity and as it does not introduces major changes, the interaction between the different deformation modes are neglected by choosing $\boldsymbol{\mathcal{F}} = 0$. Let us now detail the elastic parameters used in the strain and bending energy for the cortex and the lipid bilayer:

Strain energy. The cortex is idealized as a permeable isotropic linear elastic membrane with contractile abilities. The pre-stress $\mathbf{T}^0$ can therefore be directly related to the surface tension created by the contraction of the acto-myosin complexes that are present throughout the cortex. Furthermore, for a linear elastic material the elasticity tensor is written as $\boldsymbol{\mathcal{C}} = \bar{\lambda}\mathbf{1} \otimes \mathbf{1} + 2\bar{\mu}\mathbf{I}$, with $\bar{\lambda}$ and $\bar{\mu}$ the first and second Lamé coefficients. On the other hand, the lipid bilayer is usually described as a surface fluid with no resistance to shear forces but high resistance to surface dilation. This behavior can be modelled by choosing an incompressible linear elastic material (but not inextensible, since the lipid bilayer can sustain around 4% of surface dilation) where the first and second Lamé coefficient are respectively equal to the bulk modulus $\bar{\lambda} = \bar{K}$ and zero $\bar{\mu} = 0$. However, in certain types of cells such as leukocytes for examples, the presence of undulation of the lipid bilayer over the cortex has been observed. These undulations, stabilized by the membrane-cortex bonds, constitute a reserve of lipid bilayer area (that can

reach up to 2.6 time the apparent area in some white blood cells) that impart the membrane with a non-linear elastic behavior and allow it to endure deformations much larger than 4% in processes such a cell blebbing. A constitutive relation between the membrane tension and the membrane increase of area was introduced in [133] as:

$$\epsilon = \frac{\Delta A}{A_0} = \frac{k_b T}{8\pi k_c} ln\left(1 + \frac{c\tau_m A}{K_h^{lipid}}\right) + \frac{\tau_m}{K_A} \tag{5.3}$$

with $\epsilon = \frac{\Delta A}{A_0}$ the membrane dilation or relative increase of apparent area, K_A the elastic modulus for direct stretchm, k_bT the thermal energy, c=0.1 reflects the type of modes used to describe the undulations and τ_m the membrane tension. Eq.5.3 has two main regimes: for low values of area increase, the membrane stiffness remains low and increases logarithmically, which corresponds to the smoothing of the membrane undulations. For higher values of area increase,

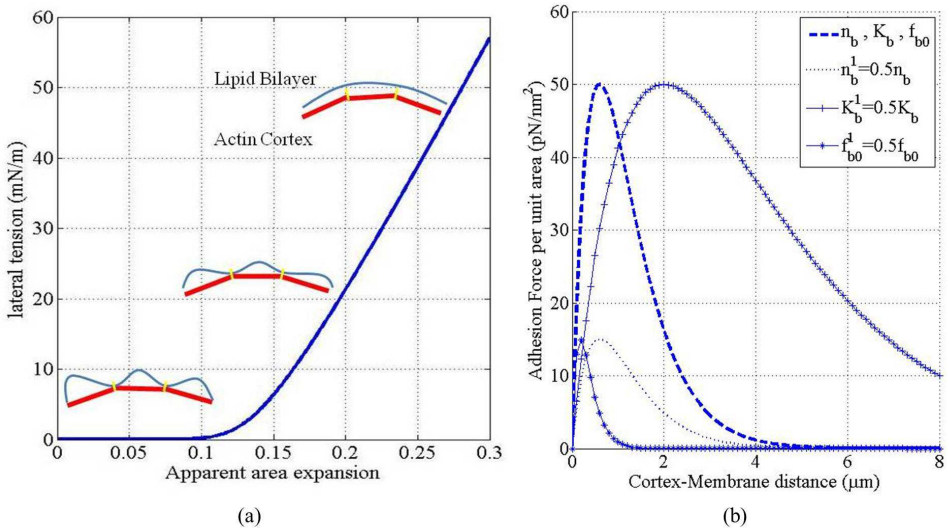

Figure 5.2: *Fig (a) shows the tension-dilation curve for the unfolding membrane [133]. In Fig (b) we see the behaviour of the function* $\mathbf{f}_b$ *for different values of parameters* K_b, f_b0 *and* n_b.

the lipid bilayer is completely smoothed out and enters a pure stretch regime, that is governed by an elastic linear relationship with a much higher elastic modulus, making the lipid bilayer essentially inextensible (Fig.5.2a). From equation (5.3), one can find the lipid bilayer non-linear bulk modulus $\bar{\lambda}(\epsilon) = \bar{K}(\epsilon)$ such that $\tau_m = \bar{K}(\epsilon)\epsilon$. Finally, the pre-stress $\mathbf{T}^0$ is taken to be zero in the case of the lipid bilayer since it has not been shown to exhibit contractile abilities.

Bending energy. For both the cortex and the lipid bilayer, we choose to use the widely accepted Canham-Helfrich bending energy, with different bending stiffnesses as the cortex offers a greater resistance to bending than the lipid bilayer. The Canham-Helfrich energy is written $E_h(\bar{\mathbf{C}}^{ip}) = K_h/2(H - C_0)^2 + K_g K$ with H and K the mean and Gauss curvatures, K_h and K_g the bending parameters and C_0 the spontaneous curvature [75]. If the membrane is closed (as it is the case in the different problems considered here), the Gaussian curvature energy $K_g K$ has no contribution and can be discarded.

With the elasticity parameters defined, the elastic energy densities for the cortex and the lipid bilayer now reads:

$$\text{cortex} \quad \bar{\Phi}(\bar{\mathbf{E}}^{ip}, \bar{\mathbf{C}}^{ip}) = \underbrace{\mathbf{T}^0 : \bar{\mathbf{E}}^{ip} + \frac{1}{2}\bar{\mathbf{E}}^{ip} : \boldsymbol{\mathcal{C}} : \bar{\mathbf{E}}^{ip}}_{\text{strain energy}} + \underbrace{\frac{K_h^{cortex}}{2}(H - C_0)^2}_{\text{bending energy}} \tag{5.4}$$

$$\text{lipid bilayer} \quad \bar{\Phi}(\bar{\mathbf{E}}^{ip}, \bar{\mathbf{C}}^{ip}) = \underbrace{1/2\bar{K}\epsilon^2}_{\text{strain energy}} + \underbrace{\frac{K_h^{lipid}}{2}(H - C_0)^2}_{\text{bending energy}} \tag{5.5}$$

where $\epsilon = \operatorname{tr} \bar{\mathbf{E}}^{ip}$ and $H = \operatorname{tr} \bar{\mathbf{C}}^{ip}$. Having defined the strain and bending energy densities of both the cortex and the lipid bilayer membrane, let us now turn to the Membrane-cortex attachment energy to investigate the mechanical behavior of the MCC, and in particular the debonding between the lipid bilayer membrane and the cortex that occurs during cell blebbing.

Membrane-cortex attachment energy. The interaction between the lipid bilayer membrane and the cortex plays a critical role in many cellular processes. Under normal conditions, the lipid bilayer membrane and the cortex are bonds together via an ensemble of attachment proteins or bonds called ERM (Exrin/Radixin/Moesin). However, when subjected to sufficiently large forces, these bonds start disassembling, effectively freeing the lipid bilayer from the cortex. This mechanism is at the origin of the large spherical membrane protrusions, or blebs, observed in cell motility processes for example. Here we propose to model the membrane to

cortex bonds using the following assumptions: (1) the force in one bond follows Hook's law of elasticity: $f_b = K_b d$, with d distance from the bond's resting position, and K_b the elasticity modulus [55, 183], and (2) the bonds probability to disassemble increases exponentially with the force to which the bonds are subjected [17]. To model the later assumption, we choose to use the Weibull probability of failure [179], function of the force in the bond and written as follows: $P(f_b) = 1 - \exp\left(-\frac{f_b}{f_{b0}}\right)$, where f_{b0} is related to the critical force f_{crit} at which the bond starts failing, found to be f_{crit} =5 pN in [25], via the relation $f_{b0} = f_{crit} \exp(1) = 13.5pN$. One can now compute the force per unit area $\mathbf{f}_b$ that binds the lipid bilayer to the cortex as the force in one bond times its probability of failure multiplied by the bonds surface density n_b as follows:

$$\mathbf{f}_b \;=\; f_b n_b \exp\left(-\frac{f_b}{f_{b0}}\right)\bar{\mathbf{n}} \;=\; K_b d\, n_b \exp\left(-\frac{K_b d}{f_{b0}}\right)\bar{\mathbf{n}} \tag{5.6}$$

where $\bar{\mathbf{n}}$ is the unit vector normal to the surface. Using the experimental results from [29] the bonds surface density is found to be $n_b = 100/nm^2$ and the elasticity modulus $K_b = 2.25{\cdot}10^{-2} pN/nm$ is computed from [30] by matching the energy required for debonding. Fig.5.2b shows the behavior of the attachment force for different parameter values: reducing the bond elastic modulus K_b increases the total energy required to break the bonds, whereas decreasing the bond density n_b or the bond critical force f_{b0} has the opposite effect. The membrane-cortex attachment energy (or power) density can then be found as the force $\mathbf{f}_b$ times the membrane-cortex relative displacement (or velocity).

Finally, the MCC total elastic energy is computed as the sum of the lipid bilayer membrane and cortex elastic energy plus the membrane-cortex attachment energy. Lets us now turn to the interaction between the lipid bilayer membrane and the external environment, and in particular to the adhesion forces that allow the cell to intake external particles during the endocytosis process.

5.1.2 Interaction of the membrane with the outer environment

An important aspect of the MCC mechanics is to understand how the cell (and particularly the membrane) senses and interacts with its external environment. Membrane adhesion is at the heart of these interactions and plays a primordial role in the intake of external bodies such as vesicles, viruses or other nanoparticles [18]. This process known as endocytosis is one of the mechanisms the cell uses to absorb particles that are too large to simply diffuse through the lipid bilayer membrane. Here, we choose to focus on the receptor mediated endocytosis that is used by the cell for the uptake of particles with a diameter of the order of tens of nanometers. In this context, the mechanism of endocytosis consists in the wrapping of particles by the lipid bilayer until complete absorption. During this process, two forces are at play and compete against each other: the adhesion between the membrane and the particle and the lipid bilayer bending resistance. If the adhesion that pulls the membrane toward the particle is strong enough to overcome the lipid bilayer bending resistance, the particle becomes completely wrapped and eventually absorbed inside the cell. On the other hand, if the bending resistance is stronger than the adhesion forces, only partial wrapping is observed and the endocytosis process cannot be achieved.

One of the well accepted models for the cell adhesion was proposed by [18], who developed a thermodynamic approach to the cell adhesion. In this work, three main variables are at play: the concentration of free ligand on the particle surface, the concentration of free receptors on the membrane surface, and the number of bound ligand-receptor complexes (Fig.5.3a.). The system's equilibrium is found by minimizing its total free energy ΔG given by:

$$\begin{aligned}\Delta G = &\left[\left(N_r - N_b\right)\left(\mu_r(N_r - N_b)\right) - N_r\left(\mu_r\left(N_r\right)\right)\right] + \\ &+ \left[\left(N_l - N_b\right)\left(\mu_l(N_l - N_b)\right) - N_l\left(\mu_l\left(N_l\right)\right)\right] + \\ &+ N_b\left(\mu_b\left(S, N_b\right)\right) + \Gamma\left(d\right)\end{aligned} \tag{5.7}$$

where N_r, N_l and N_b are the densities (number per unit surface) of free receptors, ligands and bounds respectively, and μ_r, μ_l and μ_b are their chemical potentials. For dilute solutions, the chemical potentials of the free ligands and receptors is equal to the reference chemical potential

plus the entropy of configuration:

$$\mu_\alpha = \mu_\alpha^0 + k_B T \ln\left(N_\alpha - N_b\right) \quad \text{with} \quad \alpha = r, l \tag{5.8}$$

In the case of the bound ligand-receptor complexes however, the free energy also includes the elastic energy that comes from stretching these bonds. Considering the bonds as linear elastic "springs" of stiffness K_{bond} and natural length l_0, the bonds mechano-chemical potential μ_b is written:

$$\mu_b = \mu_b^0 + \frac{1}{2} K_{bond} \left(d - l_0\right)^2 + k_B T \ln\left(N_b\right) \tag{5.9}$$

where d denotes the distance between the membrane and the particle. The term $\Gamma(d)$ in (5.7) was introduced to take into account the Van der Waals repulsive force between the membrane and particle at small distances. This energy depends on a characteristic decay length τ, and on a strength parameter γ as:

$$\Gamma(d) = \frac{\gamma}{d} \exp\left(-\frac{d}{\tau}\right) \tag{5.10}$$

The force produced by the attached complexes must overcome this repulsion in order to be able to uptake the external particle. One can then translate the total free energy (5.7) to a tension $\bar{\mathbf{t}}$ applied on the cell membrane by taking its derivative with respect to the separation distance:

$$\bar{\mathbf{t}} = \frac{\partial \Delta G}{\partial \mathbf{d}} = \left[N_b K_{bond} \left(d - l_0\right) - \frac{\gamma}{d^2 \cdot \tau} \exp\left(\frac{-d}{\tau}\right) (d + \tau) \right] \mathbf{n} \tag{5.11}$$

where $\mathbf{d} = d\mathbf{n}$ and $\mathbf{n}$ is a unit vector normal to the particle surface. The first term of this equation represents the force associated to the bond complex deformation while the latter part represents the repulsion due to the Van der Waals forces. In this chapter and for the sake of simplicity, we consider both the free ligands and receptors to be abundant enough for their concentration to be considered constant and their diffusion instantaneous. However, the concentration of bound ligand-receptor complexes needed to find $\bar{\mathbf{t}}$ in (5.11) varies with time and the separation distance.

The following equation relates the chemical potential of the bound ligand-receptor complexes to their change of concentration [119, 46]:

$$\frac{\partial N_b}{\partial t} = -k_r N_b \left(1 - K_L \exp\left(-\frac{1}{2}\frac{K_{bond}\left(d - l_0\right)^2}{k_B T}\right)\frac{\left(N_r - N_b\right)\left(N_l - N_b\right)}{N_b}\right) \tag{5.12}$$

Since the evolution of the membrane is much slower then the ligands/receptors binding rate, we are only interested in the stationary solution of the above equation, which is given by:

$$N_b = K_L \exp\left(\frac{-K_{bond}(d - l_0)^2}{2k_B T}\right)(N_r - N_b)(N_l - N_b) \tag{5.13}$$

Once the number of bound complexes is known, the adhesion force can be calculated for any distance and time. Figure 5.3b shows the steady state of (5.11) for different distances between the particle and the membrane. For large distances, the receptors and ligands are not able

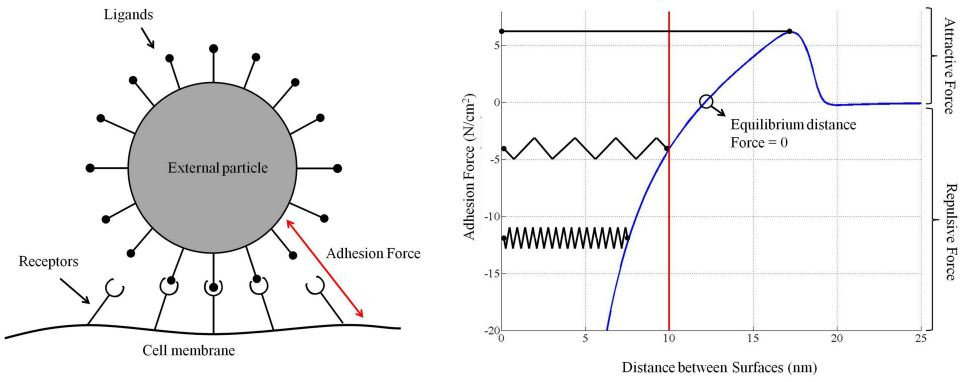

Figure 5.3: *Equilibrium force for different fixed distances*

to attach and there is no interaction between the particle and the membrane. As they come closer together, a few receptors are able to attach to the particle's ligands and act as stretched springs exerting an attractive force between the membrane and the particle. As the process unfolds, the bonds concentration increases and the membrane wraps around the particle until complete absorption. With the interaction forces $\mathbf{f}_b$ and $\bar{\mathbf{t}}$ defined, let us now derive the equations governing the evolution of the MCC.

5.1.3 Governing equations for the MCC problem

Consider a two-dimensional incompressible viscous flow in the domain Ω delimited by a boundary $\partial\Omega$ in which exists a closed MCC, where the cortex Γ_c and lipid bilayer Γ_l that are able to move with the surrounding fluid. The problem is characterized by the Reynolds number $\mathcal{R}_e = HV\rho/\mu$ where H is the characteristic length scale, V the characteristic fluid velocity, μ the kinematic viscosity and ρ the fluid densities in and out of the MCC. We choose here to remain in the Stokes flow assumption with $\mathcal{R}_e \ll 1$, where inertial effect may be neglected. The velocity of a fluid particle is given in terms of its material time derivative $\mathbf{v}(\mathbf{x}, t) = D\mathbf{x}/Dt$, where $\mathbf{x}$ is the current position of the fluid particle at time t. Similarly to the case of a single vesicle in chapter 1, the governing equations and boundary conditions for the Stokes flow are written:

$$\nabla \cdot \boldsymbol{\sigma} = \mathbf{0} \qquad \forall \mathbf{x} \in \Omega/\Gamma \tag{5.14}$$

$$\nabla \cdot \mathbf{v} = 0 \qquad \forall \mathbf{x} \in \Omega/\Gamma \tag{5.15}$$

where $\boldsymbol{\sigma}$ is the Cauchy stress tensor in the fluid and the second equation imposes the condition of incompressibility. These equations are combined with the governing equations of the lipid bilayer Γ_l:

$$[\boldsymbol{\sigma} \cdot \bar{\mathbf{n}}] = \bar{\mathbf{f}}_l - \bar{\mathbf{t}} - \bar{\mathbf{f}}_b \qquad \forall \mathbf{x} \in \Gamma_l \tag{5.16}$$

$$(\boldsymbol{\sigma} \cdot \bar{\mathbf{n}})^{\parallel\pm} = \frac{\mu}{l^{\pm}}[\mathbf{v}]^{\parallel\pm} \qquad \forall \mathbf{x} \in \Gamma_l \tag{5.17}$$

$$\frac{d\mathbf{r_l}(\xi^{\mathbf{1}}, \xi^{\mathbf{2}}, \mathbf{t})}{dt} = \bar{\mathbf{v}}(\xi^1, \xi^2, t) \tag{5.18}$$

and on the cortex Γ_c:

$$\bar{\mathbf{f}}_c + \bar{\mathbf{f}}_b = 0 \qquad \forall \mathbf{x} \in \Gamma_c \tag{5.19}$$

$$\frac{d\mathbf{r_c}(\xi^{\mathbf{1}}, \xi^{\mathbf{2}}, \mathbf{t})}{dt} = \bar{\mathbf{v}}(\xi^1, \xi^2, t) \tag{5.20}$$

where the forces $\mathbf{f_l}$ and $\mathbf{f_c}$ are the unbalanced forces due to the deformation of the lipid bilayer and the cortex respectively, and $\mathbf{r}_l, \mathbf{r}_c$ denote the position of the lipid bilayer and cortex. Equation

(5.17) is the Navier boundary conditions at the interface, where $l^{\pm} > 0$ is known as the slip length, a physical parameter that depends on the surface roughness. The case $l = 0$ corresponds to the no slip condition while $l = \infty$ is the free sleep condition between the fluid and the lipid bilayer.

5.2 Examples

5.2.1 Cell endocytosis

The cell endocytosis is currently being studied in different areas such as the creation of new drug delivery tools or the allergies control. Different investigations proved that there is a close dependence between the size and shape of the nanoparticle and the rate of endocytosis, explaining why different particles have more or less affinity to be uptaken. In this section, we show that our model is able to represent the endocytosis of a single nanoparticle, and could be used in the future to investigate the effect of different factors such as particles shape and elasticity.

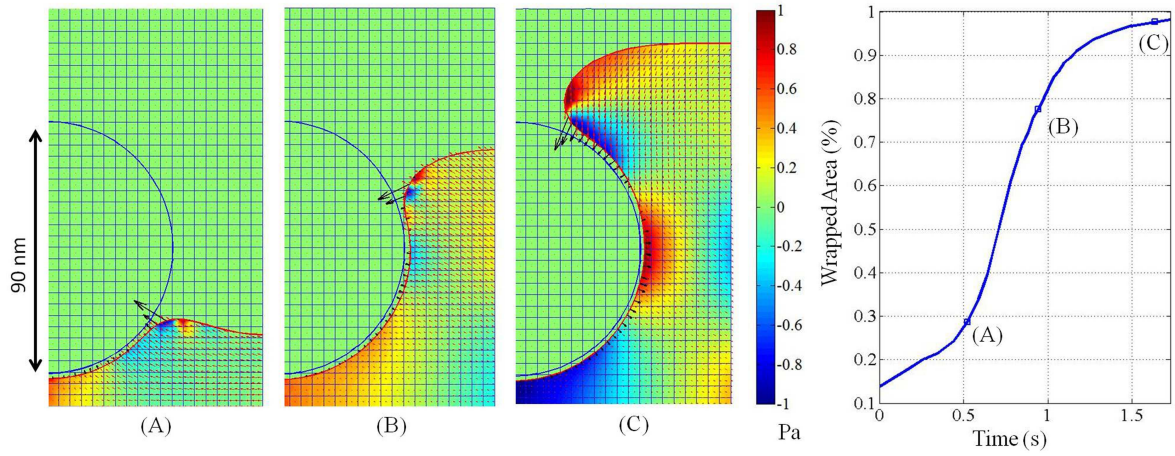

Figure 5.4: *The evolution of the cell membrane around a nanoparticle of 45 nm in Radius. Figures A, B and C represent the pressure and velocity field of the fluid in different moments of the endocytosis. The last one is the evolution of the wrapped area with the time. The values of the different parameters are* K_{bond}=$2 \cdot 10^{-3} N/m$, l_0=$10nm$, $N_r = 5 \cdot 10^{-3} 1/nm^2$, N_l=$5 \cdot 10^{-}31/nm^2$, K_L=$10^9 nm^2$, k_BT=$4.1e-21J$, τ=$5nm$ *and* γ= $1\ pN$

The case of endocytosis being studied here involves the uptake of a single, rigid particle in the range of tens of nanometers in diameter. At this scale, the cell membrane can be represented as

a flat surface since the cell is orders of magnitude ($\simeq 50\mu$m) larger than the particle. As a result, we impose a constraint on the membrane on the right edge of the (axysimmetric) computational domain to ensure that the membrane remains flat away from the particle. Moreover, both the membrane and the cytosol can flow freely in and out of bottom and right edges of the computational domain. This choice of boundary conditions is motivated by the fact that a nano particle only displaces an infinitesimal portion of the total cell volume, and that the membrane has enough area reserves to wrap around the particle without being stretched (the membrane stays in the unfolding regime). In figure (5.4) shows the evolution of a cell membrane around a particle of 45 nm in radius. The blue line is a level set function representing the nano-particle, while the red line is a second level set representing the cell membrane. The adhesion force represented by the black arrows is shown to be much larger in the leading edge of the membrane as it uptakes the particle.

A critical question in the cell endocytosis problem is to find the minimal particle size for a complete particle uptake. When a spherical particle is considered, most studies agree that the minimum radius for complete wrapping lies between 20-25 nm [33],[65],[187],[184],[185]. Figure 5.5 shows how the total wrapped area in the steady state increases with the size of the particle. This is explained by the fact that curvature, and therefore the bending energy decrease with the size of the particle, allowing the adhesion force to push the membrane higher around the particle, until complete wrapping occurs. Our simulations predict that this occurs for a particle radius of around 22-23 nm, which is in good agreement with experiments and other studies such as [44] and [65].

5.2.2 Cell Blebbing

The blebbing of a cell has been shown to be involved in the spreading of cancerous cell as an alternative mechanism of motility [155, 56, 32]. The typical evolution of a bleb may be describe in the following manner [31]. First, the cell cortex generates surface tension by contracting itself via the acto-myosin mechanism that leads to an increase of the internal pressure in the cytosol. This first stage can then be followed by two possible outcomes : the rupture of the actin cortex, or delamination of the cell membrane, i.e. the debonding between the lipid bilayer and the

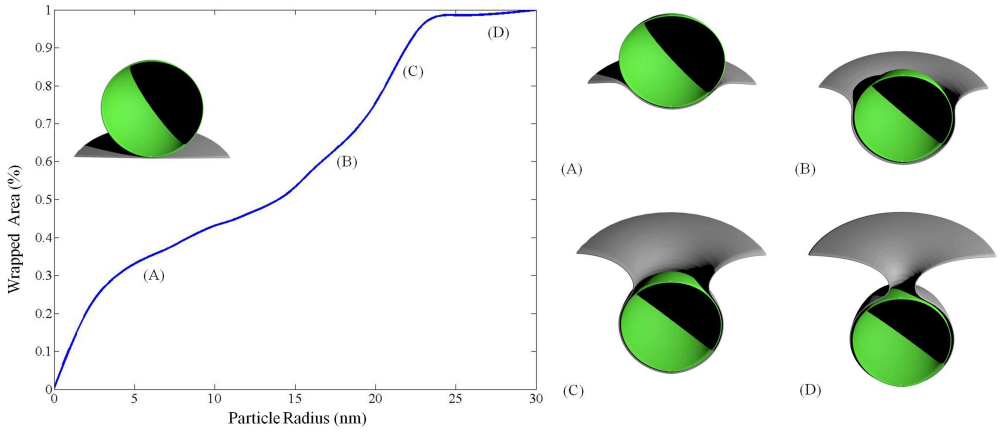

Figure 5.5: *Percentage of particle area wrapped by the membrane as a function of the particle size.*

cortex. Both of these outcomes produce a local decrease of pressure at the rim of the cell which drives cytosol into that region and initiate bleb growth. As bleb grows (the growth time is in order of the minute), the actin cortex starts reassembling beneath the bleb membrane. The newly formed actin cortex in the bleb region generates tangential contraction ($\mathbf{T}_0$) that locally raises the pressure in the bleb, effectively slowing down the growth and reversing the process. This last stage is known as bleb retraction and ends once the bleb has disappeared [31].

Numerically, this process can be described by introducing two level-set functions associated with the debonding lipid bilayer and cortex. The interactions between the two level-set are governed by the membrane-cortex binding force $\mathbf{f}_b$ given in equation (5.6). This force is not homogeneous throughout the cell surface, in fact its heterogeneity is responsible of the bleb initiation: as the cortex increases the cell's internal pressure, the debonding between the lipid bilayer and the cortex starts in the cell region that has the lowest binder concentration.

Figure 5.6a shows the evolution of the blebbing process from the bleb initiation to its retraction, while figure 5.6b shows the relationship between the cell cortex contractile tension and the resulting bleb volume. The results compare qualitatively with the experimental data by [155], however the simulations show bigger volumes of blebs. This could be explained by the fact that the experiments in [155] uses a pipette to create the bleb, adding friction energy on the pipette's wall that potentially reduces the bleb sizes. While the bleb is growing, the cell

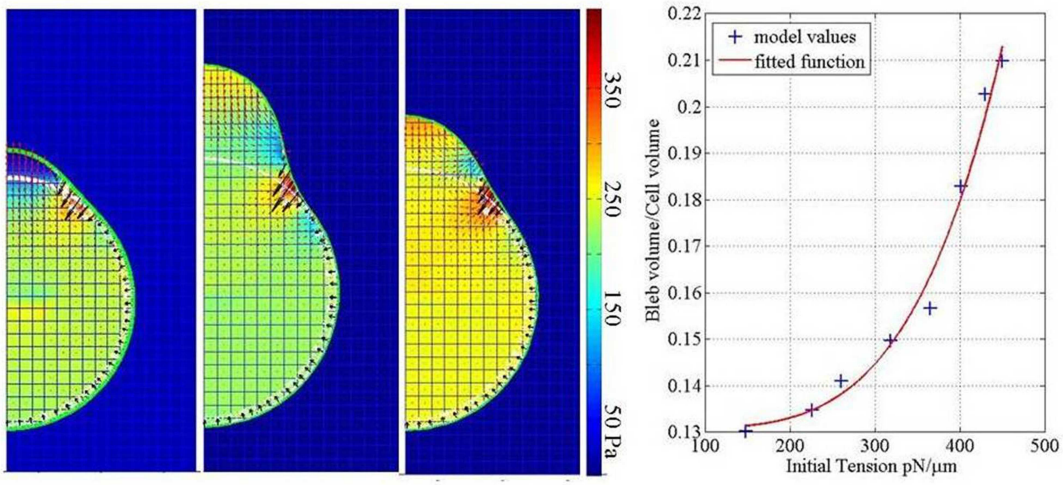

(a) (b)

Figure 5.6: *(a) evolution of the blebbing process. The white arrows deonte the adhesion force between the cortex and the membrane. (b) bleb volume as a function of cortical tension*

membrane stretches so that its surface increases up to 2.6 times its initial surface [30] thanks to the mechanism of undulations unfolding described in part 2.2 . Here we assume the cell membrane stays in the unfolding regime and therefore offers very small resistance to stretching. Let us now turn to the retraction phase of the blebbing process. The reconstruction of the bleb cortex is led by the polymerisation of actin monomers (associated with myosin) into contractile filaments described by the following equation [92, 177, 24]:

$$C_p(t) = C_{m0}(1 - \exp(-k_1 C_{m0} t) \tag{5.21}$$

where C_p is the polymerized actin concentration, C_{m0} the initial actin monomer concentration with $C_{m0} = 0.6\ \mu$ and $k_1 = 12\ \mu\ M^{-1}\ s^{-1}$ is the polymerization rate [157]. The cortex contraction can then be found as follows:

$$\gamma_c = \gamma_{c0} \frac{C_p}{C_{m0}} \tag{5.22}$$

where $\gamma_{c0} = 1000 pN/\mu m$ is the maximum cortex tension [154]. This equation assumes that the cortex tension is directly proportional to the actin/myosin concentration. The following

figure shows the surface of the bleb with three different values of polymerisation rates. As expected, we observe that a higher polymerisation rate results in a smaller bleb and a faster retraction (Fig.5.7). Here we have shown that the proposed formulation is able to capture the

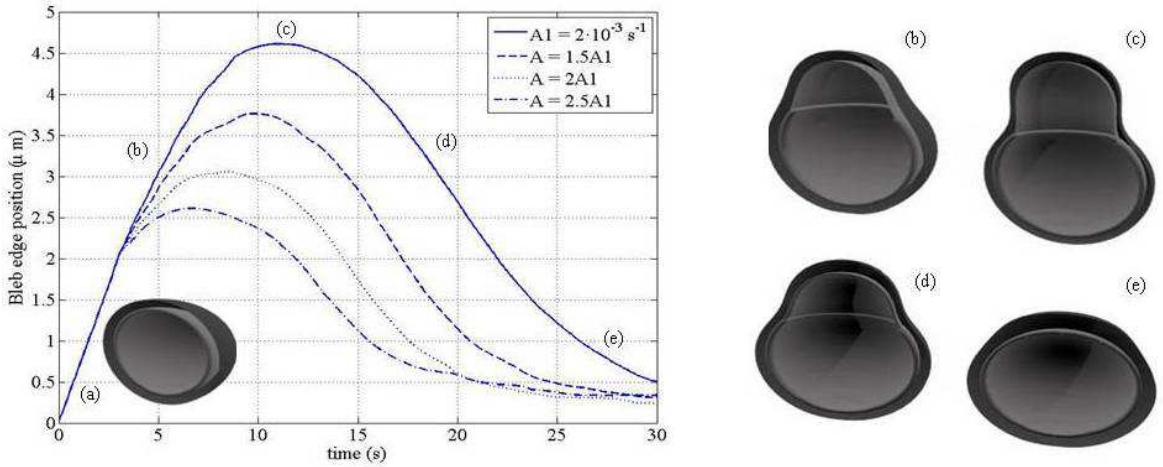

Figure 5.7: *Bleb evolution for different values of actin polymerization rates.*

basic stages of bleb growth and retraction, including the large deformations inherent to the cell blebbing problem, based on a simplified model of retraction. However, better descriptions of actin polymerization can later be incorporated, such as a thermodynamical model of actin polymerisation that depends on the strains in the bleb [62].

5.3 Conclusion

In this chapter, we presented a full Eulerian formulation for the analysis of the fluid-membrane problem, coupled with X-FEM, a numerical method that allows a natural implementation of velocity and pressure discontinuities across the membrane, and the grid based particle that tracks the geometry and large deformations of the MCC. We showed that the formulation is capable of reproducing different equilibrium shapes exhibited by the red blood cell, and can handle the very large deformations experienced by the membrane in the endocytosis and blebbing problems. This is the first formulation capable of fully describing the mechanics of the MCC, including the membrane-cortex debonding, and can be used with more detailed models of actin polymerization or adhesion forces in order to describe biological problems in a way that is both biologically and

mechanically accurate.

One of the advantages of the full Eulerian method presented here is the complete absence of mesh distortion that is inherent to a Lagrangian description of large deformations. Furthermore, the coupling of the formulation with a finite element method that permits discontinous fields in elements cut by the membrane enables an easy enforcement of a wide variety of boundary conditions on the membrane. In the present state, the finite element mesh size is limited by the maximum curvature along the membrane. Using a curvature based refinement algorithm (easy to implement on a fixed structured mesh, and naturally compatible with the grid based particle method) could greatly improve the method's performance by coarsening or refining the mesh in regions of low or high curvature respectively.

Chapter 6

Tutorial for the PMIM

In this chapter, we will describe a simplified version of the PMIM that simulates a fluid droplet resting on a flat surface and deforming under the action of gravitational forces. Large sections of the Matlab code "surface_tension.m" will be cited and put into context. The code can be found at the following address: http://vernereygroup.wordpress.com/

6.1 Initialization

Before all the parameters and geometry of the interface and fluids at time t=0 are initialized, the lines `matlabpool close force local` and `matlabpool open 4` first open a pool of processors (in this example, a pool of 4 processors is open) that will be used and the parallelized sections of the code, such as the computation of the stiffness matrix **K**. Next, the mesh size and initial position of the droplet are defined as shown below:

```
1 % ++++++++++++++++++++++++++++++
2 %              INPUT
3 % ++++++++++++++++++++++++++++++
4
5 % Initial level-set radius and center and number of elements
6
7 plane_axi = 'axi1'; %plane_axi = 'axi1' : axisymmetric problem
```

```
8                       %plane_axi = 'plane' : plane strain problem
9   switch plane_axi
10      case 'axi1'
11          % Dimension of the domain (it is simply a rectangular region Lx x Ly)
12          element_y = 60; %number of nodes in y direction
13          element_x = 40; %number of nodes in x direction
14
15          element_length = 0.1;
16
17          Ly = element_y*element_length/2 ; %y
18          Lx = element_x*element_length/2; %x
19
20          R2 = 1.01; %droplet radius
21          c2 = [-Lx/2 0]; %position of the droplet center
22
23          close_DBC2=0;
24      case 'plane'
25          % Dimension of the domain (it is simply a rectangular region Lx x Ly)
26          element_y = 80; %number of nodes in y direction
27          element_x = 100; %number of nodes in x direction
28
29          element_length = 0.1;
30
31          Ly = element_y*element_length/2 ; %y
32          Lx = element_x*element_length/2; %x
33
34          R2 = Ly/2-0.521; %droplet radius
35          c2 = [0 0]; %position of the droplet center
36          close_DBC2=1;
37  end
```

The mechanical properties of the interface, the fluid and the interaction between the fluid and the interface are then specified:

```
1   % ++++++++++++++++++++++++++++++ %
```

```
%       Material properties       %
% ++++++++++++++++++++++++++++++ %

%interface mechanical properties:
Kc = 0; %bending rigidity
gamma = 1e-6; %surface tension
nu = 0; %Poisson's ratio
mu_membrane = 0; %first lame parameter
lambda_membrane = 0; %second lame parameter

%fluid mechanical properties:
mu_f_minus = 1e-10; %viscosity indide droplet
mu_f_plus = 1e-10; %viscosity outside droplet
rho = 2e-7; % fluid density

%fluid/interface interaction:
l_plus = 0.00000001*R2; %slip length outside
l_minus = 0.00000001*R2; %slip length inside
```

Given the initial geometry of the system, the next steps consists in generating the fixed finite element mesh that is used to spatially discretize the system. Two superimposed meshes are generated: one with 9-node elements for the velocity

```
% 9-nodes element mesh for velocity
elemType9 = 'Q9' ;
[node9,element9,¬] = meshRectangularRegion(pt1, pt2, pt3, pt4, ...
    nnx9,nny9,elemType9);
```

and one with 4-node elements for the pressure

```
% 4-nodes element mesh for the pressure
elemType4 = 'Q4' ;
[node4,element4,¬] = meshRectangularRegion(pt1, pt2, pt3, pt4, ...
    nnx4,nny4,elemType4);
```

where `pt1, pt2, pt3, pt4` correspond to the four corner points of the computational domain. The levelset function (which stores the signed shortest distance between the nodes of the mesh and the interface) that initially describes the geometry of the droplet is then calculated using the radius and center defined earlier:

```
%---------------------------------%
%compute level set value at nodes%
%---------------------------------%
% circle%
for n=1:numnode9
    Phi92(n) = (((node9(n,1)-c2(1)))^2 + ((node9(n,2)-c2(2)))^2)^(1/2)- R2;
end
```

Knowing the initial level-set function for the droplet allows us to generate particles along the droplet's interface, which will be used to track the interface position and deformation:

```
%---------------------------------%
% initialize Grid Based Particles %
%---------------------------------%

[ Foot_points, n_Foot_points, Active_points] = Init_Foot_points_func( ...
    element_length(1),Phi92,Phi91,enrich_node91,enrich_node92, ...
    Grad_phi_x,Grad_phi_y );
```

where `Foot_points, n_Foot_points, Active_points` respectively denote the coordinates of the particles (referred to here as "Foot points"), the unit vector normal to the interface a each particle, and the nodes from the underlying finite element mesh that were used to define the particles (see section 2.2.3 on the grid based particle method). This concludes the initialization step. Let us now move to steps 1 and 2 as described in chapter 1. Both steps 1 and 2 are nested inside a while loop that goes through iterations in time until the convergence criteria given in

section 2.2.2 are satisfied, as follows:

```
while(errorP>1e-9) || (errorV>0.001*element_length)
    t = t+dt
    %%%%%%%%%%%%%%%%%%%%%%%%%%%%%%%%%%%%%%%%%%%%%%%%%%%%%%%%%%%%%%%%
    %--STEP1: compute the pressure and velocity fields--%
    %%%%%%%%%%%%%%%%%%%%%%%%%%%%%%%%%%%%%%%%%%%%%%%%%%%%%%%%%%%%%%%%

    %%%%%%%%%%%%%%%%%%%%%%%%%%%%%%%%%%%%%%%%%%%%%%%%%%%%%%%%%%%%%%%%%%%%%%%
    %--STEP2: update the interface's position and deformation--%
    %%%%%%%%%%%%%%%%%%%%%%%%%%%%%%%%%%%%%%%%%%%%%%%%%%%%%%%%%%%%%%%%%%%%%%%
end
```

6.2 Step 1: solving the system for the fluid velocity and pressure fields

This steps consists in first computing the stiffness matrices $\mathbf{K}^t$, $\bar{\mathbf{K}}$, $\mathbf{I}_1^t$ and $\mathbf{I}_2^t$ necessary to solve equation (2.26) for the velocity and pressure fields. This is done by looping over each element and computing the element stiffness matrices detailed in the appendix of chapter 2. This process is summarized in the following few lines (modified, simplified and commented version of the actual code to clarify the algorithm):

```
while(errorP>1e-9) || (errorV>0.001*element_length)
    t = t+dt
    %%%%%%%%%%%%%%%%%%%%%%%%%%%%%%%%%%%%%%%%%%%%%%%%%%%%%%%%%%%%%%%%
    %--STEP1: compute the pressure and velocity fields--%
    %%%%%%%%%%%%%%%%%%%%%%%%%%%%%%%%%%%%%%%%%%%%%%%%%%%%%%%%%%%%%%%%

    %initialize K,F%

    for iel=1:numelem9 %loop over the elements
```

```
10
11          %find the connectivity matrix for each element (i.e. the adress of ...
                each degree of freedom that belongs to the element being considered)
12          [sctrBv,sctrBp, sctrBl_plus, sctrBl_minus,sctrBv_m, sctrBlp] = ...
                assembly_fluid_XFEM_ndiscont_v2_parallel(iel,numnode9_local...);
13
14         %The element stiffness matrices are the computed by performing the ...
               integration over each element using a Gauss integration scheme:
15         %*********loop over gauss points************
16         for ix=1:ngp(iel)
17             %computes and sums the value of the element stiffness matrix K at ...
                   each gauss point
18             K_vv = K_vv + Bv'*Bv*mu*W(iel,ix)*det(J0);
19             K_vp = K_vp - Bv'*[Np;Np;0;0]*W(iel,ix)*det(J0);
20             K_pv = K_pv - Np'*B_dot_v*W(iel,ix)*det(J0);
21             Fp = Fp - Np'*Np*se*W(iel,ix)*det(J0);
22             Fv = Fv + Nv'*[0 ; 0 ]*W(iel,ix)*det(J0);
23
24         end
25
26        % Next, the components of the interaction and interface stiffness ...
              matrices I_1, I_2 and \bar{K} are computed if  the element is ...
              crossed by the interface:
27
28        if (ismember(iel,Split_ordered))     % split element
29             %loop over the gauss points to perform the integation along the ...
                   interface
30             for ix = 1 : nogp2(iel)
31
32                 % First, find the interface force \bar{f}
33                 [ force_membrane force_membrane_stretch] = ...
                       find_membrane_force_pt_parallel23(Gpt_proj,Foot_points...
34                 ,n_Foot_points,..);
35
36                 %compute the components of the interface matrix
```

```
37                  K_lpp(:,5:8) = K_lpp(:,5:8) + Nl'*Np(1:4)*Wl2(iel,ix)*J0*r;
38                  K_plp(5:8,:) = K_plp(5:8,:) + Np(1:4)'*Nl*Wl2(iel,ix)*J0*r;
39
40                  %compute the components of the interface force vector
41                  Fv_m = Fv_m + Nl'*(t*force_membrane')*Wl2(iel,ix)*J0*r;
42
43                  Flp  = Flp   + (n_Gpt*(force_membrane + ...
                        force_repulsion)'*Nl')*Wl2(iel,ix)*J0*r;
44
45                  Fv  = Fv   + (n_Gpt*(force_membrane + ...
                        force_repulsion)'*Nv'*n_Gpt')*Wl2(iel,ix)*J0*r;
46              end
47          end
48      end
49      %%%%%%%%%%%%%%%%%%%%%%%%%%%%%%%%%%%%%%%%%%%%%%%%%%%%%%%%%%%%%%%%
50      %--STEP2: update the interface's position and deformation--%
51      %%%%%%%%%%%%%%%%%%%%%%%%%%%%%%%%%%%%%%%%%%%%%%%%%%%%%%%%%%%%%%%%
52  end
```

Once the global stiffness matrix $\mathbf{K} = [\mathbf{K}^t \ \mathbf{I}_1^t; \bar{\mathbf{K}} \ \mathbf{I}_2^t]$ and force vector $\mathbf{F}$ is computed, finding the fluid velocity and pressure fields consists in inverting the matrix $\mathbf{K}$ as follows:

```
1
2   %-----------------------------------%
3   %  solve for velocity and pressure  %
4   %-----------------------------------%
5   d = K\F;
```

At this point, the pressure and velocity field (stored in vector `d` shown above) is known everywhere and can be used to update the position of the interface in step 2 as detailed in the next section.

6.3 Step 2: Updating the position and deformation of the interface

Here we use the velocity field calculated in step 1 to update the interface. This is achieved by moving individually each particle that sample the interface, as described in section 2.2.3:

```
for in =1:length(Active_points)
     Foot_points(in,:) = Foot_points(in,:)+ vel_Foot_points_update(in,:)*dt;
end
```

Finally, in order to keep their repartition homogeneous along the interface, the particles along the interface are ressampled (this step is described in section 2.2.3):

```
%-------------------------------------------------------------------%
% RESAMPLE FOOTPOINTS AND CALCULATE GEOMETRICAL QUANTITIES %
%-------------------------------------------------------------------%

[Active_points, Foot_points,n_Foot_points,..] = ...
    Foot_point_ressampling_v2(Active_points, Foot_points,n_Foot_points..);
```

If the interface is elastic, the deformation measure of the interface also has to be updated as follows:

```
for k = 1:length(Foot_points)
     p = Foot_points(k,:);
     [ d d_cont E Fd Ja] = ...
         find_velocity_gradient_d(p,Foot_points,n_Foot_points,..);
     F_Foot_points(k,:) = Fd.*expm(d*dt);
end
```

This concludes step 2 and the tutorial for the PMIM. If the convergence criteria are not satisfied, the algorithm keeps iterating steps 1 and 2 alternatively inside the while loop until

convergence is attained.

Part II

The immersed soft matter system

Chapter 7

A coupled Eulerian-Lagrangian extended finite element formulation for the study of embedded soft matter

Many important and challenging problems in the areas of geophysics (e.g. ice sheet flow, mantle dynamics), soft materials (e.g. deformation of hydrogels and biological cells) and material science (e.g. metal forming) involve large deformations or flow of solid material. In these conditions, it can be convenient to work with a fully Eulerian description of solid deformation, especially when the boundaries of the solid domain are not moving [45, 53]. For problems where domain boundaries are free to move, however, a Lagrangian (material) description is required to map solid deformation between reference and current configurations. Such a moving boundary problem also needs the introduction of specialized numerical methods that can track an interface without remediating to expensive remeshing techniques. In this context, we propose to address the challenges with describing the evolution of free boundaries through the introduction of a coupled Eulerian–Lagrangian formulation, based on the combination of the extended finite element method (XFEM) and the grid based particle method (GPM) [98].

Traditionally, a purely Lagrangian finite element formulation is used for solid mechanics because it is simple to implement, computationally less expensive and does not need any interface-tracking techniques; however, in the case of severe material distortion, it may suffer from numerical issues due to excessive mesh distortion. Many strategies have been elaborated to tackle this issue including the use of remeshing with interpolation techniques between old and new meshes [39, 95, 35], but the latter is generally cumbersome and displays a lack of accuracy. Another approach consists in using the Deforming Spatial Domain or Stabilized Space Time (DSD/DST) formulation [152, 153] which has been powerful to handle fluid-structure interactions with large deformation of the fluid-solid interface. A more popular approach is to employ the arbitrary Lagrangian–Eulerian (ALE) formulation, wherein, a deformation step on a distorted Lagrangian mesh is followed with a remap step onto a spatially fixed Eulerian mesh. Some early work on ALE formulations can be found in [83, 71, 102, 21, 22, 181, 87] and for a complete literature review of ALE and Space-Time methods for moving boundaries and interfaces, the reader is referred to [13]. In both the ALE and DSD/DST formulations, the mesh moving techniques typically aims at reducing the frequency of remeshing [148].

An alternative approach is to use a purely Eulerian formulation for solid mechanics. Although not as popular as the ALE formation, a handful of Eulerian formulations have been proposed in the literature [45, 118, 78, 53, 135]. The two main advantages of the Eulerian approach, as pointed by Benson [22], are: (1) it can handle arbitrarily large deformations, so it can be suitable for studying soft matter and viscoelastic fluids, for example and (2) it allows the creation, merging and vanishing of free surfaces or interfaces in a natural manner, so it can be used for studying growth and phase transformation processes. Since the material is not fixed to the finite element mesh, but rather flows through the mesh, an Eulerian formulation does not suffer from mesh distortion issues. The drawback of Eulerian formulation for solids is its higher computational cost due to the need for computing velocity and deformation variables separately, as opposed to a Lagrangian formulation, wherein only the velocity needs to be computed. In three-dimensions, this means in an Eulerian finite element formulation for a compressible hyperelastic medium, there will be 13 unknown (3 velocity, 9 deformation gradi-

ent, 1 Jacobian determinant) nodal degrees of freedom (DOFs), whereas in a Lagrangian finite element formulation there will be only 3 unknown (3 velocity) nodal DOFs [53]. Moreover, in Eulerian formulations material interfaces and free boundaries need to be tracked using moving interface methods, which adds to the numerical challenge and computational expense.

A critical issue in the case of Eulerian formulations is the handling of heterogeneous or multi-phase materials. For two-phase materials that are a bonded well (i.e. no slip conditions at the interface) mixture theory approaches work well, but for more general applications the discontinuity in material properties across the interface needs to handled carefully. Previously, Vitali and Benson have employed the extended finite element method (XFEM) to model contact in multi-material arbitrary Lagrangian–Eulerian (MMALE) formulations [167, 168]. Herein, we develop a multi-material coupled Eulerian–Lagrangian (CEL) formulation by employing the XFEM [19, 112] and a level set representation of the interface [138]. By enriching the standard finite element shape functions with a Heaviside step function, a sharp discontinuity in the material properties across the embedded interface can be incorporated within a finite element. Tracking the deformation-driven motion of the interface can then be accomplished by for instance, using the GPM [98] or, alternatively, using an interface-capturing scheme such as the level set method [120, 137]. Among the two options, the GPM is computationally less expensive, simpler to implement, and can also handle arbitrary topological transitions such as merging and vanishing of material interfaces. Another issue arising from the existence of a moving interface is the imposition of interface constraints, however, recent work provides viable weak formulations by employing either the Lagrange multiplier method [15, 90] or a Nitsche's method [49, 5]. Therefore, the imposition of interface conditions is not currently addressed herein and the reader is refereed to the above cited work.

In the present work, we develop a coupled Eulerian-Lagrangian formulation with moving interface associated with the large deformations of soft solids. The momentum equations and the transport equations for the deformation gradient are solved in a staggered manner in time. The velocity field is first calculated by solving the momentum equation in a Eulerian framework, and is then used to update the isochoric and volumetric parts of the deformation gradient,

separately, using an updated Lagrangian description. The position of the material interface is tracked using the GPM [98] and the velocity field projected in the direction normal to the interface. We show that the method is accurate in the regime of finite deformation and viable for investigating soft matter mechanics. The organization of the chapter is as follows: section 7.1 introduces the kinematics, the governing and constitutive equations, and the resulting weak form for the mechanical equilibrium of an elastic body. In section 7.2, we present a numerical strategy to discretize the weak form, the tracking of the interface and the Lagrangian transport of the deformation gradient tensor components. Finally, the numerical convergence and accuracy of the method is considered in section 7.3 through the examples of a uniaxial extension of a rectangular bar, and the simple shear of a rectangular block. The mesh-independent geometric discretization and the absence of mesh distortion problem is then demonstrated with the test of a cylinder under compression and the indentation of a rectangular block. The latter results are validated by comparing them with those from traditional Lagrangian formulation in the commercial software Abaqus. Some concluding remarks are made in section 7.4.

7.1 Formulation of the governing equations

7.1.1 Kinematics

In this study we consider a domain Ω containing an elastic body in the region $\Omega^{\mathrm{s}}(t)$. The domain Ω is delimited by a boundary $\partial\Omega$ while the interface describing the current shape of the elastic body is denoted $\Gamma(t)$. Thus, Γ splits the domain Ω into the solid domain $\Omega^{\mathrm{s}}(t)$ and its complement denoted by $\Omega \setminus \Omega^{\mathrm{s}}(t)$. We employ the Eulerian description of the motion and choose a fixed right-handed Cartesian system of coordinates $\{\mathbf{x} = x_j\ \hat{e}_j, j = 1, 2, 3\}$, where $\hat{e}_j$ are the orthonormal basis vectors [106]. The motion of a physical particle P is expressed by the mapping function $\mathbf{x} = \boldsymbol{\chi}(\mathbf{X}, t)$ between its reference coordinates $\{\mathbf{X} = X_j\ \hat{e}_j, j = 1, 2, 3\}$ at an initial time $t = t_0$ and its current coordinates $\mathbf{x}$ at a subsequent time $t > t_0$ (see Fig. 7.1). We assume that the function $\boldsymbol{\chi}(\mathbf{X}, t)$ is sufficiently differentiable and single valued with the region $\Omega^{\mathrm{s}}(t)$. From an Eulerian viewpoint, the spatial velocity field $\mathbf{v}(\mathbf{x}, t)$ gives the velocity of the

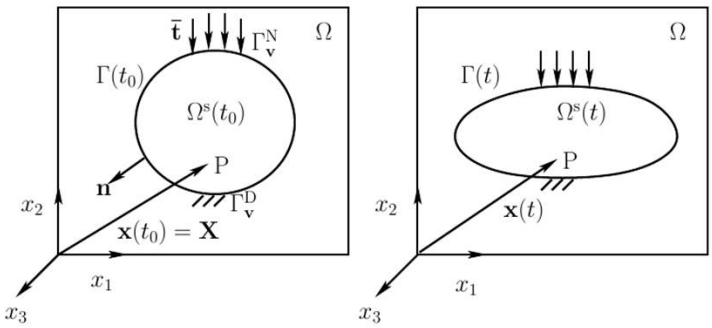

Figure 7.1: *Schematic diagram of the domain and its evolution under an applied traction. The moving interface* $\Gamma(t)$ *at any time* t *separates the solid domain* $\Omega^{\mathrm{s}}(t)$ *from its complement* $\Omega \setminus \Omega^{\mathrm{s}}(t)$.

particle located at $\mathbf{x}$ at time t and is defined as

$$\mathbf{v} = \left(\frac{\partial \boldsymbol{\chi}}{\partial t}\right)_{\mathbf{X}} = \left(\frac{\partial \mathbf{x}}{\partial t}\right)_{\mathbf{X}} = \mathbf{g}\left[\mathbf{x}(\mathbf{X}, t), t\right], \tag{7.1}$$

where $\mathbf{g}$ is a sufficiently differentiable function. The deformation of a solid particle is described by the tensor given by $\mathbf{F} = \dfrac{\partial \mathbf{x}}{\partial \mathbf{X}}$. The isochoric part of this tensor $\hat{\mathbf{F}}$ is given by:

$$\mathbf{F} = J^{-1/3}\ \hat{\mathbf{F}}, \tag{7.2}$$

where $J = \det[\mathbf{F}]$ is the Jacobian determination of the deformation. The rate of change of the deformation gradient is given by,

$$\dot{\mathbf{F}} = \frac{\mathrm{d}\mathbf{F}}{\mathrm{d}t} = \frac{\mathrm{d}}{\mathrm{d}t}\left(\frac{\partial \mathbf{x}}{\partial \mathbf{X}}\right) = \left(\frac{\partial \mathbf{v}}{\partial \mathbf{x}}\right) \cdot \left(\frac{\partial \mathbf{x}}{\partial \mathbf{X}}\right) = \mathbf{L}\mathbf{F}, \tag{7.3}$$

where $\dfrac{\mathrm{d}}{\mathrm{d}t}$ denotes the material time derivative and $\mathbf{L} = \dfrac{\partial \mathbf{v}}{\partial \mathbf{x}} = (\nabla \mathbf{v})^T$ is the velocity gradient with respect to the current coordinates. We note here that the superscript T is used for the transpose of a tensor. The above equation can be split into its volumetric and isochoric parts as,

$$\frac{\mathrm{d}\hat{\mathbf{F}}}{\mathrm{d}t} = \frac{\partial \hat{\mathbf{F}}}{\partial t} + \mathbf{v} \cdot \nabla \hat{\mathbf{F}} = \left[\mathbf{L} - \frac{1}{3}(\nabla \cdot \mathbf{v})\mathbf{I}\right] \hat{\mathbf{F}}, \tag{7.4}$$

$$\frac{\mathrm{d}J}{\mathrm{d}t} = \frac{\partial J}{\partial t} + \mathbf{v} \cdot \nabla J = J\ \nabla \cdot \mathbf{v}, \tag{7.5}$$

where $\nabla = \dfrac{\partial}{\partial x_j}\hat{e}_j$ is the spatial gradient operator, $\mathbf{I}$ is the second order identity tensor and $\cdot$ denotes the dot product.

7.1.2 Strong from

The strong form of the governing equations, which include both mechanical equilibrium and transport equations, can be written in the elastic body in $\Omega^{\mathrm{s}}(t)$ as [53]:

$$\nabla \cdot \boldsymbol{\sigma} + \rho \mathbf{f} = \mathbf{0}, \tag{7.6}$$

$$\frac{\mathrm{d}J}{\mathrm{d}t} - J\nabla \cdot \mathbf{v} = 0, \tag{7.7}$$

$$\frac{\mathrm{d}\hat{\mathbf{F}}}{\mathrm{d}t} - \left[\nabla \mathbf{v} - \frac{1}{3}(\nabla \cdot \mathbf{v})\mathbf{I}\right]\hat{\mathbf{F}} = \mathbf{0}, \tag{7.8}$$

where $\boldsymbol{\sigma}$ is the Cauchy stress tensor and $\mathbf{f}$ the body force per unit volume in the current configuration. The above equations are subjected to the following boundary and initial conditions:

$$\mathbf{v} = \bar{\mathbf{v}} \text{ on } \Gamma^{\mathrm{D}}_{\mathbf{v}}, \tag{7.9}$$

$$\mathbf{n} \cdot \boldsymbol{\sigma} = \bar{\mathbf{t}} \text{ on } \Gamma^{\mathrm{N}}_{\mathbf{v}}, \tag{7.10}$$

$$\hat{\mathbf{F}}(t=0) = \mathbf{I} \text{ in } \Omega^{\mathrm{s}}(0), \tag{7.11}$$

$$J(t=0) = 1 \text{ in } \Omega^{\mathrm{s}}(0), \tag{7.12}$$

where $\Gamma^{\mathrm{D}}_{\mathbf{v}}$ and $\Gamma^{\mathrm{N}}_{\mathbf{v}}$ represent the Dirichlet and Neumann parts of Γ for the boundary conditions on velocity and traction, respectively.

Remark 1 *If the transport equations (7.7) and (7.8) are discretized using an Eulerian description, one needs to specify boundary conditions on $\hat{\mathbf{F}}$ and J, in addition to initial conditions (7.11) and (7.12). To simplify our analysis, we propose here to use a Lagrangian (particle) description to update $\hat{\mathbf{F}}$ and J and does not necessitate the use of above boundary conditions. Ultimately, the formulation only requires initial conditions on $\hat{\mathbf{F}}$ and J.*

7.1.3 Constitutive equations

To model the large deformations of the compressible hyperelastic domain, we consider the isochoric-volmetric decoupling of the strain energy function as,

$$W = U(J) + \hat{W}(\hat{\mathbf{b}}), \tag{7.13}$$

where $\hat{\mathbf{b}} = \hat{\mathbf{F}}\hat{\mathbf{F}}^T = J^{-2/3}\mathbf{F}\mathbf{F}^T$. The specific functional forms of U and $\hat{W}$ are to be chosen to satisfy physical conditions. Herein, we assume the functions proposed by Simo et al. [143, 142] as,

$$\begin{aligned} U(J) &= \frac{\kappa}{2}\left[\ \ln(J)\ \right]^2, \\ \hat{W}(\hat{\mathbf{b}}) &= \frac{\mu}{2}\left[\mathrm{tr}(\hat{\mathbf{b}}) - 3\right], \end{aligned} \tag{7.14}$$

where μ and κ represent the shear and bulk modulus of the material, respectively, and 'tr' denotes the trace of the tensor and $\hat{\mathbf{b}} = \hat{\mathbf{F}}\hat{\mathbf{F}}^T$. The expression for the Cauchy stress is [53],

$$\boldsymbol{\sigma}(J, \hat{\mathbf{F}}) = \frac{1}{J}\left[\kappa \ln(J)\mathbf{I} + \mu\ \mathrm{dev}(\hat{\mathbf{b}})\right] \tag{7.15}$$

where $\mathrm{dev}(\hat{\mathbf{b}}) = \hat{\mathbf{b}} - \dfrac{1}{3}\mathrm{tr}(\hat{\mathbf{b}})\mathbf{I}$ is deviatoric part.

Remark 2 *The above functional form for $U(J)$ is chosen so that it satisfies several requirements [50]. First, in the limit case when Ω^{s} is compressed to a single point or is stretched to be infinitely large the strain energy always tends to positive infinity, that is,*

$$\lim_{J\to+0} U = +\infty \quad \textit{and} \quad \lim_{J\to+\infty} U = +\infty. \tag{7.16}$$

Second, the volumetric stress tends to negative infinity when Ω^{s} is compressed to a single point and to positive infinity when stretched to infinitely large, that is,

$$\lim_{J\to+0} \frac{\partial U}{\partial J} = -\infty \quad \textit{and} \quad \lim_{J\to+\infty} \frac{\partial U}{\partial J} = +\infty. \tag{7.17}$$

Hence U has to be an even power of $\ln(J)$ so that $U > 0$ for all J.

Remark 3 *As pointed out in [50] the assumed volumetric part of the strain energy function U does not satisfy the polyconvexity because $\dfrac{\partial^2 U}{\partial J^2} < 0$ for $\ln(J) > 1$, that is, for all $J > e$ where e is Euler's number. However, this inconsistency is not a issue in the current work as all our investigations are carried out for $J < e$.*

7.1.4 Weak Form

Introducing the test functions $\mathbf{w}$, integrating by parts and using the divergence theorem, the weak form of the equilibrium equation in the elastic domain can be written as: *find* $\mathbf{v} \in \mathcal{V}$ *for all* $\mathbf{w} \in \mathcal{V}^0$ *such that,*

$$-\left(\nabla \mathbf{w}, \boldsymbol{\sigma}\right)_{\Omega^{\mathrm{s}}} - \left(\mathbf{w}, \bar{\mathbf{t}}\right)_{\Gamma^{\mathrm{N}}_{\mathbf{v}}} + \left(\mathbf{w}, \rho \mathbf{f}\right)_{\Omega^{\mathrm{s}}} \quad = \quad 0, \tag{7.18}$$

where the notation $(\cdot, \cdot)_{\Omega^{\mathrm{s}}}$ indicates the L^2 inner product with respect to the domain Ω^{s}, and $\mathcal{V}$ and $\mathcal{V}^0$ are spaces of sufficiently smooth functions for the continuous fields and their variations. By construction, we also require that the test function $\mathbf{w}$ vanishes on the Dirichlet boundaries. We do not write the weak form for the transport equations (related to $\hat{\mathbf{F}}$ and J) because we will use an explicit scheme to update of the variables for each Lagrangian particle, individually, as described in Section 7.2.5.

7.2 Solution strategy

We now present a novel numerical strategy that couples the Eulerian and updated Lagrangian formulations with the objective of evolving the moving interface on a fixed Eulerian grid. For this the solid boundary Γ is represented by a evolving level set function across which a discontinuity in velocity and deformation is described using the extended finite element method. The interface describing the deformed shape of the elastic body is moved in an incremental manner until equilibrium. For any increment, the method consists in computing the velocity field $\mathbf{v}$ in the current domain $\Omega^{\mathrm{s}}(t_n)$ by solving the equilibrium equation (7.18). The field variables $\hat{\mathbf{F}}$ and J are

then updated point-wise by using an explicit updated Lagrangian mapping algorithm between the material configurations at the current and next increments (denoted by pseudo-time steps $t_n = t$ and $t_{n+1} = t+dt$, respectively). Between these increments the interface is moved using the particle-based moving interface method. In the following sections, a more detailed description of the methodology is presented.

7.2.1 Level-set representation of the solid interface

Mathematically, we here represent the boundary $\Gamma(t)$ of the solid domain with the level set function ϕ defined as,

$$\Gamma = \{\mathbf{x} \in \Omega \mid \phi(\mathbf{x}, t) = 0\}, \tag{7.19}$$

so that $\phi < 0$ inside the solid domain $\Omega^s(t)$ and $\phi > 0$ outside the solid domain $\Omega \setminus \Omega^s(t)$. Although there are several choices for ϕ, for stability, we choose it to be the signed distance function defined by:

$$\phi(\mathbf{x}, t) = \pm \min_{\mathbf{x}' \in \Gamma} ||\mathbf{x} - \mathbf{x}'|| \quad \text{for all} \quad \mathbf{x} \in \Omega. \tag{7.20}$$

Practically, the function ϕ can be reinitialized at every increment using the locations of the interface in order to maintain the properties of the signed distance function. When the interface is described by particles, the reinitialization procedure is discussed in [98]. A more detailed description of the implementation of the interface evolution algorithm will be given later in this chapter (section 7.2.4).

Remark 4 *We note here that the level set method (LSM) [138] may also be used for evolving the interface in time. However, the GPM [98] employed here provides an attractive solution to explicitly track Lagrangian particles on the solid boundary instead of resorting to solving a level set evolution equation.*

7.2.2 The extended finite element approximation

Following an Eulerian approach, a fixed and structured finite element discretization is introduced for the entire physical domain Ω (including the space that does not belong to the solid body).

The boundary of the body Ω^s is then defined with a multi-segment closed surface Γ that cuts through some of the elements. Since the field variables, namely, $\mathbf{v}$, $\hat{\mathbf{F}}$ and J have non-zero values in Ω^s but identically vanish in $\Omega \setminus \Omega^s(t)$, field discontinuities naturally occur across Γ. To handle this issue, we employ the extended finite element method (XFEM), as it is able to capture the presence of discontinuities within elements and thus render the discretization of the interface Γ easy and computationally efficient. We adopt a mixed formulation wherein the velocity field $\mathbf{v}$ is interpolated with nine-node (biquadratic) element shape functions and the isochoric part of the deformation gradient $\hat{\mathbf{F}}$ and its Jacobian J are interpolated with four-node (bilinear) element shape functions (see Figure 7.2). This reads:

$$v_i(\mathbf{x},t) = \sum_{I=1}^{9} N^I(\mathbf{x}) v_i^I(t) + \sum_{I=1}^{9} N^I(\mathbf{x}) \mathcal{S}^I(\mathbf{x},t) a_i^I(t), \tag{7.21}$$

$$\hat{F}_{ij}(\mathbf{x},t) = \sum_{I=1}^{4} \hat{N}^I(\mathbf{x}) \hat{F}_{ij}^I(t) + \sum_{I=1}^{4} \hat{N}^I(\mathbf{x}) \mathcal{S}^I(\mathbf{x},t) D_{ij}^I(t), \tag{7.22}$$

$$J(\mathbf{x},t) = \sum_{I=1}^{4} \hat{N}^I(\mathbf{x}) J^I(t) + \sum_{I=1}^{4} \hat{N}^I(\mathbf{x}) \mathcal{S}^I(\mathbf{x},t) C^I(t), \tag{7.23}$$

where N^I and $\hat{N}^I$ denote the 9-node element and the 4-node element Lagrange shape functions, respectively; the superscript index I is used for node numbering and the subscript indices i, j are used for numbering the Cartesian components; $\mathbf{v}^I$, $\hat{\mathbf{F}}^I$, J^I denote the standard degrees of freedom (DOFs) and $\mathbf{a}^I$, $\mathbf{D}^I$ C^I denote the corresponding enriched DOFs at node I, respectively; the step enrichment function $\mathcal{S}^I$ at enriched node I used to incorporate the jump discontinuity in the fields is defined as,

$$\mathcal{S}^I = H\left(\phi(\mathbf{x},t)\right) - H\left(\phi(\mathbf{x}^I,t)\right) \tag{7.24}$$

and the Heaviside function H is defined as,

$$H(\phi(\mathbf{x},t)) = \begin{cases} 1 & \phi > 0, \\ 0 & \phi < 0. \end{cases} \tag{7.25}$$

Note that the level set function ϕ is continuous across the interface and so that it can be interpolated using the shape functions N^I and $\hat{N}^I$.

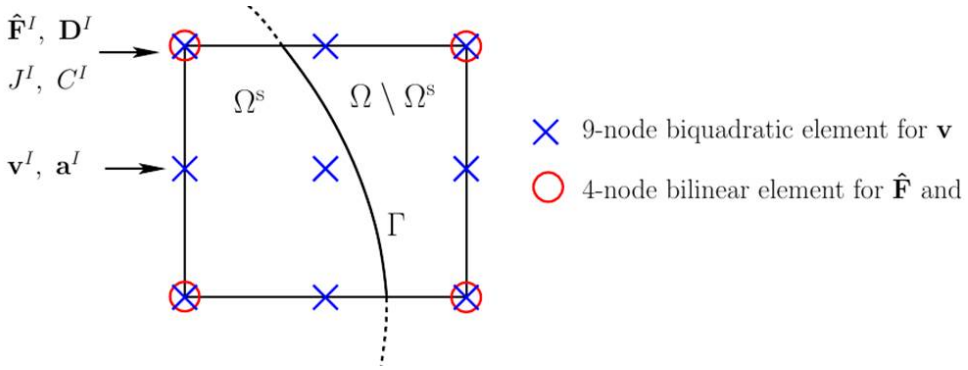

Figure 7.2: *Illustration of the mixed extended finite element and the location of the degrees of freedom. Circles (○) show the location of bilinear element nodes and crosses (×) show the location of biquadratic element nodes. The interface cutting through the element is represented implicitly using the level set function ϕ.*

Remark 5 *Previously, Duddu et al. [53] proposed the above mixed formulation to ensure stability in the case of nearly incompressible elastic solids (e.g. rubber with Poisson's ratio $\nu = 0.48 - 0.5$. However, even for a compressible solid, the mixed formulation results in better accuracy and hence requires less number of iterations to reach the tolerance limit for the residual.*

In this study, we reduce the dimension of the domain by considering that it is uniform in the x_3 direction (plane strain conditions apply). This implies that $v_3(\mathbf{x},t) = 0$, $F_{33}(\mathbf{x},t) = 1$, $F_{13}(\mathbf{x},t) = F_{32}(\mathbf{x},t) = 0$; this allows us to not consider them as nodal degrees of freedom (DOFs) in our analysis. Moreover, for clarity, we write the linear system in the following matrix form:

$$\begin{cases} \mathbf{v}(\mathbf{x},t) = \bar{\mathbf{N}}_{\mathbf{v}}(\mathbf{x},t)\bar{\mathbf{v}}(t), \\ \hat{\mathbf{F}}(\mathbf{x},t) = \bar{\mathbf{N}}_{\hat{\mathbf{F}}}(\mathbf{x},t)\bar{\mathbf{F}}(t), \\ J(\mathbf{x},t) = \bar{\mathbf{N}}_{J}(\mathbf{x},t)\bar{J}(t). \end{cases} \tag{7.26}$$

Here, the shape function matrices $\bar{\mathbf{N}}_{\mathbf{v}}$, $\bar{\mathbf{N}}_{\hat{\mathbf{F}}}$ and $\bar{\mathbf{N}}_{J}$ and element vectors $\bar{\mathbf{v}}$, $\bar{\mathbf{F}}$ and $\bar{J}$ contain both standard and enriched DOFs and are defined as:

$$\text{nodal DOFs}\begin{cases} \bar{\mathbf{v}} = \left[\bar{\mathbf{v}}^{\text{reg}}; \bar{\mathbf{v}}^{\text{enr}}\right]_{36\times 1}, \\ \bar{\mathbf{v}}^{\text{reg}} = \left[v_1^1,\ v_2^1,\ \ldots\ v_1^9,\ v_2^9\right]_{18\times 1}^T; \bar{\mathbf{v}}^{\text{enr}} = \left[a_1^1,\ a_2^1,\ \ldots\ a_1^9,\ a_2^9\right]_{18\times 1}^T \\ \bar{\mathbf{F}} = \left[\bar{\mathbf{F}}^{\text{reg}}; \bar{\mathbf{F}}^{\text{enr}}\right]_{32\times 1}, \\ \bar{\mathbf{F}}^{\text{reg}} = \left[\hat{F}_{11}^1,\ \hat{F}_{22}^1,\ \hat{F}_{12}^1,\ \hat{F}_{21}^1,\ \ldots\ \hat{F}_{11}^4,\ \hat{F}_{22}^4,\ \hat{F}_{12}^4,\ \hat{F}_{21}^4\right]_{16\times 1}^T, \\ \bar{\mathbf{F}}^{\text{enr}} = \left[D_{11}^1,\ D_{22}^1,\ D_{12}^1,\ D_{21}^1,\ \ldots\ D_{11}^4,\ D_{22}^4,\ D_{12}^4,\ D_{21}^4\right]_{16\times 1}^T \\ \bar{J} = \left[\bar{J}^{\text{reg}}; \bar{J}^{\text{enr}}\right]_{8\times 1}, \\ \bar{J}^{\text{reg}} = \left[J^1, \ldots\ J^4\right]_{4\times 1}^T; \bar{J}^{\text{enr}} = \left[C^1, \ldots\ C^4\right]_{4\times 1}^T, \end{cases} \tag{7.27}$$

$$\text{shape functions}\begin{cases} \bar{\mathbf{N}}_{\mathbf{v}} = \left[\ \mathbf{N}_{\mathbf{v}}^{\text{reg}},\ \mathbf{N}_{\mathbf{v}}^{\text{enr}}\ \right]_{2\times 36} \\ \bar{\mathbf{N}}_{\hat{\mathbf{F}}} = \left[\ \mathbf{N}_{\mathbf{F}}^{\text{reg}},\ \mathbf{N}_{\mathbf{F}}^{\text{enr}}\ \right]_{4\times 32} \\ \bar{\mathbf{N}}_{J} = \left[\ \mathbf{N}_{J}^{\text{reg}},\ \mathbf{N}_{J}^{\text{enr}}\ \right]_{1\times 8} \end{cases} \tag{7.28}$$

with

$$\mathbf{N}_{\mathbf{v}}^{\text{reg}} = \left[\ \mathbf{N}_{\mathbf{v}}^1, \ldots, \mathbf{N}_{\mathbf{v}}^9\ \right]_{2\times 18}, \mathbf{N}_{\mathbf{v}}^{\text{enr}} = \left[\ \mathcal{S}^1\mathbf{N}_{\mathbf{v}}^1, \ldots, \mathcal{S}^9\mathbf{N}_{\mathbf{v}}^9\ \right]_{2\times 18}$$
$$\mathbf{N}_{\mathbf{F}}^{\text{reg}} = \left[\ \mathbf{N}_{\mathbf{F}}^1, \ldots, \mathbf{N}_{\mathbf{F}}^4\ \right]_{4\times 16}, \mathbf{N}_{\mathbf{F}}^{\text{enr}} = \left[\ \mathcal{S}^1\mathbf{N}_{\mathbf{F}}^1, \ldots, \mathcal{S}^4\mathbf{N}_{\mathbf{F}}^4\ \right]_{4\times 16}$$
$$\mathbf{N}_{J}^{\text{reg}} = \left[\ \hat{N}^1, \ldots, \hat{N}^4\ \right]_{1\times 4}, \mathbf{N}_{J}^{\text{enr}} = \left[\ \mathcal{S}^1\hat{N}^1, \ldots, \mathcal{S}^4\hat{N}^4\ \right]_{1\times 4}$$

and $\mathbf{N}_{\mathbf{v}}^I = \begin{bmatrix} N^I & 0 \\ 0 & N^I \end{bmatrix}$, $\mathbf{N}_{\mathbf{F}}^I = \begin{bmatrix} \hat{N}^I & 0 & 0 & 0 \\ 0 & \hat{N}^I & 0 & 0 \\ 0 & 0 & \hat{N}^I & 0 \\ 0 & 0 & 0 & \hat{N}^I \end{bmatrix}$.

7.2.3 Linearization of the equilibrium equation

The discretized form of the equilibrium equation can be written from the weak form (7.18) by introducing the XFEM approximation. Neglecting body forces, the element residual vector is given by,

$$\mathbf{R_v} \;=\; -\int_{\Omega^e} \mathbf{B}_\mathbf{v}^T \tilde{\boldsymbol{\sigma}}\, \mathrm{d}\Omega - \int_{\Gamma_\mathbf{v}^e} \bar{\mathbf{N}}_\mathbf{v}^T \bar{\mathbf{t}}\, \mathrm{d}\Gamma, \tag{7.29}$$

where Ω^e is the part of the domain Ω^s contained in the finite element e, $\Gamma_\mathbf{v}^e$ is the segment of the Neumann boundary $\Gamma_\mathbf{v}^N$ intersecting the element e. Furthermore, $\tilde{\boldsymbol{\sigma}} = [\sigma_{11},\ \sigma_{22},\ \sigma_{21},\ \sigma_{12}]_{4\times1}^T$ is the symmetric Cauchy stress matrix, $\tilde{\mathbf{t}} = [\bar{t}_1,\ \bar{t}_2]_{2\times1}^T$ is the surface traction vector and the gradient matrix of the 9-node element shape functions $\mathbf{B_v}$ is given by:

$$\mathbf{B_v} = \left[\mathbf{B}_\mathbf{v}^1,\ ...,\ \mathbf{B}_\mathbf{v}^9,\ \ \mathcal{S}^1\mathbf{B}_\mathbf{v}^1,\ ...,\ \mathcal{S}^9\mathbf{B}_\mathbf{v}^9\right]_{4\times36} \quad \text{with} \quad \mathbf{B}_\mathbf{v}^I = \begin{bmatrix} \frac{\partial N^I}{x_1} & 0 \\ 0 & \frac{\partial N^I}{x_2} \\ \frac{\partial N^I}{x_2} & 0 \\ 0 & \frac{\partial N^I}{x_1} \end{bmatrix}_{4\times2} \tag{7.30}$$

Although, due symmetry it is sufficient to represent the stress tensor $\tilde{\boldsymbol{\sigma}}$ as a 3×1 array in Voight notation, for the purpose of matrix operations related to the divergence of stress in the above residual we prefer to use 4×1 array. Using a Taylor's expansion, we linearize equation (7.29) at time t_{n+1} as [45] and obtain:

$$\mathbf{0} = \mathbf{R_v}\left(t_{n+1}\right) = \mathbf{R_v}\left(t_n\right) + \left[\frac{\partial \mathbf{R_v}}{\partial t}\right]\ \Delta t, \tag{7.31}$$

which yields:

$$\left[\frac{\partial \mathbf{R_v}}{\partial t}\right] = -\frac{1}{\Delta t}\ \mathbf{R_v}\left(t_n\right), \tag{7.32}$$

Using the transport equations (7.7) and (7.8) together with the constitutive relation (7.15), the above equation can be written in the form of a linear system as [53]:

$$\mathbf{K_v}(t_n)\bar{\mathbf{v}}(t_{n+1}) = -\frac{1}{\Delta t}\ \mathbf{R_v}(t_n), \tag{7.33}$$

where $\mathbf{K_v}$ is the consistent tangent stiffness matrix. The discretization of the domain integrals using the extended finite element approximation for obtaining the tangent matrix $\mathbf{K_v}$ is described in 7.4.

7.2.4 The grid based particle method

To track the deformation of the interface Γ, we propose to use a grid based particle method similar to what was introduced in [98]. This method indeed possesses the double advantage of tracking the interface explicitly with particles while using the underlying fixed finite element mesh; this ensures a fairly uniform repartition of the particles throughout the interface. Herein, we review the basic idea behind the particle based moving interface method and discuss the procedure to update of the interface position and deformations measures within the current numerical scheme. The interface particles on Γ, whose position is denoted by the vector $\mathbf{y}$, are

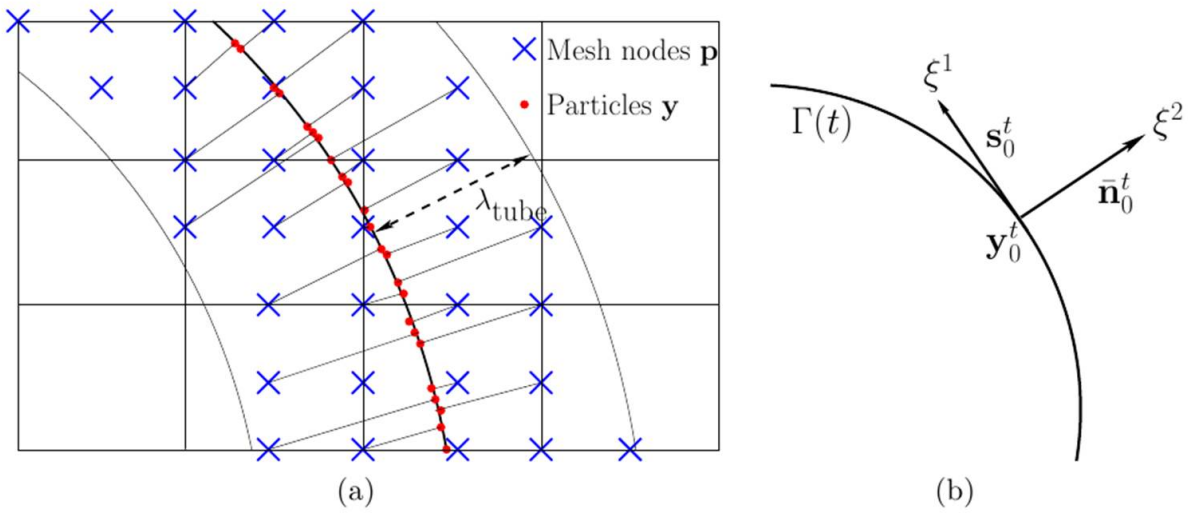

Figure 7.3: *Grid particle scheme . Figure (a) shows the one to one correspondence between the particles and the nodes inside the computational tube, while (b) shows the local basis, centred on the particle* $\mathbf{y}_0$ *closest to the node considered* $\mathbf{p}$.

chosen as the normal projection of the underlying mesh nodes with position vector $\mathbf{p}$. Since the interface is initially described implicitly as the zero level set of a signed distance function $\phi(\mathbf{p}, 0)$ at initial time $t = t_0$, its value gives the perpendicular distance between mesh point and interface point. Considering that the gradient of level set function gives the local interface

normal, the initial coordinates of particles $\mathbf{y}$ are given by [98]:

$$\mathbf{y} \;=\; \mathbf{p} - \phi(\mathbf{p},0)\mathbf{n} = \mathbf{p} - \phi(\mathbf{p},0)\nabla\phi(\mathbf{p},0) \tag{7.34}$$

Note that the above expression is only valid when $\|\nabla\phi\| = 1$, that is, when ϕ is a signed distance function. To limit the number of particles, we define a so-called computational tube such that only nodes $\mathbf{p}$, whose distance to Γ is smaller than a cut-off value λ_{tube}, are taken into account (see Fig. 7.3(a)).

Remark 6 *It is important to note here that there is a one to one correspondence between each particle* $\mathbf{y}$ *and node* $\mathbf{p}$*, thus, providing each interface particle an Eulerian reference mesh point. This ensures a quasi-uniform repartition of particles along the interface throughout its evolution and avoids the need for node point redistribution schemes, unlike the standard marker particle methods [67]*

Between two subsequent time steps $t_n = t$ and $t_{n+1} = t + dt$, the particles are moved with the normal interface velocity $\mathbf{v}^{\perp} = (\mathbf{v}\cdot\mathbf{n})\mathbf{n}$ using a second order Runge-Kutta time integration procedure as follows:

$$\mathbf{y}^{t+dt/2} \;=\; \mathbf{y}^t + \mathbf{v}^{\perp}(\mathbf{y}^t,t)\frac{dt}{2} + \boldsymbol{\Omega}\cdot\mathbf{v}^{\perp}(\mathbf{y}^t),t\frac{dt^2}{4} \tag{7.35}$$

$$\mathbf{y}^{t+dt} \;=\; \mathbf{y}^t + \mathbf{v}^{\perp}(\mathbf{y}^{t+dt/2},t)dt + \boldsymbol{\Omega}\cdot\mathbf{v}^{\perp}(\mathbf{y}^{t+dt/2},t)\frac{dt^2}{2}, \tag{7.36}$$

where $\boldsymbol{\Omega}$ is the matrix of the angular velocity of the interface normal. Introducing the local coordinates ξ_1 and ξ_2 that respectively run in the directions tangent and normal to the interface at point $\mathbf{y}^t$, the angular velocity can be written as,

$$\boldsymbol{\omega} \;=\; -\left(\mathbf{v}^{\perp}\cdot\mathbf{n}\right)_{,\xi^1}\mathbf{z} \quad\text{and}\quad \Omega_{ik} \;=\; \epsilon_{ijk}\omega_j \tag{7.37}$$

with the permutation tensor $\epsilon_{ijk} = \frac{1}{2}(i-j)(j-k)(k-i)$, indices $i,j,k = \{1,2.3\}$ and the normal vector out of plane $\mathbf{z} = [0\ 0\ 1]^T$. The term $(\mathbf{v}^{\perp}\cdot\mathbf{n})_{,\xi^1}$ indicates the derivative of the magnitude of the normal velocity with respect to the coordinate ξ^1. The relationship between the local and

global coordinates ξ^1 and $\mathbf{y}$ is given bellow.

After the position of the interface has been updated, the particle distribution on Γ may become uneven, and this can affect the geometrical resolution of the interface. To overcome this issue, the interface is ressampled after motion by recomputing the particles as the closest points on Γ to the nodes $\mathbf{p}$ inside the updated computational tube (which has moved with the interface). This is done by first approximating the interface with polynomials locally around each particle. The procedure, explained here in the two dimensional case, is as follows: for each node $\mathbf{p}$ inside the computational tube, the closest m particles $\mathbf{y}_0^t ... \mathbf{y}_m^t$ are collected at time t, carrying with them the tangent $\mathbf{s}_0^t ... \mathbf{s}_m^t$ and normal $\bar{\mathbf{n}}_0^t ... \bar{\mathbf{n}}_m^t$ to the interface before motion. Denoting $\mathbf{y}_0^t$ as the particle closest to $\mathbf{p}$, a polynomial of degree $n < m$ is fitted to the particles $\mathbf{y}_0^t ... \mathbf{y}_m^t$ in the local coordinate system $\{\mathbf{s}_0^t; \bar{\mathbf{n}}_0^t\}$ centered on $\mathbf{y}_0^t$. The location $\tilde{\mathbf{y}}_i^t$ of particle i in this local coordinate system is given by:

$$\tilde{\mathbf{y}}_i \;=\; \left\{ \begin{array}{c} \xi_i^1 \\ \xi_i^2 \end{array} \right\} \;=\; \mathbf{R}^t \cdot (\mathbf{y}_i^t - \mathbf{y}_0^t) \quad \text{with} \quad \mathbf{R}^t \;=\; \left[\begin{array}{c} (\mathbf{s}_0^t)^T \\ (\bar{\mathbf{n}}_0^t)^T \end{array} \right]. \tag{7.38}$$

Taking the example of a quadratic polynomial ($n = 2$), the interface around particle $\mathbf{y}_0$ is represented in the local referential as the graph function $\xi^2(\xi^1) = c_0 + c_1\xi^1 + c_2(\xi^1)^2$, where the coefficients c_0, c_1 and c_2 are found by minimizing the L^2 difference between the $\xi^2(\xi_i^1)$ and the ξ_i^2. The coordinates $\left\{\xi^1, \xi^2(\xi^1)\right\}$ defines a local parameterization $\mathbf{r}^l(\xi^1)$ of Γ in the neighbourhood of $\mathbf{y}_0^t$ (Fig. 7.3(b)):

$$\mathbf{r}^l(\xi^1) \;=\; \left\{ \begin{array}{c} \xi^1 \\ \xi^2(\xi^1) \end{array} \right\}. \tag{7.39}$$

The relationship between the local parameterization $\mathbf{r}^l(\xi^1, \xi^2)$ and the global parameterization of the interface $\mathbf{r}(\xi^1, \xi^2)$ is then found via rotation and translation operations in the form:

$$\mathbf{r}(\xi^1, \xi^2, t + dt) \;=\; (\mathbf{R}^t)^{-1}\, \mathbf{r}^l(\xi^1, \xi^2) + \mathbf{y}_0^t \tag{7.40}$$

$$\text{with } \mathbf{R}^t \;=\; [\mathbf{s}_0^t \;\; \bar{\mathbf{n}}_0^t]^T, \tag{7.41}$$

where $\mathbf{R}^t$ is the rotation matrix from the local basis $\{\mathbf{s}_0^t; \bar{\mathbf{n}}_0^t\}$ to the global basis $\{\mathbf{e}_1; \bar{\mathbf{e}}_2\}$. The parameterization $\mathbf{r}(\xi^1, t+dt)$ can now be used to ressample the interface, i.e. recalculate the closest point on the interface to the nodes $\mathbf{p}$. This is done by minimizing the distance function $d(\mathbf{r}(\xi^1, t+dt); \mathbf{p}) = 1/2\left|\mathbf{r}(\xi^1, t+dt) - \mathbf{p}\right|$ with respect to ξ^1. In two dimensions, the solution can be found explicitly by solving a cubic equation. Other geometrical quantities can also be found using the parameterization $\mathbf{r}(\xi^1, t+dt)$, such as the updated basis $\left\{\mathbf{s}^{t+dt}, \bar{\mathbf{n}}^{t+dt}\right\}$:

$$\mathbf{s}^{t+dt} = \mathbf{r}(\xi^1, t+dt)_{,1} = \mathbf{R}^t \frac{\partial \mathbf{r}^l(\xi^1, t+dt)}{\partial \xi^1} \tag{7.42}$$

$$\bar{\mathbf{n}}^{t+dt} = \mathbf{s}^{t+dt} \times \mathbf{z} / |\mathbf{s}^{t+dt} \times \mathbf{z}|. \tag{7.43}$$

Finally, a new level-set function $\phi(\mathbf{p}, t+dt)$ can be calculated as the signed distance function to Γ at nodes $\mathbf{p}$ as follows [98]:

$$\phi(\mathbf{p}, t+dt) = -\text{sgn}\left(\frac{\mathbf{y}^{t+dt} - \mathbf{p}}{|\mathbf{y}^{t+dt} - \mathbf{p}|} \cdot \bar{\mathbf{n}}_0^t\right) |\mathbf{y}^{t+dt} - \mathbf{p}|, \tag{7.44}$$

where $\mathbf{y}^{t+dt}$ is the particle associated with $\mathbf{p}$ at time $t+dt$ and the "sgn" is the sign or signum function. The reconstruction of the level set function using the local polynomial approximation of the interface is computationally inexpensive, and is used in the XFEM part of the algorithm. Let us summarize the GPM scheme in a pseudo algorithm as follows:

1. Given the initial level set function ϕ, find the coordinates of the particles that corresponds to the nodes inside the computational tube (initialization step).

2. Given the velocity field $\mathbf{v}^t$, update the position of the particle $\mathbf{y}^t$ to its current position $\mathbf{y}^{t+dt}$.

3. For each particle $\mathbf{y}_0$, find the neighbouring particles to construct a local polynomial interpolation $\mathbf{r}(\xi^1, t+dt)$ of the surface Γ around $\mathbf{y}_0$.

4. Given $\mathbf{r}(\xi^1, t+dt)$, find the new particles by projecting the nodes inside the computational tube on the surface Γ.

5. Compute the new geometrical quantities such as the normal $\bar{\mathbf{n}}^{t+dt}$ and the level set function

ϕ^{t+dt}

7.2.5 Lagrangian transport of $\hat{\mathbf{F}}$ and J

As the elastic body deforms, the material flows through the mesh, allowing finite element nodes to come in and out of the domain Ω^{s}. Because the interface $\Gamma(t)$ describing the solid domain is moving, the transport of $\hat{\mathbf{F}}$ and J cannot be described with a simple convection term, unlike when the domain boundaries are fixed [53]. To overcome this issue, herein we propose to transport deformation quantities by employing an updated Lagrangian description. It this scheme, first, the regular degrees of freedom $\bar{J}^{\mathrm{reg}}$ and $\bar{\mathbf{F}}^{\mathrm{reg}}$ are updated as follows:

1. Given the velocity field $\mathbf{v}^t$ computed with (7.33) and using the PMIM, the domain $\Omega^{\mathrm{s}}(t)$ and the interface $\Gamma(t)$ are updated to their new position $\Omega^{\mathrm{s}}(t+dt)$ and $\Gamma(t+dt)$.

2. For each node i inside $\Omega^{\mathrm{s}}(t+dt)$, material particle at its spatial location $\mathbf{x}_i^{t+dt}$ is backtracked to its position $\mathbf{x}_i^t$ at time t in accordance with the velocity field $\mathbf{v}^t$.

3. The fields J_i^t and $\hat{\mathbf{F}}_i^t$ known at time t are interpolated at point $\mathbf{x}_i^t$ in $\Omega^{\mathrm{s}}(t)$ using the extended finite element approximation.

4. Using the transport equations (7.7) and (7.8), J_i^{t+dt} and $\hat{\mathbf{F}}_i^{t+dt}$ at point $\mathbf{x}_i^{t+dt}$ are computed as:

$$J_i^{t+dt} = J_i^t(1+\nabla\cdot\mathbf{v}^t(\mathbf{x}_i^t)dt), \tag{7.45}$$

$$\hat{\mathbf{F}}_i^{t+dt} = \hat{\mathbf{F}}_i^t(\mathbf{I}+\nabla\mathbf{v}^t(\mathbf{x}_i^t)dt-\frac{1}{3}\nabla\cdot\mathbf{v}^t(\mathbf{x}_i^t)\mathbf{I}dt), \tag{7.46}$$

   and assigned to the new regular degrees of freedom $\bar{J}_i^{\mathrm{reg}} = J_i^{t+dt}$ and $\bar{\mathbf{F}}_i^{\mathrm{reg}} = \hat{\mathbf{F}}_i^{t+dt}$.

At the end of step 4, the regular degrees of freedom $\bar{J}^{\mathrm{reg}}$ and $\bar{\mathbf{F}}^{\mathrm{reg}}$ have been updated at each node inside the new domain $\Omega^{\mathrm{s}}(t+dt)$. However, since the interface has moved, the intersection between Γ and the underlying mesh has changed and the enriched degrees of freedom $\bar{J}^{\mathrm{enr}}$ and $\bar{\mathbf{F}}^{\mathrm{enr}}$ have to be updated as well. This is done by solving the following equations in the elements

cut by Γ:

$$J^{t+dt} - \tilde{J} = 0 \ \forall \ \mathbf{x} \in \Omega^{\Gamma}, \tag{7.47}$$

$$\hat{\mathbf{F}}^{t+dt} - \tilde{\mathbf{F}} = 0 \ \forall \ \mathbf{x} \in \Omega^{\Gamma}, \tag{7.48}$$

where Ω^{Γ} is the ensemble of the elements Ω_e that are cut by Γ. The terms $\tilde{J}$ and $\tilde{\mathbf{F}}$ are the updated values of the fields, which can be calculated at any points $\mathbf{x}$ inside element cuts by Γ using equations (7.45) and (7.46). The weak form of the above equations read,

$$\Big(w_J, \ (J^{t+dt} - \tilde{J})\Big)_{\Omega^{\Gamma}} = 0, \tag{7.49}$$

$$\Big(\mathbf{w}_F, \ (\hat{\mathbf{F}}^{t+dt} - \tilde{\mathbf{F}})\Big)_{\Omega^{\Gamma}} = 0, \tag{7.50}$$

and the corresponding discretized forms of are given by,

$$\mathbf{K}_J^{\text{enr}} \bar{\mathbf{J}}_g^{\text{enr}} = \mathbf{R}_J^{\text{enr}}, \tag{7.51}$$

$$\mathbf{K}_F^{\text{enr}} \bar{\mathbf{F}}_g^{\text{enr}} = \mathbf{R}_F^{\text{enr}}, \tag{7.52}$$

where $\bar{\mathbf{J}}_g^{\text{enr}}$ and $\bar{\mathbf{F}}_g^{\text{enr}}$ are the unknown global vectors of all enriched degrees of freedom; the global tangent matrices are given by,

$$\mathbf{K}_J^{\text{enr}} = \sum_e \int_{\Omega^e} (\mathbf{N}_J^{\text{enr}})^T \, \mathbf{N}_J^{\text{enr}} \ \mathrm{d}\Omega^e, \tag{7.53}$$

$$\mathbf{K}_F^{\text{enr}} = \sum_e \int_{\Omega^e} (\mathbf{N}_F^{\text{enr}})^T \, \mathbf{N}_F^{\text{enr}} \ \mathrm{d}\Omega^e; \tag{7.54}$$

tand the residuals matrices are given by,

$$\mathbf{R}_J^{\text{enr}} = \sum_e \int_{\Omega^e} (\mathbf{N}_J^{\text{enr}})^T \left(\tilde{J} - \mathbf{N}_J^{\text{reg}} \bar{J}^{\text{reg}}\right) \ \mathrm{d}\Omega^e, \tag{7.55}$$

$$\mathbf{R}_F^{\text{enr}} = \sum_e \int_{\Omega^e} (\mathbf{N}_F^{\text{enr}})^T \left(\tilde{\mathbf{F}} - \mathbf{N}_F^{\text{reg}} \bar{\mathbf{F}}^{\text{reg}}\right) \ \mathrm{d}\Omega^e. \tag{7.56}$$

In the above equations $\sum_e$ indicates the matrix assembly of the global system from the element matrices. Thus, the idea here is to simply calculate the enriched DOFs by performing the L^2 projections (7.49) and (7.50) [111] such that the deformation field quantities are accurately described in the elements cut by the interface.

7.2.6 Algorithm

The numerical strategy progressively converges towards equilibrium by solving a series of pseudo steady states of flow until the velocity vanishes everywhere in the domain. The initially non-linear problem is decomposed in linear momentum and transport equation that are solved in a staggered way as follows:

1. At time $t = 0$, $\hat{\mathbf{F}}(0) = \mathbf{I}$ and $J(0) = 1$
2. In the elastic domain $\Omega^s(t)$, given $\hat{\mathbf{F}}^t$ and J^t, compute $\mathbf{v}^{t+dt}$ by solving (7.33).
3. Given $\mathbf{v}^{t+dt}$, update the position of Γ, which yields the new domains Ω^s_{t+dt}.
4. Given $\mathbf{v}^{t+dt}$ and $\Omega^s(t+dt)$ compute regular and enriched nodal degrees of freedom for $\hat{\mathbf{F}}^{t+dt}$ and J^{t+dt}.
5. if $||\hat{\mathbf{F}}^{t+dt} - \hat{\mathbf{F}}^t|| < \text{Tol}_F$ and $||J^{t+dt} - J^t|| < \text{Tol}_J$ and $||\mathbf{v}^{t+dt}|| < \text{Tol}_v$, end of computation. Else, set $t = t + dt$ and go to step 2.

7.3 Numerical Examples

In this section, we present two numerical studies aimed at validating the CEL formulation using 1D theoretical results for uniaxial tension and simple shear loading. Next, we consider a macroindentation test typically used to characterize hydrogels and validate our numerical results with those from the standard Lagrangian formulation in Abaqus. Finally, we study the case of extreme deformations by simulating the lateral compression of a soft cylinder to demonstrate the capability of the CEL formulation.

7.3.1 Uniaxial extension of a rectangular bar

Let us consider a rectangular domain of dimensions 0.2 m (width x_1) $\times$ 0.25 m (depth x_2) containing a soft hyperelastic solid that is of dimensions 0.2 m $\times$ 0.11 m. We assume that the solid, characterized by a Young's modulus $E_Y = 15.0$ MPa and Poisson's ratio $\nu = 0.25$, is fixed at the top end and subjected to normal traction of $\bar{\mathbf{t}} = -2\hat{e}_2$ MPa at the bottom end (see Figure 7.4). The sides of the solid are constrained in the horizontal direction so that deformation gradient component $F_{11} = 1$ at all times. We discretize the domain using square (9-node and 4-node) finite elements of size $h = 0.0125$ m. We neglect the effect of gravity and assume zero body forces. The boundary and initial conditions of this simplified benchmark problem are:

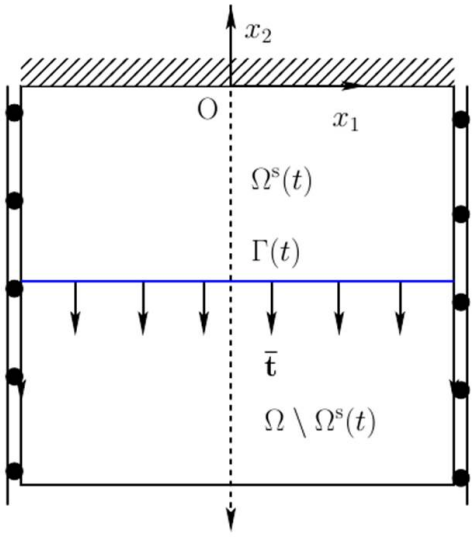

Figure 7.4: *Schematic diagram of the uniaxial extension of a soft rectangular bar. A traction of* $\bar{\mathbf{t}} = -2$ *MPa is applied to the end of the bar to deform it elastically.*

$$\left.\begin{aligned} \bar{\mathbf{t}} &= 2\hat{e}_2 \quad \text{on } \Gamma, \\ v_1(x_1 = -0.1,\ x_2) = v_1(x_1 = 0.1,\ x_2) &= 0, \\ \mathbf{v}(x_1,\ x_2 = 0) &= \mathbf{0}, \\ \mathbf{v}(\mathbf{x},\ t = 0) &= \mathbf{0}. \end{aligned}\right\} \tag{7.57}$$

As soon as the traction is applied at pseudo-time $t = 0$, the material in the solid domain moves downwards with a non-zero velocity $\mathbf{v}$ and consequently the solid elongates in the x_2

direction. The vertical component of the velocity field v_2 is negative (downward motion) and varies linearly in the x_2 direction as shown in Figure 7.5. With each pseudo-time step (or iteration) the component v_2 decreases and eventually the solid reaches its equilibrium state when $v_2 \to 0$.

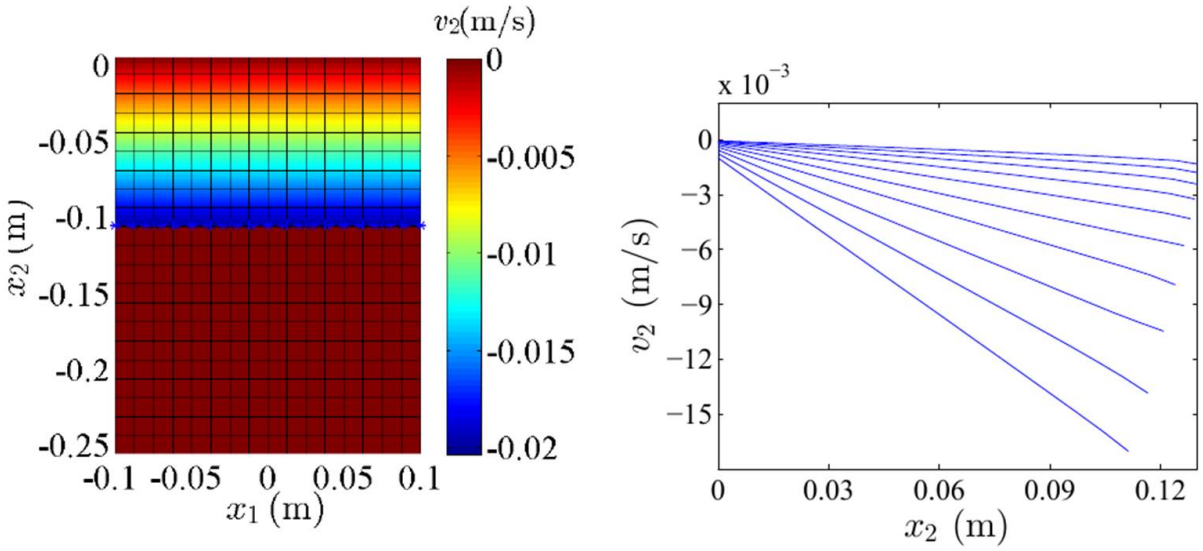

Figure 7.5: *Numerical results from the CEL formulation for the downward flow of material under applied uniaxial tension.*

Next, we investigate the performance of the mixed formulation for simulating compressible hyperelastic behavior for $\nu = 0$ and $\nu = 0.25$ using three different finite element (FE) interpolation strategies:

1. **Bilinear**: 4-node FE interpolation of $\mathbf{v}$, $\hat{\mathbf{F}}$ & J

2. **Biquadratic**: 9-node FE interpolation of $\mathbf{v}$, $\hat{\mathbf{F}}$ & J

3. **Mixed**: 9-node FE interpolation of $\mathbf{v}$ and 4-node FE interpolation of $\hat{\mathbf{F}}$ & J

In the case of uniaxial extension in x_2, we have $J = F_{22} > 1$, since $F_{11} = F_{33} = 1$ and all other components of $\mathbf{F}$ vanish. Therefore, it is sufficient to only observe the behavior of F_{22} from $t = 0$ until equilibrium. In the following figures, we plot the variation of F_{22} in the x_2 direction at every 50 iterations. Note that the length of the solid increases and the change in F_{22} decreases with each iteration as we approach equilibrium. We can see from Figure 7.6 that for

$\nu = 0$ the bilinear and mixed interpolation strategies work equally well, whereas the biquadratic interpolation strategy suffers from spurious oscillations close to the traction boundary. From Figure 7.6 we can observe that for $\nu = 0.25$ both the bilinear and biquadratic interpolation strategies suffer from spurious oscillations, whereas the mixed interpolation strategy is least affected. This study demonstrates that the mixed interpolation strategy leads to better accuracy and stability compared to the uniform interpolation strategies.

We next investigate the accuracy of the scheme by comparing the analytical and numerical equilibrium stress versus deformation curves. Using the constitutive law given in equation (7.15), we can derive the analytical expression for the Cauchy stress component σ_{22} as,

$$\sigma_{22} \quad = \quad \frac{1}{F_{22}} \left[\kappa \log(F_{22}) + \frac{2}{3} \mu F_{22}^{-2/3} (F_{22}^2 - 1) \right] \tag{7.58}$$

Now, for different values of applied normal traction $\bar{\mathbf{t}} \cdot \hat{e}_2 = \sigma_{22} \in [-4\ 4]$ MPa we numerically evaluate the equilibrium value of F_{22} for three different values of Poisson's ratio $\nu = 0$, 0.25 and 0.45. These numerical results are then plotted as a scatter over the analytical solution (solid lines) given in (7.58). The excellent match of the numerical results with the analytical solution in Figure 7.7(a) illustrates the accuracy of the method. We also evaluate the variation of the error in the reference (initial) volume of the solid at each iteration to check for the conservation of mass. The initial volume $V^{(0)} = 0.044$ m^3 and at each iteration (i) we can calculate the percentage error as,

$$\epsilon^{(i)} = \frac{V^{(0)} - V^{(i)}}{V^{(0)}} \times 100, \quad \text{where} \quad V^{(i)} = \int_{\Omega^s} \frac{1}{J^{(i)}} \, dV. \tag{7.59}$$

The variation of $\epsilon^{(i)}$ with iterations is plotted in Figure 7.7(b). As we can see the error initially oscillates and after 500 iterations or so it gradually reaches a steady state. However, it is important to note that percentage error $\epsilon^{(i)} < 0.06$ (i.e. error is 0.0006) indicating that the scheme is quite accurate in conserving the mass of the elastic solid. Since the volume error is so low at all times, the convergence criterion is based on the L^2 error in velocity or deformation gradient.

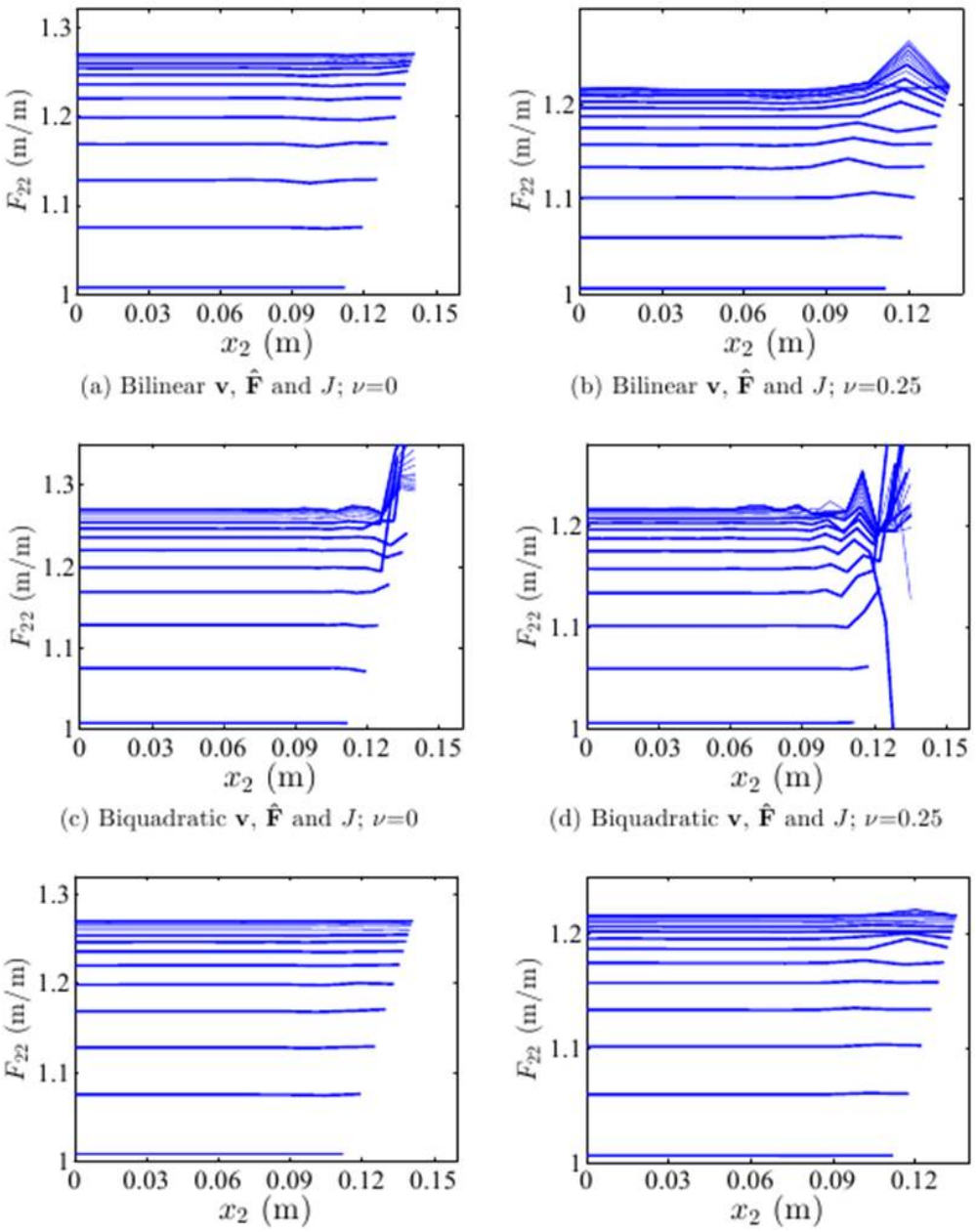

Figure 7.6: *Performance of the mixed element formulation for uniaxial tension test. Variation of F_{22} along the length of domain is shown for bilinear, biquadratic and mixed formulation for two compressible materials with Poisson's ratio ν=0 (left column) and ν=0.25 (right column).*

7.3.2 Simple shear of a rectangular block

Let us now study the shear flow of a solid under applied shear traction. Once again, we consider a rectangular domain of dimensions 0.2 m × 0.25 m and solid domain of dimensions 0.2 m ×

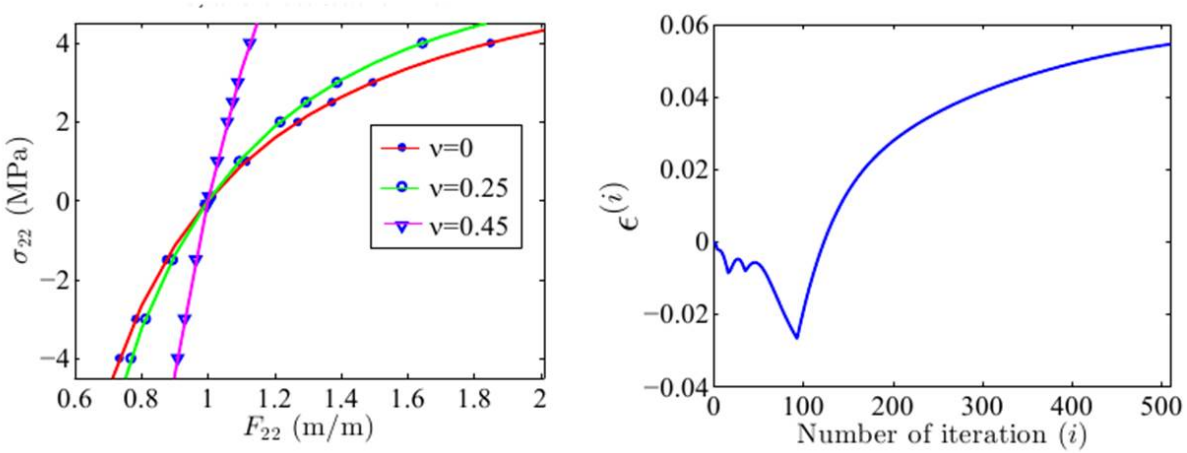

Figure 7.7: *Validation and error analysis of numerical results from the CEL formulation for uniaxial tension test*

0.11 m. The domain is discretized with an element size $h = 0.0125$ m. We assume the Young's modulus $E_Y = 15.0$ MPa and Poisson's ratio $\nu = 0.25$. The solid is fixed at the top end and subjected to shear traction of $\bar{\mathbf{t}} = -0.4\hat{e}_1$ MPa at the bottom end. On the left and right boundaries, we impose zero velocity in the $\mathbf{e_2}$ direction to strictly prescribe horizontal shear flow. The boundary and initial conditions of this simplified benchmark problem are,

$$\left.\begin{aligned} \bar{\mathbf{t}} &= -0.4\hat{e}_1 \quad \text{on } \Gamma, \\ \hat{\mathbf{F}}(x_1 = -0.1,\ x_2 \leq 0.11) = \hat{\mathbf{F}}(x_1 = 0.1,\ x_2) &= \mathbf{I}, \\ J(x_1 = -0.1,\ x_2) = J(x_1 = 0.1,\ x_2) &= 1, \\ \mathbf{v}(x_1,\ x_2 = 0) &= \mathbf{0}, \\ \mathbf{v}(\mathbf{x},\ t = 0) &= \mathbf{0}. \end{aligned}\right\} \tag{7.60}$$

We discretize the domain using the mixed interpolation strategy as discussed in the previous section with an element length of $h = 0.0125$ m in both x_1 and x_2 directions. Due to the applied shear, the material flows from right to left as shown in Figure 7.8a, so the velocity is negative. In the case of simple shear flow in x_1 direction, we have $F_{12} > 0$, $F_{22} = F_{11} = F_{33} = 1$ and all other components of $\mathbf{F}$ are zero. Therefore, it is sufficient to only observe the behavior of F_{12} from $t = 0$ until equilibrium.

We next plot the match between the analytical and numerical equilibrium stress versus

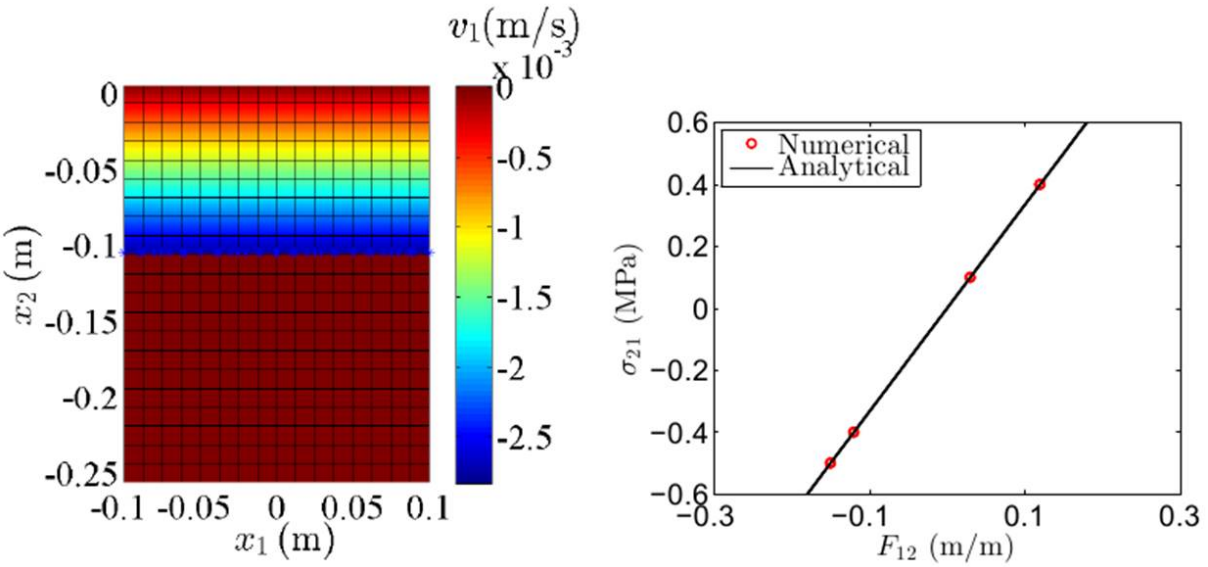

Figure 7.8: *Numerical results from the CEL formulation for the shear flow of material under applied shear traction. The results are in agreement with theory, thus, validating our scheme.*

deformation curves. From the constitutive relation in equation (7.15), we can write the analytical expression for the Cauchy stress component $\sigma_{12} = \mu F_{12}$. For four different values of applied shear stress, we plot the numerical results (scatter) against the analytical solution (solid line) in Figure 7.8(b). We observe an excellent agreement between theory and simulation with a linear response in the applied stress range. Since shear flow is isochoric, the error in volumetric deformation identically vanishes.

7.3.3 Indentation of a rounded rectangular solid

Let us consider a rounded rectangular solid made up of the same soft material as in the previous example ($E_Y = 15.0$ MPa and $\nu = 0.25$). The dimensions of the straight portion of the rounded rectangle is 3.5 cm $\times$ 0.92 cm and the rounded edges are semicircles with radius 0.46 cm. The solid domain and test configuration are chosen to mimic a hydrogel placed onto a relatively rigid substratum, typically seen in tissue printing. The total computational domain is 5.2 cm $\times$ 1.2 cm that is discretized using an element size $h = 0.1$ cm. A Gaussian-shaped vertical pressure field with amplitude p (MPa) is prescribed on the top surface centered at mid-span as follows:

$$p(x_1) \quad = \quad p_0 \exp\left(-x_1^2/\alpha^2\right) \tag{7.61}$$

where $\alpha = 0.25$ cm is the standard deviation and represents the spread of the applied pressure around the central point. The solid is restrained in the x_1 and x_2 directions on the bottom surface. It is important to note that the bottom surface is restrained in the x_1 and x_2 directions by enforcing these Dirichlet conditions on the underlying grid nodes that are closest to the interface, and not on the interface itself. In order to limit the error created in doing so, we position the rounded rectangle such as its bottom interface remains very close to the nodes of the underlying mesh. Alternatively, Dirichlet boundary conditions can easily be enforced directly on the interface with the use of Lagrange multipliers. The geometry and the boundary conditions are illustrated in the Figure 7.9. The initial undeformed shape and the final or equilibrium deformed shape of the solid under an applied pressure amplitude of $p_0 = 6$ MPa are shown in Figures 7.10a and 7.10b. The surface plot of the Jacobian determinant J in Figure 7.10b shows that the material experiences compression at the center ($J < 1$) and some tension as we move towards the ends; however, far away from the center the material is unstressed $J = 1$.

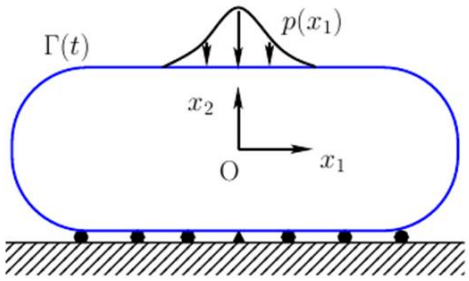

Figure 7.9: *Schematic diagram of the indentation of soft solid. A Gaussian type pressure load is applied to simulate the contact between a rigid indenter and the solid. At the bottom the solid is allowed to slip, however, due to symmetry the center node is pinned.*

To benchmark our simulation, we analyzed the problem with a fully Lagrangian finite element formulation (using the software Abaqus with the UHYPER subroutine). For $p_0 = 6$ MPa, the deformed shape of the top surface of the solid and the variation of J obtained from Abaqus and our coupled Eulerian-Lagrangian (CEL) formulation are plotted against each other in Figure 7.11a and Figure 7.11b, respectively. The maximum error in the displacement of the top surface δ is 1.28 % and the maximum error in Jacobian J along the free surface is 0.39 %. Next, we check the mass conservation behavior of the CEL implementation by plotting the error in mass

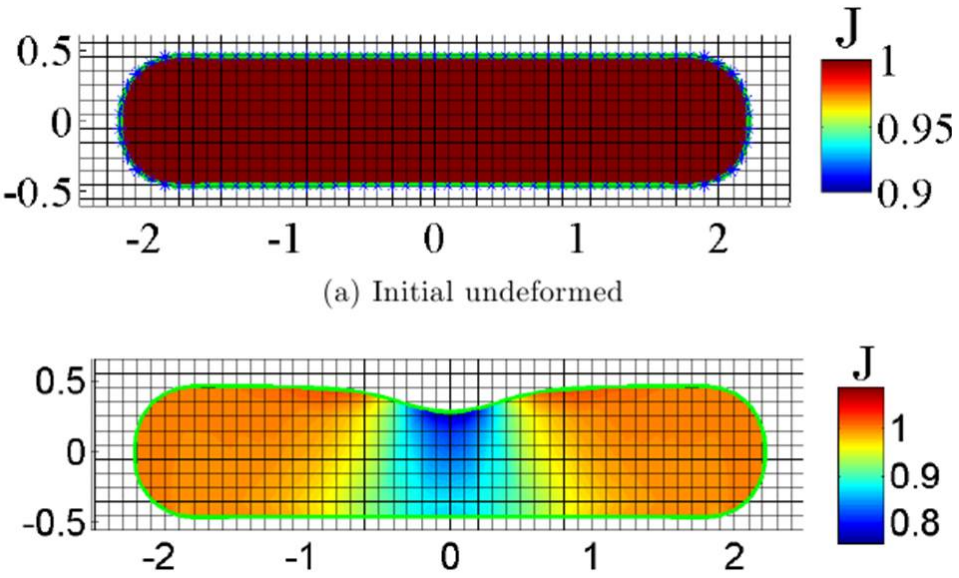

(a) Initial undeformed

Figure 7.10: *Numerical results showing the Jacobian determinant of the deformation and the shape evolution of a soft rounded rectangular solid for $p_0 = 6$ MPa during indentation.*

ϵ_{mass} with iterations or pseudo-time steps, as given in Figure 7.11c. The error increases initially, reaches a maximum around 100^{th} iteration and then decreases to reach a steady state value as the equilibrium is attained. We also find that the L^2 norm of error in Von Mises stress and pressure decreases very rapidly with element size h, as shown in Figure 7.11d. Next, to demonstrate the robustness and viability of the approach, we apply a larger pressure amplitude of $p_0 = 40$ MPa so as to simulate large material distortions. The final equilibrium shape of the solid is shown in Figure 7.12a where we note that material below the load undergoes large compressive strains with $J = 0.5$ (that is, the material is confined to half it original volume). The evolution of the solid boundary with pseudo-time is then shown in Figure 7.12b. As we can see that interface initially moves with a high velocity and eventually reaches its final equilibrium shape after about 150 iterations. It is to be noted that at even moderate load of $p_0 = 10$ MPa the UHPYER implementation in Abaqus crashed just after a few iterations due to convergence issues. For higher loads, ALE algorithms can work; however, CEL formulations have the advantage that it can be used to simulate extreme deformations without requiring mesh moving or remeshing schemes.

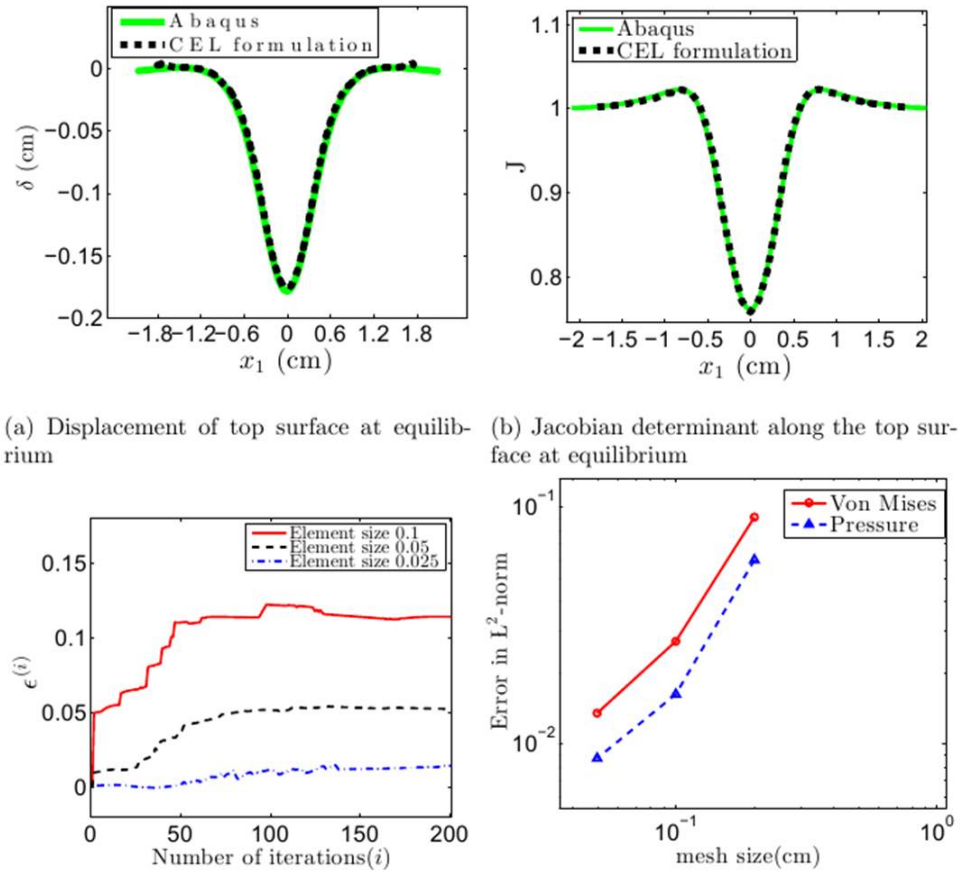

(a) Displacement of top surface at equilibrium

(b) Jacobian determinant along the top surface at equilibrium

Figure 7.11: *Validation of numerical results from the CEL formulation with the standard Lagrangian formulation in the commercial software Abaqus for the indentation of a rounded rectangular solid. The L^2 error is calculated by taking the Abaqus solution from a very fine mesh as the exact solution.*

7.3.4 Lateral compression of a cylinder

In the previous two benchmark examples, the interface remained flat at all times. Herein, we shall consider an example problem with a curved interface and demonstrate the ability of our formulation to handle its evolution as the solid undergoes very large deformation. Let us consider an elastic compressible cylinder of radius $R = 0.81$ cm, with $E_Y = 15.0$ MPa and $\nu = 0.25$, which is compressed between two planes on the top and bottom. The total computational domain is 3.2 cm $\times$ 2.4 cm is discretized using an element size $h = 0.08$ cm. Plane strain conditions apply and body forces are neglected. We set up the problem with four-fold symmetry about the origin.

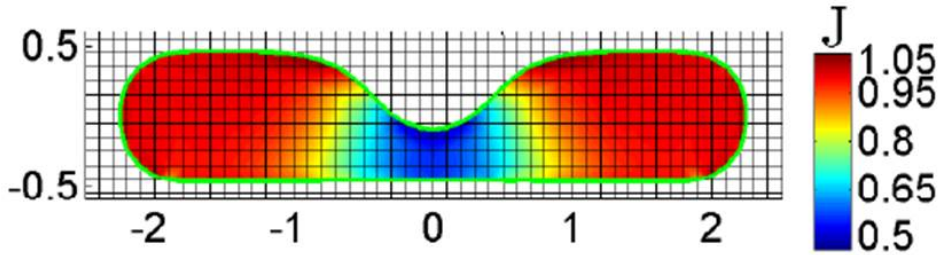

(a) Equilibrium deformed

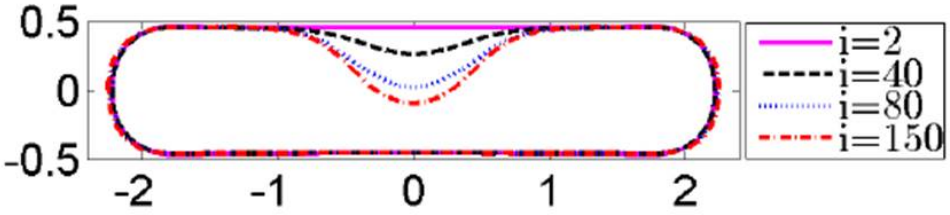

Figure 7.12: *Numerical results showing the Jacobian determinant of the deformation and the shape evolution of a soft rounded rectangular solid for $p_0 = 40$ MPa during indentation. Abaqus UHYPER subroutine did not converge for this high load case, which demonstrates the robustness of the current CEL formulation.*

The boundary and initial conditions for this problem are,

$$\left.\begin{aligned} v_2(x_1,\ x_2 = 0) = v_1(x_1 = 0,\ x_2) &= \mathbf{0}, \\ \mathbf{v}(\mathbf{x},\ t = 0) &= \mathbf{0}, \\ \hat{\mathbf{F}}(\mathbf{x},\ t = 0) &= \mathbf{I}, \\ J(\mathbf{x},\ t = 0) &= 0. \end{aligned}\right\} \tag{7.62}$$

We define a vertical force that is applied on the portion of interface Γ that is within a certain distance $d_0 =$ from either of the planes. This force function is defined as an exponential repulsive force to avoid penetration between the cylinder and the two compressive planes:

$$\begin{cases} \bar{\mathbf{t}}(\mathbf{x}) = (\phi(\mathbf{x}) - d_0)\exp((d_0 - \phi(\mathbf{x}))\mathbf{e}_2 & \text{if } \ \phi(\mathbf{x}) \leq d_0 \\ \bar{\mathbf{t}}(\mathbf{x}) = 0 & \text{if } \phi(\mathbf{x}) > d_0 \end{cases} \tag{7.63}$$

where d_0 represent a cut-off distance over which the repulsive force is applied, and is taken here to be 1% of the radius of the cylinder. As the planes move closer, only a portion of solid cylinder is

subjected to compression, which is clear from the contour plot of J in Figure 7.13. For example, in Figure 7.13(b) we can see that the material in the center is compressed (i.e. $J < 1$), whereas the material on the sides is not (i.e. $J \approx 1$). As the planes move even closer the solid deforms into a elongated shape as shown in Figure 7.13(c) and (d), when the material at certain points is compressed to less than half its initial volume ($J \approx 0.4$). Note that the planes are gradually moved to the final position shown in Figure 7.13(d) until iteration $i = 80$ and then held in position. At iteration $i = 112$, the velocity in the domain vanishes (less than tolerance), so the stress in the solid is at static equilibrium. As opposed to the presented method, a Lagrangian finite element formulation would suffer from large mesh distortion in this deformation regime.

To check whether the numerical implementation conserves mass, we consider three mesh sizes as shown in Table 7.1 and calculate the % error in V_0 after each iteration (pseudo-time step). As expected the coarsest mesh has the highest % error of 1.6 and with the refinement of mesh, the % error reduces to as low as 0.16.

Element size	Element in X-dir	Element in Y-dir	% Error
0.16	40	30	1.6
0.08	80	60	0.28
0.04	160	120	0.16

Table 7.1: *Percentage error in elastic body mass for different finite element mesh sizes for the deforming cylinder under lateral compression at equilibrium.*

7.4 Conclusion

We presented a stable and convergent coupled Eulerian-Lagrangian (CEL) formulation for modeling the large deformations of soft compressible hyperelastic materials. The equilibrium equations are solved in an Eulerian framework and the transport equations of deformation gradient and Jacobian determinant are solved in an updated Lagrangian framework; thus, the strategy is exactly the opposite of that employed in an arbitrary Lagrangian-Eulerian (ALE) formulation. The mixed element formulation, although originally proposed in [53] for handling incompressibility, is observed to improve the accuracy of the numerical scheme even in the case of compressible media. The numerical results of uniaxial tension and simple shear studies agree well with theory

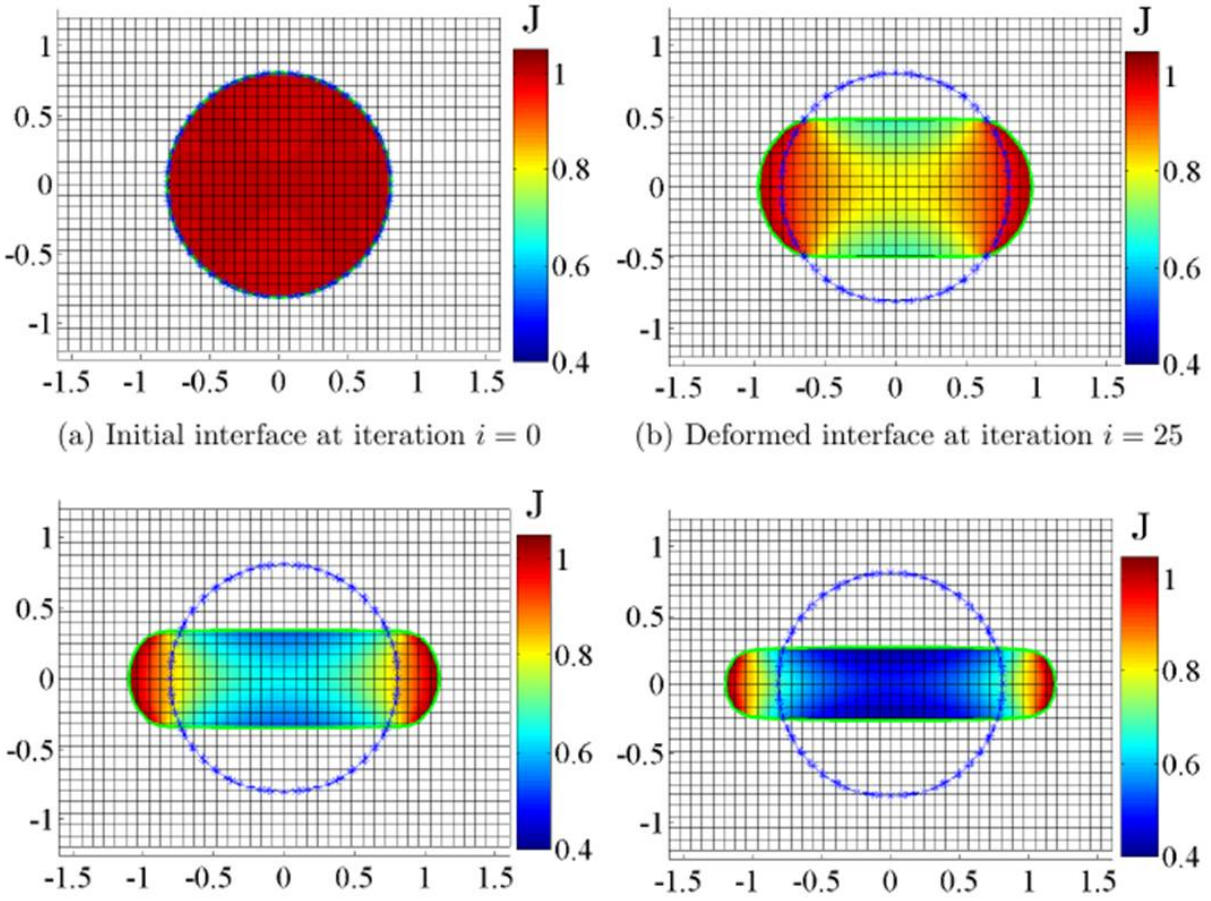

Figure 7.13: *Numerical results from the CEL formulation for lateral compression of a circular cylinder. The cylinder is located between two rigid planes on the top and bottom that moved towards each other so that four fold symmetry is maintained. The planes are gradually moved to the final position shown in (d) until iteration* $i = 80$ *and then held in position. At iteration* $i = 112$*, the velocity in the domain vanishes (less than tolerance) so that the stress in the solid is at static equilibrium.*

indicating the accuracy and feasibility of the approach. The numerical study of indentation of a rounded rectangular block demonstrates the robustness of the implementation as compared standard Lagrangian finite element implement in Abaqus. It is clear that the presented formulation is attractive when materials undergo extreme deformation and distortions such as that observed for very soft and visco-elastic media. It can also be an interesting strategy for modeling fluid-structure interactions using a fully eulerian framework. This class of problem is often encountered in biology [159, 61, 62, 161] (e.g. in cell mechanics and growth) or in studying the mechanics of soft-matter [42, 188, 97].

Appendix: Element tangent matrix for the equilibrium equation

In equation (7.33), the tangent matrix corresponding to the linear system obtained by discretizing the equilibrium equation is given by,

$$\begin{aligned}\mathbf{K}_{\mathbf{v}} &= \int_{\Omega^e} \left[\mathbf{B}_{\mathbf{v}}^T \frac{\partial \boldsymbol{\sigma}}{\partial \hat{\mathbf{F}}} \left(-\nabla \tilde{\hat{\mathbf{F}}} \bar{\mathbf{N}}_{\mathbf{v}} + \tilde{\hat{\mathbf{F}}} \mathbf{B}_{\mathbf{v}} - \frac{1}{3} \tilde{\hat{\mathbf{F}}} \check{\mathbf{B}}_{\mathbf{v}} \right) \right. \\ &+ \left. \mathbf{B}_{\mathbf{v}}^T \frac{\partial \boldsymbol{\sigma}}{\partial J} \left(-\nabla \tilde{J}^T \bar{\mathbf{N}}_{\mathbf{v}} + \tilde{J} \check{\mathbf{B}}_{\mathbf{v}} \right) \right] \, \mathrm{d}\Omega \end{aligned} \tag{7.64}$$

In the above equation,

$$\begin{aligned}\frac{\partial \boldsymbol{\sigma}}{\partial J} &= \frac{1}{J} \left[\frac{\kappa}{J} \{1 \;\; 0 \;\; 0 \;\; 0\}^T - \tilde{\boldsymbol{\sigma}} \right]_{4\times 1} \\ \frac{\partial \boldsymbol{\sigma}}{\partial \hat{\mathbf{F}}} &= \begin{bmatrix} \delta\sigma_{1111} & \delta\sigma_{1122} & \delta\sigma_{1112} & \delta\sigma_{1121} \\ \delta\sigma_{2211} & \delta\sigma_{2222} & \delta\sigma_{2212} & \delta\sigma_{2221} \\ \delta\sigma_{1211} & \delta\sigma_{1222} & \delta\sigma_{1212} & \delta\sigma_{1221} \\ \delta\sigma_{2111} & \delta\sigma_{2122} & \delta\sigma_{2112} & \delta\sigma_{2121} \end{bmatrix}_{4\times 4} \\ \delta\sigma_{ijlm} &= \frac{\mu}{J} \left(\delta_{li} \hat{F}_{jm} + \delta_{lj} \hat{F}_{im} - \frac{2}{3} \delta_{ij} \hat{F}_{lm} \right). \end{aligned}$$

The tilde superscript $\tilde{(\cdot)}$ indicates that $\nabla \tilde{\hat{\mathbf{F}}}$, $\tilde{\hat{\mathbf{F}}}$ and $\tilde{\hat{J}}$ are interpolated using the fields from the previous time step $\hat{\mathbf{F}}^t$ and J^t as follows:

$$\begin{aligned}\nabla \tilde{\hat{\mathbf{F}}} &= \left[\mathbf{B}_{\mathbf{F}1} \bar{\mathbf{F}}(t) \;\; \mathbf{B}_{\mathbf{F}2} \bar{\mathbf{F}}(t) \right]_{4\times 2} \\ \nabla \tilde{J} &= \mathbf{B}_J \bar{J}(t) \\ \tilde{\hat{\mathbf{F}}} &= \left[\bar{\mathbf{N}}_{\mathbf{F}1} \bar{\mathbf{F}}(t) \;\; \bar{\mathbf{N}}_{\mathbf{F}2} \bar{\mathbf{F}}(t) \;\; \bar{\mathbf{N}}_{\mathbf{F}3} \bar{\mathbf{F}}(t) \;\; \bar{\mathbf{N}}_{\mathbf{F}4} \bar{\mathbf{F}}(t) \right] \\ \tilde{J} &= \bar{\mathbf{N}}_J \bar{J}(t) \end{aligned}$$

and the matrices $\mathbf{B}_{\mathbf{F}k}$, $\mathbf{B}_J$, $\mathbf{N}_{\mathbf{F}l}$ and $\check{\mathbf{B}}_{\mathbf{v}}$ are written, for $k = 1, 2$ and $l = 1, 2, 3, 4$:

$$\begin{aligned}
\mathbf{B}_{\mathbf{F}k} &= \left[\mathbf{B}^1_{\mathbf{F}k},\ ...,\ \mathbf{B}^4_{\mathbf{F}k},\ \ \mathcal{S}^1\mathbf{B}^1_{\mathbf{F}k},\ ...,\ \mathcal{S}^4\mathbf{B}^4_{\mathbf{F}k}\right]_{4\times 32} \\
\hat{\mathbf{B}}_J &= \left[\mathbf{B}^1_J,\ ...,\ \mathbf{B}^4_J,\ \ \mathcal{S}^1\mathbf{B}^1_J,\ ...,\ \mathcal{S}^4\mathbf{B}^4_J\right]_{2\times 8} \\
\mathbf{N}_{\mathbf{F}l} &= \left[\mathbf{N}^1_{\mathbf{F}l},\ ...,\ \mathbf{N}^4_{\mathbf{F}l},\ \ \mathcal{S}^1\mathbf{N}^1_{\mathbf{F}k},\ ...,\ \mathcal{S}^4\mathbf{N}^4_{\mathbf{F}l}\right]_{4\times 32} \\
\check{\mathbf{B}}_{\mathbf{v}} &= \left[\check{\mathbf{B}}^1_{\mathbf{v}},\ ...,\ \check{\mathbf{B}}^9_{\mathbf{v}},\ \ \mathcal{S}^1\check{\mathbf{B}}^1_{\mathbf{v}},\ ...,\ \mathcal{S}^9\check{\mathbf{B}}^9_{\mathbf{v}}\right]_{1\times 36}
\end{aligned}$$

with

$$\begin{aligned}
\mathbf{B}^I_{\mathbf{F}1} &= \begin{bmatrix} \frac{\partial \hat{N}^I}{\partial x_1} & 0 & 0 & 0 \\ 0 & \frac{\partial \hat{N}^I}{\partial x_1} & 0 & 0 \\ 0 & 0 & \frac{\partial \hat{N}^I}{\partial x_1} & 0 \\ 0 & 0 & 0 & \frac{\partial \hat{N}^I}{\partial x_1} \end{bmatrix}_{4\times 4} \\
\mathbf{B}^I_{\mathbf{F}2} &= \begin{bmatrix} \frac{\partial \hat{N}^I}{\partial x_2} & 0 & 0 & 0 \\ 0 & \frac{\partial \hat{N}^I}{\partial x_2} & 0 & 0 \\ 0 & 0 & \frac{\partial \hat{N}^I}{\partial x_2} & 0 \\ 0 & 0 & 0 & \frac{\partial \hat{N}^I}{\partial x_2} \end{bmatrix}_{4\times 4} \\
\mathbf{B}^I_J &= \begin{bmatrix} \frac{\partial \hat{N}^I}{\partial x_1} & \frac{\partial \hat{N}^I}{\partial x_2} \end{bmatrix}_{2\times 1} \\
\check{\mathbf{B}}^1_{\mathbf{v}} &= \begin{bmatrix} \frac{\partial N^I}{x_1} & \frac{\partial N^I}{x_2} \end{bmatrix}_{1\times 2}.
\end{aligned}$$

$$\mathbf{N}_{\mathbf{F}1} = \begin{bmatrix} \hat{N}^I & 0 & 0 & 0 \\ 0 & 0 & 0 & 0 \\ 0 & 0 & \hat{N}^I & 0 \\ 0 & 0 & 0 & 0 \end{bmatrix}_{4\times4} \qquad \mathbf{N}_{\mathbf{F}2} = \begin{bmatrix} 0 & 0 & 0 & 0 \\ 0 & \hat{N}^I & 0 & 0 \\ 0 & 0 & 0 & 0 \\ 0 & 0 & 0 & \hat{N}^I \end{bmatrix}_{4\times4}$$

$$\mathbf{N}_{\mathbf{F}3} = \begin{bmatrix} 0 & 0 & \hat{N}^I & 0 \\ 0 & 0 & 0 & 0 \\ 0 & 0 & \hat{N}^I & 0 \\ 0 & 0 & 0 & 0 \end{bmatrix}_{4\times4} \qquad \mathbf{N}_{\mathbf{F}4} = \begin{bmatrix} 0 & 0 & 0 & 0 \\ 0 & 0 & 0 & \hat{N}^I \\ 0 & 0 & 0 & 0 \\ 0 & 0 & 0 & \hat{N}^I \end{bmatrix}_{4\times4}$$

Chapter 8

A thermodynamical model for stress-fiber organization in contractile cells

Numerous experimental and theoretical efforts have been directed toward explaining the biophysical mechanisms underlying the structural reorganization of SFs in different mechanical environments [160]. Techniques such as fluorescent staining of SFs in living cells coupled with high spatial and temporal resolution microscopy have permitted to measure the volume fraction and orientation of SFs when subjected to constant or cyclic stretch or to different substrate stiffnesses. Further experiments on epithelial cells and fibroblasts have demonstrated that contractility and SF density increase with substrate stiffness while SF alignment is strongly influenced by substrate anisotropy [182, 66]. In addition, SFs were shown to align in or perpendicular to the direction of maximum stretch respectively for constant or cyclic stretch [144, 88, 151]. To explain the latter, Wang and co-workers [175] proposed a physical model in which perturbations in the SFs strain energy are assumed to cause their disassembly, and were able to accurately predict SFs orientations in the case of uniaxial cyclic stretch. More recently, Stamenovitch *et al* [147] used the Maxwell stability criteria on the global mechano-chemical energy of the SF-FA complex to find SFs orientation in cells subjected to constant uniaxial stretch. While those

models were successful at capturing the alignment of SFs with respect to stretch, the effect of the substrate stiffness was not considered.

In this chapter we formulate a general thermodynamical model that captures key mechanisms of SF organization in contractile cells on substrate of variable stiffness and subjected to arbitrary stretching conditions. The model is based on the experimental observations that SF self-assembly and disassembly are governed by intracellular stress an strain: contractile stress promotes assembly and stabilizes existing SFs [36, 172] while the elastic deformation of SFs causes their disassembly [96]. We show here that by considering these two fundamental mechanisms along with the viscoelasticity of SFs [93], it is possible to predict the density and principal orientation of SFs in cells that are subjected to a variety of mechanical environments.

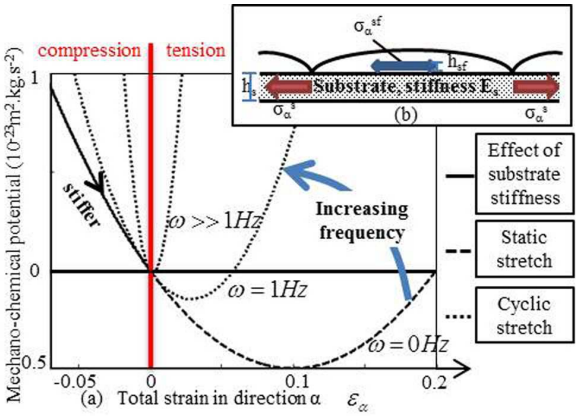

Figure 8.1: *Mechano-chemical potential* $\mu_\alpha^{sf,mech}$ *in direction* α *as a function of strain for different stretch frequencies (a). SFs assemble in direction* α *when* $\mu_\alpha^{sf,mech}$ *decreases, and disassemble when* $\mu_\alpha^{sf,mech}$ *increases. Mechanical equilibrium at angle* α*(b)*

8.1 Model formulation

For the purpose of this study, a cell is considered as a solution (the cytosol) in which a population of soluble contractile units isotropically distributed (made of actin and myosin) coexist with their polymerized form (SFs), consisting of long filaments of polar volume fraction ϕ_α^{sf}, with α as the angle that characterizes the direction of SFs. The chemical stability of unassembled and assembled contractile units, respectively, may be written in terms of their respective chemical

potentials μ^{cu} and μ_α^{sf} as follows: [122, 140, 48]:

$$\mu^{cu} = \mu_0^{cu} + k\Theta \ln \phi^{cu} \tag{8.1}$$

$$\mu_\alpha^{sf} = \mu_0^{sf} + k\Theta \left(\ln \phi_\alpha^{sf} + a_\mu \left(\frac{\phi_\alpha^{sf}}{\phi^*} \right)^{\frac{5}{4}} \right) + \mu_\alpha^{sf,mech} \tag{8.2}$$

where k is the Boltzmann constant and Θ is the absolute temperature. Note that the subscript α denotes quantities evaluated in the α-direction. The first term in (8.1) and (8.2) denotes the reference chemical potential while the second term represents the entropy of configuration. The overlapping volume fraction ϕ^* and the a_μ coefficient are correction terms for the mixing entropy of semi-dilute polymers which have not been determined for actin solutions. They are neglected in the present work since their role is not expected to impact the general results of this study. To capture the influence of stress and strain on SF stability, the chemical potential μ_α^{sf} possesses a mechanical contribution $\mu_\alpha^{sf,mech}$ [122] :

$$\mu_\alpha^{sf,mech} = \frac{V_{cu}}{T} \int_0^T \left(-\sigma^* \varepsilon_\alpha + \frac{1}{2} E_{sf}(\omega) \varepsilon_\alpha^2 \right) dt \tag{8.3}$$

where T is a stretch cycle period and V_{cu} is the volume of a contractile unit. The first term in the integral corresponds to the lost free energy due to acto-myosin contraction (σ^*) and captures the fact that contractility has a stabilizing effect on SFs, as found in experimental studies [36, 172]. In contrast, the second (positive) term contributes to SFs dissociation due to an increase in their elastic energy during stretch ε_α in direction α. Furthermore, a key component of the proposed model is the dependency of elastic modulus E_{sf} on the stretching frequency ω to capture the viscoelasticity of SFs. Here, we describe SF stiffening with loading frequency ω with a function $E_{sf}(\omega)$ of the form [171]:

$$E_{sf}(\omega) = E_l + E_v \log(1 + 9\omega) \tag{8.4}$$

where E_l and E_v characterize the static and dynamic stiffnesses of SFs at frequency $\omega = 1Hz$, respectively. Without loss of generality, we assume here that cells are subjected to sinusoidal strain variation $\varepsilon_\alpha = \bar{\varepsilon}_\alpha + \tilde{\varepsilon}_\alpha \cos(2\pi t/T)$ which, when substituted in Eq.(8.3) leads to the fol-

lowing mechano-chemical potential:

$$\mu_\alpha^{sf,mech} = \frac{(E_l + E_v \log(1+9\omega))}{2}\left(\bar{\varepsilon}_\alpha^2 + \frac{\tilde{\varepsilon}_\alpha^2}{2}\right) - \sigma^* \bar{\varepsilon}_\alpha \tag{8.5}$$

The above expression describes how contractile stress as well as static and cyclic stretch influences the chemical stability of SFs (Fig.8.1.a.). At high frequency (1 Hz cyclic stretch), SFs appear stiffer and the disassembling elastic energy $1/2E_{SF}(\omega)\varepsilon_\alpha^2$ is predominant over the contractile work. A rise in the stretch amplitude therefore increases the mechano-chemical potential $\mu_\alpha^{sf,mech}$ and has a disassembling effect on the SFs. Inversely, at a low frequency ($\omega \to 0$), softer SFs emphasizes the stabilizing role of contractile stress $\sigma^\star$ resulting in SF stabilization with increasing stretch. However, as stretch increases above a critical value at which $\mu_\alpha^{sf,mech}$ is minimum ($\varepsilon_\alpha^{crit} = \sigma^*/E_l$), the stored elastic energy becomes dominant and SFs fall into a disassembly regime.

To assess the behavior of our thermodynamical model, we consider a system made of a confluent population of cells adhering to a homogeneously deforming thin substrate (Fig.8.1.b) whose linear elasticity is governed by its Young's modulus E and Poisson's ratio ν. In these conditions, the state of any material point in the system is given by chemical and mechanical equilibrium as:

$$(a)\ \ \mu_\alpha^{sf} = \mu^{cu}\ \ \forall \alpha \in [0,\pi]\ \ , \quad (b)\ \sum_{\beta=s,sf} \boldsymbol{\sigma}^\beta = \bar{\boldsymbol{\sigma}} \tag{8.6}$$

where $\bar{\boldsymbol{\sigma}}$ denotes the externally applied stress and the internal stress arises from a combination of substrate elasticity and SF contractility. Following standard elasticity theory, the components of the substrate stress are written as $\sigma_{ij}^s = E/(1+\nu)\epsilon_{ij} + E\nu/((1+\nu)(1-2\nu))\delta_{ij}\epsilon_{kk}$, where δ_{ij} is the Kronecker delta. In contrast, the directional SF stress is evaluated in specific direction α and is comprised of both a contractile and a passive elastic components weighted by the polar volume fraction as follows: $\sigma_\alpha^{sf} = \phi_\alpha^{sf}\,(\sigma^\star + E_{sf}(\omega)\varepsilon_\alpha)$. Using expressions (8.1) and (8.2) in (8.6) and invoking mass conservation between SF and unassembled contractile units allows us

to solve for the volume fraction of SF and soluble contractile units as follows:

$$\phi_\alpha^{sf} = \phi^{cu} \exp\left(-\frac{\mu_0^{sf} - \mu_0^{cu} + \mu_\alpha^{sf,mech}(\varepsilon_\alpha)}{k\Theta}\right) \tag{8.7}$$

$$\phi^{cu} = \phi - \frac{1}{\pi}\int_0^\pi \phi_\alpha^{sf} d\alpha \tag{8.8}$$

where ϕ is the total volume fraction of contractile units (assembled and unassembled) in the cell (taken to be 5% in this chapter). These nonlinear equations can be solved numerically to determine the direction and density of SF in cell's subjected to various mechanical environments. In our computations, a set of commonly accepted material parameters was chosen: the temperature is 310K, the SF stiffnesses E_l and E_v are $100kPa$ [89] and the isometric contractile stress generated by a SF through acto-myosin interaction $\sigma^\star$ is estimated to be $10kPa$ (obtained with a tensile force of $300pN$ and a cross sectional area of 0.03 μm^2). Furthermore, SF contractile units are of the same length of a SF sarcomere ($1\mu m$), and of diameter $10nm$. The difference in the reference chemical potential $\mu_0^{sf} - \mu_0^{cu}$ is set to $-4k\Theta$ such that the average force on micropillars generated by the isotropic contractile stress of the cell $\sigma^c = \phi^{sf}\sigma^*$ on a very stiff substrate matches the one from [66], i.e $\simeq 10 - 11nN$:

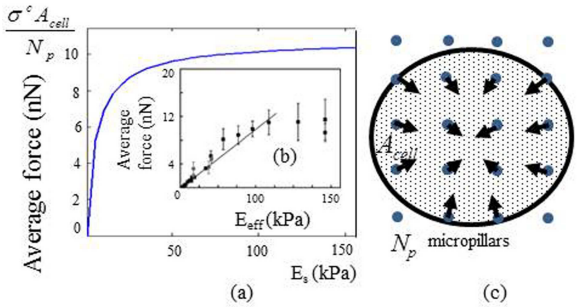

Figure 8.2: *Effect of an isotropic substrate stiffness increase on cell contractility as predicted by (a) the model and (b) experimental methods [66]. (c) schematic representation of experimental set up in [66], with* $N_p \simeq 100$.

8.2 Model prediction of SF distribution

8.2.1 Effect of substrate stiffness

We now propose to use the model to investigate the influence of substrate stiffness on cell contraction; which was shown to be significant in contracting fibroblasts for instance [182, 66]. Considering a free-standing isotropic substrate ($\bar{\boldsymbol{\sigma}} = 0$) of thickness h_s and writing the projection of the mechanical equilibrium Eq. (8.6b) in the $\alpha-$ direction, the strain ε_α is found to be:

$$\varepsilon_\alpha = \frac{-\phi_\alpha^{sf}\sigma^\star h_{sf}}{Eh_s/\left((1+\nu)(1-2\nu)\right) + \phi_\alpha^{sf}E_{sf}(\omega)h_{sf}} \tag{8.9}$$

where h_{SF} denotes the thickness of SFs. Using Eq.(8.9) in Eq.(8.7) and Eq.(8.8), one can find the density ϕ_α^{sf} and contractile stress $\phi_\alpha^{sf}\sigma^\star$ in terms of substrate stiffness E. The model predicts a pronounced nonlinear relation between contractile stress $\phi_\alpha^{sf}\sigma^\star$ and substrate stiffness (Fig.8.2a), characterized by an asymptotic value which corresponds to SF volume fraction of 4% for very large substrate stiffness. This behavior is explained by the fact that contractile strain $-\varepsilon_\alpha$ decreases with substrate stiffness, which induces SF stabilization at high stiffness (see Fig.8.1.a.). The predicted isotropic SF volume fraction and stiffness-contraction relation qualitatively matches with experimental trends [66] as shown in Fig.8.2b. Note that the discrepancy between the initial slopes of the curves likely arises from phenomena that are not accounted for in the present model, including bio-chemical signals and the strain dependency of sarcomere contraction.

8.2.2 Effect of constant stretch

Let us now turn to the case where cells are subjected to substrate deformation. Experimentally, SFs in contractile cells such as fibroblasts or myofibrils have been shown to preferably align in the direction of stretch for constant loading [127, 144] and perpendicular to it for cyclic loading (around a frequency of 1 Hz) [88]. To replicate the constant substrate stretch condition, we impose a state of uniaxial strain $\bar{\epsilon}_{11}$ to the substrate such that the angular stretch in a cell is written $\varepsilon_\alpha = \bar{\varepsilon}_\alpha = \bar{\varepsilon}_{11}\left((1+\nu)\cos^2(\alpha) - \nu\right)$. This expression is then substituted in Eq.(8.7)

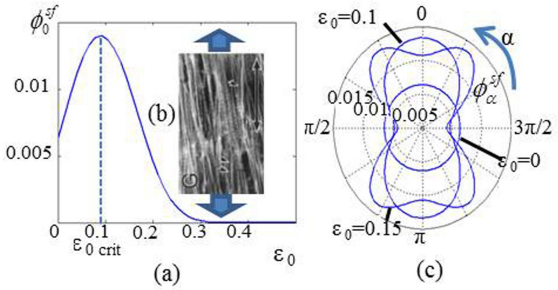

Figure 8.3: *The effect of constant stretch on the volume fraction of SF ϕ_0^{sf} in direction $\alpha = 0$ is shown in figure (a), and (b) shows the orientation and disassembly of myofibrils (when overstretched) [144] with the arrows representing the direction of stretch. Figure (c) is the angular distribution.*

and Eq.(8.8) to derive the angular variation of SF density ϕ_α^{sf}. As shown in Fig.8.3, the model predicts a strong alignment of SFs in direction of stretch (Fig.8.3c). However, once the critical strain is reached, SFs lose stability and start disassembling with stretch. This behavior can be understood by observing the curve corresponding to $\omega = 0$Hz in Fig.8.1.a. where $\mu_\alpha^{sf,mech}$ successively goes through assembling and disassenbling phases (Fig.8.3a) as strain increases; and has been experimentally observed in myofibrils (Fig.8.3b). [144, 103].

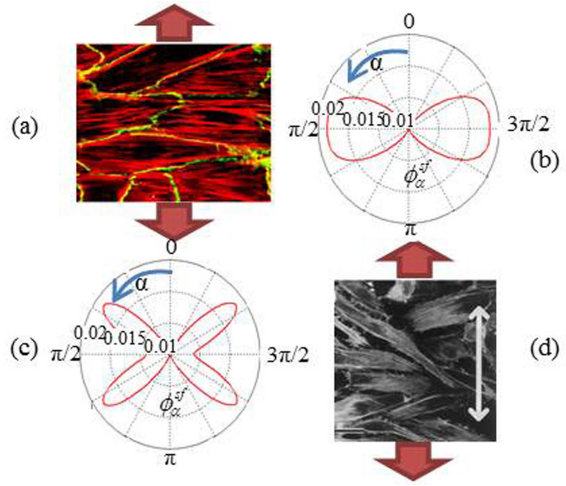

Figure 8.4: *Effect of cyclic stretching for $\nu = 0$ (b)(experimental result (a) from [88]) and $\nu = 0.5$ (c) (experimental result (d) from [151]).*

8.2.3 Effect of cyclic stretch

In the case of cyclic stretch, the angular strain in a cell becomes $\varepsilon_\alpha = \bar{\varepsilon}_\alpha + \tilde{\varepsilon}_\alpha \cos(2\pi t/T)$ with $\tilde{\varepsilon}_\alpha = \tilde{\varepsilon}_{11}\left((1+\nu)\cos^2(\alpha) - \nu\right)$ and $\tilde{\varepsilon}_{11}$ the applied cyclic uniaxial strain. Conversely to the case of constant stretch, experimental observations have shown that SFs align in the direction of minimum stretch, i.e. perpendicular to the direction of cyclic stretching for a substrate's Poisson's ratio $\nu = 0$ (no transverse compression) [88] or at a 60° angle for incompressible substrates ($\nu = 0.5$) [151] (Fig.8.4.). Indeed, introducing the cyclic stretch term $\tilde{\varepsilon}_\alpha$ and a higher frequency ω in Eq.(8.5) increases the SF's viscoelastic stiffness and the contribution of the elastic energy in the SF's mechano-chemical potential $\mu_\alpha^{sf,mech}$; and results in a more convex function $\mu_\alpha^{sf,mech}$ (curve corresponding to $\omega = 1$Hz in Fig.8.1.a.). This causes the strain to have a disassenbling effect on SFs and leads to high SF density in directions of minimum strain, i.e. 90° for $\nu = 0$ and 60° for $\nu = 0.5$. The predicted SF distributions in the case of cyclic stretching for Poisson's ratios of 0 and 0.5, shown in Fig.8.4., are amenable to direct comparison with the experimental images of [88] and [151]. These results explain how SF visco-elasticity leads to two completely different SF organizations depending on loading frequency.

8.3 conclusion

To summarize, this chapter presented a thermodynamical model that aims at describing the formation and distribution of SFs when subjected to various mechanical stimuli. Model contributions are two-folds; first by incorporating a mechanical contribution into the chemical potential of SFs, the formulation enables a natural coupling between chemical stability and stress/strain states in SFs. Second, the approach revealed the importance of a viscoelastic description of SFs to accurately describe their rate-dependent behavior under constant or cyclic stretching. It also shows that, while choosing physiological parameters consistent with experimental data, the hypotheses by which SFs are stabilized by contractile stress and disassembled by their elastic energy give results that concur with experimental observations in all the cases tested.

Chapter 9

Summary and future work

In this thesis, we developed the theoretical and numerical tools to describe the complex mechanics of biological cells and vesicles. We presented an Eulerian formulation for immersed thin membranes and have applied it to model problems of biological interest, such as the permeation of soft particles through filtration membranes, or the endocytosis of nanoparticles by the cell membrane and cell blebbing, in which the cell membrane plays a key role. We then presented an Eulerian formulation for the mechanics of embedded soft mater. These Eulerian formulations and numerical methods allowed us to completely remove issues such as mesh distortion associated with classical Lagrangian models when modelling large deformations. We showed that they are perfectly adapted to the study of the mechanics of live biological cells and their constitutive models that include constant remodelling and viscoelastic behaviors. Finally, such a constitutive model was introduced in chapter 6, where we developed a simple thermodynamical formulation that accounts for the formation and orientation of stress fibers.

Possible future work would first consist in incorporating a fluid in the embedded soft mater problem, as the present numerical implementation only accounts for the deformation of an elastic body. The thermodynamical model of the formation of stress fibers would then be used within the framework of the soft mater formulation to describe the formation and orientation of SF in more complex geometries and loading configurations (such as a cell resting on micro-pillars) and directly compare the results with experimental studies. The aim of this study here would be to understand the dynamics of SF formation as they play a key role in numerous biological cell

functions. As the numerical implementation of the immersed membrane and soft mater problem bear many similarities and were developed using many of the same tools, the next step would therefore consist in integrating them into one single formulation to study the filtration of cells and vesicles through an elastic porous membrane. This particular problem has numerous applications in water filtration systems, cancerous/healthy cell sorting or drug delivery mechanisms. The model would be able to bring insights on how deformable live cells that actively contract and adhere can plug or filtrate trough a porous membrane.

Bibliography

[1] N. Alleborn, K. Nandakumar, H. Raszillier, and F. Durst. Further contributions on the two-dimensional flow in a sudden expansion. *Journal of Fluid Mechanics*, 330:169–188, 1997.

[2] Theresa M Allen and Pieter R Cullis. Liposomal drug delivery systems: from concept to clinical applications. *Advanced drug delivery reviews*, 65(1):36–48, January 2013.

[3] John L. Anderson. Colloid Transport by Interfacial Forces. *Ann. Rev. Fluid Mech.*, 21(1):61–99, 1989.

[4] Tuan Anh, Dimitrios V Papavassiliou, Lloyd L Lee, and Alberto Striolo. Liquid water can slip on a hydrophilic surface. *PNAS*, 108(39):16170–16175, 2011.

[5] C. Annavarapu, M. Hautefeuille, and J.E. Dolbow. A robust Nitsche's formulation for interface problems. *Computer Methods in Applied Mechanics and Engineering*, 225-228:44 – 54, 2012.

[6] Marino Arroyo and Antonio DeSimone. Relaxation dynamics of fluid membranes. *Physical Review E*, 79(3), March 2009.

[7] Frank P T Baaijens. A fictitious domain / mortar element method for fluid structure interaction. (May 1999):743–761, 2001.

[8] I. Babuška and U. Banerjee. Stable Generalized Finite Element Method (SGFEM). *Computer Methods in Applied Mechanics and Engineering*, 201-204:91–111, January 2012.

[9] RW Baker. *Membrane technology and applications*. 2nd edition, 2004.

[10] Ruth E. Baltus, Appala Raju Badireddy, Wendong Xu, and Shankararaman Chellam. Analysis of Configurational Effects on Hindered Convection of Nonspherical Bacteria and Viruses across Microfiltration Membranes. *Industrial & Engineering Chemistry Research*, 48(5):2404–2413, March 2009.

[11] Francine Battaglia, Simon J. Tavener, Anil K. Kulkarni, and Charles L. Merkle. Bifurcation of low Reynolds number flows in symmetric channels, 1997.

[12] Ivan B. Bazhlekov, Patrick D. Anderson, and Han E. H. Meijer. Nonsingular boundary integral method for deformable drops in viscous flows. *Physics of Fluids*, 16(4):1064, 2004.

[13] Y. Bazilevs, K. Takizawa, and T.E. Tezduyar. *ALE and Space-Time Methods for Moving Boundaries and Interfaces*, pages 83–109. John Wiley and Sons, Ltd, 2013.

[14] E. Béchet, H. Minnebo, N. Moës, and B. Burgardt. Improved implementation and robustness study of the X-FEM for stress analysis around cracks. *International Journal for Numerical Methods in Engineering*, 64(8):1033–1056, October 2005.

[15] E. Béchet, N. Moës, and B. Wohlmuth. A stable Lagrange multiplier space for stiff interface conditions within the extended finite element method. *International Journal for Numerical Methods in Engineering*, 78(8):931–954, 2009.

[16] Rainer Beck, Britta Bruegger, and Felix T Wieland. Membrane deformation and separation. *F1000 biology reports*, 2(May):23–25, 2010.

[17] G I Bell. Models for the specific adhesion of cells to cells. *Science (New York, N.Y.)*, 200(4342):618–27, May 1978.

[18] G I Bell, M Dembo, and P Bongrand. Cell adhesion. Competition between nonspecific repulsion and specific bonding. *Biophysical journal*, 45(6):1051–64, June 1984.

[19] T. Belytschko and T. Black. Elastic crack growth in finite elements with minimal remeshing. *International Journal for Numerical Methods in Engineering*, 45:601–620, 1999.

[20] Ted Belytschko, Chandu Parimi, Nicolas Moës, N Sukumar, and Shuji Usui. Structured extended finite element methods for solids defined by implicit surfaces. *International Journal for Numerical Methods in Engineering*, 56(4):609–635, 2003.

[21] D.J. Benson. An efficient, accurate, simple ALE method for nonlinear finite element programs. *Comput. Methods Appl. Mech. Engrg.*, 72(3):305 – 350, 1989.

[22] D.J. Benson. Computational methods in Lagrangian and Eulerian hydrocodes. *Comput. Methods Appl. Mech. Engrg.*, 99(2-3):235 – 394, 1992.

[23] J Block, T E B Stradal, J Hänisch, R Geffers, S A Köstler, E Urban, J V Small, K Rottner, and J Faix. Filopodia formation induced by active mDia2/Drf3. *Journal of Microscopy*, 231(3):506–517, 2008.

[24] S L Brenner and E D Korn. On the mechanism of actin monomer-polymer subunit exchange at steady state. *The Journal of biological chemistry*, 258(8):5013–20, April 1983.

[25] Jan Brugués, Benoit Maugis, Jaume Casademunt, Pierre Nassoy, François Amblard, and Pierre Sens. Dynamical organization of the cytoskeletal cortex probed by micropipette aspiration. *Proceedings of the National Academy of Sciences of the United States of America*, 107(35):15415–20, August 2010.

[26] D.T. Butcher, T. Alliston, and V.M. Weaver. A tense situation: forcing tumour progression. *Nat. Rev. Cancer*, 9:108–122, 2009.

[27] Gregor Cevc. Lipid vesicles and other colloids as drug carriers on the skin. *Advanced drug delivery reviews*, 56(5):675–711, March 2004.

[28] Elie Chahine, Patrick Laborde, and Yves Renard. Crack tip enrichment in the XFEM method using a cut-off function. (December):1–15, 2006.

[29] F Chamaraux, O Ali, S Keller, F Bruckert, and B Fourcade. Physical model for membrane protrusions during spreading. *Physical biology*, 5(3):036009, January 2008.

[30] G T Charras. A short history of blebbing. *Journal of microscopy*, 231(3):466–78, September 2008.

[31] Guillaume Charras and Ewa Paluch. Blebs lead the way: how to migrate without lamellipodia. *Nature reviews. Molecular cell biology*, 9(9):730–6, September 2008.

[32] Guillaume T Charras, Chi-Kuo Hu, Margaret Coughlin, and Timothy J Mitchison. Reassembly of contractile actin cortex in cell blebs. *The Journal of cell biology*, 175(3):477–90, November 2006.

[33] Abhishek Chaudhuri, Giuseppe Battaglia, and Ramin Golestanian. The effect of interactions on the cellular uptake of nanoparticles. *Physical biology*, 8(4):046002, August 2011.

[34] Munir Cheryan. Membrane technology in the vegetable oil industry. *Membrane Technology*, 2005(2):5–7, 2005.

[35] E.S. Choi, L. Lavier, and M. Gurnis. Thermomechanics of mid-ocean ridge segmentation. *Physics of Earth and Planetary Interiors*, 171(1-4):374–386, 2008.

[36] M. Chrzanowska-Wodnicka and K. Burridge. Rho-stimulated contractility drives the formation of stress fibers and focal adhesions. *The Rockefeller University Press*, 1996.

[37] Georges-Henri Cottet and Emmanuel Maitre. A level set method for fluid-structure interactions with immersed surfaces. *Mathematical Models and Methods in Applied Sciences*, 16(03):415, 2006.

[38] Georges-henri Cottet, Emmanuel Maitre, and Thomas Milcent. Eulerian formulation and level set models for incompressible fluid-structure interaction. *ESAIM Mathematical Modelling and Numerical Analysis*, 42(3):471–492, 2008.

[39] P.A. Cundall. Numerical experiments on localization in frictional materials. *Ingenieur Archiv.*, 59(2):148–159, 1989.

[40] Henry Darcy. *Les fontaines publiques de la ville de Dijon.* 1856.

[41] P G De Gennes, F Brochard-Wyart, and D Quere. *Capillarity and Wetting Phenomena.* Springer, 2004.

[42] Pierre-Gilles De Gennes, Francoise Brochard-Wyart, and David Quere. *Capillarity and Wetting Phenomena: Drops, Bubbles, Pearls, Waves*, volume 57. Springer, 2004.

[43] Panadda Dechadilok and William M. Deen. Hindrance Factors for Diffusion and Convection in Pores. *Industrial & Engineering Chemistry Research*, 45(21):6953–6959, October 2006.

[44] P Decuzzi and M Ferrari. The role of specific and non-specific interactions in receptor-mediated endocytosis of nanoparticles. *Biomaterials*, 28(18):2915–22, June 2007.

[45] D. Demarco and E. N. Dvorkin. An Eulerian finite element formulation for modelling stationary finite strain elastic deformation processes. *Intl. J. Numer. Methods in Engrg.*, 62(8):1038–1063, 2005.

[46] M. Dembo, D. C. Torney, K. Saxman, and D. Hammer. The Reaction-Limited Kinetics of Membrane-to-Surface Adhesion and Detachment. *Proceedings of the Royal Society B: Biological Sciences*, 234(1274):55–83, June 1988.

[47] Tejal A Desai, Derek J Hansford, Amir H Nashat, Guido Rasi, Jay Tu, Yuchun Wang, Miqin Zhang, and Mauro Ferrari. Nanopore Technology for Biomedical Applications. pages 11–40, 2000.

[48] V. S. Deshpande, M. Mrksich, R. M. McMeeking, and A. G Evans. A bio-mechanical model for coupling cell contractility with focal adhesion formation. *J. of the Mech and Phys of Solids.*, 56,4:1484–1510, 2008.

[49] J. Dolbow and I. Harari. An efficient finite element method for embedded interface problems. *Intl. J. Numer. Methods in Engrg.*, 78(2):229–252, 2009.

[50] S. Doll and K. Schweizerhof. On the development of volumetric strain energy functions. *Journal of Applied Mechanics*, 67(1):17–21, 2000.

[51] J L Drury and M Dembo. Hydrodynamics of micropipette aspiration. *Biophysical journal*, 76(1 Pt 1):110–28, January 1999.

[52] R Duddu, Stephane Pierre Alain Bordas, B Moran, and D Chopp. A combined extended finite element and level set method for biofilm growth. *International Journal for Numerical Methods in Engineering*, 74(October 2007):848–870, 2008.

[53] R. Duddu, L. L. Lavier, T. J. R. Hughes, and V. M. Calo. A finite strain Eulerian formulation for compressible and nearly incompressible hyper-elasticity using high-order B-spline finite elements. *Intl. J. Numer. Methods in Engrg.*, 89(6):762–785, 2012.

[54] Nagi El-Abbasi and Klaus-Jürgen Bathe. Stability and patch test performance of contact discretizations and a new solution algorithm. *Computers & Structures*, 79(16):1473–1486, June 2001.

[55] Evan Evans, Volkmar Heinrich, Andrew Leung, and Koji Kinoshita. Nano- to microscale dynamics of P-selectin detachment from leukocyte interfaces. I. Membrane separation from the cytoskeleton. *Biophysical journal*, 88(3):2288–98, March 2005.

[56] Oliver T Fackler and Robert Grosse. Cell motility through plasma membrane blebbing. *The Journal of cell biology*, 181(6):879–84, June 2008.

[57] Rs Faibish, M Elimelech, and Y Cohen. Effect of Interparticle Electrostatic Double Layer Interactions on Permeate Flux Decline in Crossflow Membrane Filtration of Colloidal Suspensions: An Experimental Investigation. *Journal of colloid and interface science*, 204(1):77–86, August 1998.

[58] Mehdi Farsad and Franck J Vernerey. An XFEM-based numerical strategy to model mechanical interactions between biological cells and a deformable substrate. *Int. J. Numer. Meth. Engng*, 2012.

[59] Mehdi Farsad, Franck J Vernerey, and Harold S Park. An extended finite element / level set method to study surface effects on the mechanical behavior and properties of nanomaterials. *Int. J. Numer. Meth. Engng*, 2010.

[60] R. M. Fearn, T. Mullin, and K. A. Cliffe. Nonlinear flow phenomena in a symmetric sudden expansion, 1990.

[61] L. C Foucard and F. J Vernerey. Particle-based Moving Interface Method for the study of immersed soft vesicles. *IJNME (under review)*, pages 1–31, 2014.

[62] Louis Foucard and Franck J Vernerey. A thermodynamical model for stress-fiber organization in contractile cells. *Applied Physics Letters*, 100(1):13702–137024, 2012.

[63] Louis C Foucard and Franck J Vernerey. An X-FEM based numerical-asymptotic expansion for simulating a Stokes flow near a sharp corner. *IJNME (under review)*, 2014.

[64] Thomas-peter Fries and Ted Belytschko. The extended / generalized finite element method : An overview of the method and its applications. (April):253–304, 2010.

[65] Huajian Gao, Wendong Shi, and Lambert B Freund. Mechanics of receptor-mediated endocytosis. *Proceedings of the National Academy of Sciences of the United States of America*, 102(27):9469–74, July 2005.

[66] M. Ghibaudo, A. Saez, L. Trichet, A. Xayaphoummine, J. Browaeys, P. Silberzan, A. Buguin, and B. Ladoux. Traction forces and rigidity sensing regulate cell functions. *Soft Matter*, 2008.

[67] J. Glimm, J. W. Grove, X. L. Li, and D. C. Tan. Robust computational algorithms for dynamic interface tracking in three dimensions. *SIAM J. Sci. Comput.*, 21(6):2240–2256, 1999.

[68] R Glowinski, T Pan, T I Hesla, and D D Joseph. A distributed Lagrange multiplier / ctitious domain method for particulate ows. 25, 1999.

[69] Roland Glowinski, Tsorng-Whay Pan, and Jacques Periaux. A fictitious domain method for external incompressible viscous flow modeled by Navier-Stokes equations. *Computer Methods in Applied Mechanics and Engineering*, 112(1-4):133–148, February 1994.

[70] G Gregoriadis and AT Florence. Liposomes in drug delivery. Clinical, diagnostic and ophthalmic potential. *Drugs*, 45(1):15–28, 1993.

[71] R.B. Haber. A mixed Eulerian-Lagrangian displacement model for large-deformation analysis in solid mechanics. *Comput. Methods Appl. Mech. Engrg.*, 43(3):277 – 292, 1984.

[72] A.K. Harris, D. Stopak, and P. Wild. Fibroblast traction as a mechanism for collagen morphogenesis. *Nature*, 290:249–251, 1980.

[73] G. Hattori, R. Rojas-Díaz, a. Sáez, N. Sukumar, and F. García-Sánchez. New anisotropic crack-tip enrichment functions for the extended finite element method. *Computational Mechanics*, 50(5):591–601, March 2012.

[74] Takumi Hawa and Zvi Rusak. Numerical-Asymptotic Expansion Matching for Computing a Viscous Flow Around a Sharp Expansion Corner. pages 265–281, 2002.

[75] W Helfrich. Elastic properties of lipid bilayers: theory and possible experiments. *Zeitschrift fur Naturforschung Teil C Biochemie Biophysik Biologie Virologie*, 28(11):693–703, 1973.

[76] W Helfrich. Helfrich.pdf, 1973.

[77] S.E. Hieber and P. Koumoutsakos. An immersed boundary method for smoothed particle hydrodynamics of self-propelled swimmers. *Journal of Computational Physics*, 227(19):8636–8654, October 2008.

[78] D.J. Hill, D. Pullin, M. Ortiz, and D. Meiron. An Eulerian hybrid WENO centered-difference solver for elastic-plastic solids. *J. Comp. Physics*, 229(24):9053 – 9072, 2010.

[79] Eric M. V. Hoek, Albert S. Kim, and Menachem Elimelech. Influence of Crossflow Membrane Filter Geometry and Shear Rate on Colloidal Fouling in Reverse Osmosis and Nanofiltration Separations. *Environmental Engineering Science*, 19(6):357–372, November 2002.

[80] Richard Holdich, Serguei Kosvintsev, Iain Cumming, and Sergey Zhdanov. Pore design and engineering for filters and membranes. *Philosophical transactions. Series A, Mathematical, physical, and engineering sciences*, 364(1838):161–74, January 2006.

[81] P.A.A. Hoogstraten, P.M.A. Slaats, and F.P.T. Baaijens. A Eulerian approach to the finite element modelling of neo-Hookean rubber material. *Applied Scientific Research*, 48(1):193–210, 1991.

[82] L Howarth. On the flow past a quarter infinite plate using Oseen s equations. *Fluid Mechanics*, 7, 1959.

[83] T.J.R. Hughes, W.K. Liu, and T.K. Zimmermann. Lagrangian-Eulerian finite element formulation for incompressible viscous flows. *Comput. Methods Appl. Mech. Engrg.*, 29(3):329 – 349, 1981.

[84] Kuo-Jen Hwang, Chien-Yao Liao, and Kuo-Lun Tung. Effect of membrane pore size on the particle fouling in membrane filtration. *Desalination*, 234(1-3):16–23, December 2008.

[85] S II, K Sugiyama, S Takeuchi, S Takagi, and Y Matsumoto. An implicit full Eulerian method for the fluid structure interaction problem. *Library*, 65(October 2010):150–165, 2011.

[86] Har Jason and Tamma Kumar. *Advances in Computational Dynamics of Particles, Materials and Structures*. John Wiley & Sons, Ltd, 2012.

[87] A.A. Johnson and T.E. Tezduyar. Mesh update strategies in parallel finite element computations of flow problems with moving boundaries and interfaces. *Comput. Methods Appl. Mech. Engrg.*, 119(1-2):73 – 94, 1994.

[88] K. Kaunas, P. Nguyen, S. Usami, and S. Chien. Cooperative effects of rho and mechanical stretch on stress fiber organization. *pnas*, 2005.

[89] K. Kawabata, Y. Sado, M. Nagayama, T. Nitta, K. Nemoto, Y. Koyama, and H. Haga. Visualization of dynamic organization of cytoskeleton gels in living cells by hybrid-spm. *Chinese J. of Polymer Science*, 21,2:169–174, 2003.

[90] T.-Y. Kim, J. Dolbow, and T. Laursen. A mortared finite element method for frictional contact on arbitrary interfaces. *Comput. Mech.*, 39(3):223–235, 2007.

[91] Bathe KJ. *Finite element procedures*. Prentice Hall, Englewood Clis, N.J, 1996.

[92] E D Korn. Actin polymerization and its regulation by proteins from nonmuscle cells. *Physiological reviews*, 62(2):672–737, April 1982.

[93] S. Kumar, I. Z. Maxwell, A. Heisterkamp, T. R. Polte, T. P. Lele, M. Salanga, E. Mazur, and D. E. Ingber. Viscoelastic retraction of single living stress fibers and its impact on cell shape, cytoskeletal organization, and extracellular matrix mechanics. 85:3762–3773, 2006.

[94] L.D. Landau and E.M. Lifshitz. *Fluid Mechanics (2nd Ed)*. Pergamon Press, 1987.

[95] L.L. Lavier and W.R. Buck. Half graben versus large-offset low-angle normal fault: Importance of keeping cool during normal faulting. *Journal of Geophysical Research - Solid Earth*, 107(B6):2122, 2002.

[96] C. F. Lee, C. Haase, S. Deguchi, and R. Kaunas. Cyclic stretch-induced stress fiber dynamics - dependence on strain rate, rho-kinase and mlck. *Biochemical abd Biophysical Research Communications*, 401(3):344–349, 2010.

[97] F M Leslie. Continuum Mechanics Thermodynamlcs Continuum theory for nematic liquid crystals. *Continuum*, 4:167–175, 1992.

[98] S. Leung and H. Zhao. A grid based particle method for moving interface problems. *J. Comp. Physics*, 228(8):2993 – 3024, 2009.

[99] Shingyu Leung, John Lowengrub, and Hongkai Zhao. A Grid Based Particle Method for Solving Partial Differential Equations on Evolving Surfaces and Modeling High Order Geometrical Motion. pages 2540–2561, 2011.

[100] Shingyu Leung and Hongkai Zhao. A grid based particle method for moving interface problems. *Journal of Computational Physics*, 228(8):2993–3024, May 2009.

[101] Chun Liu and Noel J Walkington. An Eulerian Description of Fluids Containing Visco-Elastic Particles. *Archive for Rational Mechanics and Analysis*, 159(3):229–252, 2001.

[102] W.K. Liu, C. Herman, C. Jiun-Shyan, and T. Belytschko. Arbitrary Lagrangian-Eulerian Petrov-Galerkin finite elements for nonlinear continua. *Comput. Methods Appl. Mech. Engrg.*, 68(3):259 – 310, 1988.

[103] L. Lu, Y. Feng, W. J. Hucker, S. Oswald, G. D. Longmore, and F. C-P. Yin. Actin stress fiber pre-extension in human aortic endothelial cells. *Cell Motility and the Cytoskeleton*, 65:281–294, 2008.

[104] Lin Ma and William S Klug. Viscous regularization and r-adaptive remeshing for finite element analysis of lipid membrane mechanics. *Methods*, 227:5816–5835, 2008.

[105] M. Makale. Cellular mechanobiology and cancer metastasis. *Birth Defects Research (Part C)*, 81:329–343, 2007.

[106] L. E. Malvern. *Introduction to the Mechanics of a Continuous Medium*. Prentice-Hall, Englewood Cliffs, NJ, USA, 1969.

[107] P. Martin. Wound healing: Aiming for perfect skin regeneration. *Science*, 276:75–81, 1997.

[108] Miccal T. Matthews and James M. Hill. Micro/nano sliding plate problem with Navier boundary condition. *Zeitschrift für angewandte Mathematik und Physik*, 57(5):875–903, June 2006.

[109] Harvey T McMahon and Jennifer L Gallop. Membrane curvature and mechanisms of dynamic cell membrane remodelling. *Nature*, 438(7068):590–6, December 2005.

[110] Alexander Menk and Stéphane P A Bordas. A robust preconditioning technique for the extended finite element method. (October 2010):1609–1632, 2011.

[111] R. Merle and J. Dolbow. Solving thermal and phase change problems with the extended finite element method. *Comp. Mech.*, 28(5):339–350, 2002.

[112] N. Moës, J. Dolbow, and T. Belytschko. A finite element method for crack growth without remeshing. *International Journal for Numerical Methods in Engineering*, 46(1):131–150, 1999.

[113] Nicolas Moës, Eric Béchet, and Matthieu Tourbier. Imposing Dirichlet boundary conditions in the extended finite element method. *International Journal for Numerical Methods in Engineering*, 67(12):1641–1669, September 2006.

[114] Nicolas Moës, John Dolbow, and Ted Belytschko. A finite element method for crack growth without remeshing. *International Journal for Numerical Methods in Engineering*, 46(1):131–150, 1999.

[115] H K Moffatt. Viscous and resistive eddies near a sharp corner. 18:1–18, 1963.

[116] T. Mullin, J. R. T. Seddon, M. D. Mantle, and a. J. Sederman. Bifurcation phenomena in the flow through a sudden expansion in a circular pipe. *Physics of Fluids*, 21(1):014110, 2009.

[117] S Okazawa, K Kashiyama, and Y Kaneko. Eulerian formulation using stabilized finite element method for large deformation solid dynamics. *Online*, 72(May):1544–1559, 2007.

[118] S. Okazawa, K. Kashiyama, and Y. Kaneko. Eulerian formulation using stabilized finite element method for large deformation solid dynamics. *Intl. J. Numer. Methods in Engrg.*, 72(13):1544–1559, 2007.

[119] J E Olberding, M D Thouless, E M Arruda, and K Garikipati. IUTAM Symposium on Cellular, Molecular and Tissue Mechanics. *Stress: The International Journal on the Biology of Stress*, 16, 2010.

[120] S. Osher and J. A. Sethian. Fronts propagating with curvature-dependent speed: Algorithms based on Hamilton-Jacobi formulations. *J. Comp. Physics*, 79(1):12–49, November 1988.

[121] M. Paszek, N. Zahir, K Johnson, J. Lakins, G. Rozenberg, A Gefen, C.A. Reinhart-King, S. Margulies, M. Dembo, D. Boettiger, D.A. Hammer, and V.M. Weaver. Tensional homeostasis and the malignant phenotype. *Cancer Cell*, 8:241–254, 2005.

[122] A. Pathak, V. S. Deshpande, R. M. McMeeking, and A. G. Evans. The simulation of stress fibre and focal adhesion development in cells on patterned substrates. *J.The. Roy. Soc. Int..*, 5:507–524, 2008.

[123] Blair Perot and Ramesh Nallapati. A moving unstructured staggered mesh method for the simulation of incompressible free-surface flows. *Journal of Computational Physics*, 184(1):192–214, January 2003.

[124] C Peskin. Flow patterns around heart valves: A numerical method. *Journal of Computational Physics*, 10(2):252–271, 1972.

[125] Charles S. Peskin. The immersed boundary method. *Acta Numerica*, 11(1):1–39, 2002.

[126] C.S. Peskin. Numerical analysis of blood flow in the heart.pdf. *Journal of Computational Physics*, 25(1):220–252, 1977.

[127] P. P. Pirentis and K. A. Lazopoulos. On stress bre reorientation under plane substrate stretching. *Arch Appl Mech*, 79:263–277, 2009.

[128] Thomas D Pollard and Gary G Borisy. Cellular motility driven by assembly and disassembly of actin filaments. *Cell*, 112(4):453–65, February 2003.

[129] A Ponti, M Machacek, S L Gupton, C M Waterman-Storer, and G Danuser. Two distinct actin networks drive the protrusion of migrating cells. *Science*, 305(5691):1782–6, 2004.

[130] Julian J Pop. Acceleration Waves in Isotropic Elastic Membranes. *Archive for Rational Mechanics and Analysis*, 77(1):47–93, 1981.

[131] C. Pozrikidis. Flow-induced deformation of an elastic membrane adhering to a wall. *International Journal of Solids and Structures*, 46(17):3198–3208, August 2009.

[132] C. Pozrikidis. *Introduction to Theoretical and Computational Fluid Dynamics*. Oxford University Press, Oxford, 2011.

[133] W Rawicz, K C Olbrich, T McIntosh, D Needham, and E Evans. Effect of chain length and unsaturation on elasticity of lipid bilayers. *Biophysical journal*, 79(1):328–39, July 2000.

[134] Casey L Richardson, Jan Hegemann, Eftychios Sifakis, Jeffrey Hellrung, and Joseph M Teran. An XFEM method for modelling geometrically elaborate crack propagation in brittle materials. pages 1–41, 2009.

[135] T. Richter. A fully Eulerian formulation for fluid-structure-interaction problems. *J. Comp. Physics*, 233:227 – 240, 2013.

[136] Henning Sauerland and Thomas-peter Fries. The stable XFEM for two-phase flows.

[137] J. A. Sethian. A marching level set method for monotonically advancing fronts. *Proceedings of the National Academy of Sciences*, 93(4):1591–1595, 1996.

[138] J. A. Sethian. *Level Set Methods & Fast Marching Methods: Evolving Interfaces in Computational Geometry, Fluid Mechanics, Computer Vision, and Materials Science*. Cambridge University Press, Cambridge, UK, 1999.

[139] M. Shapira, D. Degani, and D. Weihs. Stability and existence of multiple solutions for viscous flow in suddenly enlarged channels, 1990.

[140] T. Shemesh, B. Geiger, A. D. Bershadsky, and M. M. Kozlov. Focal adhesions as mechanosensors: A physical mechanism. *pnas*, 2005.

[141] S O Sher. A Level Set Formulation of Eulerian Interface Capturing Methods for Incompressible Fluid Flows. 464(124):449–464, 1996.

[142] J. C. Simo and T. J. R. Hughes. *Computational Inelasticity*. Springer, Berlin, 1998.

[143] J.C. Simo. A finite strain beam formulation. the three dimensional dynamic problem. part 1. *Computer Methods in Applied Mechanics and Engineering*, 49:55–70, 1986.

[144] D.G. Simpson, Majeski, T.K. M. Borg, and L. Terracio. Regulation of cardiac myocyte protein turnover and myofibrillar structure in vitro by specific directions of stretch. *Circulation Research*, 1999.

[145] Shri Singh. *Liquid Crystals: Fundamentals*. 2002.

[146] Lianfa Song. Flux decline in crossflow microfiltration and ultrafiltration: mechanisms and modeling of membrane fouling. *Journal of Membrane Science*, 139(2):183–200, February 1998.

[147] D. Stamenovic, K. A. Lazopoulos, A. Pirentis, and B. E. Suki. Mechanical stability determines stress fiber and focal adhesion orientation. *Cellular and Molecular Bioengineering*, 2009.

[148] K. Stein, T.E. Tezduyar, and R. Benney. Mesh moving techniques for fluid-structure interactions with large displacements. *Journal of Applied Mechanics*, 70(1):58–63, 2003.

[149] Y. Sui, Y. Chew, P. Roy, X. Chen, and H. Low. Transient deformation of elastic capsules in shear flow: Effect of membrane bending stiffness. *Physical Review E*, 75(6):066301, June 2007.

[150] Mingzhai Sun, Nathan Northup, Francoise Marga, Tamas Huber, Fitzroy J Byfield, Irena Levitan, and Gabor Forgacs. The effect of cellular cholesterol on membrane-cytoskeleton adhesion. *Journal of Cell Science*, 120(Pt 13):2223–2231, 2007.

[151] T. Takemasa, K. Sugimoto, and K. Yamashita. Amplitude-dependent stress fiber reorientation in early response to cyclic strain. *Experimental Cell Research*, 230(2):407–410, 1997.

[152] T.E. Tezduyar, M. Behr, and J. Liou. A new strategy for finite element computations involving moving boundaries and interfaces - The deforming-spatial-domain/space-time procedure: I. The concept and the preliminary numerical tests. *Comput. Methods Appl. Mech. Engrg.*, 94(3):339 – 351, 1992.

[153] T.E. Tezduyar, M. Behr, S. Mittal, and J. Liou. A new strategy for finite element computations involving moving boundaries and interfaces - The deforming-spatial-domain/space-time procedure: II. Computation of free-surface flows, two-liquid flows, and flows with drifting cylinders. *Comput. Methods Appl. Mech. Engrg.*, 94(3):353 – 371, 1992.

[154] O Thoumine, O Cardoso, and J J Meister. Changes in the mechanical properties of fibroblasts during spreading: a micromanipulation study. *European biophysics journal EBJ*, 28(3):222–34, 1999.

[155] Jean-Yves Tinevez, Ulrike Schulze, Guillaume Salbreux, Julia Roensch, Jean-François Joanny, and Ewa Paluch. Role of cortical tension in bleb growth. *Proceedings of the National Academy of Sciences of the United States of America*, 106(44):18581–6, November 2009.

[156] H S Udaykumar. *An Eulerian method for computation of multimaterial impact with ENO shock-capturing and sharp interfaces*, volume 186. 2003.

[157] Jasper van der Gucht and Cécile Sykes. Physical model of cellular symmetry breaking. *Cold Spring Harbor perspectives in biology*, 1(1):a001909, July 2009.

[158] Raoul van Loon, Patrick D. Anderson, Frank P.T. Baaijens, and Frans N. van de Vosse. A three-dimensional fluidstructure interaction method for heart valve modelling. *Comptes Rendus Mécanique*, 333(12):856–866, December 2005.

[159] F. J Vernerey and M. Farsad. A constrained mixture approach to mechano-sensing and force generation in contractile cells. *Journal of the mechanical behavior of biomedical materials*, 4(8):1683–99, November 2011.

[160] F. J. Vernerey and M. Farsad. On stress bre reorientation under plane substrate stretching. *A constrained mixture approach to mechano-sensing and force generation in contractile cells*, page doi:10.1016/j.jmbbm.2011.05.022, 2011.

[161] F. J. Vernerey and M. Farsad. A mathematical model of the coupled mechanisms of cell adhesion, contraction and spreading. *Journal of Mathematical Biology*, 68(4):989–1022, 2014.

[162] F. J. Vernerey, C. Greenwald, and S. J. Bryant. Triphasic mixture model of cell-mediated enzymatic degradation of hydrogels. *Computer Methods in Biomechanics and Biomedical Engineering*, pages 1–14, 2011.

[163] Franck Vernerey, Wing Kam Liu, and Brian Moran. Multi-scale micromorphic theory for hierarchical materials. *Journal of the Mechanics and Physics of Solids*, 55(12):2603–2651, December 2007.

[164] Franck J. Vernerey. A theoretical treatment on the mechanics of interfaces in deformable porous media. *International Journal of Solids and Structures*, 48(22-23):3129–3141, November 2011.

[165] Franck J. Vernerey. The Effective Permeability of Cracks and Interfaces in Porous Media. *Transport in Porous Media*, 93(3):815–829, March 2012.

[166] Franck J. Vernerey, Louis Foucard, and Mehdi Farsad. Bridging the Scales to Explore Cellular Adaptation and Remodeling. *BioNanoScience*, 1(3):110–115, July 2011.

[167] E. Vitali and D.J. Benson. An extended finite element formulation for contact in multi-material arbitrary Lagrangian-Eulerian calculations. *Intl. J. Numer. Methods in Engrg.*, 67(10):1420–1444, 2006.

[168] E. Vitali and D.J. Benson. Contact with friction in multi-material arbitrary Lagrangian-Eulerian formulations using X-FEM. *Intl. J. Numer. Methods in Engrg.*, 76(6):893–921, 2008.

[169] G J Wagner, N Moes, W K Liu, and T Belytschko. The extended ÿnite element method for rigid particles in Stokes ow. (September 2000):293–313, 2001.

[170] Haim Waisman and Ted Belytschko. Parametric enrichment adaptivity by the extended finite element method. (July 2007):1671–1692, 2008.

[171] T Wakatsuki, M. S. Kolodney, G. I. Zahalak, and E. L. Elson. Cell mechanics studied by a reconstituted model tissue. *Biophysical Journal*, 79:2353–2368, 2000.

[172] Sam Walcott and Sean X. Sun. A mechanical model of actin stress fiber formation and substrate elasticity sensing in adherent cells. *pnas*, 2010.

[173] W A Wall, A Gerstenberger, and U K. An XFEM Based Fixed-Grid Approach for 3D Fluid-Structure Interaction. In Hans-Joachim Bungartz, Miriam Mehl, and Michael Schäfer, editors, *Fluid Structure Interaction II*, volume 73 of *Lecture Notes in Computational Science and Engineering*, pages 327–349. Springer Berlin Heidelberg, Berlin, Heidelberg, 2010.

[174] Tobias C Walther, Jason H Brickner, Pablo S Aguilar, Sebastián Bernales, Carlos Pantoja, and Peter Walter. Eisosomes mark static sites of endocytosis. *Nature*, 439(7079):998–1003, February 2006.

[175] J.H. Wang. Substrate deformation determines actin cytoskeleton reorganization: a mathematical modeling and experimental study. *J. Theor. Biol.*, 2007.

[176] Xiaodong Wang and Wing Kam Liu. Extended immersed boundary method using FEM and RKPM. *Computer Methods in Applied Mechanics and Engineering*, 193(12-14):1305–1321, March 2004.

[177] a Wegner. Head to tail polymerization of actin. *Journal of molecular biology*, 108(1):139–50, November 1976.

[178] Huibin Wei, Bor-han Chueh, Huiling Wu, Eric W Hall, Cheuk-wing Li, Romana Schirhagl, Jin-Ming Lin, and Richard N Zare. Particle sorting using a porous membrane in a microfluidic device. *Lab on a chip*, 11(2):238–45, January 2011.

[179] Waloddi Weibull. A statistical distribution of wide applicability, 1951.

[180] J.-Z. Wu, Y.-T. Yang, Y.-B. Luo, and C. Pozrikidis. Fluid kinematics on a deformable surface. *Journal of Fluid Mechanics*, 541(-1):371, October 2005.

[181] T. Yamada and F. Kikuchi. An arbitrary Lagrangian-Eulerian finite element method for incompressible hyperelasticity. *Comput. Methods Appl. Mech. Engrg.*, 102(2):149 – 177, 1993.

[182] T. Yeung, P. C. George, L. A. Flanagan, B. Marg, M. Ortiz, M. Funaki, N. Zahir, W. Ming, V. Weaver, and P. A. Janmey. Effects of substrate stiffness on cell morphology, cytoskeletal structure, and adhesion. *Cell Motility and the Cytoskeleton*, 60:24–34, 2005.

[183] Jennifer Young and Sorin Mitran. A numerical model of cellular blebbing: a volume-conserving, fluid-structure interaction model of the entire cell. *Journal of biomechanics*, 43(2):210–20, January 2010.

[184] Hongyan Yuan, Changjin Huang, and Sulin Zhang. Virus-inspired design principles of nanoparticle-based bioagents. *PloS one*, 5(10):e13495, January 2010.

[185] Hongyan Yuan and Sulin Zhang. Effects of particle size and ligand density on the kinetics of receptor-mediated endocytosis of nanoparticles. *Applied Physics Letters*, 96(3):033704, 2010.

[186] Lucy Zhang, Axel Gerstenberger, and Xiaodong Wang. Immersed Finite Element Method. *Computer Methods in Applied Mechanics and Engineering*, (September 2003):1–25, 2002.

[187] Sulin Zhang, Ju Li, George Lykotrafitis, Gang Bao, and Subra Suresh. Size-Dependent Endocytosis of Nanoparticles. *Advanced materials (Deerfield Beach, Fla.)*, 21:419–424, January 2009.

[188] Wei Zhu, Michael Shelley, and Peter Palffy-Muhoray. Modeling and simulation of liquid-crystal elastomers. *Physical Review E*, 83(5):1–11, May 2011.

[189] Alexander Z. Zinchenko, Michael a. Rother, and Robert H. Davis. A novel boundary-integral algorithm for viscous interaction of deformable drops. *Physics of Fluids*, 9(6):1493, 1997.